

# On the nature of early-type galaxies

structure, kinematics and dynamics through  
ground and space-based observations



# On the nature of early-type galaxies

structure, kinematics and dynamics through  
ground and space-based observations

Proefschrift

ter verkrijging van  
de graad van Doctor aan de Universiteit Leiden,  
op gezag van de Rector Magnificus Dr. D.D. Breimer,  
hoogleraar in de faculteit der Wiskunde en  
Natuurwetenschappen en die der Geneeskunde,  
volgens besluit van het College voor Promoties  
te verdedigen op dinsdag 12 oktober 2004  
te klokke 15.15 uur

door

Davor Krajnović

geboren te Zagreb  
in 1975

Promotiecommissie

Promotor: Prof. dr. P.T. de Zeeuw

Co-promotor: Dr. W. Jaffe

Referent: Dr. E. Emsellem

Overige leden: Prof. dr. R. Bacon  
Prof. dr. R. Davies  
Prof. dr. M. Franx  
Prof. dr. K. Kuijken  
Dr. R. F. Peletier

## **Pangur Bán**

*I and Pangur Bán my cat  
'Tis a like task we are at:  
Hunting mice is his delight,  
Hunting words I sit all night.*

*Better far than praise of men  
'Tis to sit with book and pen;  
Pangur bears me no ill will  
He too plies his simple skill.*

*Oftentimes a mouse will stray  
In the hero Pangur's way;  
Oftentimes my keen thought set  
Takes a meaning in its net.*

*'Gainst the wall he sets his eye  
Full and fierce and sharp and sly;  
'Gainst the wall of knowledge I  
All my little wisdom try.*

*Practice every day has made  
Pangur perfect in his trade;  
I get wisdom day and night  
Turning darkness into light.*

*Written by a ninth-century Irish monk in St Gallen, Switzerland*

**Front cover:** a ceramic vessel from the Vučedol culture. Permission to reproduce the picture of this vessel was kindly granted by Gradski Muzej Vinkovci (Vinkovci City Museum). Help with the cover design was graciously given by Pedro Lacerda.

**Back cover:** A sequence of decorative symbols from the vessel shown on the front page, representing stellar constellations characteristic for individual parts of the year (see Chapter 1 for the reference with detailed explanations). Their meaning, from top to bottom: summer Cassiopeia, the Pleiades, Gemini, the Sun, Pegasus and Pisces, Orion, and winter Cassiopeia.

# Table of contents

	Page
<b>Chapter 1. Introduction</b>	<b>1</b>
1 Understanding the world . . . . .	1
2 Galaxies of the early type . . . . .	2
3 A brief guide through the formation and evolution of galaxies . . . . .	3
4 Activity in early-type galaxies . . . . .	5
5 Nuclear stellar discs in early-type galaxies . . . . .	6
6 Integral-field spectroscopy . . . . .	8
7 Two-dimensional kinematic maps . . . . .	8
8 Dynamical models . . . . .	10
8.1 Stellar dynamical models . . . . .	11
8.2 Dynamical models of gas . . . . .	12
9 Outline of this thesis . . . . .	14
10 Future prospects . . . . .	16
<b>Chapter 2. Relation between dust and radio luminosity in early type galaxies</b>	<b>21</b>
1 Introduction . . . . .	21
2 Observations . . . . .	22
2.1 Sample . . . . .	22
2.2 Data Acquisition and Reduction . . . . .	23
3 Results . . . . .	23
4 Discussion . . . . .	25
4.1 Nature of Detected Radio Sources . . . . .	25
4.2 Radio Luminosity Function . . . . .	26
5 Correlation of dust with radio emission . . . . .	28
5.1 Crude Statistics . . . . .	28
5.2 Comparison of RLFs . . . . .	29
6 Conclusions . . . . .	31
<b>Chapter 3. HST observations of nuclear stellar disks</b>	<b>35</b>
1 Introduction . . . . .	35
2 WFPC2 broad band imaging . . . . .	37
2.1 Data reduction . . . . .	38
2.2 Isophotal analysis . . . . .	39
2.3 Broad-band color images . . . . .	41
2.3.1 B-V color images . . . . .	41
2.3.2 B,V-I color images . . . . .	41
3 STIS spectroscopy . . . . .	44
3.1 Data reduction . . . . .	45

3.2	Stellar kinematics . . . . .	48
3.3	Line strengths . . . . .	52
4	Discussion . . . . .	55
4.1	NGC 4128 . . . . .	55
4.2	NGC 4570 . . . . .	56
4.3	NGC 4621 . . . . .	57
4.4	NGC 5308 . . . . .	60
5	Conclusions . . . . .	61
A	Extracted kinematics . . . . .	64
B	A transient in NGC 4128 . . . . .	67
B.1	Extraction of light and results . . . . .	67
B.2	Discussion and conclusions . . . . .	68
<b>Chapter 4. Kinemetry: a method to quantify kinematic maps</b>		<b>73</b>
1	Introduction . . . . .	73
2	Theoretical background and motivation . . . . .	74
3	The method . . . . .	76
3.1	Harmonic expansion . . . . .	76
3.2	Expansion along elliptical annuli . . . . .	78
4	Kinematic parameters and their meaning . . . . .	79
4.1	Model galaxy . . . . .	80
4.2	Odd kinematic moments . . . . .	80
4.3	Even kinematic moments . . . . .	84
4.4	Filtering . . . . .	87
4.5	Expansion of velocity maps using kinemetry along ellipses . . . . .	88
5	Application . . . . .	89
5.1	Prescription for axisymmetry . . . . .	90
5.2	A triaxial case . . . . .	90
5.3	Comparison of velocity fields of early-type galaxies with velocity fields of discs . . . . .	92
6	Conclusions . . . . .	94
<b>Chapter 5. Dynamical modelling of stars and gas in NGC 2974</b>		<b>97</b>
1	Introduction . . . . .	97
2	Observations and data reduction . . . . .	99
2.1	SAURON spectroscopy . . . . .	99
2.2	Absorption-line kinematics . . . . .	100
2.3	Distribution and kinematics of ionised gas . . . . .	101
2.4	Ground- and space-based imaging . . . . .	102
3	Quantitative analysis of velocity maps . . . . .	103
3.1	Harmonic Expansion . . . . .	104
3.2	Kinematic analysis of velocity maps . . . . .	105
3.3	Signature of bars in NGC 2974 . . . . .	107
3.4	Case for axisymmetry in NGC 2974 . . . . .	108
4	Stellar Dynamical Modelling . . . . .	109

---

4.1	The Multi-Gaussian Expansion mass model . . . . .	110
4.2	Construction of three-integral models . . . . .	113
4.3	Stellar dynamics - modelling results and discussion . . . . .	114
5	Tests of Schwarzschild's orbit-superposition models . . . . .	117
5.1	The input two-integral test model . . . . .	118
5.2	Recovery of input parameters . . . . .	119
5.3	Effect of the field coverage on orbital distribution . . . . .	122
5.4	Recovery of the internal moments . . . . .	124
5.5	Recovery of the distribution function . . . . .	124
6	Modelling of emission-line gas . . . . .	126
6.1	Inclination of the gas disc . . . . .	126
6.2	A simple dynamical model for the disc . . . . .	128
7	Concluding remarks . . . . .	130
	<b>Nederlandse samenvatting (Dutch summary)</b>	<b>135</b>
	<b>Hrvatski sažetak (Croatian summary)</b>	<b>145</b>
	<b>Curriculum vitae</b>	<b>153</b>
	<b>Nawoord / Acknowledgments</b>	<b>154</b>



---

# Chapter 1

---

## Introduction

### 1 Understanding the world

THE urge to comprehend and describe the world is a defining characteristic of mankind. One remarkable illustration of this urge is shown on the cover of this thesis. This ceramic vessel, with an ordered sequence of different symbols, is approximately 4500 years old. It was created by a craftsman of the *Vučedol* culture and excavated in 1978 in the town of Vinkovci in eastern Croatia. The classical *Vučedol* culture belongs to the European Neolithic period and was created by newly arrived Indo-European people. This widespread European culture was named after its central site on the river Danube in eastern Croatia. The meaning of the symbols on the vessel was a mystery until recently when Durman (2000) suggested they represent the different stellar constellations which dominated the *Vučedol* sky five millennia ago. The half-broken pot from Vinkovci is very likely the oldest European calendar, used by the people of *Vučedol* for the organisation of their every-day life <sup>1</sup>.

Five thousand years ago, stock-raising people of the Panonic plane were looking at the night sky. They noticed regularities and formed an elaborate system to measure the passing of time. In this way, they were able to describe a crucial aspect of the world using primitive but straightforward astronomical observations. Nowadays, astronomy is a science, having undergone the process of transformation from *predicting the future* by early astrologers to *explaining the facts* by modern astronomers observed with telescopes and instruments using the laws of physics. Still, at the centre of the science of astronomy lies the same wish that led the *Vučedol* people: to comprehend, describe and tame the world around us.

Our methods are much more sophisticated, but the astronomical themes have changed as well. Astronomy had a profound influence on the *Vučedol* people giving them the calendar. It produced valuable information relevant for life. Unlike some other sciences in the present times, astronomy does not directly influence our everyday life anymore. Modern astronomical research is focused on processes that shape the Universe, starting from our Sun, its neighbours, the Milky Way, and other galaxies, to distant quasars and relics of the Big Bang. In a broader sense, the astronomy of today is an idealised pursuit of knowledge of the Universe. Complementary to this, astronomy also records mankind's perception of the world. The advances in astronomy are reflected in changes in philosophy and culture. In the 1960s the size of the Universe

---

<sup>1</sup>An in-depth description of the *Vučedol* culture and particularly the oldest European calendar is given in the exhibition catalogue *The Vučedol Orion* (Durman 2000).

was changing almost on a daily basis with discoveries of ever more distant quasars (e.g. Schmidt 1963). It seems a matter of time only before the first Earth-like planet outside the Solar system<sup>2</sup> will be discovered. The next step will be to search for life on such a planet. Our lives do not directly depend on astronomy anymore, but it does have a long term influence on the human society. Astronomy is our window into the complexity of the Universe. This thesis focuses on a particular aspect of astronomy: the formation and evolution of galaxies.

## 2 Galaxies of the early type

Galaxies were perhaps most elegantly described by Immanuel Kant in the 18th century as “island universes”. Neither he nor anybody else until the astronomers of the early 20th century knew what these island universes, that appeared like nebulae on the sky, actually were; what they were made of, or even how far they were from Earth. Observations with the Mount Wilson 100 inch telescope provided the first clues about the nature of galaxies. They are made of stars and they are at a great distance from our own “island universe”, the Milky Way. Galaxies come in different flavours and they are usually classified in four distinctive groups according to their apparent shape (see Fig. 1 of Nederlandse Samenvatting or Hrvatski sažetak). This classification scheme was introduced by Hubble (1936) and it is known as the Hubble sequence of galaxies (Hubble diagram or Hubble tuning fork are also frequently used terms). The sequence starts with *elliptical* galaxies that seemingly have little or no structure. At the other end are disc galaxies, very different with prominent spiral arms. They are usually called *spirals* emphasising their eye-catching structure. *Lenticular* galaxies (also simply called S0s) look like transition objects between ellipticals and spirals: they have a prominent disc without a significant spiral structure embedded in a nearly spherical distribution of stars. The fourth group of galaxies consists of all galaxies without a regular shape, appropriately called *irregulars*. When constructing the diagram, Hubble was led by the idea of galaxy evolution. Spiral galaxies with their complicated and easily visible structure were natural candidates for complex and evolved systems, while elliptical galaxies were obvious examples of simpler systems. Lenticulars were seen as a stage between the two classes. Although such reasoning is not valid anymore and galaxy evolution should be viewed the other way around (e.g. Kormendy & Bender 1996), the ellipticals and lenticulars are still called early-type galaxies and the spirals are, hence, known as late-type galaxies.

Galaxies are not made only of stars. They also contain gas and dust in different amounts that change with Hubble type: late-type galaxies are observed to have more gas and dust than early-types. A big discovery of the 1970s is that spiral galaxies are embedded in dark matter halos (Rubin & Ford 1970; Rogstad & Shostak 1972; Ostriker et al. 1974). It is believed that all galaxies have dark halos, but the observational evidence for dark halos around elliptical galaxies is not as decisive (Romanowsky et al. 2003). The nature of the dark matter is, however, still unknown, but the observations clearly show that most of the matter in the Universe (> 90%) is non-baryonic, dark matter. Any theory of the formation and evolution of galaxies has to take this into account

---

<sup>2</sup>More than a hundred Jupiter-like gas giants orbiting other stars have already been found.

and explain the variety of morphologies and specific characteristics observed. Unfortunately, the timescales over which galaxies evolve is not comparable to the life span of an astronomer, who must act as a detective looking for evidence of the processes that shaped the observed galaxies. These processes are easily masked by frequent and intensive starformation which is common in late-type galaxies. By contrast, early-type galaxies are particularly well suited for investigation because they do not contain much gas and dust, and, having no recent star formation, retain fossil records of their formation history. Specifically, nearby ( $< 50$  Mpc) early-type galaxies are very interesting, since we are able to obtain accurate, spatially-resolved information (unfortunately not the individual stars, which is currently possible only for the nearest<sup>3</sup> galaxies).

Although generally fairly simple and uniform in appearance, early-type galaxies show a rich structure on a closer look. High-resolution observations are necessary to provide data that can be used to construct theoretical models of early-type galaxies. The observations can be from ground- or space-based telescopes, each contributing in a particular way. The goal is to construct theoretical models and test their description of the processes that shape galaxies with state-of-the-art observations. Indeed, the connection between theory and observations is very important because only by combining their different approaches it is possible to ascertain the nature of the early-type galaxies.

### 3 A brief guide through the formation and evolution of galaxies

Galaxies originate from fluctuations in the dark matter density of the early Universe. An area of higher density accretes material through gravitational interaction until the system becomes unstable and collapses dissipating energy into a small-scale object ( $\sim 10^6 M_{\odot}$ ). According to the hierarchical scenario of galaxy formation (e.g. Press & Schechter 1974; Kauffmann & van den Bosch 2002) small systems merge to form larger and larger objects. These objects are made of gas, but are gravitationally dominated by the dark matter distributed in halos. The temperature of the gas (infalling or already present) is crucial. Stars can form only from cold gas, but gas is easily heated by several processes: motion in the gravitational potential of a galaxy, heating by the new-born stars and supernovae, and interaction with already heated (virialised) gas (e.g. Binney 2004). Heated systems are pressure supported and have a spheroidal structure, but in certain cases cold gas can fall into the equatorial plane forming stars and creating what can be observed today as disc galaxies (e.g. White & Rees 1978).

Early-type galaxies are thought to be formed in mergers of disc galaxies (Barnes & Hernquist 1996). The gas content of the resulting galaxy can be replenished by accretion from larger gaseous structures. This may result in formation of a new disc, renewed star formation and restoration of the galaxy into a late-type. However, each merger will heat the stellar component and form spheroidal structures. These pro-

---

<sup>3</sup>Nearby is a relative term in astronomy. About 40 galaxies (Courteau & van den Bergh 1999), of which only one (the Andromeda galaxy) is comparable in size to Milky Way, make up the *Local Group* of galaxies and are our nearest neighbours, within approximately 1 Mpc. Galaxies discussed in this thesis, which we consider “nearby”, are at distances of 5 to 40 Mpc, but astronomers use the term “nearby” for object which are up to a few times further. Beyond that begins the far Universe.



that, although there are true triaxial galaxies, the majority are only mildly triaxial, almost consistent with axisymmetry (Franx et al. 1991; see also Fig. 2 for preliminary results from SAURON observations). This dark versus luminous matter discrepancy is a stimulus to both theoretical models and observations in search for the true answer. Galaxy formation and evolution is complex and consists of many pieces that have to be well understood individually and assembled together into a coherent picture. Each chapter of this thesis is devoted to a somewhat distinct issue of galaxy evolution. Details on each aspect are given in the following section.

## 4 Activity in early-type galaxies

The centres of many early-type galaxies emit non-stellar radiation. This so-called ‘activity’ is confined to a region within a few parsecs from the centre, and such centres are usually called *active galactic nuclei* (AGN). The same acronym is often used to also specify the whole host galaxy. AGN are sometimes even called *monsters* (Gunn 1979), because they radiate enormous amounts of energy into the surrounding space (e.g.  $E \sim 10^{61}$  erg in total). Generally, AGN appear to be very diverse, and a classification according to their properties is very broad. The bestiary of AGN includes radio-loud and radio-quiete quasars, optically violent quasars, broad and narrow line galaxies, Seyferts (of type 1 and 2) and low-ionisation narrow-line regions (LINERs)<sup>4</sup>, each with different defining characteristics (e.g., Krolik 1999). However, there are also many similarities and properties that lead to a unification scheme and a paradigm that the activity of all AGNs is produced by matter falling onto a supermassive black hole that resides at the bottom of the galaxy’s potential well (Hoyle & Fowler 1963; Lynden-Bell 1969). Different species of AGN are then the manifestation of the same process viewed from different angles and under different conditions.

Distant AGN are on average several orders of magnitude stronger than the AGN residing in the nearby galaxies. Quasars and most of the radio-loud AGN are found at higher redshifts (the population peaks at redshifts of 2-3) while the local population of AGN consists mostly of Seyferts and LINERs. Most quasars reside in early-type galaxies which look similar to normal nearby elliptical galaxies (Ho et al. 1997; McLure et al. 1999, 2000). Still, some amount of activity is present among many of the nearby galaxies, although often of barely detectable intensity: about 40% of all nearby galaxies show some AGN activity and  $\sim 60\%$  of nearby early-type galaxies show AGN characteristics (Ho et al. 1997). In a somewhat limited sample of nearby galaxies we found that 47% of early-type galaxies are active at the level of 0.1 mJy (Chapter 2, Krajnović & Jaffe 2002).

If some nearby galaxies are direct descendants of high-redshift quasars and other AGN, the supermassive black holes should still be present in the nuclei of many galaxies (Soltan 1982). This is now largely accepted and confirmed by the search for black holes in nearby galaxies over the last two decades. The success of the hunt for supermassive black holes was largely the result of the unprecedented spatial resolution offered by the HST. Masses of about thirty supermassive black holes ranging between  $10^6 - 10^9 M_{\odot}$  have been measured to date (e.g. Tremaine et al. 2002). A tight correla-

<sup>4</sup>LINERs are, however, not necessarily connected to AGN.

tion between black hole mass and velocity dispersion (of the central spheroidal part of the galaxy) suggests that the formation and evolution of supermassive black holes and their host spheroids are connected (Haehnelt et al. 1998; Richstone et al. 1998; Ferrarese & Merritt 2000; Gebhardt et al. 2000; Monaco et al. 2000). Perhaps most galaxies go through a violent quasar period that starts with intensive accretion of (cold) gas which falls towards the black hole in the centre of the galaxy. The violent process that creates the quasar's light also increases the mass of the black hole, which can reach the observed values in a few times  $10^9$  years (for details see Yu & Tremaine 2002). However, as mentioned before, in nearby galaxies, the supermassive black holes are dormant or barely emitting radiation. The activity then, clearly, has to be connected to the existence of fuel material that can be accreted by the supermassive black hole.

Large-scale dust and gas are not often seen in early-type galaxies (but more often in lenticulars than in ellipticals), and the amount of available fuel is less compared to the high-redshift objects. However, higher-resolution imaging by means of the HST shows that dust is common on smaller scales in nearby early-type galaxies (van Dokkum & Franx 1995; Verdoes Kleijn et al. 1999; Rest et al. 2001; Tran et al. 2001). Dust indicates the presence of gas: the fuel for the AGN engine. An immediate question arises: how is the presence of dust and gas connected to the activity in nearby early-type galaxies? Observations presented in this thesis (Chapter 2) suggest that although galaxies without dust have a somewhat lower probability of AGN activity, the existence of dust in HST images is certainly not a necessary condition for the existence of an AGN. On the other hand, a recent study (Kauffmann et al. 2003) showed that, although the AGN host galaxies morphologically look very similar to present-day ellipticals, they often have a young stellar population component and in this way differ dramatically from nearby ellipticals. There might be more subtle differences between the nearby normal and AGN host galaxies.

There are many processes at play that determine the activity in galactic nuclei. Major mergers and interaction between galaxies (more common at higher redshifts) act as reservoirs of fuel for starving central engines. Minor mergers and motion of gas in the gravitational potential of a galaxy perturbed by bar instabilities can have a crucial role in transporting gas to the bottom of the potential well and the black hole. The amount of gas and the specific physics of accretion will define the resulting AGN (quasar, radio galaxy with jets, LINER, etc), as well as the influence of the AGN on the evolution of the whole galaxy. Detailed observational and theoretical studies of the accretion processes in galactic nuclei as well as secular evolution are still needed to understand the nature of the activity in galaxies.

## 5 Nuclear stellar discs in early-type galaxies

The central regions of galaxies are not easily observed from the ground because of the limiting influence of atmospheric seeing on the observations. Early-type galaxies often look simple and featureless on ground-based images. High-resolution observations with HST have revolutionised our knowledge of the nuclear regions (approximately inner 1 kpc) of early-type galaxies (Jaffe et al. 1994; van den Bosch et al. 1994; Lauer et al. 1995; Carollo et al. 1997a; Carollo et al. 1997b; Rest et al. 2001). Among several

discoveries, these observations revealed the existence of small nuclear stellar discs, with sizes of the order of  $1''$ . These discs can be remarkably thin (30 pc compared with 300 pc of disc in our galaxy) and are often related in some way to the large scale discs, but are not necessarily connected to them since outer discs often have an inner cut-off radius (Scorza & Bender 1995; Scorza & van den Bosch 1998; van den Bosch 1998; Chapter 3 of this thesis). These features clearly point to a complex formation scenario, possibly involving secular evolution. Studies of larger samples of galaxies showed that they occur in about 50% of early-type galaxies, and since discs are easily found only if seen near to edge-on (Rix & White 1990), they might be very common features.

Discs are generally dynamically simpler than spheroids. They are very flattened axisymmetric structures dominated by rotation which can be used to determine the galaxy's potential (assuming circular motion of stars in the disc). It is easy to determine the inclination of a disc and correct for its effects. As a result, nuclear stellar discs can be used to measure the mass of the black hole in the centre of the galaxy. Perhaps the most interesting consequence of the existence of nuclear discs is the fact that they can be used as probes of galaxy evolution scenarios.

There are two likely scenarios for nuclear disc formation. Discs could be the end result of a minor merger of galaxies. In this scenario a satellite galaxy interacts with the bigger host galaxy and the captured gas is transported to the centre where it settles in (one of) the principal planes of the host galaxy. Frequently the infalling gas has enough angular momentum to form a disc. Interaction with the black hole can result in an AGN, but also stabilises the disc leading to the formation of stars (Loeb & Rasio 1994). An alternative scenario, that, unfortunately, can result in similar observational properties, invokes the secular evolution of galaxies, where bar instabilities play a critical role in transporting gas towards the centre of the galaxy, creating a nuclear disc (e.g. van den Bosch & Emsellem 1998). Discriminating between these two very different scenarios (positioned in opposite corners of Fig. 1 - upper right and lower left) is difficult. However, it is probably a combination of both scenarios that occurs in galaxies leaving signatures in the observed structures. Generally, the different formation paths of a nuclear stellar disc and the rest of the galaxy, are expected to result in differences in the age and metallicity of their stellar component.

In edge-on galaxies, where nuclear stellar discs are most easily detected, the effects of bar instabilities are hard to observe. A range of different observations, including imaging and spectroscopy are necessary to investigate the effects of the above mentioned processes. Chapter 3 presents such a comprehensive observational study of galaxies with four previously-known nuclear stellar discs. Assembling all observational evidence from Chapter 3, there are no clear proofs of bar-driven evolution in any of the observed galaxies, although some are strong candidates. Our long-slit spectroscopic data are of high resolution, but they cover only a small fraction of the nuclei and discs. Additional observations of the two-dimensional kinematic properties and their connection to the distribution of line-strengths (metal content and age of stellar populations) would probably offer decisive insight in the formation of the nuclear stellar discs.

## 6 Integral-field spectroscopy

Recent developments in instrument design have introduced a new acronym in the astronomical jargon, IFU (integral-field unit), specifying an instrument capable of producing simultaneous spectroscopic measurements over an area (field) rather than along a slit. There are several possible ways to construct an IFU. All IFUs have a mechanism for separating the light coming from the sky, whilst retaining the information of the sky coordinates from which each separated light beam has originated. In this way, it is possible to observe an extended astronomical object, as with traditional imaging, but at the same time to extract spectral information from different parts of the object. An alternative is to stack a number of long-slit measurements together, but since the spectra are not taken simultaneously it is generally not considered to be an IFU measurement, nor it is anywhere near being efficient in time. Due to the time limitations, the multiple-slit approach has been used for only a few galaxies (e.g. Statler & Smecker-Hane 1999). The final observational product of an IFU is a three-dimensional data-cube with spatial and spectral information  $(x, y, \lambda)$ . These data can be presented as two-dimensional kinematic and line-strength maps<sup>5</sup>, bringing a wealth of spatially-resolved information of observed objects (e.g. Bacon et al. 1995, 2001).

The true power of IFUs is revealed when observing objects with complicated morphologies whose properties cannot be accurately measured with just one or two long-slits. Galaxies of all types, and merging objects, are typical examples. Astronomical objects, in general, are three-dimensional structures, but we see them only as two-dimensional projections onto the sky. With an IFU we can efficiently observe the projected distribution of light and obtain spectra integrated along the line-of-sight. This gives valuable additional information for understanding and constraining the internal structure of the observed objects. Chapters 4 and 5 of this thesis analyse the integral-field observations of early-type galaxies showing their advantages and usefulness for the study of internal structure of galaxies.

IFU observations are currently mostly used to observe nearby galaxies (e.g. the SAURON project de Zeeuw et al. 2002), with the purpose to construct dynamical models of galaxies, and constrain the distribution of their stellar content. The diversity of the science done with IFUs is, however, continuously growing: solar system bodies, planetary nebulae, young stellar objects, supernova remnants, extragalactic supernovae, merging galaxies, gravitationally-lensed galaxies and deep-field studies to name a few (e.g. Swinbank et al. 2003; Bower et al. 2004). The next generation of IFUs mounted on 8-10m telescopes with a wide field coverage and assisted with adaptive-optics systems, will be capable of observing objects at higher redshifts, probing earlier stages of galaxy formation and evolution.

## 7 Two-dimensional kinematic maps

Assuming there are no objects in front and behind an observed stellar system, spectroscopic observations can be used to constrain the system's kinematic properties. Each

---

<sup>5</sup>It is important to note that radio astronomers have observed two-dimensional velocity fields for more than thirty years. The IFU technology is, however, a relative novelty in optical astronomy.

(unresolved) star will contribute to the observed spectrum. Its absorption lines will be Doppler shifted according to the star's line-of-sight (LOS) velocity. Generally, stars have different velocities and directions of motion which are reflected in the integrated spectrum as a broadening of the (combined) absorption lines. The distribution of stellar velocities along the line-of-sight can be described by a *broadening function*, usually called the line-of-sight velocity distribution (LOSVD)<sup>6</sup>. Commonly, the LOSVD is decomposed into orthogonal functions, e.g., as a *Gauss-Hermite series*. This expansion exploits the fact that LOSVDs are to first order well-approximated by a Gaussian, so that the deviations can be described by a small number of Gauss-Hermite terms. The spectra of bright nearby galaxies can be used to extract the first four terms of the Gauss-Hermite series measuring: the mean velocity  $V$ , the velocity dispersion  $\sigma$ , and two Gauss-Hermite coefficients,  $h_3$  and  $h_4$ . These coefficients measure the asymmetric ( $h_3$ ) and symmetric ( $h_4$ ) departures of the LOSVD from a Gaussian (van der Marel & Franx 1993; Gerhard 1993).

Observing nearby galaxies with an IFU provides two-dimensional kinematic maps, i.e., maps of their kinematic moments  $V$ ,  $\sigma$ ,  $h_3$ ,  $h_4$ . The maps offer a wealth of information important for understanding the shape and properties of a galaxy, as well as for constructing dynamical models that describe its internal structure. However, the important information has to be extracted efficiently from the maps. A simple and straightforward approach is to use a harmonic expansion along concentric annuli to describe each two-dimensional map. The result is a set of coefficients describing the amplitude and orientation of the kinematic moments. These parameters are related to the intrinsic properties of the observed galaxy. A similar approach is used in photometric analysis of optical surface brightness images (e.g. Lauer 1985; Jedrzejewski 1987). Chapter 4 presents a general method for analysing and describing two-dimensional kinematic maps of early-type galaxies. Due to the similarities with the surface photometry of early-type galaxies, we called our technique *kinemetry*<sup>7</sup>.

The internal kinematic moments of stationary triaxial systems show a high degree of symmetry. Following these symmetries we distinguish between even and odd moments. This is reflected in the symmetries of the observed kinematic maps. Generally, maps of even moments are *point-symmetric* [ $\mu_e(r, \theta + \pi) = \mu_e(r, \theta)$ ], while maps of odd moments are *point-anti-symmetric* [ $\mu_o(r, \theta + \pi) = -\mu_o(r, \theta)$ ], where  $\mu_o$  and  $\mu_e$  are arbitrary odd and even moments of the LOSVD, respectively, with dependence on radius  $r$  and angle  $\theta$ . As a consequence, the terms of the harmonic expansion will behave accordingly: the even terms will be nearly zero for maps of odd moments and the odd terms will be nearly zero for maps of even moments. Alternatively, the observed symmetry of kinematic maps makes it possible to ascertain the symmetry of the density distributions and kinematics of the observed galaxy. If all kinematic maps of a galaxy show an additional signature of *mirror-(anti)-symmetry* [ $\mu_e(r, \pi - \theta) = \mu_e(r, \theta)$  for even and  $\mu_o(r, \pi - \theta) = -\mu_o(r, \theta)$  for odd moments] the galaxy will be consistent with being intrinsically axisymmetric. An example of the application of kinemetry on velocity maps is shown in Fig. 2. Using kinemetry we analysed velocity maps of 48

<sup>6</sup>Sometimes, the broadening function is simply called the velocity profile (VP)

<sup>7</sup>Again, radio astronomers pioneered a similar although less general technique (Begeman 1987; Schoenmakers et al. 1997)

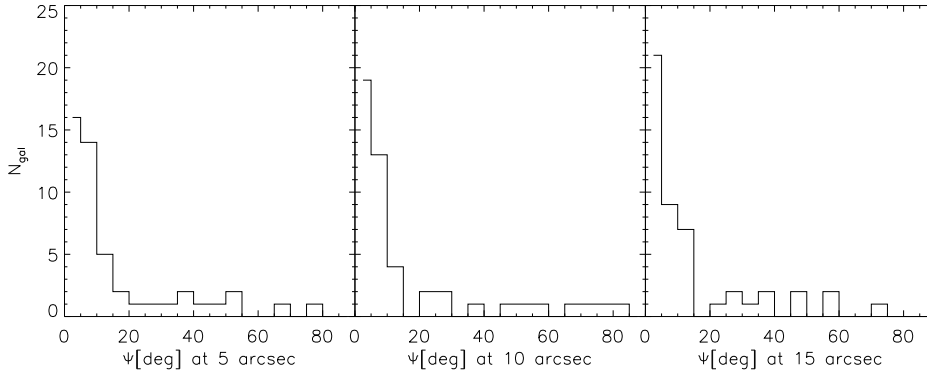


**Figure 2** — Histogram of the kinematic misalignment angle  $\psi$  measured for a sample of 48 E/S0 galaxies from the SAURON survey (de Zeeuw et al. 2002). The angle  $\psi$  is the angle between the photometric and kinematic axes (Franx et al. 1991). The kinematic major axes were measured using *kinemetry* (Chapter 4) at radii of 5'', 10'' and 15''. The photometric major axis was determined using the inner 15'' of the galaxy. About 35% of galaxies have small misalignment angle ( $< 5^\circ$ ) and are consistent with axisymmetry at the given radii. The measured number of galaxies consistent with axisymmetry increases with radius, showing that the central regions are often very different from the rest of the galaxy.

galaxies from the SAURON survey, extracting the position angle of the maps, the so-called *kinematic angle*. Comparing this angle with the photometric position angle, the position angle of the light distribution, we can measure the apparent (projected on the sky) misalignment between the two angles, which constrains the intrinsic shape of the galaxy (Franx et al. 1991).

Kinemetry is a powerful tool for describing and analysing kinematic maps, but it can be also used as a noise filter. Its most obvious usage is on the mean velocity maps which were already studied theoretically (e.g. Franx et al. 1991; Statler 1991, 1994a; Statler & Fry 1994; Statler 1994b; Arnold et al. 1994), but, as presented in Chapter 4, kinemetry can also be applied to higher moment maps. Kinemetry can hence be used to extract useful information from the observed objects, and so to serve as a bridge between observations and theoretical modelling.

## 8 Dynamical models

A full understanding of the intrinsic shape and structure of galaxies can only be obtained through detailed dynamical modelling. Construction of such models is a theoretical undertaking which is based on the general laws of physics and incorporates ideas and assumptions about the investigated objects (or processes). However, only models which can reproduce the observations (experiments) can be considered as physically meaningful. Theoretical constructions are limited only by the inventiveness of the human mind, but the natural world around us is unique. In order to explain it, theory must agree with the observations.

### 8.1 Stellar dynamical models

The structure and dynamical properties of a collisionless stellar system are fully specified by its phase space density or distribution function,  $f = f(\vec{x}, \vec{v}, t)$ , where  $\vec{x}$  and  $\vec{v}$  label the position and velocity of stars at a time  $t$ . The distribution function must be non-negative, must satisfy the continuity equation and if it describes a system in a steady state (no changes with time), it does not depend on the time variable  $t$ . The distribution function, however, cannot be measured directly because individual stars are resolved only in the nearest stellar systems and observations cannot be expected to be complete. The distribution function can be partially constrained by observations of the object's surface brightness, which is the line-of-sight projection of the density of the system. Unfortunately, the deprojection of the surface photometry is non-unique (Williams 1981; Rybicki 1987) and the density itself does not fully constrain the possible orbits of stars. On the other hand, the projected kinematics (two-dimensional observation with large coverage of the object) provide a significant additional constraints on the stellar distribution function.

The six-dimensional phase-space  $(\vec{x}, \vec{v})$  dependence of the distribution function can be substituted by, in the most general case, a dependence on only three conserved quantities. The Jeans theorem (Jeans 1915; Lynden-Bell 1962) states that  $f$  is a function of the *isolating integrals of motion*, functions of  $\vec{x}$  and  $\vec{v}$  that are constant along every orbit in a given gravitational potential. The reduction from six to at most three variables is a significant simplification. The actual number of integrals of motion depends on the symmetry of the potential. Spherical potentials, with an isotropic velocity distribution, correspond to a one-integral distribution function:  $f = f(E)$  having energy  $E$  as the integral of motion<sup>8</sup>. Axisymmetric potentials conserve the energy and the one component of the angular momentum,  $L_z$ , but most of the orbits in a realistic potential are regular and also conserve an effective third integral of motion,  $I_3$  (Contopoulos 1960, Ollengren 1962). This quantity is non-classical in the sense that it cannot be analytically known, except in the rather special, but instructive case of Stäckel potentials (Kuzmin 1956; de Zeeuw 1985a), so we expect  $f = f(E, L_z, I_3)$ . The most complicated is the case of the triaxial potential. Non rotating triaxial potentials<sup>9</sup> conserve energy and two non-classical integrals,  $I_2$  and  $I_3$  (Schwarzschild 1979; de Zeeuw 1985b).

In Chapter 5 we construct axisymmetric models that conserve two- and three-integrals of motion,  $(E, L_z)$  and  $(E, L_z, I_3)$  respectively. Two-integral models can be constructed following the Hunter & Qian (1993) method. Since both integrals are analytically known, it is possible to derive a distribution function,  $f = f(E, L_z)$ . On the other hand, the distribution function of the three-integral models, cannot be computed directly due to the nature of the unknown third integral,  $I_3$ . An elegant numerical method for the construction of three-integral dynamical models, however, was introduced by Schwarzschild (1979, 1982). In this method, the galaxy is built as an ensemble of stellar orbits, that are assumed to be independent. Each orbit contributes with

<sup>8</sup>In spherical potentials it is also possible to construct models of the form  $f = f(E, \vec{L})$  and  $f = f(E, L^2)$ . The former have a preferred axis and are usually not considered, while the latter conserve the amplitude of angular momentum, but not its direction.

<sup>9</sup>Bars provide examples of rotating triaxial systems. Although there is lack of observational evidence, elliptical galaxies are generally considered to have nearly stationary figures.

certain mass and kinematic properties. Determining a superposition of orbits that best reproduces the observed galaxy (surface brightness and kinematics), one obtains an orbital representation of the galaxy. Since the method results in a superposition of orbits, specified by the integrals of motion  $(E, L_z, I_3)$ , it is possible to construct an equivalent form of the distribution function,  $f = f(E, L_z, I_3)$ , describing the galaxy. The three-integral method is more general than the two-integral method and produces more realistic models of the observed galaxies. The finite number of orbits, however, is much smaller than the number of stars and even sometimes than the number of observables used to constrain the model (10000 orbits vs  $10^{11}$  stars vs  $\sim 5000$  kinematic observables in the case of integral-field data), and the effects of the discreteness of the method have to be properly understood. Schwarzschild's method has been successfully applied in a number of cases to recover the mass of central black holes, the mass-to-light ratios, and to describe the internal (kinematic) structure of the modelled galaxies (e.g van der Marel et al. 1998; Cretton et al. 1999; Cretton & van den Bosch 1999; Cappellari et al. 2002; Verolme et al. 2002; Gebhardt et al. 2003).

Properties of the observed galaxies are not known *a priori*, and we do not know whether the models recover the true galaxy parameters and its correct orbital structure. One way of testing the modelling results is to construct artificial models of galaxies for which one knows all details to arbitrary accuracy. Two-integral models are useful for this purpose and one can use them as inputs to the three-integral models. Comparing the results with known inputs, one can attach confidence levels to the three-integral models. The physics of stellar motion belongs to classical Newtonian dynamics, but the observed galaxies are complex systems with innumerable stars. A proper understanding of the dynamical structure of galaxies continues to pose a challenge.

## 8.2 Dynamical models of gas

In the interstellar medium of galaxies some of the gas, if present, is ionised by the radiation of stars or an AGN and gaseous emission-lines are often easily observed. In an axisymmetric potential, gas eventually settles in a disc in the equatorial plane of the galaxy. Gas is said to be dynamically *cold* if it is observed in a disc configuration where non-selfintersecting clouds of gas move in circular orbits in the equatorial plane. This situation is observed in galaxies such as M87 (van der Marel 1994) and NGC 7052 (van den Bosch & van der Marel 1995), but gas is often observed with irregular morphologies and disturbed kinematics. In these cases the treatment of gas needs to go beyond gravitational forces, by including hydrodynamical effects. There are also intermediate cases<sup>10</sup> when gas is observed in a regular disc but its velocity dispersion is high (gas is not cold) and is comparable with the measured rotation velocity.

The velocity dispersion of a settled (cold) gas disc is expected to be  $\sim 10 \text{ km s}^{-1}$  (Osterbrock 1989) due to its temperature ( $\sim 10^4 \text{ K}$  in galaxies without any or with low ionisation activity). However, the measured velocity dispersion is often larger for reasons that are presently not well understood. In some cases it is possible to assume

---

<sup>10</sup>The gas disc can also display spiral structure, which happens when the mass of gas is large and self-gravity becomes important, or, generally, as a result of a perturbation in the potential, like a bar-instability or interaction with a neighbour galaxy.

that the velocity dispersion is the result of *local turbulence* which does not disturb the bulk flow of gas rotating at nearly the circular velocity (e.g. van der Marel & van den Bosch 1998; Verdoes Kleijn et al. 2000) and the gas bulk motion is explained with cold gas disc models. Alternatively, the non-thermal component of the velocity dispersion comes from collisionless gravitational motion of the gas: gas clouds act as stars moving on self-intersecting orbits. In this case one can use the epicyclic approximation<sup>11</sup> to the motions of gas clouds and evoke the so-called asymmetric drift correction to the circular motion of collisionless gas clouds (Cinzano & van der Marel 1994; Cretton et al. 2000; Barth et al. 2001; Aguerri et al. 2003; Debattista & Williams 2004; Chapter 5 of this thesis). Neither of these approaches are entirely physically justified, although these approximations often do reproduce observations.

Flattened potentials are prone to perturbations which disrupt their shape. An example of such a perturbation is the bar instability, which is typical for disc systems (roughly two thirds of disc galaxies have bars). Bars are triaxial structures that rotate with a *pattern speed*,  $\Omega_p$ . Stars, having their own rotation speed,  $\Omega$ , feel the gravitationally pull of the bar potential which perturbs their orbits. This effect is seen in the existence of several resonances in the galaxy, one of which happens when the rotational speed of the bar (pattern speed,  $\Omega_p$ ) matches the speed of the stars and it is called *corotation* (CR,  $\Omega_p = \Omega$ ). Other strong resonances are: *Inner Lindblad* (ILR,  $\Omega_p = \Omega - \kappa/2$ ), *Outer Lindblad* (OLR,  $\Omega_p = \Omega + \kappa/2$ ) and *Ultra-Harmonic* (UHR,  $\Omega_p = \Omega + \kappa/4$ ), where  $\kappa$  is its radial epicyclic frequency. The allowed orbits are aligned with the bar between the ILR and CR, and perpendicular to the bar between the CR and OLR. Each time a resonance is crossed stellar orbits change direction perpendicularly (Binney & Tremaine 1987; Athanassoula 1992).

The existence of resonances will also shape the gas disc pushing gas away from corotation towards the Inner and Outer Lindblad resonances. Unlike stars, gas can collide and the orbits of cold gas change smoothly between resonances. In strong bars this will result in the formation of gas rings, followed by starformation. On the other hand weak bars do not betray their existence so easily and are hard to detect. Often they are not visible on images of galaxies. Twists of velocity contours on two-dimensional maps are, however, likely signatures of bars. For an in-depth review of bars see Sellwood & Wilkinson (1993) and Kormendy & Kennicutt (2004).

Observations of gas kinematics in many galaxies is simpler than measuring the stellar kinematics, because the gas emission-lines are bright and easier to detect than stellar absorption lines. Dynamical models of gas discs can be used to determine the properties of the gravitational potential, its symmetry, inclination as well as mass of the central black hole. Gas particles move in the same potential as the stars and so dynamical models of gas and stars should give the same results, or at least can be used to verify each other and their underlying assumptions. Observation and models of gas shed light on the evolutionary stage of the observed host galaxy.

---

<sup>11</sup>The epicyclic approximation is valid in the limit of small radial oscillations.

## 9 Outline of this thesis

The research presented in this thesis deals with different aspects of galaxy formation and evolution. It is based on observations with ground- and space-based telescopes, in the radio and optical wavelength range. The work focuses on nearby early-type galaxies and their properties, ranging from nuclear structures and activity to global kinematic and dynamical properties. A short outline of each chapter is given here.

**Chapter two** presents a survey of an optical/IR selected sample of nearby E/S0 galaxies with and without nuclear dust structures on the HST images. The observations were obtained with the Very Large Array radio interferometer at 3.6 cm to a sensitivity of 100  $\mu\text{Jy}$ . The Radio Luminosity Function (RLF) of the observed galaxies down to  $\sim 10^{19} \text{ W Hz}^{-1}$  shows that  $\sim 50\%$  of these galaxies have AGNs at the surveyed level. The space density of these AGN equals that of starburst galaxies (at the same luminosity). The main result of the survey is that several dust-free galaxies have low-luminosity radio cores, and their RLF is not significantly less than that of the dusty galaxies. This implies that the existence of dust visible with the HST is not a necessary requirement for the existence of an AGN in nearby early-type galaxies.

**Chapter three** discusses observations of four nearby early-type galaxies with previously known nuclear stellar discs. The galaxies were observed using two instruments on-board the Hubble Space Telescope. The Wide Field Planetary Camera 2 observed NGC 4128, NGC 4621 and NGC 5308. The Space Telescope Imaging Spectrograph observations also included NGC 4570. Numerous nuclear colour features were detected, such as: a red nucleus in NGC 4128, a blue nucleus in NGC 4621, and a blue disc in NGC 5308 only 30 pc thick. Additionally, a blue disc-like feature with position angle  $\sim 15^\circ$  from the major axis in NGC 4621, possibly related to the kinematically decoupled core discovered by Wernli et al. (2002), was found. In NGC 5308 there is evidence for a blue region along the minor axis. A blue transient on the images of NGC 4128 at a position of  $0''.14$  west and  $0''.32$  north from the nucleus was discovered. The nature of the transient is not certain, although it could have been a supernova.

The extracted kinematic profiles belong to two distinct groups: fast (NGC 4570 and NGC 5308) and kinematically disturbed rotators (NGC 4128 and NGC 4621). The discovery of a kinematically decoupled core in NGC 4128 is also reported. Galaxies have mostly old (10-14 Gyr) stellar populations with a large spread in metallicities (sub- to super-solar). In this chapter possible formation scenarios are discussed, including bar-driven secular evolution and the influence of mergers, which can explain the observed colour and kinematic features. The available evidence unfortunately cannot entirely distinguish between the two cases, and it is likely that a combination of processes may have shaped the galaxies.

**Chapter four** describes a general method for analysing and describing two-dimensional kinematic maps of galaxies observed with integral-field spectrographs. The method is based on the harmonic expansion of kinematic maps along concentric annuli in the plane of the sky similar to those used in observations of cold gas (e.g. Bege-man 1987; Franx et al. 1994; Schoenmakers et al. 1997) and in the surface photometry approach to broad-band imaging, but without assuming any *a priori* knowledge of the galaxies (Lauer 1985; Jedrzejewski 1987; Franx et al. 1989). We call it *kinemetry*. Using

symmetries of the kinematic moments (even moments are point-symmetric and odd moments are point-anti-symmetric) it can be used to parametrise trends and detect properties of the host galaxies and as a diagnostic tool of underlying symmetries of the gravitational potential. Kinemetry is also a powerful filter. The method is presented, tested and applied to model maps of kinematic moments as well as actual SAURON observations of a few galaxies. An interesting, preliminary, finding is that the velocity maps of nearby early-type galaxies are very similar to the velocity maps of discs. This is somewhat unexpected since early-type galaxies are (flattened) spheroidal systems, and warrants a detailed study of a larger sample of two-dimensional velocity maps of early-type galaxies.

**Chapter five** contains a detailed dynamical study of the E4 galaxy NGC 2974. The observations include ground- and space-based imaging and integral-field spectroscopy with SAURON, which were used to extract stellar and gaseous kinematics. The kinematic maps are quantified with *kinemetry* and the large-scale kinematics show only small deviations from axisymmetry (which are, however, visible in the central  $3''$  of the gas kinematic maps). General axisymmetric dynamical models for the stellar motions are compared to the observations of the galaxy. The three-integral models ( $f = f(E, L_z, I_3)$ ) presented here are based on Schwarzschild's orbit superposition method. The models are constructed to determine the mass-to-light ratio,  $\Upsilon$ , and inclination,  $i$ , of the galaxy, as well as its internal orbital structure. The best fitting parameters are  $\Upsilon = 4.5 \pm 0.1 M_\odot / L_\odot$  and  $i = 65 \pm 2.5^\circ$ .

The results of the stellar dynamical modelling are tested on the gas kinematics. The inclination of the gas disc can be obtained from its velocity field. The measured value,  $i = 58 \pm 5^\circ$ , is close to the stellar dynamical value. The observed gas disc was modelled with the asymmetric drift approximation in the potential derived from the stellar models. The gas models are able to accurately reproduce the large-scale kinematic structure, but fail to do so in the inner  $3''$ , which are influenced by the non-axisymmetric perturbations.

A large section of Chapter 5 is devoted to tests of the three-integral method, as well as the importance of the two-dimensional maps for constraining models of observed galaxies. The robustness of the method is tested against two-integral models with analytic DF ( $f = f(E, L_z)$ ). We used these models to test: (i) the influence of the radial coverage of the kinematic data on the internal structure, (ii) the recovery of the test model parameters ( $\Upsilon, i$ ), and (iii) the recovery of the test model DF.

Results show that increasing the radial coverage of the kinematic data from  $1r_e$  to  $2r_e$  does not change the internal structure within  $1r_e$ . The results of the dynamical models of the SAURON observations of NGC 2974 would not change if the radial coverage would be increased by a factor of 2. Also, three-integral models can accurately recover the mass-to-light ratio. Although the models are also able to constrain the inclination of the test model formally, the apparent differences between the models are very small (as in the case of real observations). Under a careful examination, it is possible to choose the best model by eye, but the decisive kinematic features are below (or at) the level of the systematics in the data (e.g. template mismatch) and might be influenced by uncertainties in the models (e.g. regularisation or variations in the sampling of observables with orbits). This suggests a degeneracy of models with respect to the recovery

of inclination. More general tests on other galaxies and theoretical work is needed for a better understanding of this issue. Finally, three-integral models are able to recover the true input DF, to the level of the discreteness effects in the models.

## 10 Future prospects

Basic concepts of galaxy formation and evolution, as well as the cosmological background, are generally agreed upon and can be used as a working paradigm of modern astronomy. We believe we understand the processes that shape and control the nature and nurture of galaxies. N-body simulations and three-integral Schwarzschild models are able to simulate interactions and create representative models of observed galaxies, respectively. We may even boast that we understand the global picture and certainly it is true that observations and theory are starting to agree. However, there are a number of loose ends to be tied and questions to be answered.

The advent of integral-field units opens a detailed view into the structure of galaxies. Two-dimensional spectroscopic observations are clearly very important in constraining the models (kinematic maps), but also complementary to the photometric observations for distinguishing the stellar populations of galaxies (maps of line-strength indices). This is shown by the results of the SAURON survey of nearby galaxies (Verolme et al. 2002; Emsellem et al. 2004; Chapter 5 of this thesis; McDermid et al. 2005; Kuntschner et al. 2005; Cappellari et al. 2005, Sarzi et al. 2005). The next natural step is to look back in time, using new two-dimensional spectroscopic glasses that are being commissioned on the 8-10 meter class telescopes, towards higher redshifts and earlier epochs when interactions between galaxies were more frequent and galaxies look different from today. Comparing the properties of galaxies at redshifts between 0.5 and 1, when the Universe was between three-quarters and half its current age respectively, with the properties of nearby galaxies will show the actual evolution of galaxies.

Another approach is to observe (with the same new instruments on the largest telescopes) nearby objects that were not often studied up to now due to technical limitations. One such class of objects are small galaxies with low-surface brightness. These galaxies are interesting because they have not yet participated in merger events (in a way they are real fossils of Universe), they have experienced only limited starformation, and clearly reside in different potential wells than large luminous galaxies. Dynamical models of dwarf galaxies will also give low-redshift constraints to cosmological models.

There are possible advances on the modelling front. Firstly, models of triaxial galaxies which also fit the observed kinematics will soon be ready (van den Ven et al. in prep). They are more complex than axisymmetric models, due to the large parameter space that describes a triaxial body. On the other hand, models of real galaxies must include both kinematic and line-strength information, because, after all, galaxies are not made of one population of stars and a true distribution function is dependent on the age and metallicity of stars. The modelling approach here differs from the conventional approach: instead of fitting LOSVDs, new models will directly fit observed spectra giving simultaneous information about the kinematics and distribution of stellar populations (Cappellari et al. in prep.).

The impact of the Hubble Space Telescope on modern astronomy cannot be properly acknowledged in a single paragraph (nor in a much thicker book!), however, at this moment of its uncertain future and perhaps even a premature demise, and, here, thinking of the next steps, it is important to remember its profound role in the increase of our understanding of the Universe. Discoveries related to the nearby early-type galaxies are numerous, some of which are presented and discussed in the following chapters. Modern ground-based telescopes are almost an order of magnitude larger than HST and have a huge advantage in the collecting power: very important in astronomy where every photon counts. The new technology of adaptive optics with natural or laser guide stars is almost completely able to correct for atmospheric seeing (although currently at longer wavelengths only) and scientific observations from the ground are entering a promising new era. From this point of view we can be satisfied and encouraged because new observations will surely bring new excitements. Still, HST will remain a unique human eye into the vastness of the Universe.

## References

- Aguerre J. A. L., Debattista V. P., Corsini E. M., 2003, *MNRAS*, 338, 465  
 Arnold R., de Zeeuw P. T., Hunter C., 1994, *MNRAS*, 271, 924  
 Athanassoula E., 1992, *MNRAS*, 259, 328  
 Bacon R., Adam G., Baranne A., Courtes G., Dubet D., Dubois J. P., Emsellem E., Ferruit P., et al. 1995, *A&AS*, 113, 347  
 Bacon R., Copin Y., Monnet G., Miller B. W., Allington-Smith J. R., Bureau M., Marcella Carollo C., Davies R. L., et al. 2001, *MNRAS*, 326, 23  
 Barnes J. E., Hernquist L., 1996, *ApJ*, 471, 115  
 Barth A. J., Sarzi M., Rix H., Ho L. C., Filippenko A. V., Sargent W. L. W., 2001, *ApJ*, 555, 685  
 Begeman K. G., 1987, Ph.D. Thesis, University of Groningen  
 Binney J., 2004, astro-ph/0407238, to appear in *Phil. Trans. Roy. Soc.*  
 Binney J., Tremaine S., 1987, *Galactic Dynamics*. Princeton, NJ, Princeton University Press, 1987, 747 p.  
 Bower R. G., Morris S. L., Bacon R., Wilman R. J., Sullivan M., Chapman S., Davies R. L., de Zeeuw P. T., et al., 2004, *MNRAS*, 351, 63  
 Cappellari M., Verolme E. K., van der Marel R. P., Verdoes Kleijn G. A., Illingworth G. D., Franx M., Carollo C. M., de Zeeuw P. T., 2002, *ApJ*, 578, 787  
 Carollo C. M., Franx M., Illingworth G. D., Forbes D. A., 1997a, *ApJ*, 481, 710  
 Carollo C. M., Danziger I. J., Rich R. M., Chen X., 1997b, *ApJ*, 491, 545  
 Cinzano P., van der Marel R. P., 1994, *MNRAS*, 270, 325  
 Combes F., 2004, astro-ph/0406306  
 Contopoulos G., 1960, *Zeitschrift fur Astrophysics*, 49, 273  
 Courteau, S., van den Bergh, S., 1999, *AJ*, 118, 337  
 Cretton N., de Zeeuw P. T., van der Marel R. P., Rix H-W., 1999, *ApJS*, 124, 383  
 Cretton N., Rix H-W., de Zeeuw P. T., 2000, *ApJ*, 536, 319  
 de Zeeuw P. T., Bureau M., Emsellem E., Bacon R., Carollo C. M., Copin Y., Davies R. L., Kuntschner H., et al., 2002, *MNRAS*, 329, 513  
 de Zeeuw P. T., 1985a, *MNRAS*, 216, 273  
 de Zeeuw P. T., 1985b, *MNRAS*, 215, 731  
 de Zeeuw P. T., 2001, in *Black Holes in Binaries and Galactic Nuclei*, p. 78, eds. Lex Kaper, Edward P. J. van den Heuvel, Patrick A. Woudt, Springer  
 Debattista V. P., Williams T. B., 2004, *ApJ*, 605, 714  
 Durman A. 2000, *The Vučedol Orion, Exhibition Catalogue, Zagreb 2000*  
 Ferrarese L., Merritt D., 2000, *ApJ*, 539, L9  
 Franx M., Illingworth G., de Zeeuw P. T., 1991, *ApJ*, 383, 112

- Franx M., Illingworth G., Heckman T., 1989, *AJ*, 98, 538
- Franx M., van Gorkom J. H., de Zeeuw P. T., 1994, *ApJ*, 436, 642
- Frenk, C. S., White, S. D. M., Bode, P., Bond, J. R., Bryan, G. L., Cen, R., Couchman, H. M. P., Evrard, A. E., Gnedin, N., et al. 1999, *ApJ*, 525, 554F
- Gebhardt K., Bender R., Bower G., Dressler A., Faber S. M., Filippenko A. V., Green R., Grillmair C., et al., 2000, *ApJ*, 539, L13
- Gebhardt K., Richstone D., Tremaine S., Lauer T. R., Bender R., Bower G., Dressler A., Faber S. M., et al., 2003, *ApJ*, 583, 92
- Gerhard O. E., 1993, *MNRAS*, 265, 213
- Gunn J. E., 1979, in *Active galactic nuclei*, Cambridge, Cambridge University
- Haehnelt M. G., Natarajan P., Rees M. J., 1998, *MNRAS*, 300, 817
- Ho L. C., Filippenko A. V., Sargent W. L. W., 1997, *ApJ*, 487, 579
- Hoyle F., Fowler W. A., 1963, *MNRAS*, 125, 169
- Hubble E. P., 1936, *The Realm of Nebulae*, Yale University Press
- Hunter C., Qian E., 1993, *MNRAS*, 262, 401
- Jaffe W., Ford H. C., O'Connell R. W., van den Bosch F. C., Ferrarese L., 1994, *AJ*, 108, 1567
- Jeans J. H., 1915, *MNRAS*, 76, 70
- Jedrzejewski R. I., 1987, *MNRAS*, 226, 747
- Kauffmann G., Heckman T. M., Tremonti C., Brinchmann J., Charlot S., White S. D. M., Ridgway S. E., Brinkmann J., et al., *MNRAS*, 346, 1055
- Kauffmann G., van den Bosch F., 2002, *Scientific American*, 286, 36
- Kormendy J., Bender R., 1996, *ApJ*, 464, L119
- Kormendy, J., Kennicutt, R. C., 2004, astro-ph/0407343, *ARAA*, in press
- Krajinović D., Jaffe W., 2002, *A&A*, 390, 423
- Krolik J. H., 1999, *Active galactic nuclei : from the central black hole to the galactic environment*, Princeton, N. J. : Princeton University Press, 1999
- Lauer T. R., 1985, *MNRAS*, 216, 429
- Lauer T. R., Ajhar E. A., Byun Y.-I., Dressler A., Faber S. M., Grillmair C., Kormendy J., Richstone D., et al., 1995, *AJ*, 110, 2622
- Loeb A., Rasio F. A., 1994, *ApJ*, 432, 52
- Lynden-Bell D., 1962, *MNRAS*, 124, 1
- Lynden-Bell D., 1969, *Nature*, 223, 690
- McLure R. J., Dunlop J. S., Kukula M. J., 2000, *MNRAS*, 318, 693
- McLure R. J., Kukula M. J., Dunlop J. S., Baum S. A., O'Dea C. P., Hughes D. H., 1999, *MNRAS*, 308, 377
- Monaco P., Salucci P., Danese L., 2000, *MNRAS*, 311, 279
- Naab T., Burkert A., 2003, *ApJ*, 597, 893
- Navarro J. F., Frenk C. S., White S. D. M., 1996, *ApJ*, 462, 563
- Ollongren A., 1962, *Bull. Astron. Inst. Neth.*, 16, 241
- Osterbrock D. E., 1989, *Astrophysics of gaseous nebulae and active galactic nuclei*, University Science Books, 1989, 422 p.
- Ostriker J. P., Peebles P. J. E., Yahil A., 1974, *ApJ*, 193, L1
- Press W. H., Schechter P., 1974, *ApJ*, 187, 425
- Rest A., van den Bosch F. C., Jaffe W., Tran H., Tsvetanov Z., Ford H. C., Davies J., Schafer J., 2001, *AJ*, 121, 2431
- Richstone D., Ajhar E. A., Bender R., Bower G., Dressler A., Faber S. M., Filippenko A. V., Gebhardt K., et al., 1998, *Nature*, 395, A14
- Rix H., de Zeeuw P. T., Cretton N., van der Marel R. P., Carollo C. M., 1997, *ApJ*, 488, 702
- Rix H., White S. D. M., 1990, *ApJ*, 362, 52
- Rogstad D. H., Shostak G. S., 1972, *ApJ*, 176, 315
- Romanowsky A. J., Douglas N. G., Arnaboldi M., Kuijken K., Merrifield M. R., Napolitano N. R., Capaccioli M., Freeman K. C., 2003, *Science*, 301, 1696
- Rubin V. C., Ford W. K. J., 1970, *ApJ*, 159, 379
- Rybicki G. B., 1987, in *IAU Symp. 127: Structure and Dynamics of Elliptical Galaxies*, p 397, ed. P. T. de Zeeuw (Reidel, Dordrecht)

- Schmidt M., 1963, *Nature*, 197, 1040  
Schoenmakers R. H. M., Franx M., de Zeeuw P. T., 1997, *MNRAS*, 292, 349  
Schwarzschild M., 1979, *ApJ*, 232, 236  
Schwarzschild M., 1982, *ApJ*, 263, 599  
Scorza C., Bender R., 1995, *A&A*, 293, 20  
Scorza C., van den Bosch F. C., 1998, *MNRAS*, 300, 469  
Sellwood J.A., Wilkinson A., 1993, *Rep. Prog. Phys.*, 56, 173  
Soltan A., 1982, *MNRAS*, 200, 115  
Statler T. S., 1991, *AJ*, 102, 882  
Statler T. S., 1994a, *ApJ*, 425, 458  
Statler T. S., 1994b, *ApJ*, 425, 500  
Statler T. S., Fry A. M., 1994, *ApJ*, 425, 481  
Statler T. S., Smecker-Hane T., 1999, *AJ*, 117, 839  
Swinbank, A. M., Smith, J., Bower, R. G., Bunker, A., Smail, I., Ellis, R. S., Smith, G. P., Kneib, J.-P. et al., 2003, *ApJ*, 598, 162  
Tran H. D., Tsvetanov Z., Ford H. C., Davies J., Jaffe W., van den Bosch F. C., Rest A., 2001, *AJ*, 121, 2928  
Tremaine S., Gebhardt K., Bender R., Bower G., Dressler A., Faber S. M., Filippenko A. V., Green R., et al., 2002, *ApJ*, 574, 740  
van Albada T. S., 1982, *MNRAS*, 201, 939  
van den Bosch F. C., 1998, Ph.D. Thesis  
van den Bosch F. C., Emsellem E., 1998, *MNRAS*, 298, 267  
van den Bosch F. C., Ferrarese L., Jaffe W., Ford H. C., O'Connell R. W., 1994, *AJ*, 108, 1579  
van den Bosch F. C., van der Marel R. P., 1995, *MNRAS*, 274, 884  
van der Marel R. P., 1994, *MNRAS*, 270, 271  
van der Marel R. P., Cretton N., de Zeeuw P. T., Rix H-W., 1998, *ApJ*, 493, 613  
van der Marel R. P., Franx M., 1993, *ApJ*, 407, 525  
van der Marel R. P., van den Bosch F. C., 1998, *AJ*, 116, 2220  
van Dokkum, P. G., Franx, M., 1995, *AJ*, 110, 2027  
Verdoes Kleijn G. A., Baum S. A., de Zeeuw P. T., O'Dea C. P., 1999, *AJ*, 118, 2592  
Verdoes Kleijn G. A., van der Marel R. P., Carollo C. M., de Zeeuw P. T., 2000, *AJ*, 120, 1221  
Verolme E. K., Cappellari M., Copin Y., van der Marel R. P., Bacon R., Bureau M., Davies R. L., Miller B. M., et al., 2002, *MNRAS*, 335, 517  
Wernli F., Emsellem E., Copin Y., 2002, *A&A*, 396, 73  
White S. D. M., Rees M. J., 1978, *MNRAS*, 183, 341  
Williams T. B., 1981, *ApJ*, 244, 458  
Yu Q., Tremaine S., 2002, *MNRAS*, 335, 965



---

## Chapter 2

---

# Relation between dust and radio luminosity in optically selected early type galaxies

Davor Krajnović, Walter Jaffe, 2002, *Astronomy and Astrophysics*, Vol. 390, p. 423

We have surveyed an optical/IR selected sample of nearby E/S0 galaxies with and without nuclear dust structures with the VLA at 3.6 cm to a sensitivity of  $100 \mu\text{Jy}$ . We can construct a Radio Luminosity Function (RLF) of these galaxies to  $\sim 10^{19} \text{ W Hz}^{-1}$  and find that  $\sim 50\%$  of these galaxies have AGNs at this level. The space density of these AGNs equals that of starburst galaxies at this luminosity. Several dust-free galaxies have low luminosity radio cores, and their RLF is not significantly less than that of the dusty galaxies.

### 1 Introduction

RESEARCH conducted during the last decade gave a new view of nearby elliptical galaxies previously considered as old, uniform systems with little gas or dust. Images from the Hubble Space Telescope (HST) have shown that many early-type galaxies have a large amount of dust ( $10^3 - 10^7 M_{\odot}$ ), either in the form of a nuclear disk or in the more diverse form of filaments. Among different studies there is a large variation in the detection rates which may be due to the different methods, resolutions, and sensitivities of the observations (Sadler & Gerhard 1985 40%; Goudfrooij et al. 1994 41%; van Dokkum & Franx 1995 48%; Ferrari et al. 1999 75%; Tomita et al. 2000 56%; Rest et al. 2001 43%; Tran et al. 2001 (IRAS bright sample) 78%), but the general conclusion is that dust is common in nearby ellipticals.

Establishing the presence of dust in nearby early-type galaxies is only the first step towards determining the role of dust in these systems. It is already a well-known fact that radio-loud ellipticals often have large amounts of dust but there are some open questions, especially for the radio-weak sources. Verdoes Kleijn et al. (1999) found that the incidence of dust in radio-loud early type galaxies is 89% while Tran et al. (2001) has a value of 43% for the occurrence of dust in their snapshot sample of relatively radio-quiet nearby early-type galaxies (for a description of the sample see Sec. 2). In the same sample, 66% of dusty galaxies have NRAO VLA Sky Survey (NVSS) 1.4 GHz flux detections (Condon et al. 1998), while only 8% of galaxies without dust are listed as radio sources.

These results raise a question: how important is the presence of dust for radio emission in the nuclei of ellipticals? Plausibly, dust indicates the presence of gas, and gas is necessary to fuel the activity of a central massive black hole (BH). However, this line of reasoning is highly incomplete. Gas may be present without dust. Dust may be present but not visually detectable (Goudfrooij & de Jong 1995). Dust and gas that have fed a BH in the past may not be observable at the time when the nuclear activity is observed. These arguments justify a careful study of the relation between dust and nuclear radio emission to determine the relevance of radio luminosity, dust morphology and other effects.

There are two approaches to the study of extragalactic radio sources. The first one is based on catalogs of discrete radio sources followed by an analysis of the optical counterparts. The second involves searching for radio emission from optically chosen objects. The first approach (e.g. de Koff et al. 2000) is relatively efficient in finding radio galaxies, but emphasizes powerful radio sources and may not provide a good counter-sample of radio-quiet galaxies. The second approach conversely emphasizes weak radio sources (e.g. Sadler, Jenkins & Kotanyi 1989; Wrobel 1991; Wrobel & Heeschen 1991; Sadler et al. 2002).

Both types of radio surveys are important. Here we have chosen the second method primarily so that the optical selection of the sample, including Hubble type and especially dust content, is not biased by *a priori* selection for radio emission or other “interesting” properties of the galaxies. The survey objects are selected on their optical/IR properties only and then observed with the VLA with the purpose of establishing the presence of nuclear AGNs. We compare our dusty and non-dusty parts of the sample to investigate the importance of dust (as a fuel reservoir) for the existence of nuclear activity.

In Section 2 we present the sample and discuss the observations and the data reduction. In Section 3 we present the results of our study. They are followed with a discussion in Section 4. Section 5 brings a discussion on correlation of dust with radio emission. The conclusions are given in Section 6.

## 2 Observations

### 2.1 Sample

Our sample is compiled from two different samples described by Rest et al. (2001) and Tran et al. (2001). The first sample was created by selecting E/S0 galaxies on their optical properties only from the Lyon/Meudon Extragalactic Database (LEDa). A randomly selected subset of 68 galaxies from this sample was observed with HST using WFPC2 in snapshot mode and thus this sample is referred to as the “snapshot” sample. An additional sample of galaxies was assembled from archival HST images of nearby E/S0 galaxies selected for their 100  $\mu\text{m}$  IRAS emission as these were likely to contain large amount of dust (Tran et al. 2001). This sample is referred to as the “IRAS sample”. From these two samples, we have selected 36 objects (18 from each) according to their optical/IR properties, with no regard to radio properties. The reason for this selection was to avoid biasing in picking *a priori* “interesting” objects and objects with strong radio fluxes. Galaxies in our sample are nearby ellipticals and lenticulars

(E/S0),  $cz < 3200 \text{ km s}^{-1}$ , at galactic latitude exceeding  $20^\circ$  to minimize Galactic extinction, and with absolute V-band magnitude less than -17. Because of their optical/IR selection they tend to have low radio powers.

The global properties of galaxies in our sample are listed in Table 1 of Rest et al. (2001) and in Table 7 of Tran et al. (2001). In the list of 36 galaxies, 18 of them were chosen because they have dust in the form of disks or filaments. The other 18 non-dusty galaxies were selected to match dusty galaxies in optical properties, redshift, magnitude, and IRAS flux. However, after the initial selection, more detailed studies (Rest et al. 2001, Tran et al. 2001) showed that 6 of the “non-dusty” galaxies showed faint dust structures and have here been included in the “dust” class. We used  $H=80 \text{ km s}^{-1} \text{ Mpc}^{-1}$  to be consistent with the papers defining the samples.

## 2.2 Data Acquisition and Reduction

The observations were undertaken with the VLA in C configuration at 3.6 cm wavelength. All sources were observed at two frequencies in the 8 GHz X-band (8.4351 and 8.4851 GHz) with a bandwidth of 50 MHz for each frequency. We observed 68 sources in total, 36 galaxies and 32 calibrators. Each galaxy was observed for 15 minutes while calibrators were observed for 130 seconds. Most of the calibrators had position code A (positional accuracy  $< 0''.002$ ), but four calibrators had B ( $0''.002 - 0''.01$ ) and three had C ( $0''.01 - 0''.15$ ) as is indicated on the calibrator web page of the VLA. The radio positions of the detected sources are limited by this positional accuracy of the calibrators, as well as by the accuracy of the Gaussian fit to the source brightness distribution, which is dependent on the signal-to-noise ratios. Taking this in account the overall accuracy is about 50 mas for mJy sources and about 100 mas for  $100 \mu\text{Jy}$  sources. The observations were taken on March 13, 2000.

We used the Astronomical Image Processing System (AIPS) to reduce the data using the standard procedures from the AIPS cookbook. After initial calibration, the data were imaged using the task IMGR. The data were self-calibrated in phases to improve the image dynamic range, using a model derived from the same data. In some cases amplitude self-calibration was performed on the data to improve the final images. For our astrometric purpose, the positions of the sources were extracted before self-calibration so that phase information was preserved. All the images were examined using the tasks JMFIT and IMSTAT.

## 3 Results

Twenty galaxies in our sample of 36 were detected as radio sources. Three detected sources (associated with NGC 2986, NGC 3610, NGC 4125) cannot be matched with the central regions of the galaxies and there are no visible counterparts on the available HST pictures, hence they are most likely background sources. The radio sources lay far from the nuclei (about  $2'.67$  for NGC 2986,  $3'.84$  for NGC 3160, and  $1'.44$  for NGC 4125). Although the fluxes and positions of these sources are listed in Table 1 (with asterisks) we treat them as *non-detections* of central AGNs in the surveyed galaxies. This leaves 17 AGN detections in 36 galaxies (47 % detection rate). The smallest signal to noise ratio (SNR) is about  $10\sigma$  with a survey average rms  $\sigma = 2.8 \times 10^{-5} \text{ Jy/beam}$ . For non-

name (1)	dust (2)	D (3)	peak flux (4)	RA (5)	DEC (6)	L (7)	$\delta$ (8)	NVSS flux (9)
ngc1400	2	25.4 <sup>P</sup>	2.092 ± 0.02	03 39 30.815	-18 41 17.42	1.61 ± 0.02	1.80	2.5 ± 0.5
ngc1439	4	20.9 <sup>T</sup>	<0.1					
ngc2549	0	15.7 <sup>R</sup>	<0.1					
ngc2592	4	25.5 <sup>R</sup>	0.41 ± 0.02	08 27 08.040	25 58 13.00	0.32 ± 0.01	0.65	
ngc2699	4	21.8 <sup>R</sup>	<0.1					
ngc2768	4	16.7 <sup>T</sup>	10.71 ± 0.02	09 11 37.418	60 02 14.84	3.59 ± 0.01	0.54	14.5 ± 0.6
ngc2778	0	25.4 <sup>T</sup>	<0.1					
ngc2974	3	25.9 <sup>T</sup>	5.22 ± 0.02	09 42 33.310	-03 41 57.09	4.19 ± 0.02	0.93	10.4 ± 0.5
ngc2986*	0	22.3 <sup>T</sup>	8.40 ± 0.03	09 44 27.256	-21 16 11.23		160.14	
ngc3078	4	29.0 <sup>R</sup>	124.95 ± 0.04	09 58 24.630	-26 55 36.09	125.73 ± 0.04	1.45	279 ± 8
ESO437-15	3	32.3 <sup>R</sup>	1.76 ± 0.04	10 36 58.100	-28 10 34.70	2.20 ± 0.05	0.80	3.2 ± 0.6
ngc3156	2	14.0 <sup>T</sup>	<0.1					
ngc3226	3	17.3 <sup>R</sup>	7.29 ± 0.05	10 23 27.005	19 53 54.75	2.61 ± 0.02	0.97	
ngc3348	0	38.5 <sup>R</sup>	1.66 ± 0.02	10 47 10.000	72 50 22.71	2.94 ± 0.04	1.36	7.8 ± 0.5
ngc3377	1	9.1 <sup>T</sup>	<0.1					
ESO378-20	0	35.6 <sup>R</sup>	<0.1					
ngc3595	0	30.4 <sup>R</sup>	0.22 ± 0.01	11 15 25.180	47 26 50.60	0.24 ± 0.01	3.87	
ngc3610*	3	26.8 <sup>R</sup>	1.17 ± 0.03	11 18 20.700	58 49 38.11		230.78	
ngc4125*	4	20.1 <sup>R</sup>	1.23 ± 0.02	12 08 04.180	65 09 41.32		86.29	
ngc4233	4	29.6 <sup>R</sup>	2.52 ± 0.01	12 17 07.679	07 37 27.33	2.64 ± 0.01	1.02	2.9 ± 0.5
ngc4365	0	15.7 <sup>R</sup>	<0.1					
ngc4406	4	17.0 <sup>V</sup>	0.59 ± 0.02	12 26 11.770	12 56 46.40	0.204 ± 0.07	1.37	
ngc4476	3	24.7 <sup>T</sup>	<0.1					
ngc4494	4	17.8 <sup>R</sup>	0.27 ± 0.01	12 31 24.030	25 46 30.01	0.10 ± 0.01	2.00	
ngc4552	4	17.0 <sup>V</sup>	93.40 ± 0.02	12 35 39.805	12 33 22.78	32.30 ± 0.01	0.35	100 ± 3
ngc4697	4	15.5 <sup>T</sup>	<0.1					
ngc4742	3	15.9 <sup>T</sup>	<0.1					
ngc5198	0	34.1 <sup>R</sup>	0.83 ± 0.02	13 30 11.390	46 40 14.80	1.15 ± 0.03	1.16	3.6 ± 0.4
ngc5322	4	23.9 <sup>T</sup>	13.60 ± 0.02	13 49 15.269	60 11 25.92	9.33 ± 0.01	1.08	64 ± 2
ngc5557	0	42.5 <sup>R</sup>	<0.1					
ngc5576	0	19.1 <sup>R</sup>	<0.1					
ngc5812	4	24.6 <sup>R</sup>	<0.1					
ngc5813	4	24.6 <sup>R</sup>	2.95 ± 0.02	15 01 11.234	01 42 07.10	2.14 ± 0.01	0.72	12.3 ± 0.7
ngc5845	4	18.1 <sup>T</sup>	<0.1					
ngc5982	0	39.3 <sup>R</sup>	<0.1					
ngc6278	0	37.1 <sup>R</sup>	1.06 ± 0.01	17 00 50.325	23 00 39.73	1.75 ± 0.02	0.62	

**Table 1** — Radio properties of the galaxies. Col.(1): name of the galaxy, sources with a star are far from the nuclear region of the corresponding galaxies and were treated as non detections; Col.(2): level of dust: 0 = no dust, 1 = filamentary low, 2 = filamentary medium, 3 = filamentary high, 4 = dusty disk (Tran et al. 2001); Col.(3): distance in Mpc from (P) - Perrett et al. 1997, (T) - Tran et al. 2001, (R) - Rest et al. 2001, (V) - Virgo galaxies, assumed to be at distance of 17 Mpc; Col.(4): flux at 3.6cm in mJy, or  $4\sigma$  upper limits for non-detections; Cols.(5) and (6): radio position (h, m, s) and (deg, arcmin, arcsec) from our maps (J2000); Col.(7): luminosity in  $10^{20}$   $\text{WHz}^{-1}$ ; Col.(8): offset in arcseconds, between the 3.6 cm radio position and the position of the galaxy optical nucleus on HST images (Tran et al. 2001, Rest et al. 2001); Col.(9): peak flux from NVSS survey (Condon et al. 1998).

detected sources we calculated the  $4\sigma$  upper limits on detection, thus, the detection limit of our survey is about 0.1 mJy. Radio properties of the sample are given in Table 1. By comparison, the detection limit of the NVSS (Condon et al. 1998) used by Tran et al. (2001) to discuss radio properties of our sample is  $\sim 3$  mJy, a factor of 30 higher.

Most of the detections are point-like, unresolved structures. NGC 5322 is the only galaxy with noticeable jet-like structure. Typical detected sources are on the level of a few mJy; the weakest detections were  $\sim 200\mu\text{Jy}$ . Of the 36 galaxies in the sample, 24 galaxies show disk or filamentary dust structure and 13 (54%) of them are detected as radio sources. Twelve show no dust of which four (33%) are detected.

## 4 Discussion

### 4.1 Nature of Detected Radio Sources

Most of the detections are unresolved radio sources easily associated with the central  $1''.5$  on the HST image. At 25 Mpc, the mean distance of the galaxies in the sample,  $1''$  is about 120 pc. Thus the emission is clearly (near) nuclear, but not necessarily of AGN origin. Since the sources are weak (radio power ranges from  $10^{19}$  W Hz $^{-1}$  to  $10^{21}$  W Hz $^{-1}$  with a few higher exceptions) there is a possibility that they arise from a non-AGN mechanism, e.g. nuclear starbursts. Since we are interested in the AGN/dust connection we wish to exclude this possibility. We argue here that the dominant source of radio emission in our detections is a non-thermal mechanism similar to that which operates in more powerful radio sources.

There are several radio and infrared criteria that can be used to distinguish between emission from starburst and AGN galaxies: (i) radio morphology, (ii) far-infrared to radio flux-density parameter  $u \equiv \log(S_{60\mu\text{m}}/S_{1.4\text{GHz}})$ , (iii) infrared spectral index  $\alpha_{IR} \equiv \log(S_{60\mu\text{m}}/S_{25\mu\text{m}})/\log(60/25)$  (Condon & Broderick 1988 and 1991; Condon et al. 1991; Condon, Huang & Thuan, 1991), and (iv) the steepness of the radio spectra. Radio morphology implies coherent radio jets and radio lobes that may lie well outside the optical galaxy. Starburst galaxies usually have  $u \geq 1.6$ , and  $\alpha_{IR} \geq +1.25$ . Steepness of the radio spectrum is also used as a criterion since optically thick AGN cores usually have flat spectra, while the dominant emission from star-forming regions (supernova remnants, and cosmic rays diffusing from them) have steep spectra. Nearly all spirals and unclassifiable objects (e.g. mergers) have steep spectra, while flat spectra and other AGN characteristics (radio morphology,  $u \leq 1.6$ , and  $\alpha_{IR} \leq +1.25$ ) are associated with ellipticals (Sadler, Jenkins, & Kotanyi 1989, Condon 1991).

All detected galaxies in our sample have low-luminosity unresolved sources in the innermost central regions. Although the sources are certainly nuclear in origin (suggesting AGN activity) any radio classification according to radio morphology is not possible (except in the clear case of a jet in NGC 5233). Half of the galaxies were picked based on their large-scale dust and infrared properties from the IRAS survey. This means that those galaxies are going to have larger  $\alpha_{IR}$  indices, which would mark them as starburst, although they still might have nuclear AGN which are the subject under discussion. Using the large scale IR emission to determine the nature of the nuclear radio emission does not seem to be a very good discriminator between SBs and AGNs. However, most of our objects have measured nuclear H $\alpha$  fluxes or upper

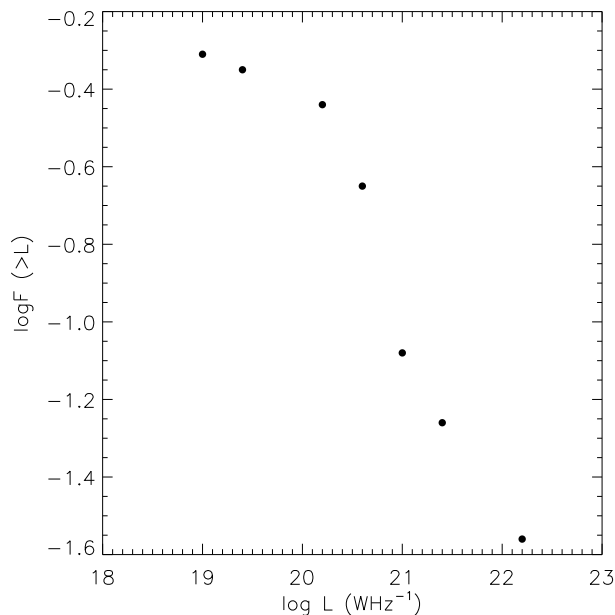


**Figure 1** — The integral luminosity function derived from 17 detected sources out of a total of 36. The dots represent a crude LF calculated from the detections as the integral of a series of delta functions. A detection at  $L_i$  contributes  $1/N_d(L_i)$  where the denominator is the number surveyed galaxies detectable at  $L_i$ . The steep rise flattens off below of  $10^{20} \text{W Hz}^{-1}$ . The error bars are not plotted since the bins in the integral RLF are not independent.

limits (Tran, private communication), and standard calculations (Osterbrock 1989) indicate that the free-free fluxes from these regions would be below  $3 \mu\text{Jy}$ , which is about two to three orders of magnitude smaller than our observed fluxes. Other evidence that we are dealing with non-thermal radiation comes from the flatness of the spectra in our sample. Eleven of the galaxies were detected before in the NVSS (Condon et al. 1998) and comparing the fluxes at our frequency (8.45 GHz) and the frequency of the NVSS (1.4 GHz) it is clear that most of the detected galaxies have flat spectra (Table 1).

Previous studies (Phillips et al. 1986; Sadler, Jenkins & Kotanyi 1989) have shown that HII regions in early type galaxies are not likely to contribute to the radio galaxy population above  $10^{19} \text{W Hz}^{-1}$ . Keeping in mind that all galaxies in our sample are Es and S0s, that emission is confined to nuclei of the host galaxies, and that the sources have flat spectra, we can assume that the dominant radio component in our case is synchrotron emission from an active nucleus producing low-luminosity counterpart of more distant, luminous AGNs.

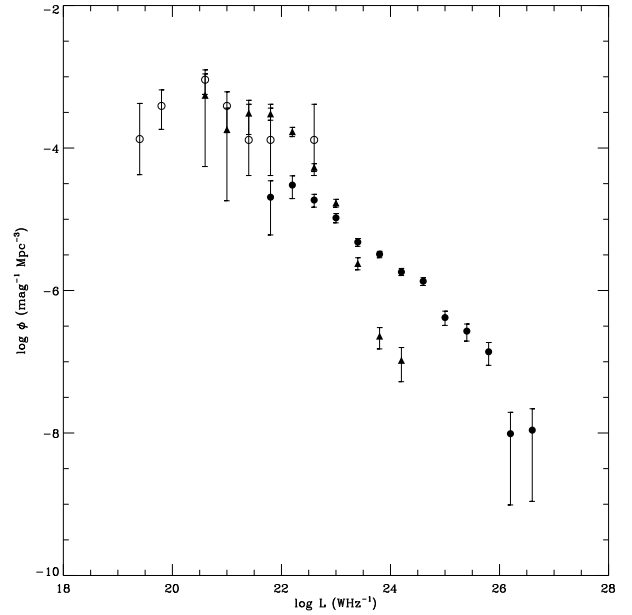
## 4.2 Radio Luminosity Function

The size of our sample is too small and too limited in radio luminosity range to construct a complete local radio luminosity function (RLF) of early-type galaxies. In any case, the sample was not constructed for that purpose. Still, we can make a useful estimate of the low luminosity end of the local RLF in order to see how it corresponds with previously found local RLFs and offer an estimate of the behavior of RLF at low luminosities. For this purpose we define the fractional luminosity function (Auriemma et al. 1977):

$$F_i(L, z) = \rho_i(L, z)/\varphi_i(z), \quad (1)$$

where  $\varphi_i(z)$  is the volume density of objects of type  $i$  at the redshift  $z$ , and  $\rho_i(L, z)$  is the density of sources associated with optical objects of type  $i$  with the given radio

**Figure 2** — Comparison of AGN and starburst (SB) local radio luminosity function. Filled symbols (circles: AGN, triangles: SB) are data from Sadler et al. (2002) and Condon (1991), while open circles are our data. The local density of AGN rises continuously at low luminosities, reaching the value of SB, suggesting that AGNs are as common as SB in local universe. It is possible that at this low luminosity level both processes are present in galaxies, but in some galaxies one of the engines is stronger.



luminosity  $L$  and at the given redshift  $z$ . The fraction of all elliptical galaxies with luminosity at a given frequency between  $L$  and  $L + dL$  at the redshift  $z$ , of optical magnitude  $M$  is given then by  $F_{E,M}(L, z)dL$ . In order to estimate the “bivariate” RLF defined in this way we can calculate the fractional detection  $f_{ij} = n_{ij}/N_{ij}$ , where  $n(L_i, M_j)$  is the number of actually detected galaxies within the optical magnitude range  $M_j \pm 0.5$  and radio luminosity interval  $\log L_i \pm 0.2$ , while  $N(L_i, M_j)$  is the number of galaxies in the sample which could have been detected if their optical magnitude and radio luminosity were in the given interval. In our case we did not bin in optical magnitude but only in radio power since the sample is limited. Our first estimate of the RLF is then given by  $f_L = n_L/N_L$  and it is shown in Fig. 1 in integral form,  $F(>L)$ . As it can be seen from the Fig. 1, the integral RLF of nearby ellipticals rises steeply with decreasing of the radio luminosity and only at the lowest intensities ( $10^{19} \text{ W Hz}^{-1}$ ) levels off at a point where  $\sim 50\%$  of all E/S0 galaxies show activity.

Previous RLFs (Auremma et al. 1977; Sadler, Jenkins, & Kotanyi 1989; Condon 1991; Sadler et al. 2002) of nearby ellipticals with an AGN signature were made for galaxies with radio luminosities higher than  $10^{21} - 10^{22} \text{ W Hz}^{-1}$ . The more recent studies considered also starburst galaxies. While AGN were found in ellipticals, starbursts inhabited spirals. These different distributions had different RLFs and often starburst RLFs extended to the level of  $10^{20} \text{ W Hz}^{-1}$ . With our low luminosity data, we are able to extend the existing RLFs of AGN down to  $10^{19} \text{ W Hz}^{-1}$  and can construct an exclusively AGN RLF.

We compare our data with two studies (Sadler, Jenkins, & Kotanyi 1989 and Condon 1991) in Fig. 2 (AGNs and starbursts plotted). We have converted our differential data from  $F(L)$  to a spatial density  $\phi$  (number of sources per  $\text{Mpc}^3$  per 0.4 in  $\log L$ ) using the value for spatial density of early type galaxies, from Sadler, Jenkins, & Kotanyi (1989), which is  $10^{-2.33} \text{ mag}^{-1} \text{ Mpc}^{-3}$ . Gratifyingly our data agrees quite well with the previous data in the region of overlap. Together these data confirm the flattening of the RLF for AGNs below  $\sim 10^{20} \text{ W Hz}^{-1}$ . It is also interesting that the space density

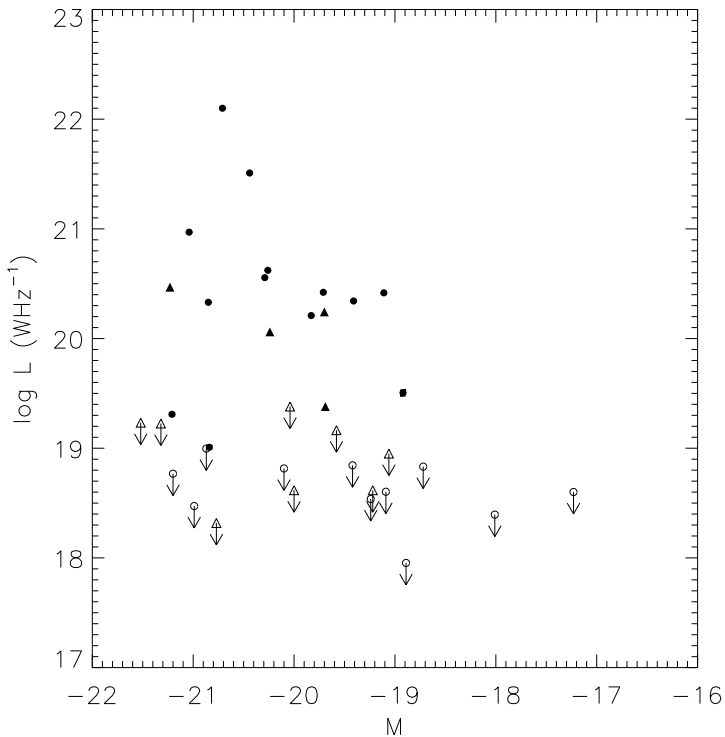


**Figure 3** — Plot of log radio luminosity in  $\text{W Hz}^{-1}$  versus absolute optical magnitude. Filled symbols are radio-detected nuclei of galaxies, while open symbols indicate upper limits for the rest of the galaxies. Triangles are sources in galaxies without dust and circles are sources in dusty galaxies. Sources in dusty galaxies have a slight tendency for being more powerful than the sources in non-dusty galaxies. Luminosity error bars are smaller than the symbols.

of low luminosity AGN is very similar to starbursts galaxies of the same luminosities. The RLFs of the two distributions are basically overlapping in this luminosity range.

## 5 Correlation of dust with radio emission

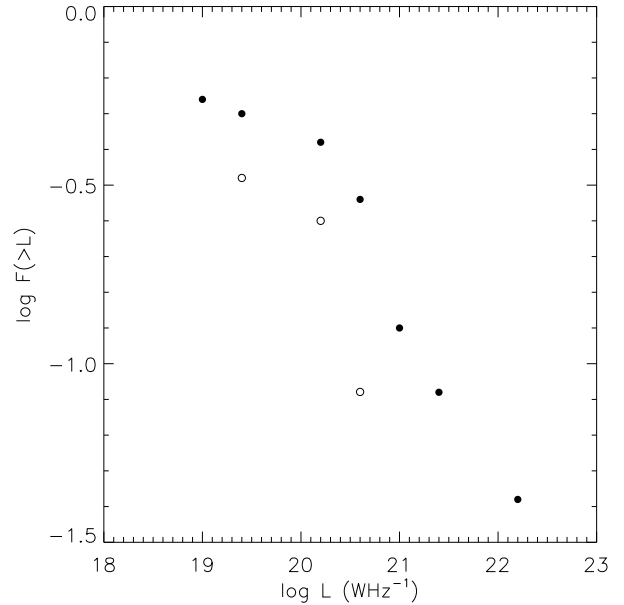
### 5.1 Crude Statistics

The HST pictures of the galaxies in the original sample (Tran et al. 2001) confirm that dust is very common in ellipticals. There are two different morphologies in which dust appears in the galaxies from our sample: disk and filamentary. We have 15 galaxies with disks and 9 with large amount of dust in filaments. Thirteen of the 24 dusty galaxies have a radio detection (54%), while 4 out of 12 non-dusty galaxies show a detection (33%). There is no significant difference in radio luminosity between the galaxies with disk and filamentary dust: 60% detections in galaxies with disks and 44% in galaxies with filaments. This finding is in general agreement with the findings by Tran et al. (2001).

The relationship between optical absolute magnitude and radio luminosity for our weak radio sources is shown in Fig. 3. There is little difference in the distributions of the dusty and non-dusty galaxies, except perhaps that the three most powerful galaxies are all dusty. As expected, the more powerful radio sources are found in the brighter galaxies.

Most nearby high luminosity radio sources are found in dusty early type galaxies (de Koff et al.(2000)), which suggests a link between dust and the existence of a radio source. Our wish now is to see if at the lower levels of radio luminosity dust also plays an important role. We divide the detections in two sets of sources: dusty and

**Figure 4** — The separated integral luminosity function. Open circles present the RLF for sources from galaxies lacking dust. Filled circles present the RLF of sources from dusty galaxies. Statistical tests show that the two distributions are not distinguishable, suggesting that dust is not important for the existence of low-luminosity AGN in nearby early-type galaxies.



non-dusty according to the descriptions in Tran et al. (2001). As we see above, the dusty galaxies show a somewhat higher detection rate, but, given the steepness of the RLF, this could be influenced by slight differences in the distances to the two samples, or slight differences in the achieved sensitivities. Therefore it is more meaningful to compare the RLFs of the two samples than the detection percentages.

## 5.2 Comparison of RLFs

The integral RLFs for the two samples, computed by the same algorithm as that in Fig. 1 for the whole sample, are shown in Fig. 4. In this representation also, the dusty galaxies seem more active, but the difference is relatively small (a factor of  $\sim 1.6$ ) and we wish to test the significance of this difference.

The integral RLFs for the two samples, computed by the same algorithm as that in Fig. 1 for the whole sample, are shown in Fig. 4. In this representation also, the dusty galaxies seem more active, but the difference is relatively small (a factor of  $\sim 1.6$ ) and we wish to test the significance of this difference.

We have tried two statistical tests: Kolmogorov-Smirnoff (K-S) and a test using maximum likelihood method (ML). The K-S test has the advantage of being parameter and form free, but the disadvantage of not being very conclusive for small samples. We have two data sets, one with 13 sources in dusty galaxies and one with 4 sources in non-dusty galaxies. We used routines from Numerical Recipes (Press et al. 1992). The probability that these two observation sets could be obtained from the *same* RLF is 64%, hence the RLFs are statistically indistinguishable. However, the K-S test is sensitive to the effective number of data points,  $N_e$ , which in our case of two distributions is  $N_e = N_1 N_2 / (N_1 + N_2) = 3.1$ . Press et al. (1992) give  $N_e \geq 4$  as a limit for a decent accuracy. Thus, the above probability is not very accurate, but it still implies that the two data sets (two luminosity functions) are not significantly different.

Another approach that is more sensitive, but requires more *a priori* assumptions, is to fit a specific, parameterized, function to the RLF data using the maximum likeli-

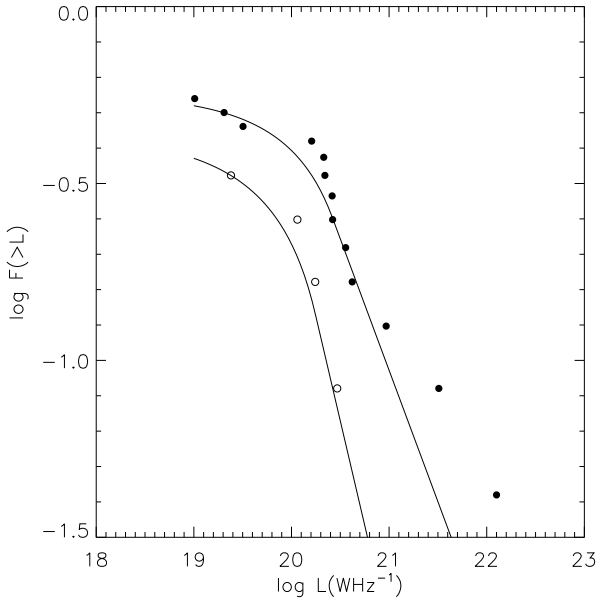


**Figure 5** — Estimated integral luminosity functions compared to the data. The drawn lines show the ML model fits (equations 2 and 3) to the data, while the points are computed from individual detections. Filled circles present dusty galaxies while open circles present non-dusty galaxies. The thick line shows the ML model fit for dusty galaxies and the thin line for non-dusty galaxies.

hood method, and compare the fitted functions. Since there are a limited number of degrees of freedom in the function, more powerful statistical statements can be made. To estimate the integral luminosity function we used a set of two power-law functions allowing for a break in the RLF. Our choice is similar to some previously used functions (Auriemma et al. 1977):

$$F = A_0 \cdot 10^{-\beta(x-x_c)} \quad \text{for } x > x_c \quad (2)$$

$$F = A_0 \cdot \left(1 + \frac{\beta}{\alpha}(10^{-\alpha(x-x_c)} - 1)\right) \quad \text{for } x < x_c \quad (3)$$

where  $x = \log_{10}L$ , and  $L$  is radio luminosity in  $W \text{ Hz}^{-1}$ . The normalization constant  $A_0$  is chosen so that at  $x = x_c$ ,  $F = A_0$ . Originally we assumed that at low luminosities the value of  $F(x)$  had to approach  $F = 1$  as  $x \rightarrow -\infty$ , thus providing an additional constraint on the model. These solutions provided poor fits to the data and were dropped. This implies, however, that there is another break (or continuous change of slope) in the RLFs below the limits of our survey.

The system of coefficients  $\alpha$ ,  $\beta$  (slopes of the curve),  $x_c$  (the position of the break) and  $A_0$  (normalization) that maximize the probability in the method, provide also the best fit to the data. Table 2 contains the calculated values for  $\alpha$ ,  $\beta$ ,  $x_c$  and  $A_0$ .

The best-fit integral luminosity functions are compared to the observed values in Fig. 5. The symbols are filled circles for dusty and open circles for non-dusty sources. The thick represents the model fit to dusty sources, while the thin line shows the fit to the non-dusty. The model curves fit the individual points reasonably well. The three radio brightest galaxies lie somewhat above the best two power-law fit in the region of the break, but the best fit value of the slope above the break,  $\beta \simeq 0.75$ , agrees with the slope measured by Sadler et al. (2002) (Fig. 2) based on much more data in the higher luminosity ranges.

The ML parameters  $\alpha$ ,  $\beta$ , and  $x_c$  are essentially identical for dusty and non-dusty galaxies, indicating that the forms of the RLF are similar. Not surprisingly the normal-

**Table 2** — Estimated integral luminosity coefficients. Values of coefficients of estimated integral luminosity function  $F$  obtained by maximum likelihood method. Errors are  $1\sigma$  estimates.

data sample	$\alpha$	$\beta$	$x_c$	$A_0$
all data	$-0.6 \pm 0.3$	$0.80 \pm 0.10$	$20.41 \pm 0.04$	$0.21 \pm 0.04$
dust data	$-0.6 \pm 0.4$	$0.74 \pm 0.09$	$20.40 \pm 0.10$	$0.25 \pm 0.07$
non-dust data	$-0.5 \pm 0.3$	$1.20 \pm 0.60$	$20.24 \pm 0.04$	$0.14 \pm 0.02$

ization  $A_0$  is higher for the dusty galaxies by a factor of about 1.8, but this is only 1.6 times the uncertainty.

Another way to globally judge the significance of the difference between these RLFs is to ask if the “true” RLF were given by the dusty model, how unlikely is it that we would only detect four (or less) of the twelve non-dusty galaxies. If this probability is small, then the samples are significantly different. From Poisson statistics the probability of 4 or less non-dusty detections given the dusty RLF (thick line on Fig. 5 or the second line values in the Table 2) is 27%, indicating a low statistical significance. If, hypothetically, the true non-dusty RLF is a factor of 1.6 lower than the dusty RLF we can ask how many non-dusty galaxies must be surveyed in order to demonstrate the RLF difference at a reliability of, say, 5%. Repeating the Poisson analysis indicates that a sample about four times the current size is needed, or about 50 non-dusty galaxies.

Perhaps the most important result of this investigation is that in any case, a sizable fraction of the non-dusty galaxies,  $\sim 30\%$ , are radio emitters, so that the presence of visible dust is *not necessary* for radio emission from an AGN.

## 6 Conclusions

We report 3.6 cm VLA observations of a sample of 36 near-by ellipticals selected on their optical/IR properties. We detected 17 unresolved (except the jet in NGC5322), compact, flat-spectrum radio cores associated with the central  $1''$  of the nuclei, suggesting that all detected sources are low luminosity AGNs. The lowest detected luminosities are  $\sim 10^{19} \text{ W Hz}^{-1}$ .

We determine the Radio Luminosity Function (RLF) from these galaxies down to a luminosity almost two orders of magnitude lower in luminosity than previously published studies. It shows the continuation in the rise of space density of sources with AGN signature, which was expected from other, unpublished, studies (Condon, private communication). At the luminosities considered (i.e  $L \sim 10^{19} - 10^{22} \text{ W Hz}^{-1}$ ), the space densities of the AGNs and starburst galaxies approach each other, becoming hardly distinguishable. At the lower luminosity end of our sample  $\sim 50\%$  of E/S0 galaxies have detectable radio-AGNs.

Although the non-dusty galaxies show an indication of a lower probability of radio emission, the difference is not statistically significant in a sample of this size. Dust detectable in HST images is certainly not necessary for nuclear radio emission. This situation may be different for the more powerful radio galaxies observed in earlier surveys.

This takes us back to the question of fuel for the central engine of our low luminosity AGNs. If fuel is necessary for nuclear activity why do we find weak AGNs without visible dust? It should be noted that our non-dusty galaxies with radio detections lay further away ( $D > 30$  Mpc) and it might be possible that small amounts of dust were not detected. Also, extremely diffuse gas and dust would not be visible (Goudfrooij & de Jong, 1995) but current theories of accretion require bars and disks and other distinct structures, so fueling from diffuse gas seems unlikely. Similarly, these galaxies could be fueled by hot, dust-free gas, but it seems unlikely that any mechanism in these low-luminosity sources would destroy dust more than in the high luminosity sources where dust is common. A more likely explanation is that the amount of dust and gas present near the nucleus is in some sense positively correlated with the AGN luminosity. The sources in our study are two to three orders of magnitude less luminous than the 3C sources in de Koff et al. (2000), where typical dust optical depths were of order unity. In the HST images, optical depths of less than 1% would probably be missed. Alternatively, AGN fueling may be cyclic, and AGN radio emission is now fueled from material at a few Schwarzschild radii, after the material in a larger circumnuclear accretion disk has been temporarily consumed.

The luminosity of an AGN is determined by the fueling rate and the mass-to-radiation conversion efficiency. The latter is influenced by the degree of advection which is in turn influenced by the Eddington luminosity and the mass of the BH. As recent evidence suggests (Ho, 2002 and references therein) many of the characteristics of low luminosity AGN could be explained by an advection-dominated accretion flow (Narayan & Yi 1995; Narayan, Mahadevan, & Quataert 1998). The explanation of the dust/radio emission/luminosity relations may perhaps be found when we know the BH masses of the galaxies, or when we understand the characteristics of non-steady accretion flows.

## Acknowledgements

DK was supported by Institute Ruđer Bošković in Zagreb and NOVA, the Netherlands Research School for Astronomy. The VLA is operated by the National Radio Astronomy Observatory for the U.S. National Science Foundation.

## References

- Auremma, C., Perola, G. C., Ekers, R. D., Fanti, R., Lari, C., Jaffe, W. J., & Ulrich, M. H. 1977, *A&A*57, 41  
Goudfrooij, P., Hansen L., Jørgensen, H. E., & Nørgaard-Nielsen, H. U. 1994, *A&AS*, 105, 341  
Goudfrooij, P., de Jong, T. 1995, *A&A*, 298, 784  
Condon, J. J., Cotton, W. D., Greisen, E. W., Yin, Q. F., Perley, R. A., Taylor, G. B., & Broderick, J. J. 1998, *AJ*, 115, 1693  
Condon, J. J. & Broderick, J. J. 1988, *AJ*, 96, 30  
Condon, J. J. & Broderick, J. J. 1991, *AJ*, 102, 1663  
Condon, J. J. 1991, *ASP Conf. Ser. 18: The Interpretation of Modern Synthesis Observations of Spiral Galaxies*, 113  
Condon, J. J., Huang, Z.-P., Yin, Q. F., & Thuan, T. X. 1991, *ApJ*, 378, 65  
Ferrari, F., Pastoriza, M.G., Macchetto, F., Caon, N. 1999, *A&AS*, 136, 269  
Ho, L. C., 2002, *ApJ*, 564, 120

- de Koff, S., Best, P., Baum, S. A., Sparks, W., Röttgering, H., Miley, G., Golombek, D., Macchetto, F., & Martel, A., 2000, *ApJS*, 129, 33
- Narayan, R., Mahadevan, R., & Quataert, E. 1998, *Theory of Black Hole Accretion Disks*, 148
- Narayan, R. & Yi, I. 1995, *ApJ*, 452, 710
- Osterbrock, D.E., 1989 *Astrophysics of gaseous nebulae and active galactic nuclei*, University Science Books
- Perrett, K. M., Hanes, D. A., Butterworth, S. T., Kavelaars, J., Geisler, D. & Harris, W. E. 1997 *AJ*, 113, 895
- Phillips, M. M., Jenkins, C. R., Dopita, M. A., Sadler, E. M., & Binette, L., 1986 *AJ*, 92, 503
- Press, W. H., Teukolsky, S. A., Vetterling, W. T., Flannery, B. P., 1992, *Numerical recipes: The Art of Scientific Computing*, CUP, Cambridge
- Rest, A., van den Bosch, F. C., Jaffe, W., Tran, H., Tsvetanov, Z., Ford, H. C., Davies, J., & Schafer, J. 2001, *AJ*, 121, 2431
- Sadler, E. M. & Gerhard, O. E. 1985, *MNRAS*, 214, 177
- Sadler, E. M., Jenkins, C. R., & Kotanyi, C. G. 1989, *MNRAS*, 240, 591
- Sadler, E. M., Jackson, C. A., Cannon, R. D., McIntyre, V. J., Murphy, T., Bland-Hawthorn, J., Bridges, T., Cole, S., Colless, M., Collins, C., Couch, W. and Dalton, G. and De Propris, R., Driver, S. P., Efsthathiou, G., Ellis, R. S., Frenk, C. S., Glazebrook, K. and Lahav, O., Lewis, I., Lumsden, S., Maddox, S. and Madgwick, D., Norberg, P., Peacock, J. A., Peterson, B. A. and Sutherland, W., & Taylor, K., 2002, *MNRAS*, 329, 227
- Tomita, A., Aoki, K., Watanabe, M., Takata, T., & Ichikawa, S. 2000, *AJ*, 120, 123
- Tran, H. D., Tsvetanov, Z., Ford, H. C., Davies, J., Jaffe, W., van den Bosch, F. C., & Rest, A. 2001, *AJ*, 121, 2928
- van Dokkum, P.G., & Franx, M. 1995, *AJ*, 110, 2027
- Verdoes Kleijn, G. A., Baum, S. A., de Zeeuw, P.T., & O'Dea, C. P. 1999, *AJ*, 118, 2592
- Wrobel, J. M. 1991, *AJ*, 101, 127
- Wrobel, J. M. & Heeschen, D. S. 1991, *AJ*, 101, 148



---

## Chapter 3

---

# HST observations of nuclear stellar disks

Davor Krajnović, Walter Jaffe, *Astronomy and Astrophysics*, in press, [astro-ph/0409061]

We present observations of four nearby early-type galaxies with previously known nuclear stellar disks using two instruments on-board the Hubble Space Telescope. We observed NGC 4128, NGC 4612, and NGC 5308 with the Wide Field Planetary Camera 2, and the same three galaxies, plus NGC 4570, with the Space Telescope Imaging Spectrograph. We have detected a red nucleus in NGC 4128, a blue nucleus in NGC 4621, and a blue disk in NGC 5308. Additionally, we have discovered a blue disk-like feature with position angle  $\sim 15^\circ$  from the major axis in NGC 4621. In NGC 5308 there is evidence for a blue region along the minor axis. We discovered a blue transient on the images of NGC 4128 at position  $0''.14$  west and  $0''.32$  north from the nucleus. The extracted kinematic profiles belong to two groups: fast (NGC 4570 and NGC 5308) and kinematically disturbed rotators (NGC 4128 and NGC 4621). We report the discovery of a kinematically decoupled core in NGC 4128. Galaxies have mostly old (10-14 Gyr) stellar populations with large spread in metallicities (sub- to super-solar). We discuss the possible formation scenarios, including bar-driven secular evolution and the influence of mergers, which can explain the observed color and kinematic features.

## 1 Introduction

THE decade of Hubble Space Telescope (HST) observations have revealed the existence of small scale nuclear stellar disks in early-type galaxies. This discovery was an important step in the long process of recognizing the complexity of early-type galaxies. Ground-based studies preceding the HST era, having lower resolution and polluted by typically  $> 1''$  seeing, already recognized two distinct classes of elliptical galaxies (Davies et al. 1983) that differed in photometric appearance – disky vs. boxy – and kinematic properties – rotationally vs. pressure supported – (Bender 1988; Bender et al. 1989). Follow-up studies discovered the existence of embedded stellar disks in elliptical and lenticular galaxies (Scorza & Bender 1995; Seifert & Scorza 1996). These disks, although similar to their counterparts in spiral and S0 galaxies, have smaller scale length and higher central surface brightness. They often do not follow the same exponential profiles, and are closer to  $r^{1/4}$  profiles, reflecting formation in a different potential: dark halo potentials for disks in late-types, and bulge potentials for disks in early-type galaxies (Scorza & Bender 1995). The existence of the embedded disks also supports the idea of the morphological connection between spiral, lenticular and elliptical galaxies (Kormendy & Bender 1996).

The properties of the nuclear regions (inner few 100 pc) of early-type galaxies are, however, not easily accessible from the ground. High resolution imaging surveys with HST discovered small scale nuclear stellar disks in early type galaxies (Jaffe et al. 1994; van den Bosch et al. 1994; Lauer et al. 1995; Rest et al. 2001, hereafter R01). They were followed by detailed photometric and kinematic studies on a few individual objects, principally NGC 4342 (Scorza & van den Bosch 1998; van den Bosch et al. 1998, hereafter BJM98), NGC 4570 (BJM98; Scorza & van den Bosch 1998; van den Bosch & Emsellem 1998), NGC 4594 (Burkhead 1986; Kormendy 1988; Emsellem et al. 1996), NGC 7332 (Fisher et al. 1994; Falc3n-Barroso et al. 2004). A detailed study of early-type galaxies with kinematically distinct components (Carollo et al. 1997a,b) found photometric evidences for faint nuclear stellar disks in a number of dust free galaxies.

The next step was a search for embedded nuclear stellar disks in bulges of spiral galaxies. The high resolution studies of spiral galaxies with HST showed that a significant fraction of galaxies classified as early-type spirals have a rich variety of central properties, and show little evidence for  $r^{1/4}$  law expected for smooth bulges (Carollo et al. 1998). Similarly, Balcells et al. (2003) found moderately large fraction (34%) of nuclear bars or disks in their HST near-infrared survey of S0 – Sbc galaxies. Using archival HST imaging, Pizzella et al. (2002) reported evidence for nuclear disks in three early-type spirals and concluded that the disks are restricted to S0 and unbarred spiral galaxies. Having in mind that nuclear stellar disks are detectable only when seen nearly edge on (Rix & White 1990), they appear to be very common, perhaps universal, in flattened ellipticals and S0s.

The large fraction of detected nuclear disks in early-type galaxies (51% in the R01 sample) presents the questions: how and when did the nuclear stellar disks form? Nuclear stellar disks are found in S0 and disky ellipticals, but they are not simple extensions of large scale disks to the center of the galaxy. Often there is clear photometric and kinematic evidences for double disk structures (van den Bosch et al. 1994; Scorza & Bender 1995; Scorza & van den Bosch 1998), where the double disk structures are represented by two morphologically separated disks, having different scale lengths, lying in nearly same plane, but possibly with different inclinations, and having an inner/outer separation radius between the disks. On the other hand, Erwin & Sparke (2002) show evidences that some inner disks seen in edge-on galaxies could be bars mistaken for disks. In any case, the two dynamically different structures are not easily distinguished in all cases.

Inner disks are also found inside bars or rings (van den Bosch & Emsellem 1998; Erwin & Sparke 1999; Erwin et al. 2003). This is important for understanding their formation. Nuclear stellar disks could be the result of mergers in hierarchical galaxy formation scenario: accretion of gas during the merger which settles in the principal plane of the galaxy and then makes stars. On the other hand, disks could be formed from the galaxy material transported to the nucleus by a bar, or perhaps from a mixture of these processes, in which a bar fuels the center effectively with gas captured at some previous epoch. Whatever scenario we choose, it has to be consistent with the high metallicities seen in the disks (BJM98; Emsellem et al. 1996) as well as their blue colors (BJM98; Kormendy et al. 2002) implying younger stellar populations.

Nuclear stellar disks with their cold dynamical properties and high surface bright-

galaxy (1)	type (2)	$M_B$ (3)	$B - V$ (4)	$v_{rad}$ (5)	PA (6)	D (7)	scale (8)
NGC 4128	S0	-19.89	1.02	2610	58	36.3	175.7
NGC 4570	S0	-20.39	0.97	1811	159	25.2	121.9
NGC 4621	E	-20.49	0.97	524	165	7.3	35.3
NGC 5308	E-S0	-20.38	0.93	2299	60	31.9	154.8

**Table 1** — The properties of sample galaxies. Col. (1): galaxy name; Col. (2): morphological type; Col. (3): absolute B-magnitude; Col. (4): apparent B-V color within the effective aperture in which half of the B-flux is emitted; Col. (5): radial velocity (cz) in  $\text{km s}^{-1}$  corrected for LG infall onto Virgo; Col. (6): major axis position angle in degrees; Col. (7): distance in Mpc, as derived from radial velocity (column 5) using Hubble constant  $H_0=72 \text{ km s}^{-1} \text{ Mpc}^{-1}$  (Freedman et al. 2001); Col. (8): distance scale in pc  $\text{arcsec}^{-1}$ . Values listed in columns 2 – 6 are taken from Lyon/Meudon Extragalactic Database (LEDA).

ness provide an excellent measure of the central mass-to-light ratio, as well as of the mass of the central black hole (van den Bosch & de Zeeuw 1996). A few studies used this to determine the mass of the back holes in galaxies with nuclear stellar disks (Kormendy et al. 1996a; Kormendy et al. 1996b; Cretton & van den Bosch 1999; Emsellem et al. 1999).

Early-type galaxies are also interesting for studying stellar populations. The absence of strong and continuous star-formation as well as emission line gas makes it easier to investigate the formation history and the connection between the photometric morphology, dynamical structures and corresponding stellar populations.

In order to increase the available dataset and to investigate the dependencies between the kinematics and line-strengths, as well as to determine the mass of black holes, we obtained high resolution spectra of four galaxies known to have nuclear stellar disks from the R01 sample: NGC 4128, NGC 4570, NGC 4621 and NGC 5308. In addition, we also imaged three of the galaxies, except NGC 4570 which was thoroughly investigated in the previous studies (BJM98, Scorza & van den Bosch 1998; van den Bosch & Emsellem 1998). In this paper we present data observed with two instruments on-board HST during Cycle 9 (Program ID 8667) and concentrate on the photometric and spectroscopic properties and dependencies. Dynamical modeling of the galaxies with the purpose of determining the masses of the central black holes will follow in a separate paper.

Section 2 presents broad band photometry, data reduction, isophotal analysis and color images. Section 3 deals with spectroscopic observations, data reduction, extraction of kinematics and measurements of line-strengths. Section 4 presents a discussion of the results for individual galaxies. The conclusions and summary of the work are presented in Section 6.

## 2 WFPC2 broad band imaging

The Wide Field Planetary Camera 2 (WFPC2) observations (Biretta et al. 1996) included imaging in V (F555W) and B band (F450W). The general properties of the sample galaxies are presented in Table 1, the observations are summarized in Table 2 and the details of the filter properties are listed in Table 3. The centers of the galaxies were positioned

galaxy	filter	date	time	# exp
NGC 4128	F450W	14.05.2001	1400	2
	F555W	14.05.2001	800	2
NGC 4621	F450W	14.05.2001	1200	2
	F555W	14.05.2001	800	2
NGC 5308	F450W	07.05.2001	1400	2
	F555W	07.05.2001	800	2

**Table 2** — Summary of HST/WFPC2 observations.

on the PC CCD. The size of the PC CCD is  $800 \times 800$  pixels of  $0.''0455 \times 0.''0455$ . All exposures were taken with the telescope in fine lock. In addition to newly acquired data, we used existing archival I (F814W) band images for NGC 4621 (Program ID 8212, PI Ajhar) and NGC 5308 (Program ID 5512, PI Faber). There were no I band observations for NGC 4128 in the archive.

## 2.1 Data reduction

The images were reduced through the standard HST/WFPC2 pipeline. Upon request of the data, the On-The-Fly reprocessing system re-reduced the data using the best calibration files. The standard reduction steps include correction for analog to digital conversion error, bias and dark current subtraction and flat-fielding (for more description see Holtzman et al. (1995)). Our observations were divided (CR-SPLIT) in two (per filter). To combine them and to remove the cosmic rays we used a set of IDL routines from The IDL Astronomy User's Library (Landsman 1993)<sup>1</sup>. The WFPC2 images (PC, WF2, WF3, and WF4 for both CR-SPLIT sections) are cross-correlated to determine a possible shift between the exposures, aligned and combined removing the cosmic rays using an IDL equivalent of the IRAF task CRREJ.

We then constructed color images: B-I, V-I and B-V. To construct the color images we had to align the individual images very precisely. This was achieved by rotating the original images for the difference in the telescope orientation angle, sub-sampling pixels by a factor of six and cross-correlating images to find the shift. After all shifts were applied, the images were rebinned to the original pixel size. Both images used for the construction of a color image were initially convolved with the PSF of the other image. The PSFs were constructed using Tiny Tim software (Krist & Hook 2001). The raw counts of the images were converted into Johnson-Cousins B,V and I magnitudes following the guidelines given by Holtzman et al. (1995), using the zero points as given by Dolphin (2000)<sup>2</sup> and iterating the calibration until convergence. Note that the iteration was not performed for the B-I color images, because there were no published transformation for the F450W filter using B and I. We estimate our relative photometric accuracy to be  $\approx 0.02$  mag, while the absolute uncertainty is  $\approx 0.05$  mag (and  $\approx 0.1$  for B-I color). In Figs. 1 and 2 we present WFPC2 observations, isophotal analysis, broadband and color images of three observed galaxies.

<sup>1</sup><http://idlastro.gsfc.nasa.gov>

<sup>2</sup>[http://www.noao.edu/staff/dolphin/wfpc2\\_calib/](http://www.noao.edu/staff/dolphin/wfpc2_calib/)

**Table 3** — Properties of the WFPC2 broad band filters used (from WFPC2 Instrument Handbook).

filter	$\lambda$	$\Delta\lambda$	band
F450W	4410	925	B
F555W	5202	1223	V

## 2.2 Isophotal analysis

In order to investigate the disk structure of the galaxies we used the IRAF task ‘ellipse’ to perform isophotal fits to the light distributions. We measured the ellipticity and position angle of the isophotes, as a function of radius. The method (for a full description see Jedrzejewski (1987)) first fits elliptical isophotes to a Fourier expansion of first and second order terms. The next step in the method is to measure the higher order terms of the Fourier expansion. The pure ellipse is given by the first two order terms in the expansion. Any non zero values of the higher order ( $> 2$ ) terms means a deviation from the perfect ellipse. Peletier et al. (1990) and Goudfrooij et al. (1994) found that  $\cos 3\theta$  terms ( $b_3$ ) are sensitive to the presence of dust (as well as the difference between the higher order terms in different bands), while the  $\cos 4\theta$  terms ( $b_4$ ) describe the shape by distinguishing boxy ( $b_4 < 0$ ) from disk ( $b_4 > 0$ ) galaxies (e.g. Lauer 1985; Bender 1988). The isophotal parameters for three galaxies are shown in Fig 1. Different studies (van den Bosch et al. 1994, R01) showed that although the isophote parameters can be fitted down to  $0''.03$ , they are not reliable and only values  $> 0''.2$  should be used for analysis.

The galaxies were selected on the basis of having a nuclear stellar disk and our isophotal analysis agrees well with the R01 results. For all three galaxies the  $b_3$  terms are consistent with being zero in the reliable range ( $> 0''.2$ ). The  $b_4$  terms have clear disk deviations, but there are differences between the galaxies. NGC 4128 shows the smallest positive values of  $b_4$  coefficient, and is the only galaxy where  $b_4$  becomes negative. It drops below zero at a radius of  $\sim 3''$  from the center. The isophotes remain boxy in the rest of the investigated range ( $3 - 10''$ ). The fourth order term in NGC 4621 is positive in the investigated range, although it starts to decrease beyond  $3''$ . NGC 5308 shows the sharpest rise of the  $b_4$  coefficient, but it drops to zero around  $7''$  before it rises again. The analysis of photometric higher order terms suggests the nuclear stellar disks are separated from the large scale disks.

The coefficients of this isophotal analysis are one-dimensional representations of 2D structures in the galaxies. In order to see more clearly the nuclear disks we constructed residual B and V images by subtracting a model galaxy from the original. The model galaxy was constructed using the IRAF task ‘bmodel’. It had the same luminosity profile as the original galaxy, but it was constructed from perfect ellipses (first two terms in the Fourier expansion). The contour maps, shown in the middle row in Fig. 2, reveal the disk structure that is responsible for the existence of the higher order terms. These disk structures do not necessarily show the full disks, because some information on the disks is also contained in the ellipticity, which was subtracted by the model. However, to the first approximation, these structures are a good representation of the relatively faint nuclear stellar disks in the observed galaxies. The disks have various sizes between  $2 - 5''$ , corresponding to  $150 - 600$  pc, and are in a good agreement with

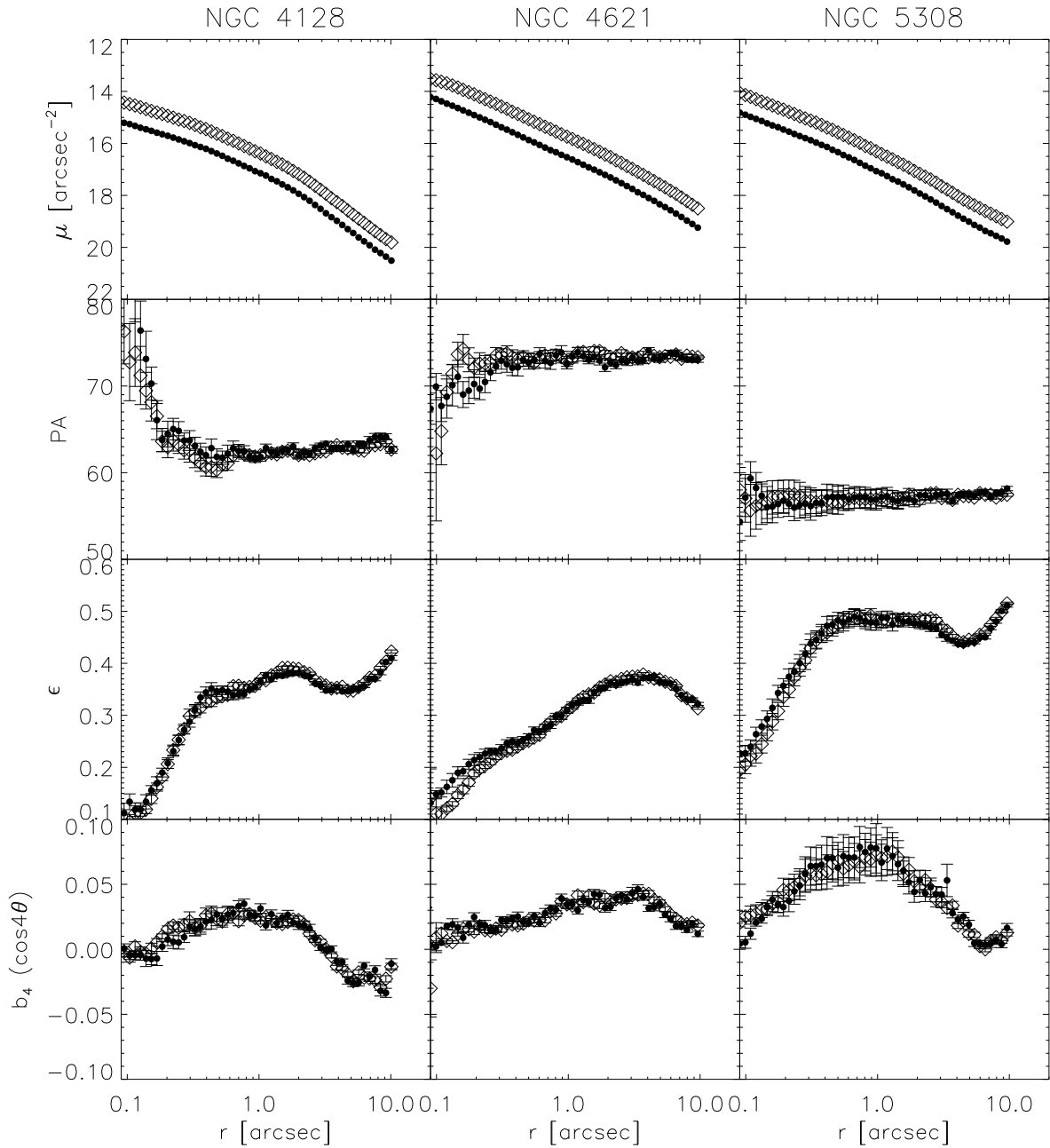


**Figure 1** — Isophotal analysis results for NGC 4128, NGC 4621 and NGC 5308 in two observed filters: B (F450W) and V (F555W). First row: surface brightness profiles. Filled symbols correspond to B and open symbols to V filter. Errors are smaller than the symbols. Second row: position angles measured east of north; in the case of NGC 4621 we added  $90^\circ$  to the measured position angle (east of north) for presentation purposes. Third row: ellipticity. Fourth row: higher order parameters  $b_4$  (the coefficient of  $\cos(4\theta)$ ), showing deviations from perfect ellipses.

the spatial extent of positive values of  $b_4$  terms. The noise structure in Fig. 2 perpendicular to the disks (along the minor axis) is not real and is an artifact of subtracting a

perfect elliptical structure from a very disk-like one.

### 2.3 Broad-band color images

We constructed several broad band images using our data and archival images as described in Section 2.1. In the bottom two rows of Fig. 2 we show B-V and B-I images for all three galaxies except for NGC 4128 which does not have archival I band images. These color images are color coded such that lighter shades indicate redder colors.

#### 2.3.1 B-V color images

The nuclei of the galaxies show different structures in the B-V color. The nucleus of NGC 4128 is redder than the surrounding bulge, NGC 4621 has a convincingly blue nucleus, while NGC 5308 is rather uniform with a slightly bluer central pixel. The magnitudes measured on the constructed color images are presented in Table 4. We measured the color within a small circular aperture (6 pixels in diameter) to point out the subtle differences in colors between different regions and features. The blue feature on the color image of NGC 4128 corresponds to a transient object detected in the galaxy. The nature of the transient is not known (see Appendix B for a detailed discussion). In NGC 4128 isochromes trace the nuclear disk, while in the case of NGC 5308 there is weak evidence of a blue disk outside  $0''.3$  of the nucleus. The difference is  $\approx 0.02$  magnitudes. NGC 4621 is a special case different from both previous galaxies. Here we have a prominent blue nucleus on top of the red bulge. The other particularity of this galaxy is in the blue component that stretches southwards from the nucleus. The average difference between this component and the rest of the bulge is again  $\approx 0.02$ .

#### 2.3.2 B,V-I color images

A bigger color difference is seen in the B-I and V-I images which we constructed for NGC 4621 and NGC 5308. The archival I-band images of NGC 4621 were of good quality, while images of NGC 5308 were saturated, and the very central parts of the images are not reliable.

The interesting blue feature southwards from the nucleus on the B-I image of NGC 4621 is more prominent and we can quantify its extent. The color difference between the red bulge-like background and the blue patch is here  $\approx 0.12$  mag in its extreme. The extent of the feature is  $\approx 1''.35$  on each side of the nucleus, being somewhat bluer on the south side. The feature lies generally in the north-south direction making an angle of  $15^\circ$  to the major axis. It is in no obvious plane of symmetry of the galaxy. The rest of the bulge is red, but a region of enhanced red color lies in the east-west direction. The angle between this reddest region and the major axis is about  $103^\circ$ , making the angle between the bluest and the reddest regions about  $118^\circ$ . The V-I color image confirms this finding, also noticed by Wernli et al. (2002), hereafter WEC02, on their V-I images. We postpone the discussion and interpretation of these features to Section 4.3.

NGC 5308 is an equally interesting case. The center of the I band image was saturated and the blue nucleus is an artifact. Generally, one has to be very careful in interpreting the saturated images. Aware of problems in dealing with saturated images, we used them to verify the faint suggestion from the B-V images of the blue disk.

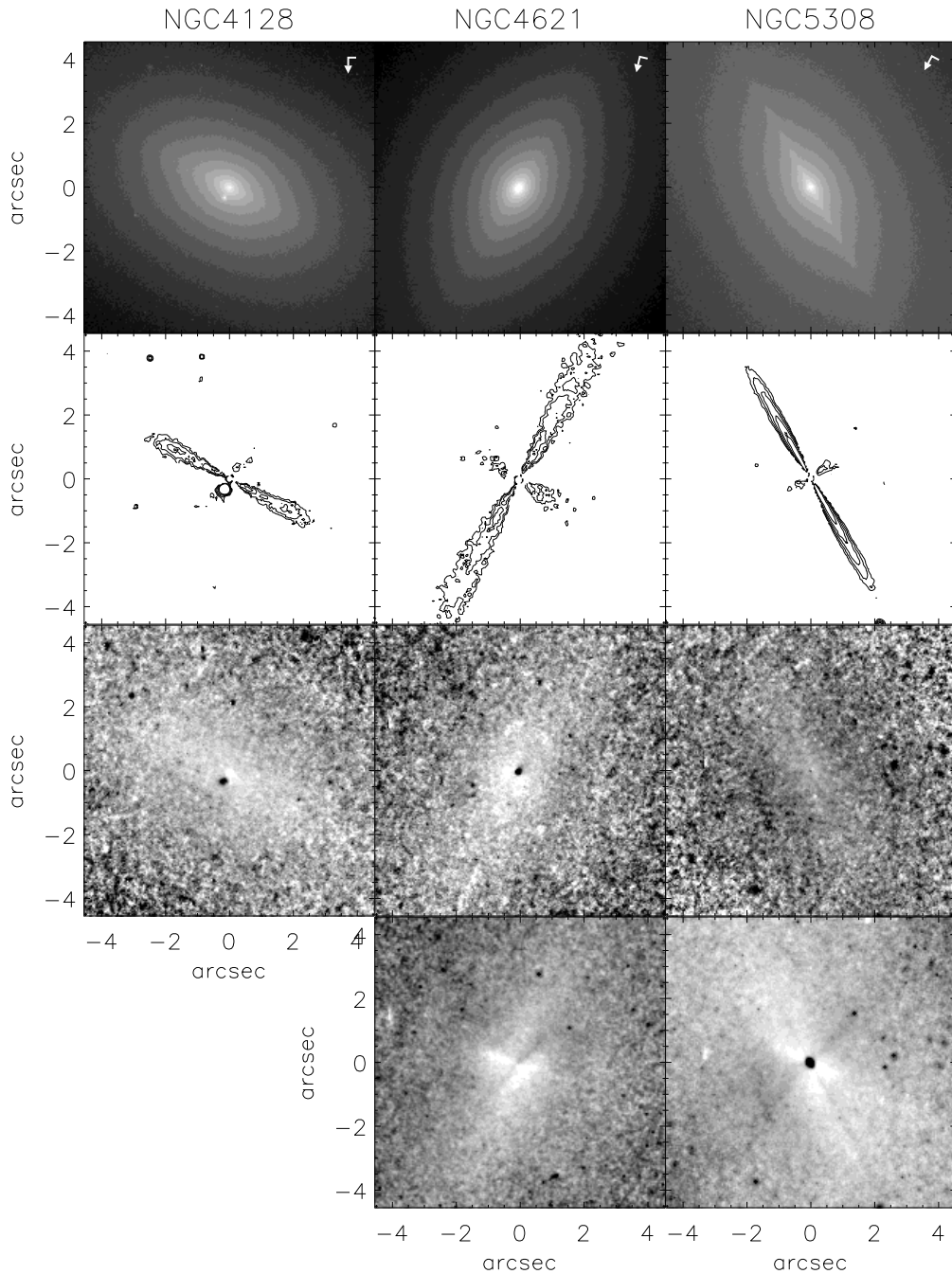


**Figure 2** — WPC2 observation of NGC 4128, NGC 4621, NGC 5308. First row: images in the V (F555W) filter. The arrows and their associated dashes mark the North and East orientation of the images. Second row: residual stellar disks after subtraction of perfect elliptical model galaxy (in V band). Contours were slightly smoothed and logarithmically scaled with steps of 0.5 magnitudes. Third row: B-V images, with grayscale such that brighter means redder. The blue feature next to the center of NGC 4128 is due to the transient and is discussed in Appendix B. The plotted range is (in magnitudes) 0.6 (black) to 1.0 (white) for NGC 4128, 0.5 (black) to 1.05 (white) for NGC 4621, and 0.5 (black) to 0.98 (white) for NGC 5308. Fourth row: B-I images. The central blue feature on the NGC 5308 color map is an artifact of saturation and was not considered in the analysis. Range is from 1.93 (black) to 2.16 (white) for NGC 4621, and 1.1 (black) to 2.07 (white) for NGC 5308.

galaxy (1)	$B - V$		$V - I$		$B - I$	
	center (2)	average (3)	center (4)	BF (5)	bulge (6)	BF (7)
NGC 4128	1.00	0.95	–	–	–	–
NGC 4621	0.87	0.99	1.22	1.16	2.14	2.05
NGC 5308	0.97	0.94	–	–	–	–

**Table 4** — Color in magnitudes measured with aperture of 6 pixel ( $0''.273$ ) diameter. Col. (1): galaxy name; Col. (2):  $B-V$  color measured at the center of the galaxies; Col. (3):  $B-V$  color averaged over 8 apertures placed around center on a square grid centered on the nucleus with size  $2 \times 14$  pixels ( $\sim 1''.27$ ), except for NGC 4128 where the blue feature next to the center was excluded; Col. (4):  $V-I$  color measured at the center of galaxy; Col. (5):  $V-I$  color measured at the blue feature (BF)  $0''.90$  from the center; Col. (6):  $B-I$  color measured at bulge of the galaxy; Col. (7):  $B-I$  color measured at the BF  $0''.90$  from the center.

We do not consider the central  $0''.5$  of the  $B-I$  and  $V-I$  color images (the area somewhat larger than the blue dip in the images), but concentrate on the larger-scale features.

Along the minor axis of the galaxy, the  $B-I$  color image also reveals blue regions on each side of the nucleus, as well as a red feature in the east-west direction. These features were not anticipated and we checked whether they are real or artifacts of saturation since they are close to the nucleus ( $r < 1''$ ). We first constructed color image from unconvolved F4550W and F814W images. On the resulting color image, there was a hint of the east-west red feature. The other approach included deconvolution of the  $B$  and  $V$  images using Richardson-Lucy algorithm with 20 iterations. The resulting images were convolved with the PSF of the  $I$  image, and used to make color images ( $B-I$  and  $V-I$ ). On both color images, next to the red east-west feature, we also detected the blue region on the minor axis. These tests suggest the color features on the last panel of the Fig. 2 are real, although could be augmented by the convolution process due to its proximity to the saturated nucleus.

The remaining and real (clearly visible on all test images), thin blue feature follows the major axis of the galaxy, along which there is clear evidence for a very thin disk on all scales, from the nucleus outwards. The position angle of the thin blue component is the same as of the nuclear stellar disk.

The marginal difference in color ( $\approx 0.01 - 0.02$  mag) is almost razor sharp and it looks like the signature of the thin disk visible also in the residual image (second row of Fig. 2). We compared the sizes of the disk in the residual image and the blue feature in the  $B-I$  color image. The comparison is made by extracting and averaging together several profiles of intensity and color perpendicular to the disk, on both sides of the nucleus (avoiding the central  $2''$ ). The final profiles were fitted with Gaussians. The size (FWHM) of the disk feature on the residual disk image is  $\sim 5.6$  pixels and the size of the color feature is  $\sim 4.4$  pixels. These numbers correspond to  $0''.25$  and  $0''.20$  respectively, and they are in good agreement, enforcing the connection between the components. At the distance of NGC 5308, the blue component in the color image is approximately 30 pc thick.

A way to quantify the relative difference in color between the disk and the bulge is shown on Fig. 3. We measured the color along slit-like apertures (1 pixel wide) along

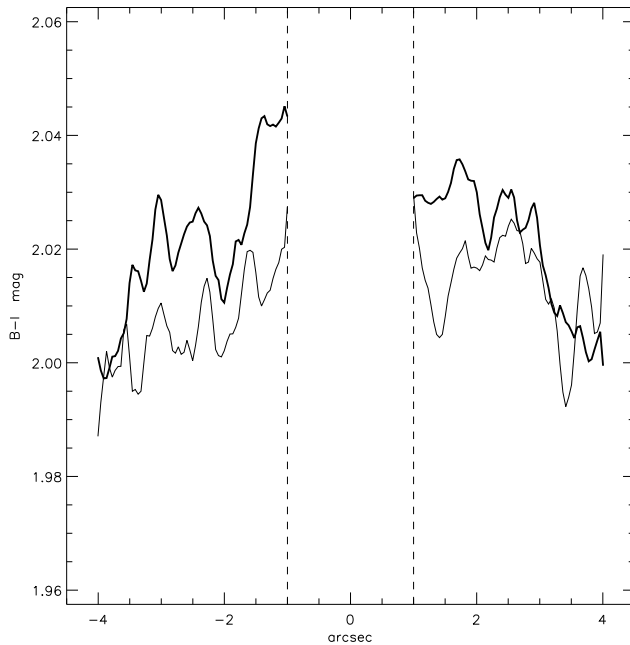


**Figure 3** — Comparison of B-I color profiles extracted (and smoothed) along the disk (thin line) and parallel to disk (thick line) in NGC 5308. The slit-like apertures were 200x1 pixels in size. One slit (thin line) was placed along the major axis (and the disk), while two other slits (averaged together and presented by the thick line) were placed parallel to the major axis, 10 pixels ( $0''.45$ ) above and below it. Vertical dashed lines show the nuclear region excluded from the measurement due to the saturation effects.

the disk and parallel to it, on both sides of the nucleus. The central  $1''$  of all slits were omitted, and the two slits, positioned on each side of the central slit, were averaged and presented as one color profile. The disk is clearly bluer than the bulge in the inner  $8''$ . Beyond  $3''.5$  on each side of the center colors of the disk and bulge become similar.

Briefly summarizing, we list below the important observed color features to which we refer later in the text:

**NGC 4128** has (i) a red nucleus and (ii) a blue feature  $0''.14$  west and  $0''.32$  north of the galaxy center;

**NGC 4621** has (i) a blue nucleus, (ii) an extended blue component with  $PA \approx 150^\circ$  (east of north), and (iii) an extended red component with  $PA \approx 268^\circ$  (east of north);

**NGC 5308** has (i) an extended blue component along the major axis and (ii) a wide blue component along the minor axis, (iii) an extended red component with an east-west orientation.

### 3 STIS spectroscopy

Spectra of all four galaxies were obtained using the Space Telescope Imaging Spectrograph (STIS) with aperture  $52'' \times 0''.2$  and grating G430M (for details see Kimble et al. (1998)). The observations are summarized in Table 5. The configuration of STIS and the properties of the grating are listed in Table 6. With this setup we chose to observe Mg lines at  $5180 \text{ \AA}$  rather than Ca lines at  $8700 \text{ \AA}$  which are commonly used for extracting stellar kinematics. The reasons were: (i) the Mg lines provide simultaneous kinematic data and a commonly used index of stellar metallicity, (ii) STIS shows problems with scattered light inside the CCD chip in the near infra-red which generates artificial “wings” on spectral features, and (iii) the spatial resolution along the slit in V-band is better by almost a factor of two due to the decreased Airy disk size.

**Table 5** — Summary of HST/STIS observations. Col. (1): galaxy name; Col. (2): the position of slit, cen – center, pos – positive offset, neg – negative offset (see text for details); Col. (3): date of observations; Col. (4): total exposure time (exposure time of central slits is the average time of all added observations); Col. (5): number of observations used in data reduction; Col. (6): distance of the center of the slit from the galaxy nucleus in arcsec; Col (7): position angle of the slit in degrees east from north.

galaxy (1)	slit (2)	date (3)	time (4)	# exp (5)	$\Delta_{cen}$ (6)	PA (7)
NGC 4128	cen	02.12.2001	2568.5	3+3	0.00	-112.9
	pos	02.12.2001	2700	3	0.16	-112.9
	neg	02.12.2001	2697	3	-0.40	-112.9
NGC 4570	cen	01.04.2001	2249.5	3+3	-0.20	152.1
	pos	01.04.2001	2369	2	0.68	152.1
	neg	01.04.2001	2520	2	-0.56	152.1
NGC 4621	cen	01.04.2001	2260.5	3+3	-0.12	161.1
	pos	01.04.2001	2380	3	0.40	161.1
	neg	01.04.2001	2520	3	-0.44	161.1
NGC 5308	cen	12.07.2000	2525.0	3+3	0.00	60.4
	pos	12.07.2000	2667	3	0.36	60.4
	neg	12.07.2000	2670	3	-0.36	60.4

**Table 6** — The configuration of STIS and the properties of the grating.

Quantity	Value
Aperture	52x0.2
Grating	G430M
$\lambda$ -range (Å)	5050.4-5381.6
$\lambda_{cen}$ (Å)	5216
Scale $\Delta\lambda$ (Å pixel <sup>-1</sup> )	0.28
Spatial scale (arcsec pixel <sup>-1</sup> )	0.05
Comparison line FWHM (pixel)	2.9
$R = \lambda/\Delta\lambda$	6461
Instrumental dispersion (km s <sup>-1</sup> )	19.76

### 3.1 Data reduction

The galaxies were observed in a similar manner with a total of four orbits per galaxy. Spectra were taken at three parallel positions per galaxy during the four orbits. Each orbit was divided (CR-SPLIT) into 3 shorter exposures. Two orbits were used for the slit placed on the center of the galaxies (*cen*), along the major axis. Between orbits, the galaxy was shifted along the slit for about 0".2, or 4 pixels, to get a better estimate of detector sensitivity variations and to identify hot pixels. This strategy was not successful for the case of NGC 4128, where the measured shift was  $\sim 1$  pixel. The remaining two orbits were split between two slit positions on either side of the central slit, covering the bulge parallel to the nuclear stellar disk. One slit was targeted at the position +0".3 away from the central slit (positive offset – *pos*), and the other at the position -0".3 away from the central slit (negative offset – *neg*).

Most of the data reduction was performed by the HST/STIS calibration pipeline CALSTIS (Hodge et al. 1998), including subtraction of overscan, bias and dark, then flat-fielding, hot pixel and cosmic-ray removal, absolute sensitivity calibration and wavelength calibration. CR-SPLIT data sets were combined automatically in the pipeline. The additional combination of the two central slit exposures was performed manually outside the pipeline in IRAF, using the STSDAS task MSCOMBINE. This task aver-

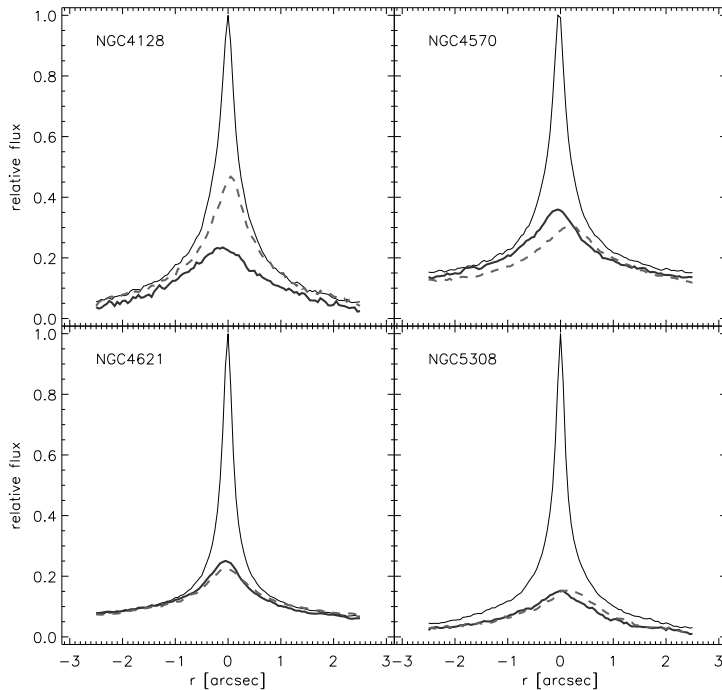


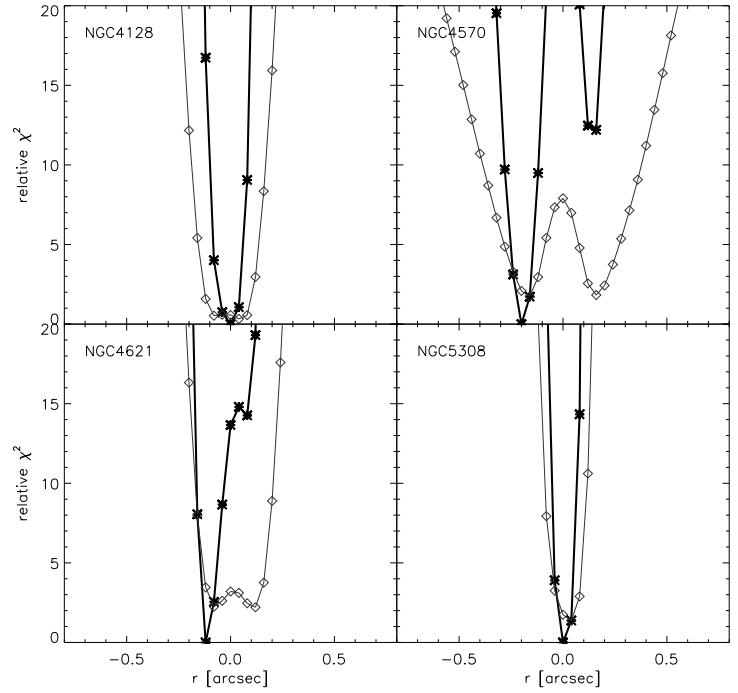
**Figure 4** — Galaxy light profile along the STIS slit. The full spectral range was used. Thin dark line is the profile along the *cen* slit, thick gray lines are profiles along the side slits: dashed line along the *pos* slit and full line along the *neg* slit. The profiles were normalized to the maximum of the *cen* slit in order to emphasize the difference of intensities.

ages the exposures scaled by their exposure times, and combines the separate exposures using a robust sigma clipping rejection method. This was done on the files that have *\_crj* extension, i.e., after pipeline co-addition of CR-SPLIT images and before the calibrations. The combined files were then returned to CALSTIS for the calibrations. The same procedure, however, was not possible on the side slits which were taken during only one orbit. As there were still some cosmic rays left after the pipeline reduction, we used Laplacian Cosmic Ray Identification (LAcosmic) developed by van Dokkum(2001) () to remove them. LAcosmic was also applied on the *\_crj* files. The detection limit for the outliers was  $3.5\sigma$ . To improve the quality of the images and remove additional negative pixels we tried a few techniques. For spectra with very low signal-to-noise it was possible to compare different exposures (e.g. the two side slits) and to recognize the same negative pixels and create a mask of them. For spectra with higher signal to noise this was not effective and a different approach was used. Using a boxcar filter we smoothed each LAcosmic-filtered image. These images were subtracted from the corresponding original LAcosmic-filtered images to emphasize the outlying pixels. They were flagged creating a mask image. Masked pixels were interpolated using IRAF task FIXPIX. The resulting images were returned to CALSTIS and processed to the end of the pipeline.

The final STIS light profiles are shown in Fig. 4. A noticeable feature is the difference in the intensity of the side slits. If the centering and shifting process worked properly, as the light profiles of the galaxies are quite symmetric, it is expected that the side slits should have very similar profiles. This is true for the case of NGC 5308 and NGC 4621, suggesting those slits were on similar but opposite positions. However, the other two galaxies show significant deviations. It is therefore necessary to find the exact positions of all slits.

We checked the actual positions of the slits by comparing the light profiles from

**Figure 5** — Plots of  $\chi^2$  versus the positions of the slits for each galaxy. The line connecting the diamonds is the relative  $\chi^2$  of the central slit. The line connecting asterisks is the total relative  $\chi^2$  obtained by including the side slits in calculations.



the STIS spectra with the WFPC2 images. The width of the slit (dispersion direction) is  $0''.2$ , which corresponds to 4 pixels on the STIS CCD. We sub-sampled the image such that the slit width projects to 5 pixels, in order to center the slits more correctly. Summing up along the dispersion axis ( $x$ -axis on the CCD) we created a STIS light profile. This was repeated for all slits. The F555W images, which were used in the comparison, were accordingly re-sampled. In each case we scanned the WFPC2 image by a combination of the three slits, independently varying the distances between the slits. The comparison of the STIS and WFPC2 profile was expressed by the relative  $\chi^2$  ( $profile(WFPC2)/profile(STIS) - 1$ ). In this process we assumed that the position angle of the telescope did not change between different slit positions. The resulting  $\chi^2$  estimates are shown in Fig. 5. If the central slit is not on the nucleus, the  $\chi^2$  is expected to have double minima and it is hard to distinguish which one is correct (NGC 4621 and NGC 4570 are clear examples). However, using the additional light profiles of the side slits tightens the constraints producing one clear minimum, which corresponds to the position of the central slit. The uncertainty of our estimate is  $0''.04$ . The positions of the central and the side slits with respect to the nucleus are given in last two columns of Table 5. The slits in NGC 5308 and NGC 4128 are centered on the galaxy nucleus, while for NGC 4621 and NGC 4570 the slits were offset. The side slits were roughly on the requested positions for NGC 4621 and NGC 5308. In the case of NGC 4128, the side slits are the least symmetrically positioned and the *pos* slit is almost coincident with the central slit; while in the case of the NGC 4570 the positions of the side slits are the farthest apart, as suggested from the profiles (Fig. 4).

The general characteristic of the spectroscopic data is their low signal-to-noise ratio ( $S/N$ ). Only the major axis spectra have an  $S/N$  sufficient for the extraction of kinematics and line-strengths as a function of radius. The side slits are much noisier and no kinematic measurements were possible. It was possible however to extract

line-strength information from a few central rows, summed together to increase  $S/N$  creating one spectrum per side slit per galaxy.

### 3.2 Stellar kinematics

All available information about the stellar kinematic properties of galaxies are given by the line-of-sight velocity distribution (LOSVD). The process of extracting kinematics is based on the deconvolution of the observed galaxy spectra in order to recover the full LOSVD. The idea behind this is that the galaxy spectrum can be reproduced using a combination of several representative stellar spectra convolved with the true LOSVD. Unfortunately, the LOSVD is not *a priori* known and the deconvolution process is ill-determined, being heavily dependent on the quality of the data. Over the last thirty years a number of methods were invented to tackle the problem and deliver the best possible estimates of the LOSVD (see de Bruyne et al. (2003) for an overview of methods). Here we choose to use a parametric method operating in the pixel space because of the low  $S/N$  of our data and very short wavelength range. We use the penalized pixel fitting (pPXF) method (Cappellari & Emsellem 2004). We derive the LOSVD parameterized by a Gauss-Hermite series (van der Marel & Franx 1993; Gerhard 1993). The method finds the best fit to a galaxy spectrum by convolving an optimal template spectrum with the corresponding LOSVD given by the mean velocity  $V$  and velocity dispersion  $\sigma$ , as well as higher order Gauss-Hermite moments  $h_3$  and  $h_4$ . The higher order moments measure asymmetric and symmetric deviation of the LOSVD from a Gaussian respectively.

An element which can heavily influence the extracted kinematics is the stellar template used to convolve the LOSVD to reproduce the galaxy spectra. There are methods, such as Fourier correlation quotient (Bender 1990) or Cross-correlation method (Statler 1995), which are less sensitive to template mismatch. Pixel fitting techniques are much more sensitive to template mismatch and it is crucial to have a good stellar template before starting the extraction. The usual way is to observe a number of representative stars (matching the spread in metallicity and age of stars in the observed galaxy) with the same instrumental set-up and to build an optimal template as a weighted linear combination of the observed stellar spectra.

After searching through the HST archive we decided to use a set of stellar population models instead of the one star from the archive that matched our set-up (the same grism being the most important, while size of the slit can be accounted for). Using single-metallicity stellar population models of Vazdekis (1999) we constructed a large stellar library from which to build the optimal stellar template. Each galaxy long-slit spectrum was summed up along the slit to make a higher  $S/N$  spectrum, which was used to obtain the optimal template. We also used additive Legendre polynomials to adapt the continuum shape of the templates. This optimal template was then used in the fit of the individual spectra along the slit.

A disadvantage of the Vazdekis models is that they are of lower resolution than the STIS data. The FWHM of the Vazdekis library is  $1.8 \text{ \AA}$  compared to  $0.8 \text{ \AA}$  from STIS. This requires a degradation of our data by  $\sim 1.6 \text{ \AA}$ . Although certain information is in this way lost and the STIS spectral resolution is degraded, the smoothing of the data helps in removing noise and the library ensures the extracted kinematics do not suf-

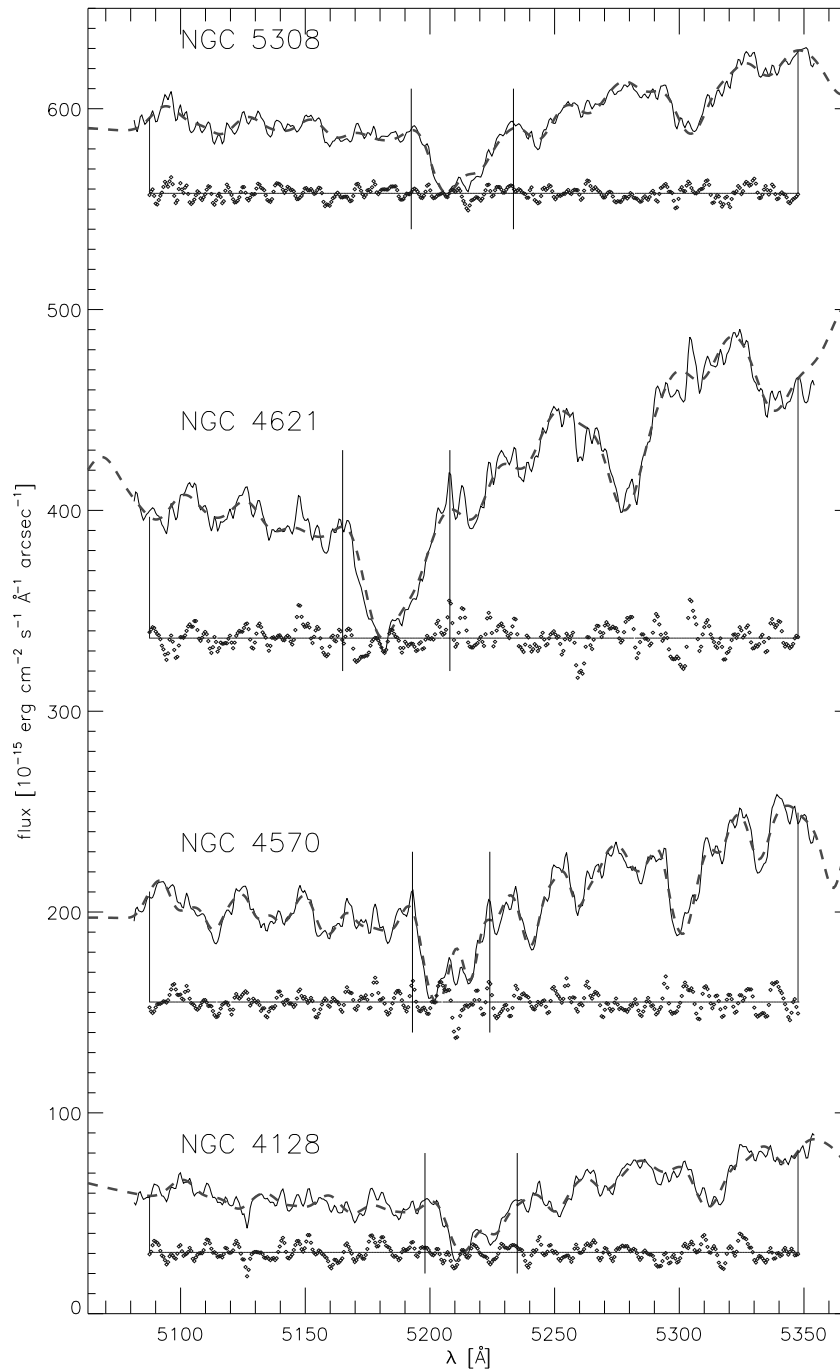


**Figure 6** — Example of spectra for the four studied galaxies. From bottom up: NGC 4128, NGC 4570, NGC 4621 and NGC 5308. The spectra are shifted vertically to avoid overlap. The thin black lines indicate spectra of galaxies. The dashed thick lines are broadened optimal templates. The dots below the spectra are residuals of the fit (difference between galaxy spectra and optimal templates). Vertical and horizontal lines shows the region used in the fit. Two solid vertical lines crossing the spectra show the spectral regions excluded from the fit which tested the influence of Mgb region to the extracted kinematics.

fer from an important systematic template mismatch effect. Examples of constructed optimal templates are shown in Fig. 6. The presented spectra are the sum of the central 10 rows, having a high  $S/N$  which is needed for properly estimating the optimal template. The overplotted dashed lines are our resulting optimal templates for the galaxies, convolved with the determined LOSVD of the galaxy. Typically a few (2-3) old-type stars from the Vazdekis library were selected by the fitting routine for the optimal template. The residuals between the galaxy and the optimal template spectra are shown below each spectrum. The presented optimal templates were used to extract the kinematics from the spatially binned spectra. An alternative way would be to construct the optimal template for each spatial bin and then use this to extract kinematics in the same bin. This method is important for galaxies with stellar populations changing between bins ( $\sim 0''.05$ ), but in this case the low  $S/N$  of the individual spectra do not justify this approach.

Table 7 summarizes the details about the spatial bins used for the extraction of kinematics. They were chosen after some experimenting as a compromise between the  $S/N$  and the spatial resolution. The galaxies have different surface brightnesses and, since the exposure times were similar, a unique scheme for all galaxies was not useful. For each galaxy we assumed a target  $S/N$  and we binned accordingly. Generally, the spectra become too noisy to measure the kinematics beyond  $1''$ . In some cases, the central few rows of spectra have  $S/N$  high enough for extraction of the higher order terms of LOSVD, but in general the  $S/N$  is too low. Hence, we decide to confine the extraction to only the first two moments (assuming a Gaussian shape for LOSVD): mean stellar velocity ( $V$ ) and velocity dispersion ( $\sigma$ ).

Another element which can heavily influence the results of the extraction is specific to the spectral region of the observations. Barth et al. (2002) compared the kinematics of a number of galaxies extracted in two spectral regions: one around  $Mgb$  lines and the other around Ca triplet. They found that if the metallicities of the galaxies and template stars are not well matched then direct template-fitting results are improved if the  $Mgb$  lines themselves are excluded from the fit and the velocity dispersion is determined from the surrounding weaker lines. For galaxies with high velocity dispersion this will be more important because of the correlation between the velocity dispersion and the  $[Mg/Fe]$  ratio (Worthey et al. 1992; Trager et al. 1998; Kuntschner et al. 2001), which increases the strength of the  $Mgb$  lines relative to the surrounding Fe lines. Following the suggestion of Barth et al. (2002) we also extracted kinematics excluding from the fit the  $Mgb$  lines (the excluded regions are shown on Fig. 6 as vertical lines crossing the spectra). When there are significant differences between the two sets of extracted kinematics we used the set obtained by excluding the  $Mgb$  lines from the fit for the further analysis and interpretations.

The errors were estimated using Monte-Carlo simulations. The LOSVD parameters were derived from 100 realizations of the input spectrum, where the value at each pixel is taken from a Gaussian distribution with the mean of the initial spectrum and standard deviation given by a robust sigma estimate of the residual of the fit to the initial spectrum. Fig. 6 shows an example of the residuals used to estimate the standard deviation used in Monte-Carlo simulations (dots under the spectra). All realizations provide a distribution of values from which we estimate the  $1\sigma$  confidence limits. The

galaxy	bin	r (arcsec)	range	width (pix)	S/N
NGC 4128	center	0.00	1	599-599	15
	r1	0.05	1	600-600	14
	r2	0.15	2	601-603	15
	r3	0.25	3	604-607	13
	r4	0.50	6	608-612	12
	r5	1.25	24	613-637	12
	l1	-0.05	1	598-598	14
	l2	-0.10	1	596-597	12
	l3	-0.15	2	593-595	14
	l4	-0.30	3	589-592	13
	l5	-0.50	5	583-588	12
	l6	-0.95	13	569-582	12
	NGC 4570	center	0.00	1	599-599
r1		0.05	1	600-600	21
r2		0.10	1	601-601	18
r3		0.15	2	602-604	20
r4		0.30	3	605-608	20
r5		0.50	5	609-614	19
r6		0.80	8	615-623	19
l1		-0.05	1	598-598	19
l2		-0.15	2	595-597	21
l3		-0.25	3	591-594	21
l4		-0.45	4	586-590	19
l5		-0.70	6	579-585	18
NGC 4621		center	0.00	1	599-599
	r1	0.05	1	600-600	34
	r2	0.10	1	601-601	25
	r3	0.20	2	602-604	26
	r4	0.35	4	605-609	27
	r5	0.65	8	610-618	26
	l1	-0.05	1	598-598	36
	l2	-0.10	1	597-597	28
	l3	-0.15	2	594-596	29
	l4	-0.30	3	590-593	26
	l5	-0.50	6	583-589	27
	l6	-0.95	11	571-582	25
	NGC 5308	center	0.00	1	599-599
r1		0.05	1	600-600	23
r2		0.10	1	601-601	17
r3		0.20	2	602-604	17
r4		0.30	3	605-608	15
r5		0.55	6	609-615	15
l1		-0.05	1	598-598	23
l2		-0.10	1	597-597	17
l3		-0.15	2	594-596	18
l4		-0.30	3	590-593	17
l5		-0.50	5	584-589	16
l6		-0.90	11	572-583	15

Table 7 — Bins for kinematic extraction

index slit	NGC 4128			NGC 4570			NGC 4621			NGC 5308		
	cen	neg	pos	cen	neg	pos	cen	neg	pos	cen	neg	pos
Mgb	5.0 ± 0.2	–	5.0 ± 0.4	4.5 ± 0.2	2.9 ± 0.3	3.7 ± 0.4	5.9 ± 0.1	6.6 ± 0.3	4.7 ± 0.3	4.8 ± 0.1	5.5 ± 0.5	5.8 ± 0.6
Fe5720	2.9 ± 0.1	–	2.6 ± 0.4	3.1 ± 0.1	1.7 ± 0.3	1.5 ± 0.4	3.7 ± 0.1	3.4 ± 0.3	3.4 ± 0.3	3.1 ± 0.1	4.1 ± 0.4	3.5 ± 0.5
Mgb	4.8 ± 0.2	–	5.0 ± 0.4	4.4 ± 0.2	2.9 ± 0.3	3.5 ± 0.4	5.6 ± 0.1	6.4 ± 0.3	4.6 ± 0.3	4.7 ± 0.1	5.3 ± 0.5	5.7 ± 0.5
Fe5720	2.8 ± 0.1	–	2.6 ± 0.4	3.1 ± 0.1	1.7 ± 0.3	1.4 ± 0.4	3.6 ± 0.1	3.4 ± 0.3	3.3 ± 0.3	3.0 ± 0.1	4.0 ± 0.5	3.5 ± 0.4
B – V	0.97	–	0.96	–	–	–	0.99	1.00	1.00	0.96	0.94	0.96

**Table 8** — Line-strength indices measured in  $0''.55 \times 0''.2$  aperture. First two rows in the table present line-strengths corrected by the velocity dispersion measured using the whole spectral region. The second two rows present line-strengths corrected by the velocity dispersion measured excluding the Mgb region from the fit during extraction of kinematics. The last row presents B-V color measured at the actual positions of slits within the same slit-like aperture used for measuring line-strengths. The errors on the color values estimated to be 0.05 mag.

values of the extracted kinematics are presented in Tables A.1-2 of Appendix A and shown in Figs. 8 – 11.

All galaxies except NGC 4621 show rather fast major axis rotation. NGC 4621 is a special case with a previously discovered counter-rotation in the center (WEC02). There are some differences between the kinematics extracted fitting the full spectral range and excluding the Mgb lines. They are the strongest for NGC 4621 and NGC 4570. The somewhat larger error bars of the kinematic measurements obtained not fitting the Mgb region are the consequence of lowering the  $S/N$  by excluding the dominant spectral feature. We postpone detailed description of all kinematic curves to Section 4.

### 3.3 Line strengths

The spectral range of our observations is very limited covering only the Mgb and Fe5270 Lick/IDS indices (for definition of Lick/IDS system and indices see Burstein et al. (1984); Worthey et al. (1994); Trager et al. (1998)). The red continuum pass band of the Fe5270 index is truncated by the edge of our spectral range and this index cannot be used in its defined form. A similar case is found in Kuntschner et al. 2004 (in preparation) and Falcón-Barroso et al. (2004) where Fe5270 cannot be mapped over the whole field-of-view of the integral-field spectrograph SAURON (Bacon et al. 2001) due to the varying bandpass of the SAURON instrument. In their case, Kuntschner et al. (2004) redefine the index to maximize the coverage of the field-of-view and retain the sensitivity of the index towards changes in age, metallicity and abundance ratios. The new index name is Fe5270s. It measures the same spectral feature, but has a reduced spectral coverage in the red pseudo-continuum band. The new index can be converted to the original Lick/IDS system via the empirical formula (Kuntschner et al. 2004, Falcón-Barroso et al. 2004):

$$\text{Fe5270} = 1.26 \times \text{Fe5270s} + 0.12$$

The  $1\sigma$  standard deviation of the above empirical calibration is  $\pm 0.05 \text{ \AA}$  for the Fe5270 index. More details on the derivation of the new index and its relation to the standard Lick/IDS index are given in Kuntschner et al. (2004).

Having this in mind we measured Fe5270s and Mgb indices. The Mgb index was measured using the Lick/IDS index definition, and all spectra were first broadened

to the resolution of the Lick/IDS system. The Fe5270s index was later converted to index Fe5270 using above relation. Unfortunately, we were not able to determine the relevant offset to the Lick/IDS system, and correct for the systematics, which come from differences in the continuum shape, because there are no reference stars in the HST archive observed by our and by the Lick/IDS instrumental setup. The size of the corrections are probably similar to (or less than) our measurement errors. To first order, as well as for determining the relative trends in a galaxy, this is not very important, but has to be noted when comparing with other studies.

Broadening of the lines by the velocity dispersion weakens most of the lines and the index we measure must be corrected for this effect. This can be achieved by determining an empirical correction factor  $C(\sigma) = \text{index}(0) / \text{index}(\sigma)$  for a star observed with the same instrumental setup.  $\text{index}(0)$  is the index measured from the stellar spectrum,  $\sigma$  is the velocity dispersion of the LOSVD with which the stellar spectrum is convolved and from which the  $\text{index}(\sigma)$  is measured. We used our unbroadened optimal template spectra to calculate the index at  $\sigma = 0$  and at the corresponding velocity dispersion,  $\sigma$ , of the galaxy spectrum. The proper correction factor  $C(\sigma)$  was then applied to both measured indices. We used two approaches to extract kinematics and measure the velocity dispersions (fitting the whole spectral region and excluding Mgb region from the fit). If the measured velocity dispersions differ, the velocity dispersion correction in the two cases will also be different. We noted the difference applying both corrections on the measured line-strengths.

We measured the Mgb and Fe5270 indices from each spectral bin used for kinematics. The corrected values and corresponding errors of the index are presented in the Tables A.1-2 and shown in the Figs. 8 – 11. The measured line-strengths for galaxies with higher  $S/N$  are relatively uniform with radius, rising towards the center, with dips in the case of the nuclei of NGC 4621 (Mgb) and NGC 5308 (Fe5270). NGC 4128 does not show any trend, but rather a scatter of values, presumably due to the low  $S/N$ , while in case of NGC 5308 Mgb line-strengths are slightly higher on one side of the galaxy. Generally, galaxies have high values of Mgb and Fe5270 indices. Detailed descriptions of spatially resolved line-strengths for all galaxies are given in Section 4.

The slits that were offset to the sides of the central slit do not have the required  $S/N$  to extract kinematics, but their summed spectra can be used to determine the indices on the positions of the galaxy outside the stellar disk. The binning of spectra is only useful up to the point at which summing more spatial elements does not simply add noise. We decided to use an aperture of  $0''.55 \times 0''.2$  (summing up 5 rows on each side of the central row in the spectral direction). With this approach the final side spectra used for the measurements of line-strengths had at least  $S/N \approx 10$ . In the case of NGC 4128, however, from one side spectra we were not able to extract any trustworthy measurement. Table 8 presents line-strengths corrected for velocity dispersions measured by fitting to the whole spectral range and excluding the Mgb lines from the fit. As it can be seen, the differences between the lines are negligible and generally fall within the  $1\sigma$  error bars. Only in the case of the central slit of NGC 4621 which has the highest velocity dispersion as well as  $S/N$ , there is a significant difference. Adopting a conservative approach, we compared line-strengths from the second two rows in Table 8 with the stellar population synthesis models in Fig. 7.

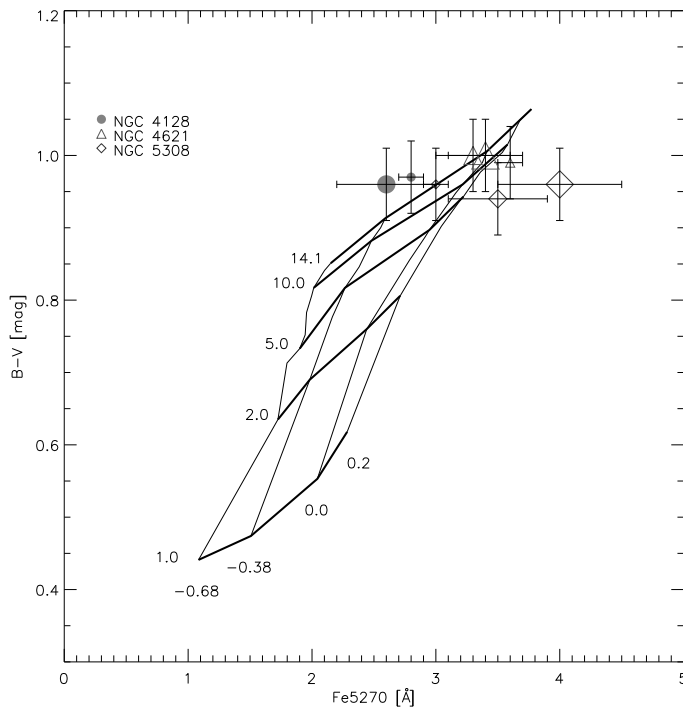


**Figure 7** — Age/metallicity diagnostic diagram ( $B-V$  color vs.  $Fe5270$  index). Horizontal thick solid lines are lines of constant age [Gyr] and vertical thin lines are lines of constant metallicity  $[Fe/H]$  of Vazdekis (1999) models. The size of symbols is related to the position of the slit: the smallest symbols are for the *cen* slits, intermediate for the *pos* slits, and the biggest for the *neg* slits.

We wish to compare the line-strengths measured on the disk with the line-strengths measured on the bulge using the three slit positions. The line-strength measurements on the summed spectra show similarly high values as the spatially resolved measurements, although with relatively lower values due to the smaller spatial resolution. The  $Mgb$  index values in NGC 4621 are particularly high. Comparing with the literature we find similar values for  $Mgb$  and  $Fe\ 5270$  index. Table 7 of Trager et al. (1998) list values of the same indices for NGC 4621 and NGC 4570 ( $Mgb\ 5.50$  and  $4.65\text{\AA}$ ,  $Fe5270\ 3.59$  and  $3.49\text{\AA}$ ), which, keeping in mind the unknown offset to the Lick system and the lower spatial resolution of Trager et al. (1998) data (aperture of  $1'' \times 4''$ ), are in good agreement with our findings.

Age and metallicity have similar effects on the integrated spectral energy distributions that we measure from unresolved sources due to a finely tuned conspiracy between age and metallicity variations (Worthey(1994)). Broad-band colors and many line-strength indices are degenerate with respect to age and metallicity. This makes the determination of the age and metallicities very difficult and ideally one would like to use two indices which can break this degeneracy. Usually, one or more Balmer lines ( $H\beta$ ,  $H\gamma$ ,  $H\delta$ ) are used as age indicators, and  $Mgb$  or some Fe index ( $Fe5270$ ,  $Fe5335$ ) as a metallicity indicator (González 1993; Fisher et al. 1996; Mehlert et al. 1998; Kuntschner 2000; Trager et al. 2000). The high index values of our measured line-strengths also suggests the presence of non-solar abundances of elements. If not properly treated, over-abundant indices can give wrong age and metallicity estimates (Kuntschner et al. 2001). A way around this issue is to define metallicity indicators which are insensitive to abundance ratios (González 1993; Thomas et al. 2003). The preferred indicator includes a combination of  $Mgb$ ,  $Fe5335$  and  $Fe5270$  indices, where  $Fe5270$  is the least sensitive to changes of  $[\alpha/Fe]$  abundance ratios (Thomas et al. 2003). We were not able to construct such a metallicity indicator with the indices from

our spectral range, and we chose to use the least sensitive Fe5270 index alone as a metallicity indicator. Since in our spectral range there are no age indicators, we decided to use a combination of broad-band B-V colors and Fe5270 index to construct an age/metallicity diagnostic diagram (Fig. 7). The models presented by solid lines are based on the Vazdekis (1999) single stellar population models: color values were obtained from A. Vazdekis web site<sup>3</sup>, while we measured the Fe5270 index from the library spectra broadening them to the Lick/IDS resolution. The combination of red colors and high metallicities puts the measured points on Fig. 7 on the top right of the model grid, indicating old stellar populations and a large spread of metallicities between the galaxies.

## 4 Discussion

In the two previous sections we presented the observational results of HST program 8667. They include photometric and spectroscopic observations of four galaxies with nuclear stellar disks. Here we analyze and discuss the observations.

### 4.1 NGC 4128

The most distant galaxy in the sample is NGC 4128 (36 Mpc). It is an S0 galaxy and it has not been detected in radio nor in IR. The isophotal parameters show that it is disk-like between 35 and 530 pc. On 1 kpc scale it has boxy parameters and on larger scales it becomes disk-like again.

The color image shows a red nucleus. The values for Fe5270 index measured with an aperture bigger than the red nucleus are the smallest in the sample of galaxies. This combination puts the points on Fig. 7 above the model grid. The difference in colors and line-strengths between the two slit positions are small and within errors indicate old stellar populations of  $\sim 14$  Gyr and metallicities between  $[\text{Fe}/\text{H}] = -0.38$  and solar.

It is probable that the difference in the color between the nucleus and the rest of the galaxy, as well as the higher metallicity detected in the nucleus is connected with the unusual spatially resolved kinematic profiles (Fig. 8). The velocity dispersion is flat in the center. The velocity curve also shows an unusual flattening in the central  $0''.2$ , measurements being positive on the both sides of the galaxy nucleus. Outside this radii the galaxy rotates fast, as expected for a disk galaxy. Kinematics extracted fitting to two different spectral regions are in a good agreement, confirming the results. Having in mind the boxiness in the central tens of arcseconds, the extracted kinematic indicates the existence of a small ( $\sim 35$  pc in diameter) core, kinematically distinct from the nuclear stellar disk.

The B-V color profile on the last panel of Fig. 8 shows a slightly shifted ( $\sim 17$  pc from the center) peak of the red nucleus. This supports the presence of a distinct component in the nucleus. On the other hand, the spatially resolved line-strengths do not follow this trend. The spectral observations of this galaxy have the smallest  $S/N$  ratio, and the significance of this discovery is just above  $1\sigma$ . Deeper exposures of high spatial resolution, preferably with an integral-field unit to cover the 2D structure, are needed

<sup>3</sup><http://www.iac.es/galeria/vazdekis/>

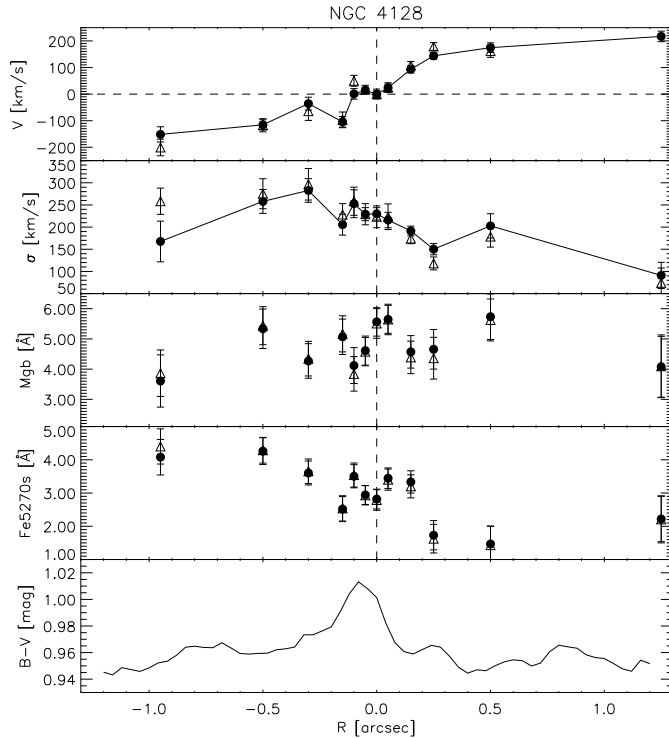


**Figure 8** — Kinematic and line-strength profiles for NGC 4128. From top to bottom: mean velocity, velocity dispersion, Mgb index, Fe5270 index and B-V color profile. The color profile was extracted along the slit position averaging  $0''.2$  perpendicular to the slit. The closed symbols represent measurement obtained by fitting the whole spectral region. The open symbols represent measurement by excluding the Mgb line from the fit.

to confirm this result.

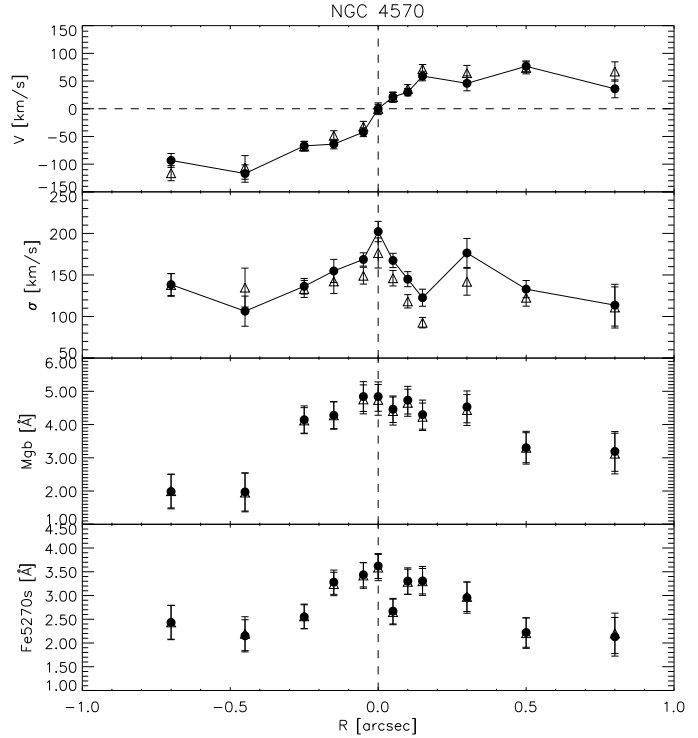
## 4.2 NGC 4570

NGC 4570 is a well-studied galaxy with HST. The main result from previous studies is that the inner region of the galaxy was shaped under the influence of a weak bar (van den Bosch & Emsellem 1998). The colors reveal no difference between the disk and the bulge, and a comparison with the stellar-population models indicate that the stars in the galaxy are of intermediate age, but the FOS spectral data gave a very high  $H\beta$  line-strength suggesting recent star formation (BJM98). One of the questions raised by these studies is whether all double-disk structures are the result of bar-driven secular evolution.

To the previous photometric and spectroscopic observations we add new spatially resolved spectroscopic measurements with STIS (Fig. 9). The probed region corresponds to the nuclear disk and inner  $2''$ . The velocity curve shows regular rotation peaking at  $\sim 0''.15$  from the nucleus. The velocity dispersion steeply rises and peaks in the center. The kinematic profiles are similar to BJM98 ground based data, except the STIS data have a steeper velocity curve and higher velocity dispersion. In contrast, the FOS velocity dispersion from the same authors is about  $50 \text{ km s}^{-1}$  higher than STIS measurements; however, considering the error bars of both measurement (their error on sigma is  $\approx 30 \text{ km s}^{-1}$ ) and the fact that our slit was significantly (for the width of the slit) offset from the galaxy nucleus, these measurements can be considered consistent with each other.

In the case of NGC 4570, the central velocity dispersion is somewhat dependent

**Figure 9** — Kinematic and line-strength profiles for NGC 4570. From top to bottom: mean velocity, velocity dispersion, *Mgb* index, *Fe5270s* index. The closed symbols represent measurement obtained by fitting the whole spectral region. The open symbols represent measurement by excluding the *Mgb* line from the fit.



on the spectral region used in the fit. Excluding *Mgb* region systematically lowers the values by just over  $1\sigma$ , but increases the difference between this and BJM98 results.

We also measure, within the errors, similar line-strengths to BJM98, but with higher spatial resolution and we can give an estimate of the spatial changes in the indices. As can be seen from the Fig. 9, both measured indices show flattening in the central  $0''.5$  ( $\sim 60$  pc). At larger radii the metallicity drops. Also, the slits positioned on both side of the center measure the smallest metallicity (Table 8) in the sample and the largest drop in values with respect to the center. This measurement shows that the nuclear disk consists of different stellar populations than the rest of the bulge, which is consistent with bar-driven evolution.

### 4.3 NGC 4621

The closest galaxy of the four is NGC 4621 (7 Mpc). It is also the only galaxy classified as an elliptical and is the only galaxy from the sample detected with IRAS (in the  $12 \mu\text{m}$  band). In the investigated range the galaxy is disk. The  $b_4$  coefficient steadily rises from the center to the distance of 140 pc when it drops, but never reaching negative values. With increasing radius it rises again, implying an outer disk.

The color images reveal the most interesting features in the nucleus. The few central pixels are clearly much bluer than the rest of the bulge (Table 4). Another striking characteristic of the galaxy, mentioned in section 2.3.2, is the extended blue and red features visible on B-I (Fig. 2) and V-I images. The blue feature makes an angle of  $15^\circ$  with the major axis. Although the red feature spreads generally in the east-west direction (angle with major axis is  $103^\circ$ ), it is not as clearly defined as the blue feature.

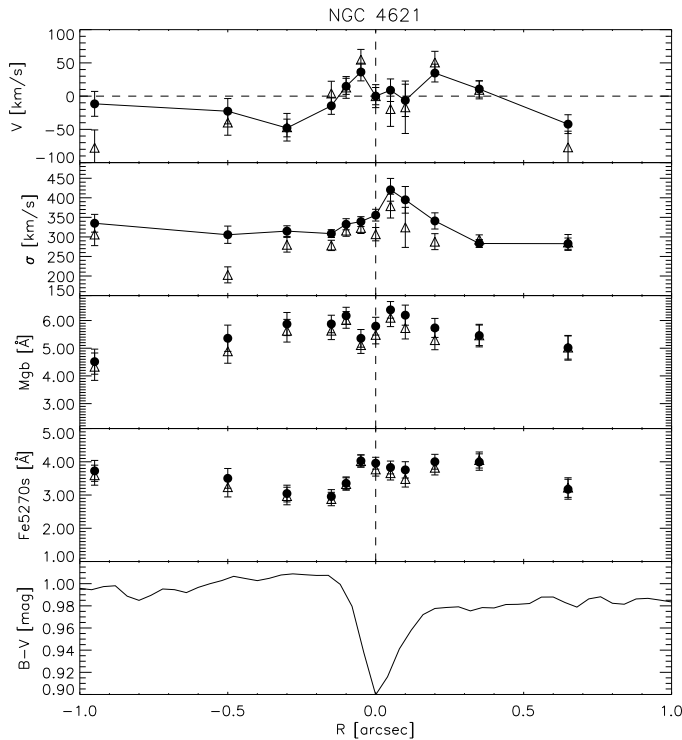


**Figure 10** — Kinematic and line-strength profiles for NGC 4621. From top to bottom: mean velocity, velocity dispersion, Mgb index, Fe5270 index and B-V color profile. The color profile was extracted along the slit position averaging  $0''.2$  perpendicular to the slit. The closed symbols represent measurement obtained by fitting the whole spectral region. The open symbols represent measurement by excluding the Mgb line from the fit.

We conclude, examining all color images, that the shape and the extent of the two features can be interpreted as a blue disk-like structure imbedded in the red bulge. The position angle of the blue feature is unexpected for an axisymmetric galaxy with a nuclear stellar disk. This significant structure perhaps can be explained considering the kinematics of this galaxy.

The velocity and velocity dispersion panels in Fig. 10 clearly show the existence of a kinematically decoupled core (KDC). This core was already detected by WEC02 who observed the galaxy with integral field spectrograph OASIS mounted on CFHT and assisted by the PUEO adaptive optics system. Complementing their OASIS observations, WEC02 also extracted kinematics from an archival STIS observations in the Ca triplet region, showing a peak in velocity dispersion  $0''.05$  from the center as well as confirming the KDC with the same spatial resolution as in the data presented here. The difference between the WEC02 and our kinematic profiles is largest in the velocity dispersion profile, where our values lie systematically above the WEC02 measurements. This difference is lower, but still present if we compare the kinematics extracted excluding the Mgb line from the fit ( $\sim 60 \text{ km s}^{-1}$  for the velocity dispersion peak, but with large error-bars in both cases). This discrepancy could arise from the different slit positions in the two studies, our slit being offset from the center and not covering the KDC uniformly. The counter-rotation of the KDC could lower the overall measured dispersion if the slit is placed over its center, and, alternatively, if the slit misses the center of the KDC the measured velocity dispersion will be higher.

The KDC on the WEC02 OASIS data is not aligned with the major axis and it has a similar position angle as the blue feature on the color images presented here. Although the extent of the KDC is smaller (total of  $\sim 2''$  or 60 pc) than the blue feature on the B-

I image, the existence of two structures could be connected as a result of the same formation process.

Both *Mgb* and Fe5270 line-strengths indices in NGC 4621 are the highest in the sample, also suggesting the over-abundance ratios of elements similar to trends for giant ellipticals (Kuntschner 1998; Kuntschner et al. 2001). Our metallicity indicator, Fe5270, also has high values, with the central slit being slightly more metal-rich than the side slits as well as super-solar. Colors at the slit positions are red and the comparison with the stellar population models indicates the age of the stars is between 10 and 14 Gyr and the metallicity between solar and +0.2.

Our spatially resolved measurements of the indices, shown in Fig. 10, are higher than in previous studies (e.g. Kuntschner et al. (2001) have central *Mgb*  $\sim 5.21$  with aperture of  $3''.4$ ), but our aperture is much smaller ( $\sim 0''.05$ ) than that of any previous study, and the values outside the central arc-second approach the observed values from the literature. The *Mgb* index follows to some extent the changes in colors, showing a small dip in the center, while this can not be said for Fe5270 measurements.

The existence of the KDC and the blue features in the red bulge of the NGC 4621 indicate two possible evolutionary scenarios. The visible structures could be the result of a hierarchical formation scheme (e.g. Kauffmann et al. 1994) involving a merger followed by a starburst where the KDC is the remnant of the ejected stars that later fell back in. These structures are relatively long lived, having a relaxation time of  $\sim 1$  Gyr (Binney & Tremaine 1987); however, this is not long enough to explain the detected old age of the stars. Alternatively, the structure could be produced by weak bar-driven evolution, as in the case of NGC 4570 (van den Bosch & Emsellem 1998), where the observed double disk structure is the consequence of resonant frequencies in the galaxy, while the blue feature and the KDC are the result of gas captured on retrograde ('anomalous') orbits which are tilted with respect to the equatorial plane (Pfenniger & Friedli 1991; Friedli & Udry 1993; Emsellem & Arsenault 1997). Of course, a combination of both processes can also lead to the present situation.

Distinguishing between the two scenarios is also difficult because the galaxy has no obvious merger companion and it is nearly edge-on, making the detection of a weak bar more difficult. There are other cases of barred galaxies with similar properties to NGC 4621: i.e. an edge-on system with double-disk structure, unusual photometric and kinematic features and the difference in metallicity between the bulge and the disk. An example of a similar, although boxier, galaxy with a strong bar is NGC 7332. This galaxy was recently studied in detail by Falc3n-Barroso et al. (2004). NGC 7332 is classified as an S0 galaxy and has a double disk structure (Seifert & Scorza 1996). Examining their SAURON spectroscopic observations, Falc3n-Barroso et al. find a counter rotating stellar component within the central 250 pc. The galaxy also has complex gas morphology and the line-strength maps show it is young everywhere. The authors conclude that NGC 7332 is an S0 galaxy with a bar viewed close to edge on. NGC 4621 and NGC 7332 are similar in their morphologies, and, although different in the stellar content, it is possible that NGC 4621 went through a similar formation process as NGC 7332.

#### 4.4 NGC 5308

In many aspects NGC 5308 is different from the other galaxies in this study. Our photometry reveals the largest nuclear stellar disk in the sample of galaxies in this study. Unlike in the other galaxies, the nuclear disk of NGC 5308 is very thin and bright. The diskiness parameter,  $b_4$ , rises from the center and peaks at about 150 pc, dropping to zero at  $\sim 1$  kpc and suggesting a distinction between the two disks. At large radii the galaxy again becomes disk-like.

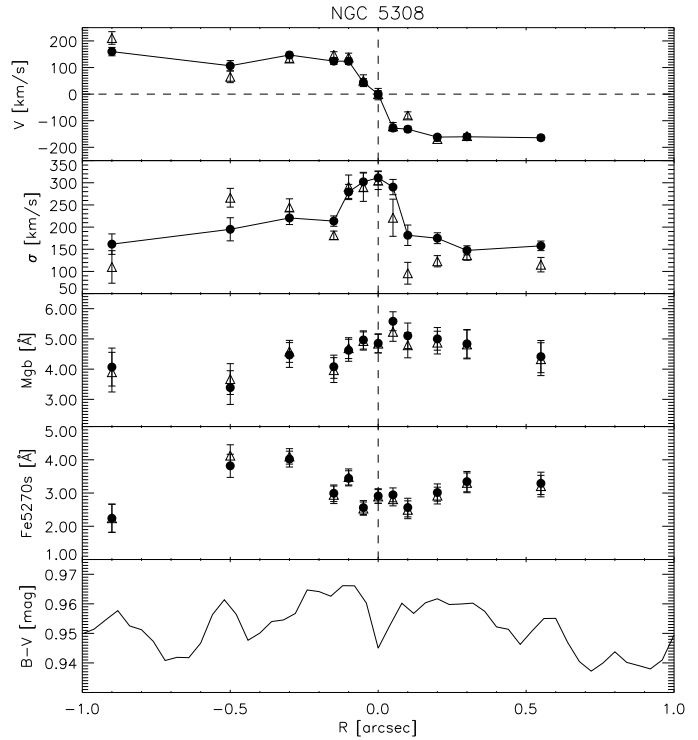
The stars in the disk of NGC 5308 rotate fast, reaching  $\sim 100$  km s<sup>-1</sup> within 15 pc from the nucleus (Fig. 11). The velocity dispersion has a peak of about 300 km s<sup>-1</sup> in the center and is relatively flat in the inner 15 pc. This trend is also visible in the kinematics measured excluding the Mgb line from the fit, although the right hand side of the plot shows considerably lower velocity dispersion values. This is reflected in the panel with Mgb values, which are slightly higher on the right hand of the plot. The Mgb and Fe5270 index values have opposite trends. The small variations in the B-V color along the slit, including the sudden blue dip in the center, are followed by the line-strength measurements.

There is a big difference between the line-strengths measured on the different slit positions (Table 8 and Fig. 7). The nucleus, being just below solar metallicity, is more metal-poor than the bulge which has a non-solar abundance ratio of elements and the highest metallicity in the sample. The nucleus and the investigated part of the bulge also have different colors, with the center being redder. Comparing these results with the stellar population synthesis models reveals an old stellar population in the nucleus (14 Gyr), while the colors of the bulge suggest an intermediate age stellar component ( $\sim 5$ -10 Gyr).

The color difference between the bulge and the nucleus is measured because the side slits were positioned in the region of the minor axis blue feature, especially visible on B-I image. This region is also special for its high metal content. There are no hints of specific morphological structures (such as a polar ring) along the minor axis and the question is whether the rest of the bulge, especially the red feature, and the nuclear stellar disk share the same metallicity. Unfortunately our spectral observations did not cover the necessary areas and we can only speculate on the processes that created the observed structures.

If the metallicity of the minor axis blue feature and the nuclear disk are the same, the formation of these two structures has to be connected to the same formation scenario, most probably involving a transportation of gas to the center, perhaps by a bar, for which Seifert & Scorza (1996) found evidence in NGC 5308. If the metallicity of the nuclear disk is lower than the metallicity of the minor axis blue feature, but similar to the measured metallicity of the nucleus, the two blue features in NGC 5308 were not created from the same infalling material, but they still can be from the same epoch. If the metallicity of the minor axis blue feature is equal to the rest of the bulge, which is redder and therefore older, then the younger stellar population in the blue feature must have been induced by an internal process, perhaps ionization from the radiation generated by the central black hole, which was turned on with the infall of the material that made the blue disk, and later turned off with the stabilization of the disk (Loeb &

**Figure 11** — Kinematic and line-strength profiles for NGC 5308. From top to bottom: mean velocity, velocity dispersion,  $Mgb$  index,  $Fe5270$  index and  $B-V$  color profile. The color profile was extracted along the slit position averaging  $0''.2$  perpendicular to the slit. The closed symbols represent measurement obtained by fitting the whole spectral region. The open symbols represent measurement by excluding the  $Mgb$  line from the fit.



Rasio 1994).

In section 2.3.2 we showed that the major axis blue feature in NGC 5308 corresponds to the nuclear stellar disk. It is about 30 pc thick which strongly suggest the galaxy is viewed very close to edge-on. Comparing with the vertical scalelength of 34 edge-on spirals presented by Kregel et al. (2002), which are between 0.2 and 1.4 kpc thick, the disk in NGC 5308 is a remarkably thin disk. Note that our estimate of the disk thickness can only be approximately compared with the vertical scalelength measurements of Kregel et al. It is also not possible to say much about the thickness of the other nuclear disks, due to their inclination (not as edge-on as NGC 5308). Whether this nuclear disk resembles the disks from the group of “super-thin” galaxies, like UGC 7321 or IC 5249 (Matthews et al. 1999; Matthews 2000; van der Kruit et al. 2001), is an open question. The sizes of the nuclear disk in NGC 5308 and known “super-thin” disks are quite different as well as the surrounding environment (stellar bulges and dark matter halos respectively). A proper way to compare the disks is to measure the radial and vertical sizes in a consistent manner, which is beyond the scope of this paper.

The color and metallicity of the disk in NGC 5308 suggest the disk could be made of a younger and more metal-poor stellar population than the rest of the galaxy, implying it formed at a different epoch from accreted material.

## 5 Conclusions

We have presented photometric and spectroscopic observations of four nearby early-type galaxies with nuclear stellar disks (NGC 4128, NGC 4570, NGC 4621, NGC 5308). The observations consist of high resolution images with WFPC2 using the F450W and

F555W filters, and STIS high resolution spectra through the 52x0.2 long-slit with the G430M prism.

The photometric analysis reveals similarities and differences between the galaxies. Nuclear stellar disks are clearly visible and are photometrically disconnected from the large scale disks. NGC 4128 shows boxy isophotes on the inner and outer edge of the nuclear disk. NGC 4621, the only E galaxy in the sample, is everywhere disk-like, while NGC 5308 has a razor-thin ( $\sim 30$  pc) disk.

Color images reveal interesting and unexpected structures. NGC 4128 has a red nucleus, while NGC 4621 has a blue nucleus. Prominent color features are visible on all galaxies. The blue feature in NGC 4128 is analyzed in Appendix B. and is the signature of a transient event. NGC 4621 has a blue feature at an angle of  $15^\circ$  with the major axis on top of a red bulge. It is likely connected to the KDC discovered by WEC02. The nuclear stellar disk in NGC 5308 is associated with the razor thin blue feature along the major axis. NGC 5308 has another blue feature along the minor axis. The colors of all three galaxies indicate old stellar populations except for the bulge of NGC 5308 where the combination of slightly less red colors and high metallicity lowers the age of the stellar populations.

The high resolution spectroscopy was obtained at three positions on each galaxy. One slit was positioned on the nuclear stellar disk, with the PA equal to the major axis PA. Two additional slits were positioned on both sides of the central slit,  $\sim 0''.3$  away from the disk covering the bulge. The central slits were used to extract spatially resolved kinematics and line-strengths. The  $S/N$  permitted the extraction of the mean stellar velocity and the velocity dispersion, as well as the measurement of line-strengths. The kinematics will be used in a separate paper to estimate the black hole masses in the centers of the galaxies.

Considering the shape of the spatially resolved kinematic curves, the four galaxies could be sorted in two groups: fast and kinematically disturbed rotators. NGC 4570 and NGC 5308 belong to the first group. Their rotation curves show clear signature of the stellar disks. The rotation curves of NGC 4128 and NGC 4621 are much more complicated. In the case of NGC 4621 the unusual mean velocity and velocity dispersion curves are consistent with the known KDC (WEC02) in the nucleus. Although based on a  $1\sigma$  detection, we report the discovery of a similar kinematically distinct core in the case of NGC 4128.

Spatially resolved line-strength measurements along the disk indicate that all four galaxies are more metal-rich in the inner  $0''.5$  than outside this radius. Both measured indices ( $Mgb$  and  $Fe5270$ ) increase towards the center, except in the case of NGC 5308 where  $Fe5270$  has an opposite trend to  $Mgb$  index. Non-solar abundance ratios of  $[Mg/Fe]$ , hinted by results of the extraction of kinematics, are present in NGC 4570 and NGC 4621, and to some extent also in NGC 5308.

The slits positioned on the bulges had low  $S/N$  and no spatially resolved kinematics were extracted. However, by binning the spectra, it was possible to measure the line-strengths at one position and compare them to the values of the nuclei. The objects show various structure: NGC 4128 has similar metallicities at the different slit positions, NGC 4570 and NGC 4621 have higher metallicity in the nucleus, while NGC 5308 in the bulge. Generally, the galaxies show a spread in metallicity from sub-

to super-solar.

This study shows the diversity within this class of objects, but also emphasizes the similarities in the photometry and kinematics. The red color gradient in the nuclei of NGC 4128 and the blue features in NGC 4621 and NGC 5308 suggest the existence of different stellar populations on small scales ( $\sim 100$ -500 pc). The investigated galaxies were chosen as galaxies with specific nuclear morphologies: nuclear stellar disks. However, except in the case of NGC 5308 the colors of the disks are not much different from the bulge, as previously noted by Carollo et al. (1997b). The existence of other color features is a surprise. In two galaxies (NGC 4128 and NGC 4621) these color features are followed by the existence of a KDC. The other two galaxies do not show any peculiarities in their kinematics. Also, if the KDC in NGC 4621 is connected to the misaligned blue feature, we can conclude, similar to Carollo et al. (1997a), that KDCs are not kinematic counterparts of the nuclear stellar disks. This gives credit to the complexity of formation scenarios that demands a separate study per galaxy, but there are a few most likely frameworks, outlined also in Scorza & van den Bosch (1998), in which the processes responsible for the observed structures operate.

The formation of nuclear disks, rings and double disk structures in early-type galaxies can be explained through secular evolution driven by weak bars as shown by Emsellem et al. (1996) and van den Bosch & Emsellem (1998) in the cases of M 104 and NGC 4570, respectively. This mechanism, through the evolution of the bar, explains the double-disk morphology. Support for this scenario comes from the fact that S0 galaxies have high line-strengths (Fisher et al. 1996) and there are evidences of embedded bars in early-type galaxies (e.g. M104, NGC 4570, NGC 7332, Scorza et al. 1998). This model of bar-driven evolution is consistent with the observations in the presented galaxies, even in the cases of the galaxies with KDCs, such as NGC 4621, but also NGC 4128, which is additionally boxy and presents an interesting case. The time varying triaxial potential of the bars offers exotic orbits that could explain the existence of kinematic and photometric features. In this scenario, the KDCs are created from enriched material transported inwards (perhaps even gas acquired through a merger), which gets frozen on retrograde orbits tilted with the respect to the equatorial plane.

Other possibilities involve a merger scenario (capture of gas that settles in the principle plane forming stars, and/or makes tidal inflows that create KDCs), or growth of a central black hole (Loeb & Rasio 1994). A black hole stabilizes the disk and within this scenario a connection to quasars can be made by stopping the fueling of the central engines with the formation of a stable disk. None of the previously investigated nuclear stellar disk galaxies has an active nucleus, although they do harbor  $10^{8-9} M_{\odot}$  black holes (Kormendy et al. 1996b; Kormendy et al. 1996a; Cretton & van den Bosch 1999). This makes them descendants of quasars that spent their fuel (there is not much dust or gas in most of these galaxies), or quasars that, through dynamical evolution, turned off the central engine (stabilization of the disk due to the growth of the black hole, disappearance of bars that transport the material to the center).

Nuclear disks are easier to find in edge-on systems; however, the influence of weak bars is correspondingly more difficult to ascertain. Detailed spectroscopic studies with two dimensional coverage of the major features (nuclei, stellar disks, KDC, photometric features) are necessary to chose between the present formation scenarios. A careful

investigation of the two-dimensional kinematic properties and their connection to the distribution of line-strengths (metal content and age of stellar populations) can offer decisive tools to deduce the nature and nurture of galaxies with nuclear stellar disks.

## **Acknowledgments**

We are grateful to Michele Cappellari, Eric Emsellem, Richard McDermid, Gijs Verdoes Kleijn, Frank van den Bosch, Zlatan Tsvetanov and Tim de Zeeuw for comments and discussions. DK thanks Michele Cappellari and Harald Kuntschner for making available the pPXF and line-strengths measurement software, respectively. This research has made use of the NASA/IPAC Extragalactic Database (NED) which is operated by the Jet Propulsion Laboratory, California Institute of Technology, under contract with the National Aeronautics and Space Administration. This work also used LEDA database. DK was supported by NOVA, the Netherlands Research school for Astronomy.

## **Appendix A. Extracted kinematics**

radius	V	$\delta V$	$\sigma$	$\delta\sigma$	Mgb	$\delta\text{Mgb}$	Fe5270	$\delta\text{Fe5270}$
(1)	(2)	(3)	(4)	(5)	(6)	(7)	(8)	(9)
NGC 4128								
-0.95	2323.	29.	168.	46.	3.6	0.9	4.1	0.5
-0.50	2359.	19.	258.	27.	5.3	0.7	4.3	0.4
-0.30	2438.	24.	283.	27.	4.3	0.6	3.6	0.4
-0.15	2370.	20.	206.	24.	5.1	0.6	2.5	0.4
-0.10	2475.	20.	253.	31.	4.1	0.6	3.5	0.3
-0.05	2489.	12.	229.	15.	4.6	0.5	2.9	0.3
0.00	2474.	13.	230.	14.	5.6	0.5	2.8	0.3
0.05	2498.	14.	216.	18.	5.6	0.5	3.4	0.3
0.15	2568.	14.	191.	11.	4.6	0.5	3.3	0.3
0.25	2618.	12.	150.	13.	4.7	0.7	1.7	0.4
0.50	2649.	18.	203.	27.	5.7	0.8	1.5	0.5
1.25	2691.	20.	91.	30.	4.1	1.0	2.2	0.7
NGC 4570								
-0.70	1827.	13.	138.	13.	2.0	0.5	2.4	0.4
-0.45	1803.	16.	106.	18.	2.0	0.6	2.2	0.3
-0.25	1853.	9.	136.	9.	4.1	0.4	2.6	0.3
-0.15	1856.	9.	155.	14.	4.3	0.4	3.3	0.3
-0.05	1877.	8.	169.	8.	4.8	0.4	3.4	0.3
0.00	1920.	8.	202.	12.	4.8	0.4	3.6	0.3
0.05	1941.	8.	167.	9.	4.5	0.4	2.7	0.3
0.10	1950.	7.	145.	9.	4.7	0.4	3.3	0.3
0.15	1979.	7.	123.	10.	4.3	0.4	3.3	0.3
0.30	1966.	13.	176.	17.	4.5	0.5	3.0	0.3
0.50	1996.	10.	133.	10.	3.3	0.5	2.2	0.3
0.80	1956.	16.	114.	25.	3.2	0.6	2.1	0.4
NGC 4621								
-0.95	583.	19.	335.	23.	4.5	0.5	3.7	0.3
-0.50	572.	19.	306.	22.	5.4	0.5	3.5	0.3
-0.30	546.	13.	315.	14.	5.9	0.4	3.0	0.3
-0.15	580.	13.	308.	10.	5.9	0.3	3.0	0.2
-0.10	609.	12.	332.	14.	6.2	0.3	3.4	0.2
-0.05	631.	13.	339.	13.	5.4	0.3	4.0	0.2
0.00	594.	13.	356.	15.	5.8	0.3	4.0	0.2
0.05	603.	17.	420.	29.	6.4	0.3	3.8	0.2
0.10	588.	24.	395.	34.	6.2	0.4	3.8	0.2
0.20	629.	13.	341.	21.	5.7	0.3	4.0	0.2
0.35	605.	12.	283.	10.	5.5	0.4	4.0	0.2
0.65	552.	14.	283.	14.	5.0	0.4	3.2	0.3
NGC 5308								
-0.90	2295.	16.	162.	23.	4.1	0.6	2.2	0.4
-0.50	2241.	20.	195.	26.	3.4	0.6	3.8	0.3
-0.30	2282.	11.	221.	15.	4.5	0.4	4.0	0.2
-0.15	2259.	13.	214.	12.	4.1	0.4	3.0	0.3
-0.10	2258.	12.	279.	17.	4.6	0.4	3.4	0.2
-0.05	2179.	14.	302.	21.	5.0	0.3	2.6	0.2
0.00	2135.	13.	311.	16.	4.9	0.3	2.9	0.2
0.05	2007.	12.	290.	17.	5.6	0.3	2.9	0.2
0.10	2003.	11.	182.	23.	5.1	0.4	2.6	0.3
0.20	1973.	9.	175.	12.	5.0	0.4	3.0	0.3
0.30	1974.	8.	147.	10.	4.8	0.5	3.3	0.3
0.55	1971.	10.	158.	11.	4.4	0.5	3.3	0.3

**Table A.1** — Measured kinematics and line-strengths for observed galaxies using full spectral region in the fit. Notes – Col. (1): radius of measurement (arcsec); Col. (2): mean velocity ( $\text{km s}^{-1}$ ); Col. (3) mean velocity error ( $\text{km s}^{-1}$ ); Col. (4): velocity dispersion ( $\text{km s}^{-1}$ ); Col. (5): velocity dispersion error ( $\text{km s}^{-1}$ ); Col. (6): Mgb index ( $\text{\AA}$ ); Col. (7) Mgb index error ( $\text{\AA}$ ); Col. (8) Fe5270 index ( $\text{\AA}$ ); Col. (9) Fe5270 index error ( $\text{\AA}$ ).

radius	V	$\delta V$	$\sigma$	$\delta\sigma$	Mgb	$\delta$ Mgb	Fe5270	$\delta$ Fe5270
(1)	(2)	(3)	(4)	(5)	(6)	(7)	(8)	(9)
NGC 4128								
-0.95	2294.	31.	258.	30.	3.9	0.8	4.4	0.5
-0.50	2378.	25.	275.	34.	5.4	0.6	4.3	0.4
-0.30	2431.	35.	297.	36.	4.3	0.6	3.7	0.4
-0.15	2398.	30.	228.	25.	5.1	0.6	2.5	0.4
-0.10	2545.	21.	258.	32.	3.8	0.6	3.5	0.4
-0.05	2512.	19.	229.	24.	4.6	0.5	2.9	0.3
0.00	2495.	19.	223.	25.	5.5	0.5	2.8	0.3
0.05	2520.	19.	223.	29.	5.6	0.5	3.4	0.3
0.15	2603.	15.	174.	12.	4.4	0.5	3.2	0.3
0.25	2674.	15.	118.	15.	4.4	0.7	1.6	0.4
0.50	2657.	24.	179.	24.	5.6	0.7	1.4	0.6
1.25	2688.	23.	74.	33.	4.0	1.0	2.2	0.7
NGC 4570								
-0.70	1805.	14.	138.	14.	2.0	0.5	2.4	0.4
-0.45	1815.	21.	131.	23.	2.0	0.6	2.2	0.4
-0.25	1853.	8.	133.	10.	4.1	0.4	2.6	0.3
-0.15	1872.	9.	142.	15.	4.2	0.4	3.2	0.2
-0.05	1889.	9.	149.	10.	4.8	0.4	3.4	0.3
0.00	1921.	11.	176.	18.	4.7	0.5	3.6	0.3
0.05	1942.	9.	146.	9.	4.4	0.4	2.7	0.3
0.10	1957.	8.	118.	8.	4.7	0.4	3.3	0.3
0.15	1993.	8.	93.	6.	4.2	0.4	3.3	0.3
0.30	1985.	14.	142.	16.	4.4	0.5	3.0	0.3
0.50	1995.	11.	123.	10.	3.3	0.5	2.2	0.3
0.80	1988.	17.	111.	25.	3.1	0.6	2.2	0.4
NGC 4621								
-0.95	531.	27.	306.	29.	4.3	0.5	3.6	0.3
-0.50	569.	19.	203.	20.	4.9	0.4	3.2	0.3
-0.30	562.	21.	280.	19.	5.6	0.4	3.0	0.3
-0.15	612.	18.	278.	13.	5.6	0.3	2.9	0.2
-0.10	622.	16.	316.	15.	6.0	0.3	3.3	0.2
-0.05	663.	15.	323.	14.	5.1	0.3	4.0	0.2
0.00	608.	17.	307.	17.	5.5	0.3	3.8	0.2
0.05	589.	26.	379.	30.	6.1	0.3	3.7	0.2
0.10	592.	39.	324.	51.	5.7	0.4	3.5	0.2
0.20	659.	17.	288.	20.	5.3	0.3	3.8	0.2
0.35	618.	14.	293.	12.	5.5	0.4	4.1	0.2
0.65	531.	24.	286.	20.	5.0	0.4	3.2	0.3
NGC 5308								
-0.90	2333.	24.	110.	37.	3.9	0.7	2.2	0.4
-0.50	2188.	22.	266.	21.	3.7	0.5	4.1	0.3
-0.30	2256.	14.	244.	19.	4.6	0.4	4.1	0.2
-0.15	2270.	12.	181.	10.	4.0	0.4	2.9	0.3
-0.10	2261.	16.	291.	26.	4.7	0.3	3.5	0.2
-0.05	2173.	22.	290.	32.	4.9	0.3	2.5	0.2
0.00	2122.	21.	305.	20.	4.8	0.3	2.9	0.2
0.05	2001.	14.	221.	42.	5.2	0.3	2.8	0.2
0.10	2042.	13.	96.	25.	4.8	0.4	2.5	0.3
0.20	1954.	9.	123.	13.	4.9	0.4	2.9	0.3
0.30	1965.	9.	136.	11.	4.8	0.5	3.3	0.3
0.55	1955.	10.	115.	16.	4.3	0.5	3.2	0.3

**Table A.2** — Measured kinematics and line-strengths for observed galaxies excluding Mgb region from the fit. Same as in Table A.1.

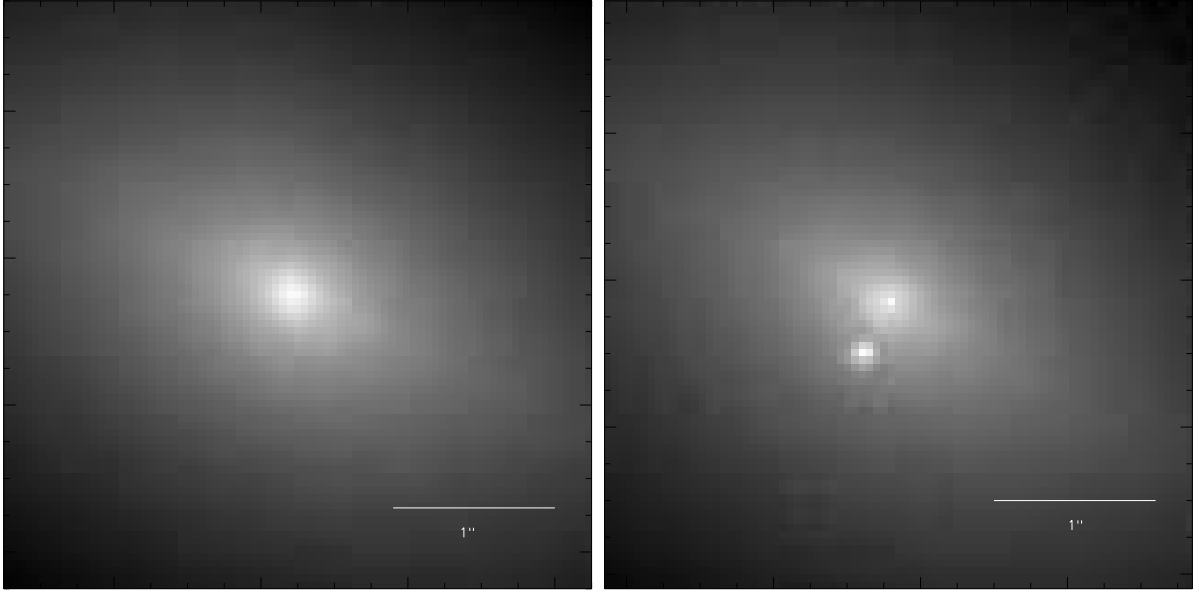


**Figure B.1** — Zoom-in on the WFPC2 images of the nucleus of the NGC 4128, in F702W (left) and F555W band (right). Both images are oriented as on Fig. 2 (north is down and east to the right). Horizontal line is  $1''$  long. The left image was taken almost two years before the right one. The offset of the peak next to the center on the right image is  $0''.143$  west and  $0''.318$  north from the center of the galaxy.

## Appendix B. A transient in NGC 4128

Examining the HST – WFPC2 images of the nearby S0 galaxy NGC 4128, taken on May 14 2001 in the F450W and F555W filters, a peculiar source of light was discovered very close to the center of the galaxy (Fig. B.1). The source is offset by  $0''.14$  west and  $0''.32$  north of the galaxy center on the WFPC2 images. In the HST archive there are images of the galaxy taken on March 17 1999, with filter F702W, observed under PID 6357 (PI Jaffe), which do not show any additional light source next to the nucleus of the galaxy. This clearly indicates the appearance of a transient object in our data. In this Appendix we try to deduce the origin of the transient. Section B.1 presents a new method of extraction of the light contribution from the background galaxy and the photometric analysis, followed by discussion on the nature of the object in section B.2.

### B.1 Extraction of light and results

The general properties of NGC 4128 were described in the main text. Here we add that the dust in the galaxy has not been detected (Tran et al. 2001). This ensures there is no significant extinction although the object is almost in the center of the galaxy. The galactic component of the reddening in the direction of the NGC 4128 is estimated to be  $E(B - V) = 0.02$  mag (Schlegel et al. 1998).

To determine the nature of the transient, it is necessary to accurately do photometry on the observed light. The first required step is to remove the contribution of the galaxy light. Since there are no pre-transient observations of the galaxy in the two filters, it was not possible to use the standard technique of subtracting a suitable image of the galaxy taken with the same instrumental set up (e.g. Filippenko et al. 1986; Hamuy

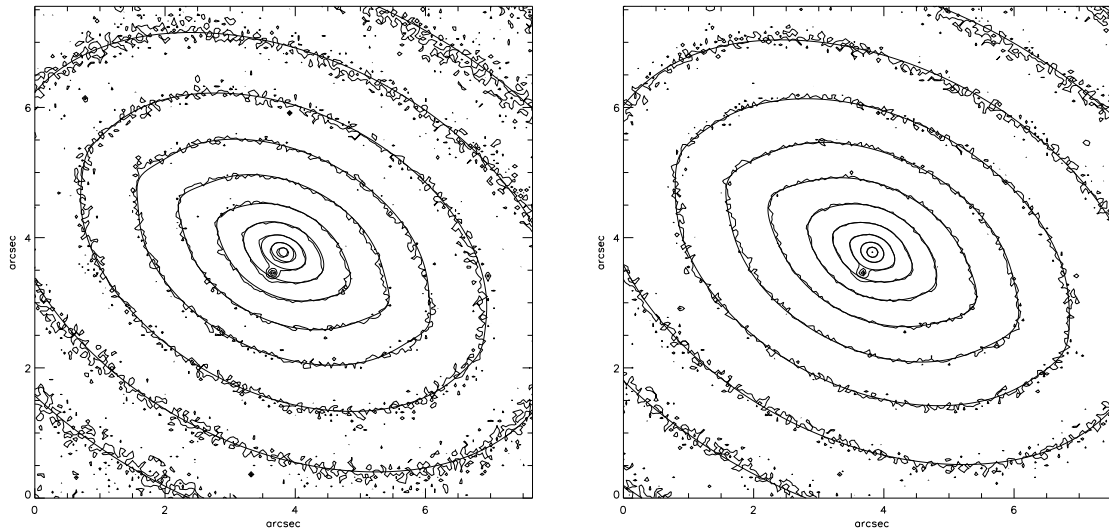


**Figure B.2** — Contour maps of WFPC2 F450W (left) and F555W (right) images of NGC4128. The images show the inner  $7''.5$ . Superposed on the two images are the contours of the MGE surface brightness, convolved with the WFPC2 PSFs for the corresponding filters. The transient was excluded from the fit, but it is shown in the images for illustration.

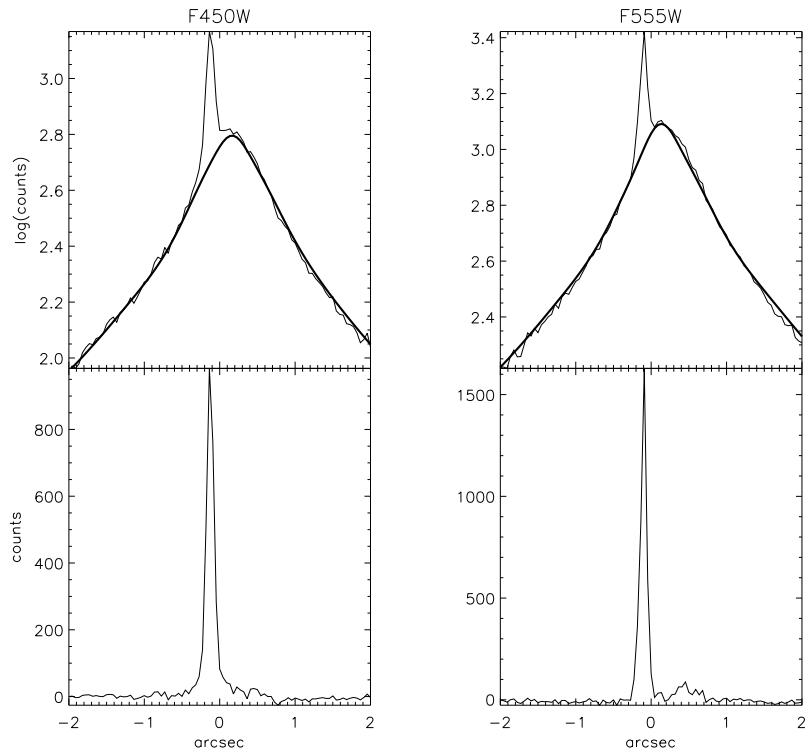
et al. 1994). To overcome this problem a Multi-Gaussian Expansion (MGE) model of the galaxy was constructed (e.g. Emsellem et al. 1994). The method and software provided by Cappellari (2002) were used. The MGE models of the galaxies were created using only the PC1 chip and masking the region of the transient by a circular mask with radius of 5 pixel (Fig. 9). For both MGE models, the total number of used Gaussians was increased until the minimum  $\chi^2$  stopped decreasing. This approach yielded the total number of 9 Gaussians and RMS error of about 2%.

The obtained models were subtracted from the original images. Figure B.3 shows a horizontal cut through the observed image at the position of the transient and the corresponding MGE model. The light of the transient is clearly distinguishable from the rest of the galaxy. Subtracting the MGE model of the galaxy from the observations it is possible to recover the transient light contribution. The residuals are symmetric and can be used to calculate the magnitude of the transient. Photometric measurements were conducted using the IRAF task PHOT. Magnitude zero points for filters were obtained from Dolphin (2000). The values calculated in an aperture of  $0''.5$  were corrected to infinite aperture by adding 0.1 mag. The correction for geometrical distortion and the CTE correction were not performed as their influence are of second order, compared to the uncertainty introduced by subtracting the model galaxy from the original image. The final transient parameters, namely its position, apparent magnitude and absolute magnitude in Johnson-Cousins system, are given in the Table B.1.

## B.2 Discussion and conclusions

Lacking any spectra of the detected object as well as a longer period of observation, it is difficult to determine the object's true nature. Since it is not visible on the F702W

**Figure B.3** — Horizontal cuts through the galaxy on the position of the SN. The thick line is the MGE model and the thin line is the observed light. The lower plots show residuals obtained subtracting the models from the observations. The transient is clearly separable from the rest of the galaxy by a MGE model.



band image while it is quite bright on the F450W and F555W band images (taken 22 months later), it is most natural to conclude the object is a transient. There are a few possibilities such as a solar system object, a nova or a supernova.

The duration of all four independent WFPC2 exposures is about 40 minutes. A solar system object would show a noticeable movement between the different exposures, except if moving directly toward an observer. If the object is at the distance of the Kuiper belt it would move approximately a few arc seconds during the observations. However, the relative position of the object (the distance between the object and the center of the galaxy) changes by less than one pixel ( $< 0''.0455$ ), the movement being less than measurement error. It seems reasonable to conclude the object is of extra-Solar system origin.

Novae are known to have a maximum absolute magnitude less bright than  $-9$  mag (Cohen 1985). With the measured absolute magnitude of  $-13.6$  (V band), this is ruled out. Similarly, because it is very faint, the observed transient is also not likely a nova in our galaxy (a compilation of novae light curves is given in van den Bergh & Younger (1987)). The observed magnitude leaves the possibility that the object in NGC 4128 is a supernova. The type of supernova is defined according to its spectrum, and here again it is hard to establish anything specific. However, the host galaxy is an S0 galaxy, and since supernovae of type II do not occur in early-type galaxies (Table 3. in Cappellaro et al. 1997b), the transient is probably a supernova of Type Ia. Comparing the measured absolute magnitude to absolute magnitudes of supernova 1994D or 1992A (Cappellaro et al. 1997a), which were also S0 galaxies, suggests that the supernova was observed about 200 days after the explosion. The  $B - V$  color of the supernova is  $-0.11$ , which is bluer than the expected color for a type Ia SN at B maximum. On the other

filter	ra	dec	$\delta x$	$\delta y$	counts	m	$\sigma_m$	M
(1)	(2)	(3)	(4)	(5)	(6)	(7)	(8)	(9)
F450W	12:08:34.84	68:46:57.15	0.142	0.315	20940.09	19.06	0.05	-13.7
F555W	12:08:34.84	68:46:57.25	0.143	0.318	18099.38	19.17	0.05	-13.6

**Table B.1** — Summary of transient measurements. Col.(1): name of the filter; Cols.(2) and (3): position of the supernova measured in (h,m,s) and (deg,arcmin,arcsec) on WFPC2 (J2000); Cols. (4) and (5): the offset in arcsec of the transient from the intensity peak of the galaxy due west and north respectively; Col. (6) total counts inside aperture of  $0''.5$ ; Col. (7) magnitude of the supernova in Johnson-Cousins system; Col. (8) the estimated error on the apparent magnitude; Col. (9) absolute magnitude using the distance to NGC 4128 from Table 1.

had, it is consistent with the  $B - V$  light curve at the later time (around 200 days) of the above mentioned reference supernovae (Salvo et al. 2001).

Private communication with the supernova-survey groups (D. Green from IAU Circulares and W. Li from LOTOSS survey) did not confirm the existence of the supernova. They checked images from January to June 2001, and after galaxy subtraction there was no signature of any transient object. However, the proximity to the nucleus of NGC 4128 is a possible reason why ground-based automated search program might have overlooked the supernova.

If the source of the light is a Type Ia supernova, it will be the first supernova discovered in NGC 4128 (Barbon et al. 1999)<sup>4</sup>. Unfortunately, without other high resolution available data it is impossible to determine the true nature of the object. Also, the estimate of the timing of the supernova in NGC 4128 is highly uncertain, since it depends on precise classification and calibration. Type Ia supernovae are known to have different absolute magnitude light curves (e.g. Cappellaro et al. 1997a). If the transient in the NGC 4128 is not a supernova of type Ia 200 days after explosion then its nature remains unknown (a flaring second black hole, an asteroid on the trajectory to Earth).

## References

- Bacon, R., Copin, Y., Monnet, G., et al. 2001, MNRAS, 326, 23  
 Balcells, M., Graham, A. W., Domínguez-Palmero, L., & Peletier, R. F. 2003, ApJ, 582, L79  
 Barbon, R., Buondí, V., Cappellaro, E., & Turatto, M. 1999, A&AS, 139, 531  
 Barth, A. J., Ho, L. C., & Sargent, W. L. W. 2002, AJ, 124, 2607  
 Bender, R. 1988, A&A, 193, L7  
 Bender, R. 1990, A&A, 229, 441  
 Bender, R., Surma, P., Doebereiner, S., Moellenhoff, C., & Madejsky, R. 1989, A&A, 217, 35  
 Binney, J. & Tremaine, S. 1987, Galactic dynamics (Princeton, NJ, Princeton University Press, 1987, 747 p.)  
 Biretta, Lubin., et al. 2002 WFPC2 Instrument Handbook, version 7.0 (Baltimore: STScI)  
 Burkhead, M. S. 1986, AJ, 91, 777  
 Burstein, D., Faber, S. M., Gaskell, C. M., & Krumm, N. 1984, ApJ, 287, 586  
 Cappellari, M. 2002, MNRAS, 333, 400  
 Cappellari, M. & Emsellem, E. 2004, PASP, 116, 138  
 Cappellaro, E., Mazzali, P. A., Benetti, S., et al. 1997a, A&A, 328, 203

<sup>4</sup><http://web.pd.astro.it/supern/>

- Cappellaro, E., Turatto, M., Tsvetkov, D. Y., et al. 1997b, *A&A*, 322, 431  
Carollo, C. M., Danziger, I. J., Rich, R. M., & Chen, X. 1997a, *ApJ*, 491, 545  
Carollo, C. M., Franx, M., Illingworth, G. D., & Forbes, D. A. 1997b, *ApJ*, 481, 710  
Carollo, C. M., Stiavelli, M., & Mack, J. 1998, *AJ*, 116, 68  
Cohen, J. G. 1985, *ApJ*, 292, 90  
Cretton, N. & van den Bosch, F. C. 1999, *ApJ*, 514, 704  
Davies, R. L., Efstathiou, G., Fall, S. M., Illingworth, G., & Schechter, P. L. 1983, *ApJ*, 266, 41  
de Bruyne, V., Vauterin, P., de Rijcke, S., & Dejonghe, H. 2003, *MNRAS*, 339, 215  
Dolphin, A. E. 2000, *PASP*, 112, 1397  
Emsellem, E. & Arsenault, R. 1997, *A&A*, 318, L39  
Emsellem, E., Bacon, R., Monnet, G., & Poulain, P. 1996, *A&A*, 312, 777  
Emsellem, E., Monnet, G., & Bacon, R. 1994, *A&A*, 285, 723  
Emsellem, E., Dejonghe, H. & Bacon, R. 1999, *MNRAS*, 303, 495  
Erwin, P., Vega Beltrán, J. C., Graham, A. W., & Beckman, J. E. 2003, *ApJ*, 597, 929  
Erwin, P. & Sparke, L. S. 1999, *ApJ*, 521, L37  
Erwin, P. & Sparke, L. S. 2002, *AJ*, 124, 65  
Falcón-Barroso, J., Peletier, R. F., Emsellem, E., et al. 2004, *MNRAS*, 350, 35  
Filippenko, A. V., Porter, A. C., Sargent, W. L. W., & Schneider, D. P. 1986, *AJ*, 92, 1341  
Fisher, D., Franx, M., & Illingworth, G. 1996, *ApJ*, 459, 110  
Fisher, D., Illingworth, G., & Franx, M. 1994, *AJ*, 107, 160  
Freedman, W. L., Madore, B. F., Gibson, B. K., et al. 2001, *ApJ*, 553, 47  
Friedli, D. & Udry, S. 1993, in *IAU Symp. 153: Galactic Bulges*, 273, eds., H.DeJonghe & H.J.Habing (Kluwer Academic Press, Dordrecht)  
Gerhard, O. E. 1993, *MNRAS*, 265, 213  
González, J. J. 1993, Ph.D. Thesis  
Goudfrooij, P., Hansen, L., Jorgensen, H. E., & Norgaard-Nielsen, H. U. 1994, *A&AS*, 105, 341  
Hamuy, M., Philips, M. M., Maza, J., et al. 1994, *AJ*, 108, 2226  
Hodge, P. E. et al. 1998, *ASP Conf. Ser. 145: Astronomical Data Analysis Software and Systems VII*, 7, 316  
Holtzman, J. A., Burrows, C. J., Casertano, S., et al. 1995, *PASP*, 107, 1065  
Jaffe, W., Ford, H. C., O'Connell, R. W., van den Bosch, F. C., & Ferrarese, L. 1994, *AJ*, 108, 1567  
Jedrzejewski, R. I. 1987, *MNRAS*, 226, 747  
Kauffmann, G., Guiderdoni, B., & White, S. D. M. 1994, *MNRAS*, 267, 981  
Kimble, R. A., Woodgate, B. E., Bowers, C. W., et al. 1998, *ApJ*, 492, L83+  
Kormendy, J. 1988, *ApJ*, 335, 40  
Kormendy, J. & Bender, R. 1996, *ApJ*, 464, L119+  
Kormendy, J., Bender, R., Ajhar, E. A., et al. 1996a, *ApJ*, 473, L91+  
Kormendy, J., Bender, R., Richstone, D., et al. 1996b, *ApJ*, 459, L57+  
Kormendy, J., Gebhardt, K., Macchetto, F.D., & Sparks, W.B. 2002, *AJ* submitted (astro-ph/0107218)  
Kregel, M., van der Kruit, P. C., & de Grijs, R. 2002, *MNRAS*, 334, 646  
Kuntschner, H. 1998, Ph.D. Thesis  
Kuntschner, H. 2000, *MNRAS*, 315, 184  
Kuntschner, H., Lucey, J. R., Smith, R. J., Hudson, M. J., & Davies, R. L. 2001, *MNRAS*, 323, 615  
Kuntschner et al. 2004. in preparation  
Krist, J., & Hook, R. 2001, *The Tiny Tim User's Manual*, version 6.0  
Landsman, W. B. 1993, in *ASP Conf. Ser. 52: Astronomical Data Analysis Software and Systems II*, 246, eds., R.J.Hanis, R.J.V.Brissenden & J.Barnes  
Lauer, T. R. 1985, *MNRAS*, 216, 429  
Lauer, T. R., Ajhar, E. A., Byun, Y.-I., et al. 1995, *AJ*, 110, 2622  
Loeb, A. & Rasio, F. A. 1994, *ApJ*, 432, 52  
Matthews, L. D. 2000, *AJ*, 120, 1764  
Matthews, L. D., Gallagher, J. S., & van Driel, W. 1999, *AJ*, 118, 2751  
Mehlert, D., Saglia, R. P., Bender, R., & Wegner, G. 1998, *A&A*, 332, 33  
Peletier, R. F., Davies, R. L., Illingworth, G. D., Davis, L. E., & Cawson, M. 1990, *AJ*, 100, 1091

- Pfenniger, D. & Friedli, D. 1991, *A&A*, 252, 75
- Pizzella, A., Corsini, E. M., Morelli, L., et al. 2002, *ApJ*, 573, 131
- Rest, A., van den Bosch, F. C., Jaffe, W., et al. 2001, *AJ*, 121, 2431
- Rix, H. & White, S. D. M. 1990, *ApJ*, 362, 52
- Salvo, M. E., Cappellaro, E., Mazzali, P. A., et al. 2001, *MNRAS*, 321, 254
- Schlegel, D. J., Finkbeiner, D. P., & Davis, M. 1998, *ApJ*, 500, 525
- Scorza, C. & Bender, R. 1995, *A&A*, 293, 20
- Scorza, C., Bender, R., Winkelmann, C., Capaccioli, M., & Macchetto, D. F. 1998, *A&AS*, 131, 265
- Scorza, C. & van den Bosch, F. C. 1998, *MNRAS*, 300, 469
- Seifert, W. & Scorza, C. 1996, *A&A*, 310, 75
- Statler, T. 1995, *AJ*, 109, 1371
- Thomas, D., Maraston, C., & Bender, R. 2003, *MNRAS*, 343, 279
- Trager, S. C., Faber, S. M., Worthey, G., & González, J. J. 2000, *AJ*, 119, 1645
- Trager, S. C., Worthey, G., Faber, S. M., Burstein, D., & Gonzalez, J. J. 1998, *ApJS*, 116, 1
- Tran, H. D., Tsvetanov, Z., Ford, H. C., et al. 2001, *AJ*, 121, 2928
- van den Bergh, S. & Younger, P. F. 1987, *A&AS*, 70, 125
- van den Bosch, F. C. & de Zeeuw, P. T. 1996, *MNRAS*, 283, 381
- van den Bosch, F. C. & Emsellem, E. 1998, *MNRAS*, 298, 267
- van den Bosch, F. C., Ferrarese, L., Jaffe, W., Ford, H. C., & O'Connell, R. W. 1994, *AJ*, 108, 1579
- van den Bosch, F. C., Jaffe, W., & van der Marel, R. P. 1998, *MNRAS*, 293, 343
- van der Kruit, P. C., Jiménez-Vicente, J., Kregel, M., & Freeman, K. C. 2001, *A&A*, 379, 374
- van der Marel, R. P. & Franx, M. 1993, *ApJ*, 407, 525
- van Dokkum, P. G. 2001, *PASP*, 113, 1420
- Vazdekis, A. 1999, *ApJ*, 513, 224
- Wernli, F., Emsellem, E., & Copin, Y. 2002, *A&A*, 396, 73
- Worthey, G. 1994, *ApJS*, 95, 107
- Worthey, G., Faber, S. M., & Gonzalez, J. J. 1992, *ApJ*, 398, 69
- Worthey, G., Faber, S. M., Gonzalez, J. J., & Burstein, D. 1994, *ApJS*, 94, 687

---

## Chapter 4

---

# Kinometry: a method to quantify kinematic maps

Davor Krajinović, Michele Cappellari, Yannick Copin, P. Tim de Zeeuw, to be submitted to Monthly Notices of the Royal Astronomical Society

We present a general method for analysing and describing kinematic maps of galaxies observed with integral-field spectrographs. It is based on a harmonic expansion of the maps along concentric rings in the plane of the sky, similar to the expansions used to quantify observed HI, CO and H $\alpha$  velocity fields, and analogous to standard surface-photometry methods for analysing broad-band imaging. We call our method kinometry. We analyse the kinematic moments (mean velocity, velocity dispersion and higher-order Gauss–Hermite moments of the line-of-sight velocity distribution) of a model elliptical galaxy, and discuss the meaning of the amplitude coefficients and corresponding phases of the expansion. The observed kinematic moments have certain symmetries in the plane of the sky, and we exploit these to filter the maps. We present diagnostics for determining the consistency of velocity maps with axisymmetric underlying geometry, based on the phase angles of the first two odd terms of the expansion. We apply this method to SAURON observations of the galaxy NGC 4365 and quantify the departures from axisymmetry. We consider kinematic expansions along circular and elliptic annuli, and find that expansion along suitably-chosen ellipses may be superior for maps of the mean velocity and the higher-order odd moments, while circles may be more suited for velocity dispersion maps and the higher-order even moments. We present evidence that the velocity maps of some early-type galaxies closely resemble the observed kinematics of inclined circular disks, but the generality of this result needs to be investigated further.

## 1 Introduction

TWO-DIMENSIONAL velocity maps were, until recently, largely the privileged property of radio astronomers. The advantages of full two-dimensional spatial coverage of extended astronomical objects are self-evident and are extensively used in e.g. HI studies of disk galaxies. The advent of integral-field spectrographs (IFS) has brought two-dimensional kinematic measurements to optical wavelengths.

The inclusion of optical wavelengths also broadens the variety of objects accessible for study. The two-dimensional radio observations are dependent on the existence of

gas, while optical observations probe both the stellar absorption- and gas emission-line spectral features, which may co-exist in the same potential with very different spatial distributions and dynamical structures. The wealth of features seen in the stellar kinematic maps of early-type galaxies (Emsellem et al. 2004) confirms the usefulness of two-dimensional data, but also poses a problem of efficiently harvesting and interpreting the important features from the maps.

An approach using harmonic expansion was developed for the analysis of the two-dimensional radio velocity maps. This method divides a velocity map into individual rings (the so-called tilted-ring method, Begeman 1987) with a harmonic expansion along these rings (e.g. Binney 1978; Teuben 1991). Assuming that the velocity map is generated by gas moving in a thin disk, it is possible to assign certain physical properties to the coefficients of the harmonic expansion: e.g. the first *cosine* term in the expansion gives the circular velocity of the gas, assuming the gas moves in circular orbits in the disk. The higher-order terms measure the departures from a simple disk model (pure circular motion) caused by e.g. elongation of the potential. This approach was pioneered by Franx et al. (1994) and Schoenmakers et al. (1997) who used it to investigate the axisymmetry of spiral galaxies, based on the prediction for harmonic coefficients coming from epicyclic theory. Recently Wong et al. (2004) used this method as a diagnostic tool for measuring radial flows in spiral galaxies.

The harmonic expansion is a simple and straight-forward tool to extract information from two-dimensional maps, and is a natural method for harvesting information from kinematic maps obtained by the new optical IFS. However, interpretation of the results depends on the intrinsic nature of galaxies. The spheroidal distribution of stars typical of early-type galaxies does not have the same dynamical properties as a gas disk. To explore those intrinsic properties, we need a more general description of the harmonic terms, without assumptions on geometry or dynamical state of the observed system. In this paper we present such a method, which we call *kinemetry* due to its complementarity with surface photometry of early-type galaxies. In its basics, kinemetry is a generalisation of the tilted ring harmonic expansion method for analysing velocity maps of gaseous discs to the kinematic observations of spheroidal systems such as elliptical and lenticular galaxies.

In Section 2 we present the theoretical background on which kinemetry operates. Section 3 presents the method and discusses two choices of expansion: along circles and along ellipses. The meaning of the kinematic coefficients for different kinematic moments is presented in Section 4. In Section 5 we present the application of kinemetry as a diagnostic tool for quantifying axisymmetry and kinematic misalignments in triaxial systems, and we discuss the advantages of the expansion along ellipses. Section 6 summarises the conclusions.

## 2 Theoretical background and motivation

The dynamics of a collisionless stellar system is fully specified by its phase-space density or distribution function  $f = f(\vec{x}, \vec{v}, t)$  (e.g. Binney & Tremaine 1987). However, this quantity is not measurable directly. When observing external galaxies, we measure properties that are integrated along the line-of-sight (LOS). The observables, which

reveal only the averages of properties of a large number of unresolved stars, are the surface brightness and the full velocity profile (for a review see de Zeeuw 1994). An additional complication is that the galaxies are viewed from a certain angle, and we actually observe only the projected properties of the integrated distribution function.

Analysis of the projected surface brightness via (broad-band) imaging is called *surface photometry*. The surface brightness is, however, only the zeroth-order projected moment of the distribution function. For a complete picture, the analysis has to include the full velocity profile, i.e. the line-of-sight velocity distribution (LOSVD):

$$\mathcal{L}(v; x, y) = \int_{\text{LOS}} dz \int \int dv_x dv_y f(\vec{r}, \vec{v}), \quad (1)$$

where  $(x, y, z)$  are the three spatial coordinates, oriented such that the LOS is along the  $z$ -axis. Observations of the LOSVD are usually presented by its moments: mean velocity  $V$ , velocity dispersion  $\sigma$  and higher-order moments commonly parametrised by Gauss-Hermite coefficients, (van der Marel & Franx 1993; Gerhard 1993),  $h_3$  and  $h_4$  being the most commonly used.

The kinematic moments of stationary triaxial systems show a high degree of symmetry which can be expressed through their parity. The mean velocity is an odd moment, while velocity dispersion is an even moment. In practice, this means that a two-dimensional map of a given moment shows corresponding symmetry. Maps of even moments are *point-symmetric*, while maps of odd moments are *point-anti-symmetric*. In polar coordinates this gives:

$$\begin{aligned} \mu_e(r, \theta + \pi) &= \mu_e(r, \theta), \\ \mu_o(r, \theta + \pi) &= -\mu_o(r, \theta), \end{aligned} \quad (2)$$

where  $\mu_e$  and  $\mu_o$  are arbitrary even and odd moments of the LOSVD, respectively. Furthermore, if the observed system is axisymmetric, the even moment of the LOSVD will also be *mirror-symmetric* or, correspondingly, an odd moment will be *mirror-anti-symmetric*:

$$\begin{aligned} \mu_e(r, \pi - \theta) &= \mu_e(r, \theta), \\ \mu_o(r, \pi - \theta) &= -\mu_o(r, \theta). \end{aligned} \quad (3)$$

Unlike surface brightness images, analysis of maps of stellar kinematic moments for early-type galaxies have not been extensively explored, due to the small number of studies with full two-dimensional kinematics. On the theoretical front, there were some studies of velocity maps of triaxial systems (e.g. Franx et al. 1991; Statler 1991, 1994a; Statler & Fry 1994; Statler 1994b; Arnold et al. 1994). The new observations with the IFS SAURON (Bacon et al. 2001), and its survey of a representative sample of nearby galaxies (de Zeeuw et al. 2002) yield high-quality maps of the kinematic moments of early-type galaxies (Emsellem et al. 2004). The structures visible on these kinematic maps are reflections of the intrinsic properties of the galaxies and kinemetry provides an efficient method for quantifying the wealth of information seen on these maps. In this way, kinemetry can be used as an analysis tool and a step between observations and theoretical modelling.

### 3 The method

In this section we present the details of the kinemetry method which exploits the high degree of symmetry observed in early-type galaxies. The errors are treated in more detail in Section 4.

#### 3.1 Harmonic expansion

Fourier analysis is the most straightforward approach to characterise any periodic phenomenon. The periodicity of a kinematic moment can easily be seen by expressing the moment in polar coordinates:  $K(x, y) \rightarrow K(r, \theta)$ . The map  $K(r, \theta)$  can then be expanded as follows to a finite number ( $N + 1$ ) of harmonic terms (frequencies):

$$K(r, \theta) = a_0(r) + \sum_{n=1}^N c_n(r) \cos[n(\theta - \phi_n(r))]. \quad (4)$$

The main advantages of this approach are: (i) linearity at constant  $r$ , and (ii) no *a priori* assumptions about the kinematic maps of the observed galaxy.

Choice of the centre and geometry of the expansion is somewhat arbitrary. We fix the centre of the polar coordinate grid at the central intensity peak in the nucleus of the galaxy, which is usually well-defined in early-type galaxies. We assume this point corresponds to the gravitational potential minimum.

We perform the expansion along a set of concentric circular annuli although in principle any geometry can be used. The main advantage of circles is that they do not introduce any *a priori* assumption about the structure of the kinematic maps (or the underlying galaxy potential). Throughout this paper we use circles to explain the basic features and properties of the kinematic expansion, but in Sections 3.2 and 4.5 we consider expanding along elliptical annuli, with its specific application to velocity maps only.

In practice, we rewrite eq. (4) in the form:

$$K(r, \theta) = a_0(r) + \sum_{n=1}^N [a_n(r) \cos n\theta + b_n(r) \sin n\theta], \quad (5)$$

where the coefficients  $a_n, b_n$  are determined by a least-squares fit using singular value decomposition with a basis  $\{1, \cos \theta, \sin \theta, \dots, \cos N\theta, \sin N\theta\}$ . The amplitude and phase coefficients ( $c_n, \phi_n$ ) of eq. (4) can be easily calculated from the  $a_n, b_n$  coefficients:

$$\begin{aligned} c_n &= \sqrt{a_n^2 + b_n^2}, \\ \phi_n &= \arctan\left(\frac{b_n}{a_n}\right). \end{aligned} \quad (6)$$

In addition to measurement errors, there are two effects which limit the reliability with which coefficients in the expansion can be determined: (i) the absolute number of points sampled along the annulus, and (ii) the regularity with which these points sample the annulus as a function of angle,  $\theta$ . Figure 1 shows an example of these effects

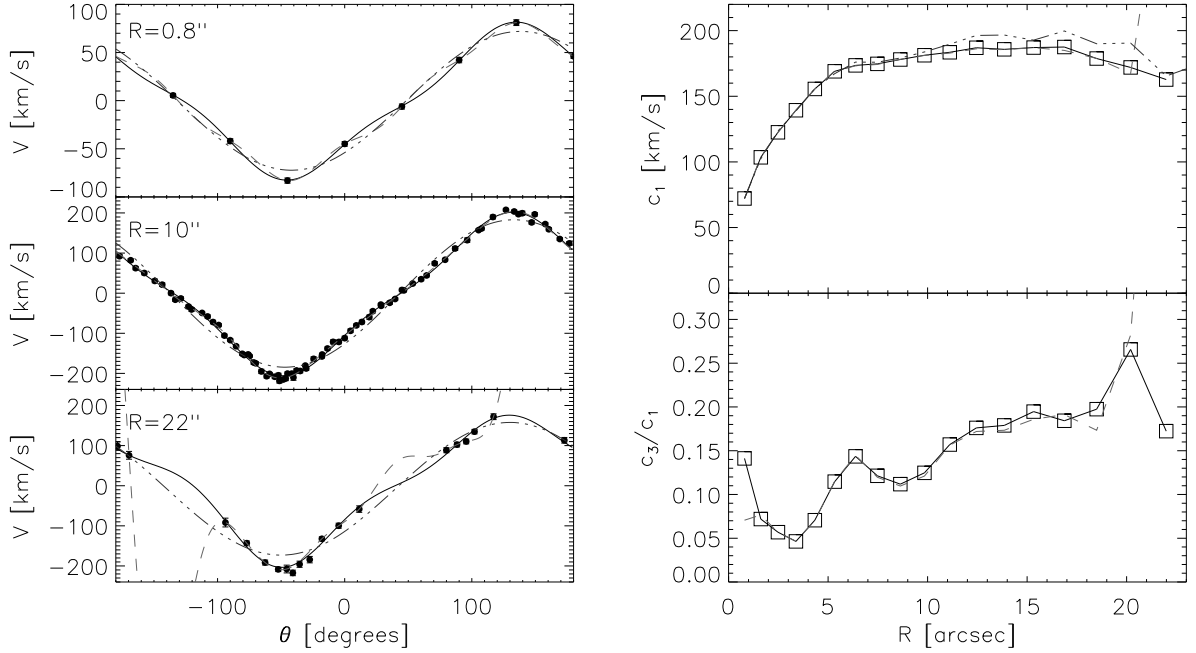


**Figure 1** — Examples of kinematic profiles and kinematic coefficients for the E4 galaxy NGC 2974 as observed with SAURON. Top left panel: the kinematic profile of the innermost annulus ( $r = 0.8''$ ). Second left panel: the kinematic profile of an annulus at  $r = 10''$  from the centre. Third left panel: the kinematic profile of an outer annulus ( $r = 22''$ ). In these panels, the observed data are indicated by field symbols. The  $1\sigma$  error bars are generally smaller than the symbols. The solid line is the fit to the data using  $n_{\max} = 4$  terms. The dashed line is the fit using  $n_{\max} = 7$  terms. The dash-dotted line is the fit using  $n_{\max} = 2$  terms. Top right panel: the amplitude of the  $c_1$  coefficient from the kinematic expansion of the full velocity map of NGC 2974. Open symbols and solid line were obtained using  $n_{\max} = 4$  terms in the expansion, while the dashed line using  $n_{\max} = 7$  and dash-dotted line using  $n_{\max} = 2$  terms. The bottom right panel:  $c_3/c_1$  coefficient ratio from the two expansions: solid symbols and solid line for  $n_{\max} = 4$  terms and dashed line for  $n_{\max} = 7$  terms.

and how they limit the number of terms which can be reliably fitted to the given kinematic profile<sup>1</sup>. The figure is based on the observed SAURON velocity map of NGC 2974 shown on Fig.9 and described in more details in Chapter 5 of this thesis. In order to prescribe the number of terms for the expansion we impose the condition that the corresponding half-wavelength of the highest term in the expansion has to be longer than the maximum angular distance between the data points. This can be expressed by a simple relation:  $n_{\max} < \pi/\Delta\theta$ , where  $n_{\max} = N + 1$  is the maximum number of terms used in the expansion and  $\Delta\theta$  is the size of the largest distance between the data points in the kinematic profile.

At small radii (top panel in Fig. 1), the annulus intersects only a few evenly-spaced points, and  $n_{\max}$  is correspondingly small (in this example  $n_{\max} = 4$ ). At intermediate radii, (the second panel in Fig. 1), the kinematic profile is well sampled allowing more

<sup>1</sup>In this study we use the term “kinematic profile” to describe the variation in the value of a kinematic moment along annuli extracted from maps.

higher-order terms. At large radii (the third panel in Fig. 1), the annulus can include regions without data (sampling beyond the edge of the map), creating “holes” in the kinematic profile. The angular size of the holes limits the number of terms that can be used for the expansion (in this example  $n_{\max} = 2$ ).

In the right panels of Fig. 1 we show the dominant odd terms,  $c_1$  and  $c_3$  of the harmonic expansion. The different lines correspond to the different number of terms used in fitting the kinematic profiles on the first three panels. The dashed-dotted line corresponds to  $n_{\max} = 2$ . These two terms alone are clearly not sufficient to fit the data. Adding more terms will increase the accuracy of the reproduction of the kinematic moment, but if too many are added, the discreteness effects will become important. The dashed line corresponds to  $n_{\max} = 7$  which is well justified at intermediate radii, but in the central annulus and in the annuli at large radii ( $r > 20''$ ), it does not satisfy the relation for maximum number of terms used in the expansion.

To combat the effects of sampling, the Fourier expansion in kinemetry is therefore performed on concentric annuli of increasing width. In general, this is the consequence of the rapidly falling signal-to-noise ratio of spectra as one goes away from the centre. The kinematic maps are necessarily binned (e.g. using adaptive Voronoi binning (Cappellari & Copin 2003) as in the presented examples), and as the bins typically increase in size with radius, the area of the annuli in which the kinematic values are selected have to increase as well to uniformly sample the kinematic profile. However, by increasing the bin size, one loses the spatial resolution and the final size of the annuli is a compromise of these two effects. We made a specific choice for the SAURON data, where the width,  $\Delta r$ , of a given annulus,  $j$ , is given by the expression  $\Delta r_j = s \times q^{j-1}$ . Here,  $s$  corresponds to the size of the smallest spatial element ( $0.8''$  for SAURON), and  $q$  is a scale factor such that  $\Delta r \approx 2''$  at a radius of  $25''$

It should be noted that the number of terms required in the expansion depends also on the purpose of the expansion, which can be to reproduce the map in detail using a large number of terms (possibly enforcing a symmetry, as in Section 4.4) or to extract a small number of coefficients to describe the main features of the map and obtain a low-order approximation to the galaxy highlighting the key terms.

### 3.2 Expansion along elliptical annuli

In the previous section we discussed the kinematic expansion of kinematic maps along circular annuli which bring no assumptions about the galaxy. However, certain physical insight for the choice of the shape of the annuli may be well justified, as in the case of surface photometry, or the analysis of velocity fields of ionised gas discs. In this section, we turn in more detail to the alternative approach of expansion along elliptical annuli. The kinematic formalism described above remains unchanged and only the selection of the data points changes from circular to elliptical annuli.

Surface photometry of early-type galaxies has the obvious choice to expand along elliptical isophotes of the light distribution. The azimuthal surface-brightness profile at a certain radius is fitted by an ellipse and the possible deviations are represented by higher-order terms of a harmonic series. The existence and amplitude of the higher-order terms quantify the deviations of the ellipses, which have physical meaning and describe the shape of the isophotes relative to the best-fitting ellipse (e.g Lauer 1985;

Jedrzejewski 1987; Bender 1988).

Observed velocity maps of disc galaxies can be well fitted by circular motion. A standard approach of the tilted ring method (Begeman 1987) in the analysis of the velocity maps of HI, CO and H $\alpha$  discs is to decompose them in a number of separate rings. Each ring is then described by six parameters: the centre coordinates, position angle, inclination, systemic velocity and circular velocity. A harmonic analysis of the rings can be performed, characterising the higher-order deviations from the pure circular motion (Franx et al. 1994; Schoenmakers et al. 1997; Wong et al. 2004).

Kinematic maps of early-type galaxies, having different symmetries and not necessarily being created by stars moving in a disc, do not offer such simply motivated geometries for the expansion. On the other hand, since their light distribution is elliptical it is reasonable to assume that an expansion along ellipses will have some advantages over the expansion along the circles. The choice of the actual ellipticity is somewhat arbitrary. For example, it is possible to expand along the galaxy isophotes or along ellipses that correspond to projected circles. In the first case, one follows the photometry and probes regions of the same projected surface brightness; while in the second case, one samples locations with equal intrinsic radii. In the second case, however, it is necessary to assume an inclination for the galaxy, which is usually difficult to estimate. Also, assuming a constant ellipticity for the whole kinematic map may not be justified.

Let us assume that the velocity maps of early-type galaxies are created by stars moving on circular orbits in thin discs. Following the tilted-ring approach, we can then divide a velocity map into a number of separate rings. The extracted velocity profile is fitted with a simple cosine function:

$$V(R, \theta) = V_0 + V_C \cos \theta, \quad (7)$$

where  $R$  is the mean radius of the ring in the plane of the galaxy,  $V_0$  is the systemic velocity,  $V_C$  is the circular velocity not corrected for the inclination and  $\theta$  is the azimuthal angle in the plane of the galaxy, which is related to the axial ratio  $q$  of the ring's major and minor axes, and is measured from the kinematic position angle of the map. Varying the axial ratio, one can find the ring whose velocity profile is the most similar to the circular velocity of a disc, with radius  $R$  and inclination  $\cos i = q$ . In other words, the axial ratio defines the ellipse on the sky,  $q = 1 - \epsilon$ , with ellipticity  $\epsilon$ , which corresponds to a circle in the plane of the galaxy, describing the orbits of stars in the disc. These independent rings are then analysed by means of harmonic expansion. This approach effectively minimises the higher-order terms. If the assumption that the investigated velocity maps are similar to disc velocity maps is satisfied, then it is to be expected that the higher-order terms will be negligible. Sections 4.5 and 5.3 present an application of this modified kinemetry approach on model and observed velocity maps, respectively.

## 4 Kinematic parameters and their meaning

Kinematic analysis is possible for all measured kinematic moments. The properties and meaning of the kinematic coefficients will differ depending on the underlying symmetry of the analysed map. The influence of the map symmetry on the coefficients can be predicted and compared to the obtained kinematic values. On the other hand,

assuming a symmetry one can obtain the properties of the map by effectively filtering the noise in the data. In this section we characterise the kinematic coefficients for odd and even kinematic moments, present the filtering capabilities of kinemetry and discuss kinemetry along ellipses.

#### 4.1 Model galaxy

We constructed a model galaxy to demonstrate the application of kinemetry. The model is axisymmetric with a distribution function which depends only on the energy and one component of the angular momentum. The model was constructed using the Hunter & Qian (1993) contour integration method and following the prescriptions of Emsellem et al. (1999) to resemble the SAURON observations of NGC 2974: surface-brightness distribution, kinematic observations, inclination, mass-to-light ratio and central black hole mass. The distribution function of the model yields the full LOSVD from which the observable kinematics can be extracted. This was done on a large  $100'' \times 100''$  field by fitting a Gauss-Hermite series ( $V$ ,  $\sigma$ ,  $h_3$  and  $h_4$ ) to spatially binned data which resemble typical SAURON observations. In order to mimic the real observations, we also assigned the typical error of the SAURON observations to each model observable. These errors were used to add intrinsic scatter to the noiseless model data by means of a Monte Carlo realisation. Further details on the construction of the model galaxy and its kinematics are given in Section 5.1 of Chapter 5 of this thesis.

This model is an example of an axisymmetric galaxy, with mirror-(anti)-symmetric kinematic maps. Although kinematic analysis of a more complicated model is also possible (and equally straightforward), here we present a simpler example to clearly quantify the main properties of the kinematic moment maps and the results of kinemetry.

#### 4.2 Odd kinematic moments

In a Gauss-Hermite parameterisation of the LOSVD, the first two odd moments are the mean velocity  $V$ , and the Gauss-Hermite coefficient  $h_3$ . The maps of these moments look different and have different interpretations, but have the same underlying symmetry. Generally, maps of odd moments show *point-anti-symmetry*. Imposing the point-anti-symmetry condition (eqs. 2–3) on the terms of the kinematic expansion (eq. 4), for the odd moments of LOSVD one has:

$$\mu_o(-x, -y) = -\mu_o(x, y) \quad \Rightarrow \quad a_0 = c_{2n} \equiv 0. \quad (8)$$

A map with additional *mirror-anti-symmetry* (an axisymmetric case) requires also:

$$\mu_o(x, -y) = \mu_o(x, y) \quad \Rightarrow \quad \phi_{2n+1} = \text{const} \equiv \text{PA}. \quad (9)$$

Therefore, one can predict that in an observed odd moment map the even terms will be considerably smaller than the odd ones, where the departures from zero are caused by noise or possible lopsidedness (departures from the assumed symmetry).

Figures 2 and 3 show the kinematic expansion of the  $V$  and  $h_3$  maps of the model galaxy. The errors were estimated using Monte Carlo simulations. The kinematic coefficients were derived from 100 realisations of the moment map, where the moment's value in each spatial bin was taken from a Gaussian distribution with the mean of the original moment and standard deviation given by the error assigned to the moment in the bin. Each realisation of the map was expanded using kinemetry providing a distribution of values from which we estimate the  $1\sigma$  confidence limit.

The zeroth-order term,  $a_0$ , measures the mean level of the map. For the first kinematic moment, this is equivalent to the systemic velocity of the galaxy. In the case of the model velocity field, the systemic velocity was zero by construction, and in an observed galaxy,  $a_0$  will be non-zero. However, if the systemic velocity is properly subtracted (as it was assumed in eq. 8),  $a_0$  will be zero. Alternatively, using the kinematic expansion it is possible to determine a reliable systemic velocity using the information of the whole velocity map. In the case of the observed  $h_3$  maps, which have mean level equal to zero by construction,  $a_0$  will be small, and like other even terms, consistent with zero.

The coefficient  $c_1$  gives the general shape and amplitude of the odd moment map and is always the dominant term. Hereafter, we normalise the higher coefficients,  $c_{i>1}$ , in the kinematic expansion of the velocity map by  $c_1$ , to simplify the comparison between the terms.

The first-order correction is given by the next odd term,  $c_3$ . This term can be named the *morphology* term because it describes most of the additional geometry of the map. Generally, the first two odd terms are enough to describe the velocity map, although the kinematic expansion can include higher terms as well,  $c_5$  and even  $c_7$ . In Fig 2 and 3 we plot the  $c_5$  term for completeness. Although in some instances this term can become significant (around  $20''$  in this case), it is generally very small, being at the level of noise in the data.

Connected to the amplitude terms are the corresponding phase terms,  $\phi_n$ . They determine the orientation of the map, but their contribution depends on the relative strength of the amplitude terms. The first phase coefficient,  $\phi_1$ , gives the mean position angle of the velocity map (measured from the horizontal axis,  $\theta = 0$ ). We name it the *kinematic angle*. The angle that  $\phi_1$  measures is the position angle of the maximum  $c_1$  term. This is, in general, slightly different from the positions of the maxima on the map, which are also influenced by the contribution from higher-order terms. However, it does give the global orientation of the map at a given radius to a good approximation and can be used to describe the symmetry of the map (Section 5.1).

The angle  $\phi_3$  is the phase angle of the third harmonic: the next significant term. For a small amplitude of  $c_3$ , its contribution to the overall orientation will be small, and the position of the maximum velocity will be given accurately by  $\theta_{max} = \phi_1$ . For an axisymmetric galaxy  $\phi_3$  will have specific values, as we will see in Section 5.1.

The error bars plotted on Fig. 2 and 3 (as well as on Fig. 4 and 5 of the next section) are typical for the SAURON observations of the nearby galaxies (Emsellem et al. 2004). As expected, due to the discreteness, they are larger at small and large radii where the sampling and edge effects play an important role. In the case of the velocity maps, at intermediated radii with dense sampling of kinematic profiles, the typical intrinsic

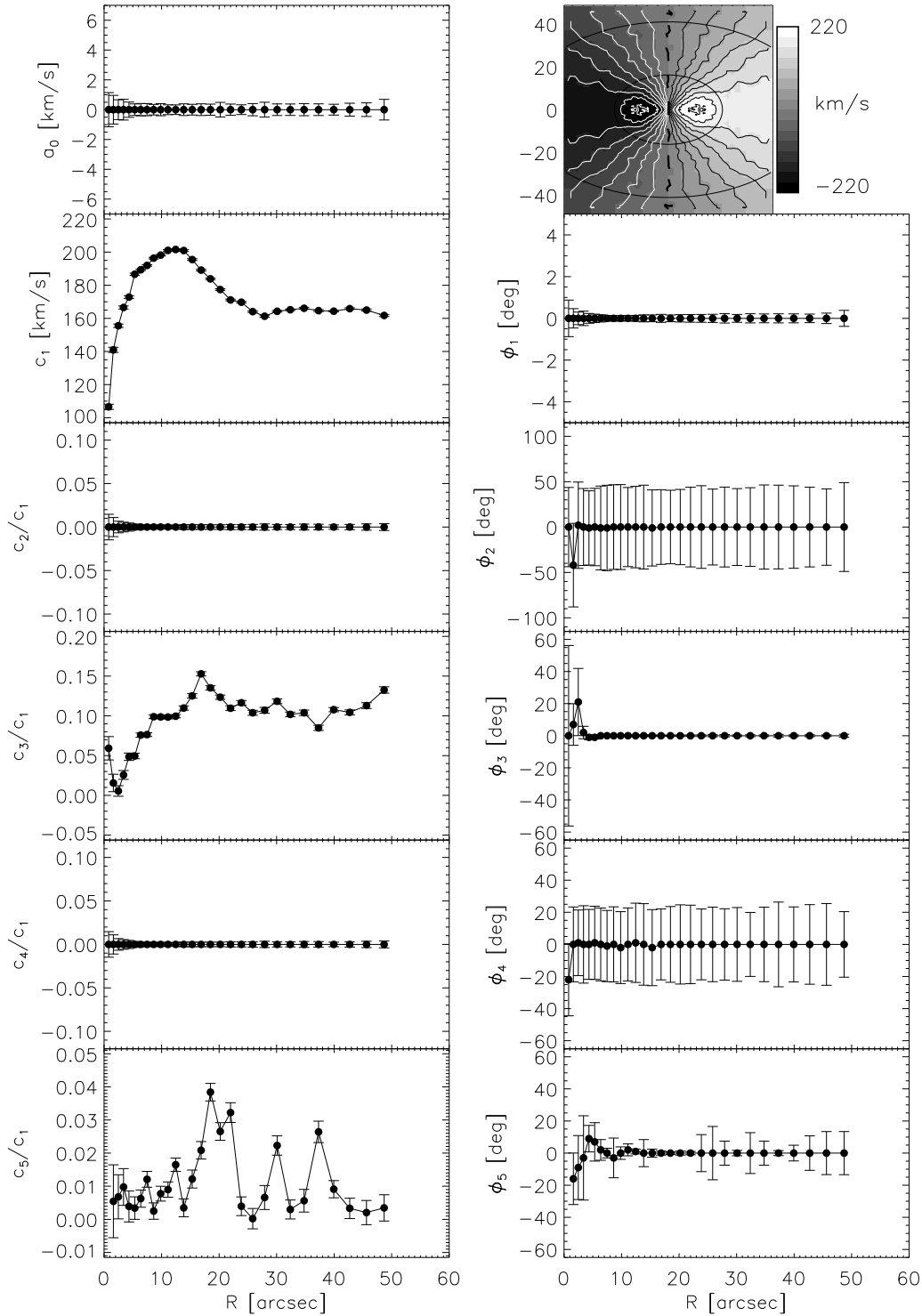


**Figure 2** — Kinematic expansion of the velocity map of the model axisymmetric galaxy. Panels of the left column show the amplitude coefficients of the kinematic expansion (from top to bottom):  $a_0$ ,  $c_1$ ,  $c_2/c_1$ ,  $c_3/c_1$ ,  $c_4/c_1$  and  $c_5/c_1$ . The velocity map is presented in the upper right, while other panels in the right column show the corresponding phase angles (from top to bottom):  $\phi_1$ ,  $\phi_2$ ,  $\phi_3$ ,  $\phi_4$  and  $\phi_5$ . The relatively large errors to the even phase angles are not significant because the associated amplitude is zero.

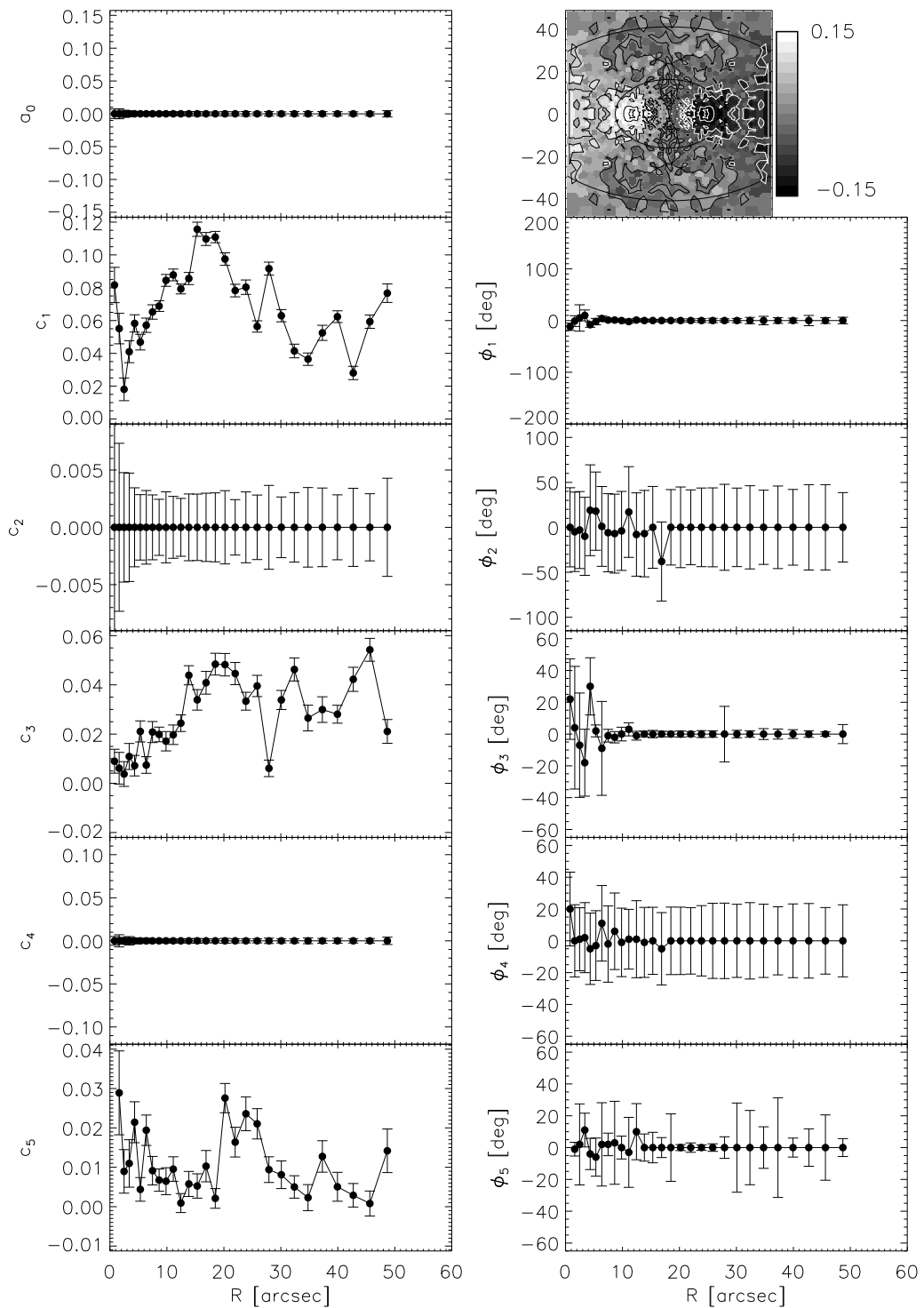


**Figure 3** — Kinematic expansion of the  $h_3$  map of the model axisymmetric galaxy. Panels of the left column show the amplitude coefficients of the kinematic expansion (from top to bottom):  $a_0, c_1, c_2, c_3, c_4$  and  $c_5$ . The  $h_3$  map is presented in the upper right panel, while the other panels show the same phase angles as in Fig 2, but for the  $h_3$  map.

errors (not accounting for systematics) for the  $c_1$  and  $c_3$  coefficients are  $0.5 \text{ km s}^{-1}$  and  $0.6 \text{ km s}^{-1}$ , respectively; and for the  $\phi_1$  and  $\phi_3$  phase angles are  $0.5^\circ$  and  $1^\circ$ , respectively. The larger errors on the phase angles of the even terms can be explained by the near-zero values of the corresponding amplitude coefficients. The same effect is visible for the phase angles of the higher-order odd terms, when they have near-zero values. Similar, but somewhat higher values are seen for the errors on the kinematic terms of higher-order kinematic moments ( $\sigma, h_3, h_4$ ).

The same description can be assigned to all terms of the kinematic expansion of  $h_3$  maps. The values of the amplitude coefficients  $c_i$  are much smaller for the  $h_3$  moment ( $c_i < 1$ ), and the rescaling of the higher terms with the dominant term is not very useful. The  $h_3$  map is noisier than the mean velocity map. This is reflected in the recovered errors of the coefficients, which are somewhat larger, even for the odd terms, than in the case of the mean velocity map. The typical intrinsic errors of kinematic expansion of  $h_3$  maps for the  $c_1$  and  $c_3$  coefficients are 0.04 and 0.005, respectively; and for the  $\phi_1$  and  $\phi_3$  phase angles are  $3^\circ$  and  $4^\circ$ , respectively.

### 4.3 Even kinematic moments

The even terms in the standard parametrisation of the LOSVD are the velocity dispersion  $\sigma$ , and the Gauss-Hermite coefficient  $h_4$ . In many ways, analysis of the even moments is analogous to that for the odd moments, taking the proper parity into account. The maps of even moments show *point-symmetry* which translates to the terms of the kinematic expansion as:

$$\mu_e(-x, -y) = -\mu_e(x, y) \quad \Rightarrow \quad c_{2n+1} \equiv 0. \quad (10)$$

A map with additional *mirror-symmetry* requires:

$$\mu_e(x, -y) = \mu_e(x, y) \quad \Rightarrow \quad \phi_{2n} = \text{const} \equiv \text{PA}. \quad (11)$$

As anticipated, the odd kinematic terms are expected to be consistent with zero on the observed maps of even moments. This is clearly visible in Figs. 4 and 5, which show the coefficients of the kinematic expansion of the model velocity dispersion and  $h_4$  maps. The  $1\sigma$  confidence levels shown in the figures were obtained via Monte Carlo simulations as in Section 4.2.

The dominant term of the even maps is  $a_0$ , and it describes the absolute level of the map as a function of radius. The next important term in the expansion is  $c_2$ , and it is the *morphology* term of the even moment maps. As seen in Figs. 4 and 5 this term describes more specific features of the maps. Features such as elongations along the minor axis or “bow-tie” shapes, often seen in observed velocity dispersion maps (Emsellem et al. 2004), should leave signatures in this term. Specifically, for the velocity dispersion maps the  $c_2$  term is mostly a few percent of the dominant  $a_0$  term, implying that these maps have near-circular symmetry, and that the choice of circles for describing these maps is a natural one.

The orientation of the morphologically distinct features are determined by the phase angles of the amplitude coefficients. When there is a feature with a specific angular dependence, e.g. an oval elongation along the major axis, the position angle of the feature

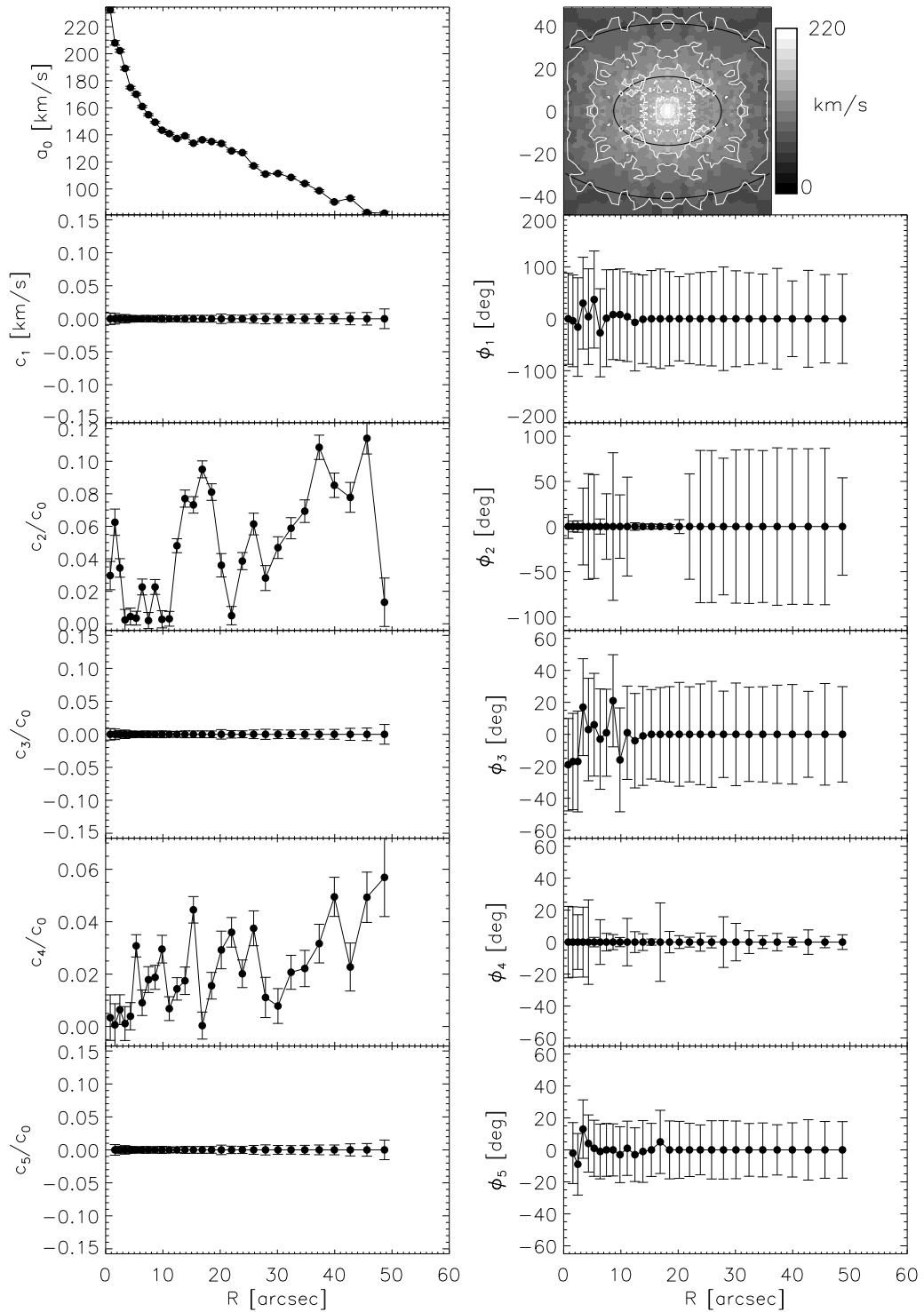


**Figure 4** — Kinematic expansion of velocity dispersion map of the model axisymmetric galaxy. Panels on the left column show amplitude coefficients of the kinematic expansion (from top to bottom):  $a_0$ ,  $c_1/a_0$ ,  $c_2/a_0$ ,  $c_3/a_0$ ,  $c_4/a_0$  and  $c_5/a_0$ . The velocity dispersion map is presented in the upper right, while other panels in the right column show the same phase angles as in Fig 2, but for the velocity dispersion map.

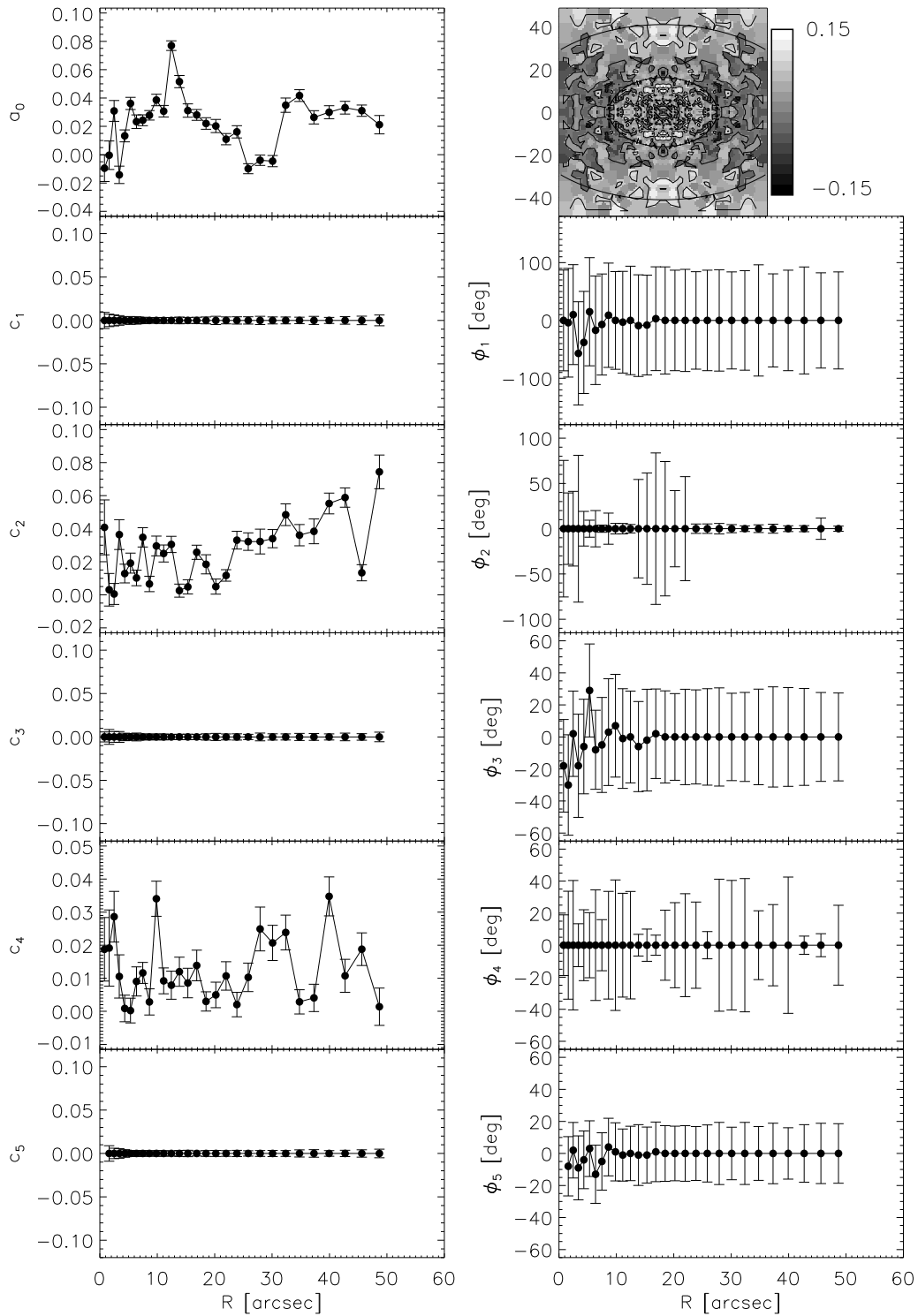


**Figure 5** — Kinematic expansion of the  $h_4$  map of the model axisymmetric galaxy. Panels on the left column show amplitude coefficients of the kinematic expansion (from top to bottom):  $a_0, c_1, c_2, c_3, c_4$  and  $c_5$ . The  $h_4$  map is presented in the upper right panel, while the other panels show the same phase angles as in Fig 2, but for the  $h_4$  map.

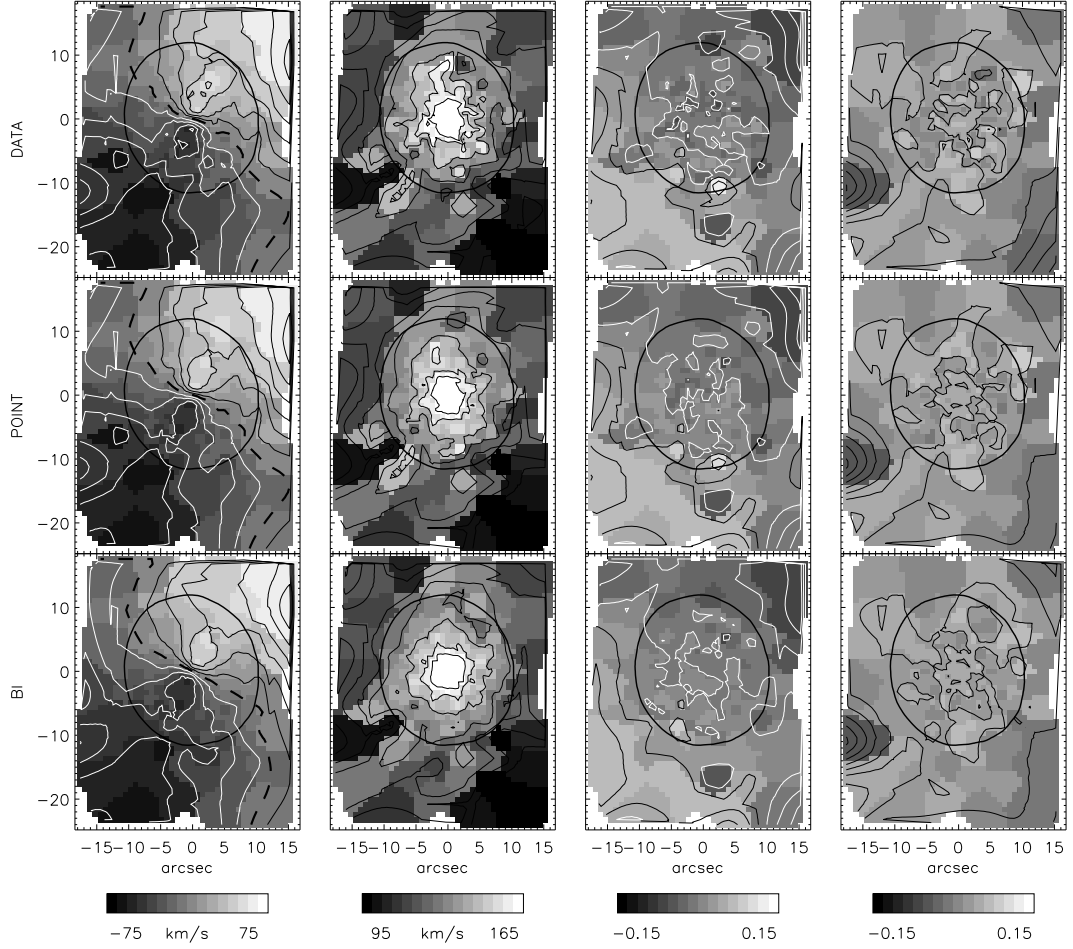


**Figure 6** — An example of kinematic filtering on kinematic maps of the galaxy NGC 474. Rows from left to right: mean velocity  $V$ , velocity dispersion  $\sigma$ , and Gauss-Hermite moments  $h_3$  and  $h_4$ . Columns from top to bottom: data, symmetrised data applying additional *point-(anti)-symmetric* condition (eqs. 8 and 10), data symmetrised applying additional *mirror-(anti)-symmetric* condition (eqs. 9 and 11). The overplotted kinematic contours were obtained by interpolation between the bin generators and extrapolation to the edge of the maps.

is given by the  $\phi_2$  phase angle of the  $c_2$  term. The phase angles of the odd terms, whose amplitude coefficients are zero, have large errors, while the errors of the even phase angles are generally smaller, although still high at certain radii, suggesting there is no preferred direction of the features on the example maps. The typical intrinsic errors for kinematic expansion of the velocity dispersion maps are:  $0.9 \text{ km s}^{-1}$  and  $1.1 \text{ km s}^{-1}$  for  $a_0$  and  $c_2$  coefficients, respectively, and  $3^\circ$  for the  $\phi_2$  phase angle in the region where the phase angle is well constrained. Similarly, for the expansion of the  $h_4$  map we obtained errors of 0.005, 0.006 and  $5^\circ$  for  $a_0$ ,  $c_2$  and  $\phi_2$ , respectively.

#### 4.4 Filtering

Kinematic filtering can also be useful as a powerful *filter* of two-dimensional kinematic maps. As already mentioned above, if the number of terms in the expansion is small, the

map will be smoothed, taking away the higher-order harmonics from the data, which may be caused by noise. However, kinemetry offers some other more specific filtering, which makes assumptions of the underlying symmetries in the kinematic maps.

Following eqs. (8) and (9), one can filter a kinematic map by fixing certain terms in the expansion to zero or to a constant value. Requiring *point-anti-symmetry* in the kinematic expansion for odd maps implies fixing the even terms to zero (in case of an even map, the odd terms are set to zero).

Similarly, a more strict requirement that all non-zero phases are set to a constant value will produce *mirror-(anti)-symmetric* maps. This symmetry removes twists of the kinematic angle, creating what is sometimes called a *bi-symmetric map*. These filtering criteria may also be applied to extract the relevant coefficients from maps with noisy data.

Figure 6 gives an example of filtering, applied to the first four observed moments of the LOSVD for SAURON observations of NGC 474 (Emsellem et al. 2004). The kinematic maps of this galaxy are consistent with *point-(anti)-symmetry* and, applying this symmetry condition to the kinematic expansion, removes much of the noise from the data. However, in the following example, we set all (non-zero) phases to the median value of the measured kinematic angle ( $\approx 60^\circ$ ), enforcing additional *mirror-(anti)-symmetry*, with which the galaxy kinematics are clearly not consistent. The results are axisymmetric kinematic maps (no kinematic twists), that, however, do not correspond to the real galaxy, but show the full filtering power of kinemetry.

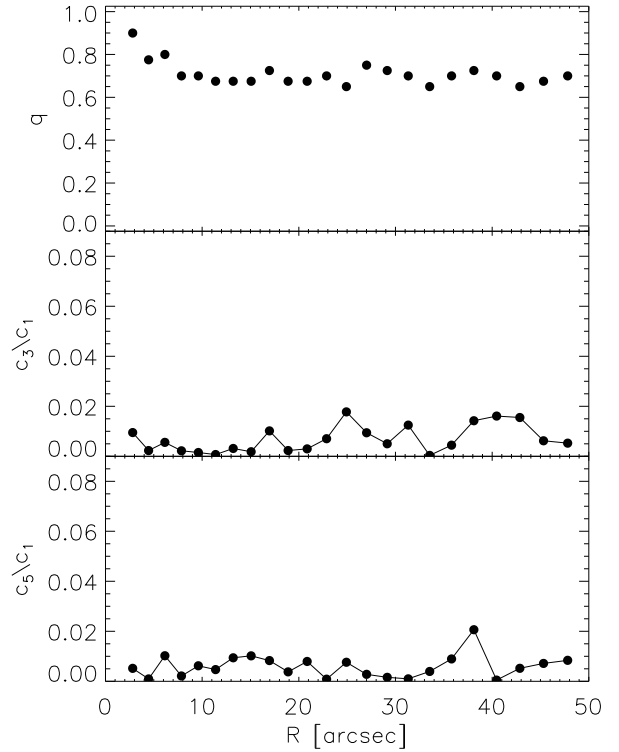
A draw-back of filtering such integral-field data with kinemetry comes from the nature of the spatial bins. Generally, the bins are not symmetrically distributed around the symmetry axes. Kinematic filtering works in annuli and if the bins are not uniformly distributed in the annuli, it will not be possible to find symmetric pairs of bins in all quadrants of the map and properly enforce the symmetry (e.g.  $K(-x, -y) = -K(x, y) = -K(x, -y) = K(-x, y)$ ). A way out is to interpolate the binned data on a regular grid and then symmetrise using kinemetry, although the best way of symmetrising the maps of the kinematic moments is to impose symmetry during the extraction of the kinematics from the observed data cube spectra.

#### 4.5 Expansion of velocity maps using kinemetry along ellipses

At this point we turn again to the special case of kinemetry along ellipses. In Section 3.2 we suggested that the tilted-ring approach to the velocity maps of early-type galaxies, although not physically founded, might give a better insight in the structure of maps. Here we show an example of the kinematic expansion of the velocity map of the model galaxy discussed in Fig. 2 along ellipses best-fitting ellipses following the prescription of Section 3.2.

We performed the expansion up to the third odd term ( $c_1$ ,  $c_3$  and  $c_5$ ), where the  $c_1$  term is by construction identical to  $V_C$  from eq. (7), while the higher-order terms describe the deviations of the velocity map from the projected circular motion. The result is shown in Fig. 7. The first panel of the figure shows the axial ratio of the elliptical rings used in the expansion. In the inner few arcseconds this ratio changes and then drops to a constant value of relatively *round* value for the axial ratio of about  $q = 0.7$ . Strikingly, the higher-order terms, plotted on the lower panels, are negligible, their

**Figure 7** — Terms of kinematic expansion of the velocity map of the model galaxy along ellipses. From top to bottom: axial ratio of the best-fitting ellipse, and the ratio of the  $c_3/c_1$  and  $c_5/c_1$  terms which measure the deviation from the circular velocity assuming the velocity map was generated by stars moving along circular orbits in a disc. The deviations are below the 1% level. See text for details.



contribution being mostly below the 1% level. This shows the power of this approach, which can describe a velocity field with basically two parameters: the axial ratio of the adopted ellipse and the first term of the harmonic expansion.

The underlying assumption of this application of kinemetry is that the velocity maps of early-type galaxies are created by stars moving along circular orbits in a thin disc. This, generally, is not true, and our intention here is only to qualitatively compare the observed velocity maps of spheroidal systems with those of thin discs. In the example shown in Fig. 7, the higher-order terms are very small and the velocity map of the model early-type galaxy seems to be consistent with a velocity map of an inclined disc. Our comparison stops here, but it is an interesting finding, worth more detailed investigation (see Section 5.3). Along the same lines, the axial ratio,  $q$ , from Fig. 7, does not imply the intrinsic inclination of the galaxy. It can, however, be used to categorise the velocity maps: velocity maps with small  $q$  are *flat* while velocity maps with high  $q$  are *round*.

## 5 Application

In this section we consider the ability of kinemetry to quantify the underlying symmetries of kinematic maps of observed galaxies, as well as give examples of kinemetry along ellipses for three early-type galaxies. For this purpose we focus on the velocity maps.

## 5.1 Prescription for axisymmetry

Two-dimensional velocity maps can be used to constrain the intrinsic shapes of early-type galaxies (Franx et al. 1991; Statler 1994b), and kinemetry can serve as a tool for extracting the necessary information from the maps. Here we consider conditions by which one can distinguish between velocity maps of axisymmetric and more general triaxial galaxies.

Axisymmetry is a special case of triaxiality, and triaxial galaxies, viewed under certain inclination can have axisymmetric appearance (e.g Stark 1977; de Zeeuw & Franx 1989). A galaxy is consistent with axisymmetry if the velocity map satisfies the following three conditions:

1. The velocity map is truly *point-anti-symmetric*, and, hence, the even terms in kinematic expansion are zero (or negligible), as given by (8).
2. The velocity map satisfies the condition (9), where all phase angles are constant.
3. All phase angles are equal to the photometric position angle. This condition can be softened by requiring that the higher-order phase angles satisfy the relation:

$$\phi_1 - \phi_i = \frac{n\pi}{i}, \quad (12)$$

where  $n \in \mathbb{Z}$  and  $\phi_i$  is the  $i$ -th order term in the expansion.

The last condition can be easily derived considering that for an axisymmetric velocity field the position of the zero velocity curve, the curve along which the velocity is zero on the map, is orthogonal to the kinematic angle given by  $\phi_1$ . This means that  $K(r, \theta) = 0$ , for  $\theta = \phi_1 + \pi/2$ . Neglecting the higher order terms, ( $c_i > c_3$ ), and substituting  $\theta = \phi_1 + \pi/2$  into eq. (4) one obtains the result of eq. (12).

Similarly, deviations from axisymmetry can be quantified following eqs. (4) and (12). If  $K(r, \theta = \phi_1 + \pi/2) = \Delta V \neq 0$ , then one finds:

$$\frac{\Delta V}{c_1} = \frac{c_3}{c_1} \sin 3(\phi_1 - \phi_3), \quad (13)$$

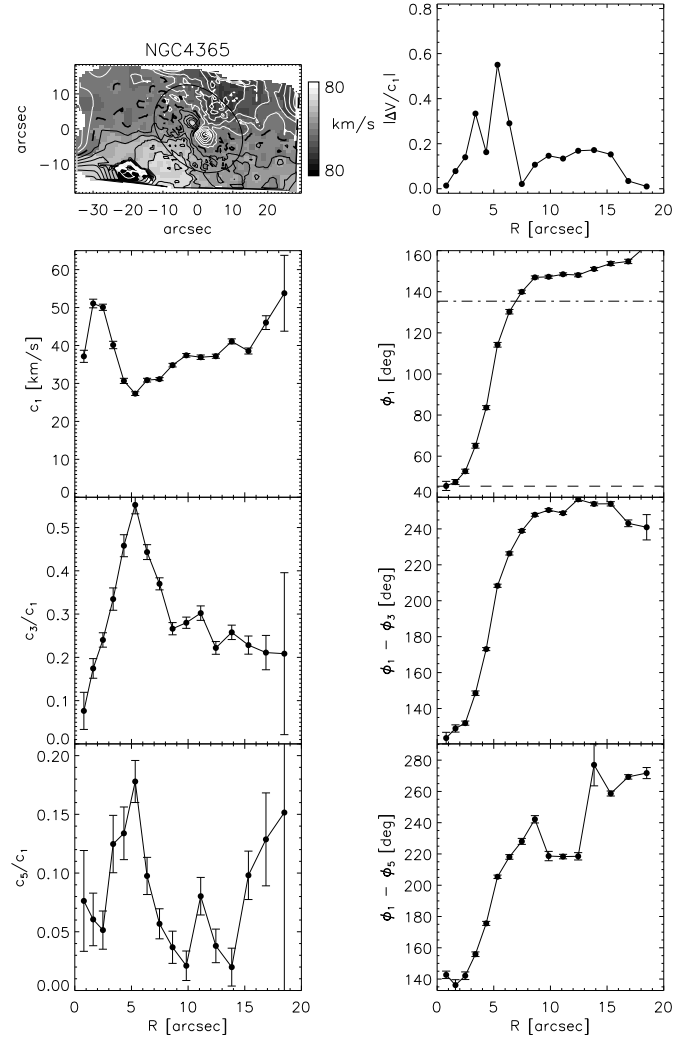
where we express the relation as a ratio of the dominant term in the expansion. This relation quantifies the contribution of the  $c_3$  term due to departures from axisymmetry and can be generalised to other higher terms. In cases of large misalignments between the kinematic and photometric position angles,  $\phi_1$  should be replaced by the photometric PA in the above equation.

Fig. 2 shows the kinematic expansion of a mirror-anti-symmetric velocity map and it is clear that all three conditions for axisymmetry are satisfied.

## 5.2 A triaxial case

In the previous section we presented the prescriptions for axisymmetry which were tested on an axisymmetric model velocity field. Here we turn to the wealth of the SAURON observations and use an observed velocity field of a triaxial galaxy, in order to show the departures from the conditions listed in the previous section. The velocity field belongs to the well studied triaxial galaxy NGC 4365. The SAURON kinematics, as

**Figure 8** — Kinematic analysis of NGC 4365. The velocity map of NGC 4365 is presented in the upper left panel. The panels in the left column show: odd amplitude coefficients:  $c_1$ ,  $c_3$  and  $c_5$ . Higher order terms are presented as fractions of  $c_1$ , the dominant term in the expansion. The first panel on the right shows the contribution of the  $c_3$  term to non-axisymmetry. Other panels in the right column present the phase angles:  $\phi_1$ ,  $\phi_3$  and  $\phi_5$ . Higher order phase angles are compared to the phase angle of the dominant terms  $\phi_1$  by subtraction. North is up and east to the left on the velocity map and  $\phi_1$  is measured east of north. Second panel on the right also shows major (lower straight line) and minor axis (upper straight line) photometric PAs.



well as the distribution of line-strengths, for this object were presented in Davies et al. (2001).

The velocity map of NGC 4365 (Fig. 8) shows a striking kinematically decoupled component (KDC) in the central  $5''$ . The structure and shape of this component led several authors to conclude that NGC 4365 is intrinsically a triaxial body showing no figure rotation (Surma & Bender 1995; Statler et al. 2004). We performed a kinematic analysis of the velocity map, expanding up to the fifth term ( $c_5$ ). The resulting coefficients and corresponding phase angles are shown in Fig. 8.

The KDC component is clearly evident in the dominant  $c_1$  terms as the fastest rotating component of the galaxy, with a well-defined radius. The main body of the galaxy shows increasing rotation with increasing radius, but remains a slow rotator ( $V/\sigma = 0.08$ , Surma & Bender 1995). The *morphology* term,  $c_3$ , is very strong, contributing up to 50% to the velocity field, and is strongest at the transition radius between the KDC and the main body of the galaxy. At larger radii, it slowly drops, but its relative contribution (about 20%) stays high. In the last extracted term,  $c_5$ , there is still considerable signal, again strongest in the transition region between the KDC and the rest of the galaxy. The contributions from the higher order terms ( $c_i, i \geq 7$ ) are on the order of

a few per cent.

The amplitude coefficients accurately describe the map, but the phase angles are useful for the determination of departures from axisymmetry. The kinematic angle,  $\phi_1$ , shows a clear twist of more than  $100^\circ$  over the map. The photometric major and minor axis PAs are overplotted on the same panel with two horizontal lines. We measured the PA on the reconstructed SAURON flux image obtained by integrating the spectra in each bin. The kinematic angle of the KDC is aligned with the major axis PA, while the main body of the galaxy rotates about an axis misaligned by about  $10^\circ$  from the major axis PA of the galaxy, as previously noted by Davies et al. (2001). This is a clear signature of non-axisymmetry. This conclusion is confirmed by the  $\phi_1 - \phi_3$  profile, which changes in step with  $\phi_1$ , nowhere strictly satisfying the relation (12). The contribution of the  $c_3$  term, expressed by eq. (13), and presented in the top left panel of Fig. 8, is high everywhere, especially in the transition region between the KDC and the main body of the galaxy.

### 5.3 Comparison of velocity fields of early-type galaxies with velocity fields of discs

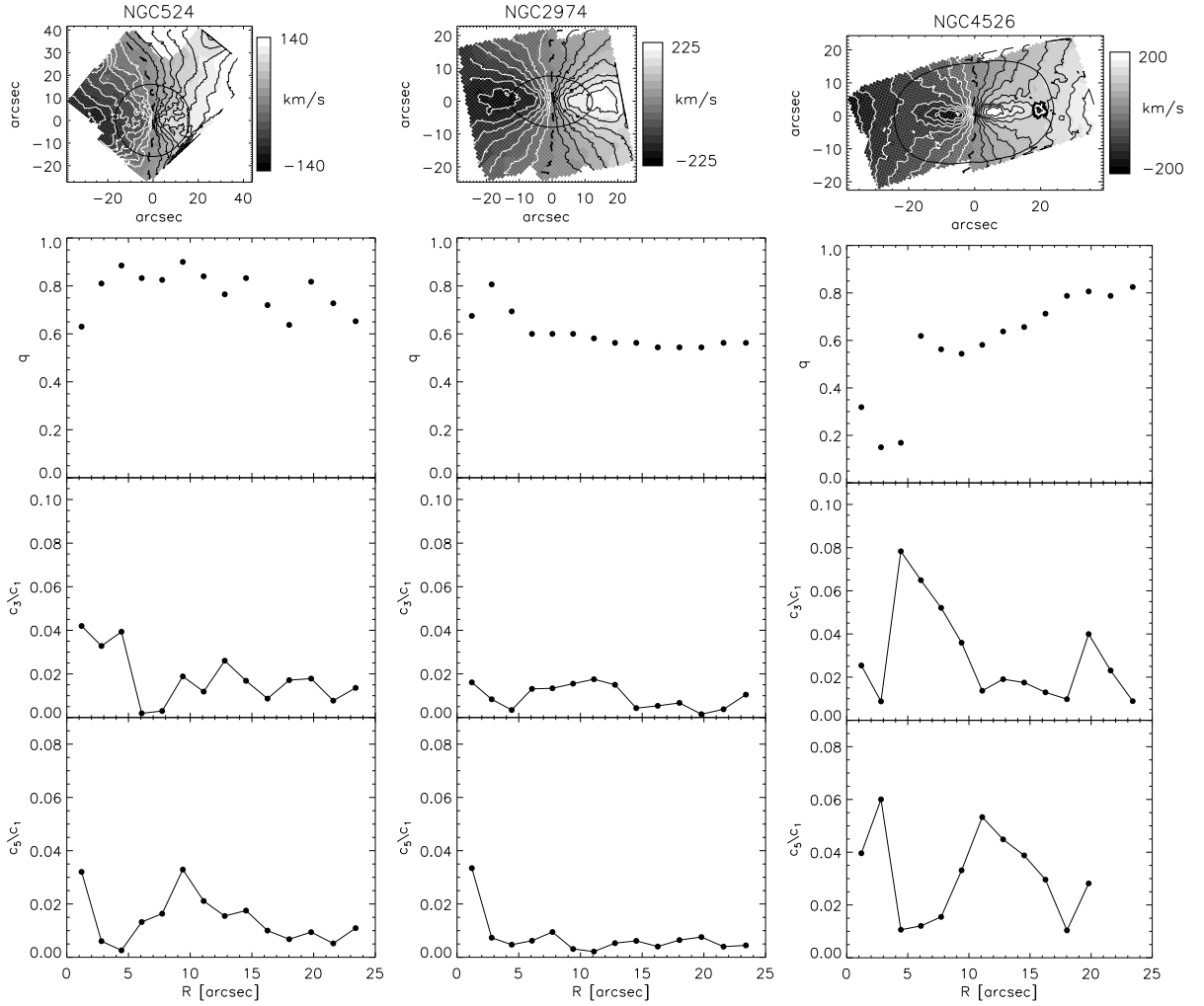
We turn again to the case of kinemetry along ellipses. Repeating the analysis from Section 4.5 we also analysed the velocity maps of three galaxies observed with SAURON as part of the SAURON survey (de Zeeuw et al. 2002). The observations and the velocity maps of NGC 524, NGC 2974 and NGC 4526 are presented in Emsellem et al. (2004). We chose these three galaxies as characteristic examples due to their shape and the pedagogical features of their velocity maps. NGC 524 is a roundish galaxy with an “open” velocity map. NGC 2974 is a fast-rotating E4 galaxy, and NGC 4526 is an S0 galaxy with a prominent embedded disc which can be also seen on the velocity map as a distinct component.

Fig. 9 presents the analysis of the three velocity maps. The analysis of the real observations with ellipses is more complicated than the analysis with circles or the analysis of the large model field (sampling issues), so, we had to rebin the velocity map to a finer grid (4 times finer). This is especially important in the centres of the field, where sampling can cause strong artifacts. The maps were also rotated such that the photometric major axes are horizontal in Fig. 9. The maps are presented above each corresponding set of kinematic expansion terms. We summarise the main results as follows:

**NGC 524** has a velocity field with high axial ratio and hence we can label it as a *round* velocity field. The higher-order terms  $c_3$  and  $c_5$  are small over the entire map, with a relative contribution to the circular velocity of about 2% and 1% respectively.

**NGC 2974** has a mean photometric flattening of  $\sim 0.6$  and the flattening of the velocity field corresponds to this value (expressed as axial ratio  $q$  on the figure). This velocity field is an example of a medium-flattened velocity field. The higher-order deviations from the circular velocity are smaller than in the case of NGC 524,  $c_3$  having a relative contribution of  $\approx 1\%$  and  $c_5$  of  $\approx 0.5\%$ .

**NGC 4526** is a more complicated map with its two kinematic components. The central disc on the velocity map is clearly visible in the inner  $10''$ . This structure is reflected in the terms of the kinematic analysis. The axial ratio is  $\approx 0.2$  in the inner  $5''$ , while beyond that radius it is much higher and varies between 0.6 and 0.8. The velocity



**Figure 9** — Kinematic analysis along ellipses for velocity maps of three early-type galaxies observed with SAURON. First row from left to right: velocity maps of NGC 524, NGC 2974 and NGC 4526. Second row from left to right: axial ratio  $q$  of the best fitting ellipse describing the *flattening* of the velocity field. Third and fourth rows from left to right: ratio of the terms in the kinematic expansion:  $c_3/c_1$  and  $c_5/c_1$ , respectively.

map in the inner few arcsec is clearly different from the rest of the map. The inner part is quite *flat*, while the outer part has more *round* features, somewhere between NGC 2974 and NGC 524. The higher-order terms are also different on this velocity map. The relative contribution of  $c_3$  is much higher than in the two other examples (up to  $\sim 5$  times), especially in the part where the velocity map is *flat*. The middle part of the field is more similar to projected circular motion, with a small  $c_3$  term. Towards the end of the map, edge effects have an increasing influence on the expansion (Section 3). At radii larger than  $20''$ , we only used the  $c_3$  term in expansion. The contribution of the  $c_5$  term is smaller, but, interestingly, not negligible in the middle part of the map.

The similarities of the velocity maps of early-type galaxies with disc velocity maps are striking. It might be the case that the three investigated galaxies have a strong disc contribution which dominates the appearance of the velocity map, while the specific

features are visible from the small departures of the higher terms. Similar result was also seen in the model velocity field, which corresponds to a model galaxy with no disc component. In analogy with photometry, the deviations of the higher-order terms are also on the order of a few percent. This warrants a detailed study of a larger sample of two-dimensional velocity maps, such as the 48 SAURON galaxies from Emsellem et al. (2004).

## 6 Conclusions

We have presented a general method for analysing and describing two-dimensional maps of the kinematic moments observed with integral-field spectrographs. The method is based on the harmonic expansion of velocity maps. It is particularly useful for describing the maps of kinematic moments of early-type galaxies. We call our method *kinemetry*.

Kinemetry is a straight-forward Fourier expansion of two-dimensional maps. Using the specific properties of the kinematic moments (symmetries) it can be used as a powerful filter to the data. The results of kinemetry, the coefficients of the harmonic expansion, can be used to parametrise trends and detect properties of galaxies. Maps of odd kinematic moments are described only by the odd terms in the expansion. Similarly, maps of even moments are described only by the even terms.

In the case of odd maps, the first term is the most dominant term and gives the overall shape of the map (the zeroth term can exist for velocity maps and gives the systemic velocity). The third term describes the additional morphological shapes. In some galaxies, higher terms can also be significant, although usually the first and third term reproduce all important features of the map. The phase angle of the first term gives the orientation of the map and it is called kinematic angle. Higher-order phase angles are useful in detecting small departures from axisymmetry.

In the case of even maps, the zeroth term is the dominant term and it describes the global shape of the map. The next important terms which describes the morphology of the map in more detail, is the second term in the expansion. The zeroth term does not have a phase angle, and the orientation of the features of the maps are given by the phase angle of the second term.

The measured values of the kinematic coefficients can be used to detect departures from axisymmetry in the observed maps, and in this way, to quantify the intrinsic shape of the galaxy. The necessary requirement for a velocity map to be consistent with axisymmetry is that the even terms in the expansion are consistent with zero and that the kinematic angle is constant and equal to the photometric position angle. We present a diagnostic tool for determining the consistency of velocity maps with axisymmetry using the phase angles of the first two odd terms as well as quantifying the departures from an axisymmetric velocity map. We apply this method to the triaxial galaxy NGC 4365 as an obvious case of a non-axisymmetric object, with a decoupled component and a strong kinematic twist.

Circular rings are the most natural choice for expansion, because they are simple, general and can be uniformly used on maps of all kinematic moments. In some cases, like for the velocity maps, it is necessary to expand the maps to a relatively large num-

ber of terms (up to  $c_5$  or even  $c_7$  of the harmonic expansion judging from a preliminary study of SAURON velocity maps (Emsellem et al. 2004)). In other cases, e.g. for the velocity dispersion maps only a small number of terms (up to  $c_2$ ) are needed when the expansion is performed along circles. We note that the maps of line-strengths, which resemble the maps of the even moments (a line-strength is the zeroth moment of the LOSVD), could also be analysed by kinemetry.

We also presented a preliminary study of kinemetry of velocity fields along ellipses instead of circles. In this approach the number of terms needed to describe the field is smaller than using circles ( $q$  and  $c_1$  versus, generally,  $c_1$ ,  $c_3$  and  $c_5$ ). Also, the axial ratio,  $q$ , provides a simple way of describing the global appearance of the velocity map, which facilitates the use of illustrative terms such as *flat* or *round*. These terms are also used to describe the surface-brightness distribution (note that  $q$  can be vary significantly from case to case), and this makes a natural connection between the different moments of the distribution function.

The main assumption used when expanding along ellipses is that the velocity maps of early-type galaxies are similar to the velocity maps generated by stars moving in circular orbits in a thin disc. Although we do not suggest this as a physical interpretation for early type galaxies, it does provide an excellent low-order approximation to the observed velocity maps. Indeed, in the presented examples we found that the velocity maps of some early-type galaxies do resemble the velocity maps of discs. The presented preliminary results are encouraging and the next step is a detailed study of the kinemetry of velocity maps along ellipses for a representative sample of early-type galaxies.

## Acknowledgments

We thank Eric Emsellem for providing a model axisymmetric galaxy. We thank Glenn van de Ven for many useful discussions and Richard McDermid for a critical reading of the paper.

## References

- Arnold R., de Zeeuw P. T., Hunter C., 1994, MNRAS, 271, 924  
Bacon R., Copin Y., Monnet G., Miller B. W., Allington-Smith J. R., Bureau M., Carollo C.M., Davies R. L., et al., 2001, MNRAS, 326, 23  
Begeman K. G., 1987, Ph.D. Thesis, University of Groningen  
Bender R., 1988, A&A, 193, L7  
Binney J., 1978, MNRAS, 183, 779  
Binney J., Tremaine S., 1987, Galactic Dynamics. Princeton, NJ, Princeton University Press, 1987, 747 p.  
Cappellari M., Copin Y., 2003, MNRAS, 342, 345  
Davies R. L., Kuntschner H., Emsellem E., Bacon R., Bureau M., Carollo C. M., Copin Y., Miller B. W., et al., 2001, ApJ, 548, L33  
de Zeeuw P. T., Bureau M., Emsellem E., Bacon R., Carollo C.M., Copin Y., Davies R. L., Kuntschner H., et al., 2002, MNRAS, 329, 513  
de Zeeuw P. T., 1994, in The Formation and Evolution of Galaxies Structure, Dynamics and Formation of Spheroidal Systems, Eds. C. Muñoz-Tuñónn and F. Snchez p 231, (Cambridge: Cambridge Univ. Press)  
de Zeeuw P. T., Franx M., 1989, ApJ, 343, 617

- Emsellem E., Dejonghe H., Bacon R., 1999, *MNRAS*, 303, 495  
Emsellem E., Cappellari M., Peletier R. F., McDermid R. M., Bacon R., Bureau M., Copin Y., Davies R. L., et al., 2004, *MNRAS*, 352, 721  
Franx M., Illingworth G., de Zeeuw P. T., 1991, *ApJ*, 383, 112  
Franx M., van Gorkom J. H., de Zeeuw P. T., 1994, *ApJ*, 436, 642  
Gerhard O. E., 1993, *MNRAS*, 265, 213  
Hunter C., Qian E., 1993, *MNRAS*, 262, 401  
Jedrzejewski R. I., 1987, *MNRAS*, 226, 747  
Lauer T. R., 1985, *MNRAS*, 216, 429  
Schoenmakers R. H. M., Franx M., de Zeeuw P. T., 1997, *MNRAS*, 292, 349  
Stark A. A., 1977, *ApJ*, 213, 368  
Statler T. S., 1991, *AJ*, 102, 882  
Statler T. S., 1994a, *ApJ*, 425, 458  
Statler T. S., 1994b, *ApJ*, 425, 500  
Statler T. S., Emsellem E., Peletier R. F., Bacon R., 2004, *MNRAS*, 353, 1  
Statler T. S., Fry A. M., 1994, *ApJ*, 425, 481  
Surma P., Bender R., 1995, *A&A*, 298, 405  
Teuben P. J., 1991, in *Warped Disks and Inclined Rings around Galaxies*, eds. S. Casertano, p.D. Sackett, & F.H. Briggs, (Cambridge: Cambridge Univ. Press), p 398  
van der Marel R. P., Franx M., 1993, *ApJ*, 407, 525  
Wong T., Blitz L., Bosma A., 2004, *ApJ*, 605, 183

---

## Chapter 5

---

# Dynamical modelling of stars and gas in NGC 2974: determination of mass-to-light ratio, inclination and orbital structure by Schwarzschild's method

Davor Krajnović, Michele Cappellari, Eric Emsellem, Richard M. McDermid, and P. Tim de Zeeuw, submitted to Monthly Notices of the Royal Astronomical Society

We study the large-scale stellar and gaseous kinematics of the E4 galaxy NGC 2974, based on panoramic integral-field data obtained with SAURON. We quantify the velocity fields with Fourier methods (kinemetry), and show that the large-scale kinematics is largely consistent with axisymmetry. We construct general axisymmetric dynamical models for the stellar motions using Schwarzschild's orbit-superposition method, and compare the inferred inclination and mass-to-light ratio with the values obtained by modelling the gas kinematics. Both approaches give consistent results. However we find that the stellar models provide fairly weak constraints on the inclination. The intrinsic orbital distribution of NGC 2974, which we infer from our model, is characterised by a large-scale stellar component of high angular momentum. We create semi-analytic test models to study the ability of Schwarzschild's modelling technique to recover the given input parameters (mass-to-light ratio and inclination) and the distribution function. We also test the influence of a limited spatial coverage on the recovery of the distribution function (i.e. the orbital structure). We find that the models can accurately recover the input mass-to-light ratio, but we confirm that even with perfect input kinematics the inclination is only marginally constrained. This suggests a possible degeneracy in the determination of the inclination, but further investigations are needed to clarify this issue. We also show that the distribution function can be reliably recovered by the modelling method inside the spatial region sampled by the integral-field kinematics.

### 1 Introduction

THE internal dynamical structure of galaxies retains evidence of their evolution. The internal dynamics, however, can only be interpreted through a combination of ob-

servational and theoretical efforts. From a theoretical point of view, one wants to know how the stars are distributed in space and what velocities they have. From the observational point of view, one wants to determine the intrinsic structure of the observed galaxies. The goals of both approaches are equivalent, and consist of the recovery of the phase-space density, or distribution function (DF) of galaxies, which uniquely specifies their properties. An insight into the DF is possible by the construction of dynamical models which are constrained by observations. There are several modelling methods established in the literature, of which Schwarzschild's orbit-superposition method is perhaps the most elegant (Schwarzschild 1979, 1982). In the past few years it has been applied successfully to a number of galaxies (van der Marel et al. 1998; Cretton & van den Bosch 1999; Cappellari et al. 2002; Gebhardt et al. 2003); but recent observational advances in spectroscopy with integral-field units offer for the first time full two-dimensional constraints on these dynamical models (Verolme et al. 2002; Copin, Cretton & Emsellem 2004).

This paper presents a case study of the early-type galaxy NGC 2974. It is one of the few elliptical galaxies known to contain an extended disc of neutral hydrogen in regular rotation (Kim et al. 1988). It also hosts extended  $H\alpha$  emission (Buson et al. 1993; Plana et al. 1998), and belongs to the "rapid rotators" (Bender 1988). The total absolute magnitude of  $M_B = -20.32$  puts NGC 2974 near the transition between giant ellipticals and the lower-luminosity objects which often show photometric and kinematic evidence for a significant disc component (e.g. Rix & White 1992). Emsellem et al. (2003, hereafter EGF03), combining WFPC2 imaging with TIGER integral-field spectroscopy of the central few arcseconds, discovered spiral structure in the  $H\alpha$  emission in the inner few arcseconds, and concluded that the galaxy contains a nuclear stellar bar. The general properties of NGC 2974 are listed in Table 1.

The availability of both stellar and gaseous kinematics makes NGC 2974 a very interesting case for detailed dynamical modelling. Cinzano & van der Marel (1994) made dynamical Jeans models of the gaseous and stellar components additionally introducing a stellar disc in order to fit their long-slit data along three position angles. They found that the stellar and gaseous discs were kinematically aligned and the inclination of both discs was consistent with  $60^\circ$ . This prompted them to suggest a common evolution, where the gas could be ionised by the stars in the stellar disc. Using more sophisticated two-integral axisymmetric models, which assume the DF depends only on the two classical integrals of motion, the energy  $E$  and the angular momentum with respect to the symmetry axis  $L_z$ , EGF03 were able to reproduce all features of Cinzano & van der Marel (1994) data as well as their integral-field TIGER data (covering the inner  $4''$ ). The models of EGF03 did not require a thin stellar disc to fit the data.

In this study we construct axisymmetric models for NGC 2974 based on Schwarzschild's orbit superposition method. This method allows the DF to depend on all three isolating integrals of motion. All previous studies with three-integral models concentrated on the determination of the mass-to-light ratio,  $Y$ , and mass of the central black hole,  $M_{\text{BH}}$ . Based on the observed stellar velocity dispersion, the  $M_{\text{BH}} - \sigma$  relation (e.g. Tremaine et al. 2002) predicts a central black hole mass of  $2.5 \times 10^8 M_\odot$ , which at the distance of NGC 2974 (21.48 Mpc, Tonry et al. 2001) has a radius of influence of  $0''.2$ . Our observations of NGC 2974, with the integral-field spectrograph SAURON (Bacon

**Table 1** — Properties of NGC 2974. Listed properties are taken from the Lyon/Meudon Extragalactic Database (LEDa). Distance modulus is from Tonry et al. (2001).

Parameter	Value
Morphological type	E4
$M_B$ [mag]	-20.46
effective B-V [mag]	1.00
PA [degrees]	42
Distance Modulus [mag]	31.66
Distance scale [pc/arcsec]	52.1

et al. 2001), do not have the necessary resolution to probe the sphere of influence of the central black hole. The dynamical models presented here are, therefore, aimed at determination of the  $\Upsilon$ , the inclination,  $i$ , and the internal orbital structure. The stellar and gaseous kinematics also provide independent estimates of  $\Upsilon$  and  $i$ , which can be used to cross-validate the results from the two approaches.

The results of the dynamical modelling are influenced by the assumptions of the models, but also by the specifics of the observations. The spatial coverage of the kinematics is one example. The two-dimensional coverage is an improvement over a few slits often used in other studies. Similarly, increasing the radial extent of the data could change the results. Another issue, associated with the modelling techniques, is the ability of the three-integral models to recover the true distribution function of the galaxy. This is very important for the investigation of the internal dynamics, since the recovered orbital distribution must represent the observed galaxy if we want to learn about the galaxy’s evolutionary history. In this paper we present tests designed to probe these issues and, in general, to determine the robustness of our three-integral method.

This paper is organised as follows. Section 2 summarises the SAURON spectroscopy and the photometric ground- and space-based data. The analysis of the velocity maps, used to quantify the presence and influence of possible non-axisymmetric motions as well as a brief discussion on bars in NGC 2974, is presented in Section 3. The three-integral dynamical models for the stellar motions are discussed in Section 4. Section 5 is devoted to tests of the three-integral method involving the determination of the model parameters ( $\Upsilon$ ,  $i$ ), influence of the radial extent of the data and the recovery of the DF. The modelling of the emission-line gas kinematics and comparison with the results of the stellar dynamical modelling is presented in Section 6. Section 7 concludes.

## 2 Observations and data reduction

The observations of NGC 2974 used in this work consist of ground- and space-based imaging, and ground-based integral-field spectroscopy. The imaging data were presented in EGF03 and the absorption-line kinematics of the SAURON observations in Emsellem et al. (2004, hereafter E04) as part of the SAURON survey (de Zeeuw et al. 2002). In this study we also use the SAURON emission-line kinematics of NGC 2974.

### 2.1 SAURON spectroscopy

NGC 2974 was observed with the integral-field spectrograph SAURON mounted on the 4.2-m William Herschel Telescope (WHT) in March 2001. The observations consisted

Field of view	33" × 41"
Aperture size	0"94
Final spatial sampling	0"8
Spectral range	4810 - 5300 Å
Spectral sampling	1.1 Å pixel <sup>-1</sup>
Spectral resolution	4.2 Å (FWHM)
# of field lenses	1431
# of sky lenses	146
# of exposures	8
Exposure time per pointing	1800 s
Instrumental dispersion( $\sigma$ )	108 km s <sup>-1</sup>
Median seeing (FWHM)	1"4

**Table 2** — The SAURON instrumental characteristics and exposure details of the observations of NGC 2974 obtained in March 2001 at the WHT. The sky apertures are pointed 1'9 away from the main field.

of eight exposures divided equally between two pointings, each covering the nuclear region and one side of the galaxy. The individual exposures of both pointings were dithered to obtain a better estimate of detector sensitivity variations and avoid systematic errors. The instrumental characteristics of SAURON and a summary of the observations are presented in Table 2.

The SAURON data were reduced following the steps described in Bacon et al. (2001) using the dedicated software *XSauron* developed at CRAL-Observatoire. The performed reduction steps included bias and dark subtraction, extraction of the spectra using a fitted mask model, wavelength calibration, low frequency flat-fielding, cosmic-ray removal, homogenisation of the spectral resolution over the field, sky subtraction and flux calibration. All eight exposures were merged into one data cube with a common wavelength range by combining the science and noise spectra using optimal weights and (re)normalisation. In this process we resampled the data-cube to a common spatial scale (0"8 × 0"8) with resulting field-of-view of about 45" × 45". The data cube was spatially binned to increase the signal-to-noise ( $S/N$ ) ratio over the field, using the Voronoi 2D binning algorithm of Cappellari & Copin (2003). The targeted minimum  $S/N$  was 60 per aperture, but most of the spectra have  $S/N$  ratio high (e.g.  $[S/N]_{max} \approx 420$ ) and about half of the spatial elements remain un-binned. The final data cube of NGC 2974 and the detailed reduction procedure was presented in E04.

## 2.2 Absorption-line kinematics

The SAURON spectral range includes several important emission lines:  $H\beta$ ,  $[OIII]\lambda\lambda 4959,5007$  and  $[NI]\lambda\lambda 5198,5200$  doublets. These lines have to be masked or removed from the spectra used for the extraction of the stellar kinematics. The method most suitable for this is the direct pixel-fitting method operating in wavelength space, which allows easy masking of the emission lines. We used the penalised pixel-fitting algorithm (pPXF) of Cappellari & Emsellem (2004), following the prescriptions of E04. The line-of-sight velocity distribution (LOSVD) was parametrised by the Gauss-Hermite expansion (van der Marel & Franx 1993; Gerhard 1993). The 2D stellar kinematic maps of NGC 2974, showing the mean velocity ( $V$ ), the velocity dispersion ( $\sigma$ ), as well as

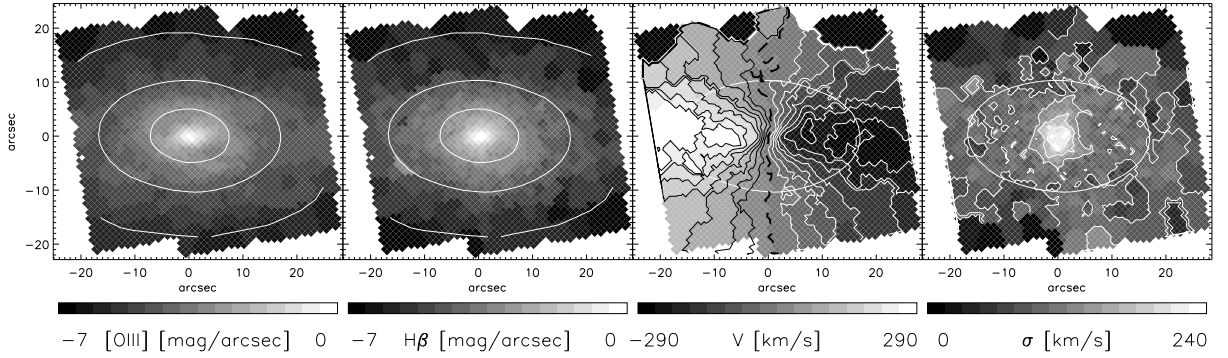


**Figure 1** — Distribution of H $\beta$  and [OIII] emission-lines and gas kinematics observed by SAURON. Gas intensities are in mag arcsec $^{-2}$  with arbitrary zero points. Gas mean velocity  $V$  and velocity dispersion  $\sigma$  are in km s $^{-1}$ . Overplotted isophotes are levels of the reconstructed total intensity from the full SAURON spectra.

higher order Gauss-Hermite moments  $h_3$  and  $h_4$ , were presented in E04, along with the kinematics of 47 other elliptical and lenticular galaxies. In this study we expand on the previously published kinematics by including two more terms in the Gauss-Hermite expansion ( $h_5$  and  $h_6$ ) to make sure all useful information was extracted from the spectra and tighten the constraints on the dynamical models. The extraction of additional kinematic terms was performed following the same procedure as in E04. The new extraction is consistent with the published kinematics (except that now the LOSVD is parameterised with 6 moments) and we do not present them here explicitly (but see Fig. 11).

We estimated the errors in the kinematic measurements by means of Monte-Carlo simulations. The parameters of the LOSVD were extracted from a hundred realisations of the observed spectrum. Each pixel of a Monte-Carlo spectrum was constructed adding a value randomly taken from a Gaussian distribution with the mean of the observed spectrum and standard deviation given by a robust-sigma estimate of the residual of the fit to the observed spectrum. All realisations provide a distribution of values from which  $1\sigma$  confidence levels were estimated. During the extraction of the kinematics for error estimates, we switched off the penalisation of the pPXF method in order to obtain the true (unbiased) scatter of the values (see Cappellari & Emsellem 2004 for a discussion).

### 2.3 Distribution and kinematics of ionised gas

NGC 2974 has previously been searched for the existence of emission-line gas. Kim et al. (1988) reports the detection of HI in a disc structure aligned with the optical isophotes. The total mass of HI is estimated to be  $8 \times 10^8 M_{\odot}$ , rotating in a disc with an inclination of  $i \approx 55^{\circ}$ . Buson et al. (1993) detected H $\alpha$  emission distributed in a flat structure along the major axis. Assuming a disc geometry, the inferred inclination is  $\approx 59^{\circ}$ , and the total mass of HII was estimated to be  $\approx 3 \times 10^4 M_{\odot}$ . Similar results are found also by Plana et al. (1998). Deep optical ground-based imaging studies suggested the existence of “arm-like” spiral structures, visible in filamentary distribution of ionised gas outside  $\sim 5''$  (Bregman et al. 1992; Buson et al. 1993). The recent high-

	JKT	HST/WFPC2
Filter band	I	F547M & F814W
Exposure time (s)	60	700 & 250
Field of view (arcsec)	380×350	32×32
Pixel scale (arcsec)	0.3106	0.0455
Date of observations	16.04.1993	16.04.1997

**Table 3** — Summary of the ground- and space-based observations of NGC 2974. The exposure times of the HST/WFPC2 observations are averages of all frames used to produce the WFPC2 association images.

resolution HST imaging in  $H\alpha$ + $[NII]$  revealed the presence of a gaseous two-arm spiral in the inner  $\sim 200$  pc, with a total mass of  $6.8 \times 10^4 M_{\odot}$  (EGF03).

The strongest emission line in the SAURON spectra of NGC 2974 is the  $[OIII]$  doublet. There is also considerable emission in  $H\beta$  and some emission from the  $[NI]$  lines. Measurement of the emission-line kinematics followed the extraction of the absorption-line kinematics. For each spectrum in the data-cube we performed three steps:

- (i) The pPXF method provided the model absorption spectrum that yielded the best fit to the spectral range with the emission lines ( $[OIII]$ ,  $H\beta$  and  $[NI]$ ) excluded.
- (ii) We then subtracted the model absorption spectrum from the original observed spectrum. This resulted in a “pure emission-line” spectrum which was used to extract the gas kinematics.
- (iii) Each emission line was approximated with a Gaussian. The fit was performed simultaneously to the three lines of  $[OIII]$  and  $H\beta$ , not using the mostly negligible  $[NI]$  doublet.

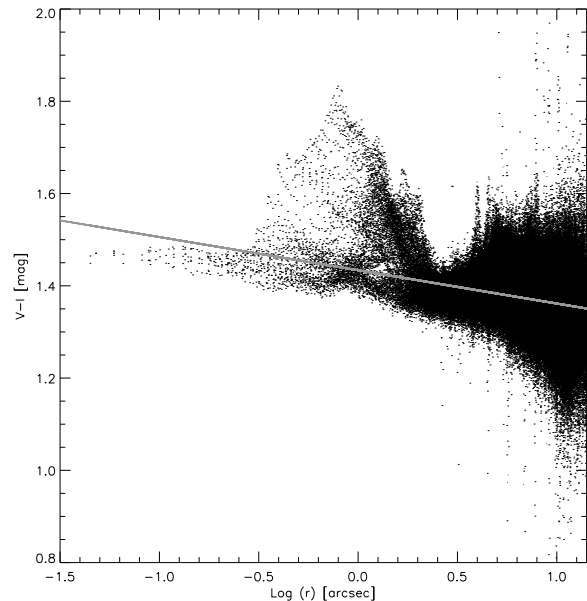
This procedure assumes that the velocity and velocity dispersion of the different emission lines are equal. Performing the simultaneous fit to the lines while allowing them to be kinematically independent yields similar results (Sarzi et al. in preparation). Following Osterbrock (1989) we assumed a 1:2.96 ratio for the components of the  $[OIII]$  doublet, while leaving the intensity of the  $[OIII]$  and  $H\beta$  lines independent. The flux maps of  $[OIII]$  and  $H\beta$  lines as well as the maps of the  $[OIII]$  emission-line mean velocity and velocity dispersion are presented in Fig. 1.

Both the  $H\beta$  and  $[OIII]$  emission lines are present over the whole extent of the maps on Fig. 1, but their intensity drops off approximately exponentially with distance from the centre. The  $[OIII]$  emission is stronger over the entire SAURON field with the  $[OIII]$  to  $H\beta$  line-ratio being  $\approx 1.7$ . The shape of the gas distributions are very similar, although  $H\beta$  follows the stellar light isophotes more precisely. The  $[OIII]$  distribution shows departures from the stellar isophotes in two roughly symmetric regions, positioned at approximately  $45^\circ$  from the vertical axis on Fig. 1. The nature of these dips in the  $[OIII]$  flux are discussed in Section 3.3.

## 2.4 Ground- and space-based imaging

In this study we used the existing ground- and space-based images of NGC 2974. The already reduced wide-field ground-based  $I$ -band image of NGC 2974 was taken from Goudfrooij et al. (1994), obtained at the 1.0-m Jacobus Kapteyn Telescope (JKT). We also retrieved the Wide Field and Planetary Camera 2 (WFPC2) association images

**Figure 2** — V-I colour versus the elliptical radius of every pixel in the inner 15'' of the WFPC2/PC1 images of NGC 2974. The straight line presents the best fit to the points obtained by minimising the absolute deviation. Notice the excess of red pixels between 0''.3 and 2''.5 caused by dust.



of NGC 2974 from the Hubble Space Telescope (HST) archive (Program ID 6822, PI Goudfrooij). The details of all imaging observations are presented in Table 3.

A major complication in the derivation of the surface brightness model needed for the dynamical modelling is the existence of dust, clearly visible on the high resolution images. We considered two possible approaches: masking the patchy dust areas and excluding it from the calculation of the model, or constructing a dust-corrected image. We decided to adopt the latter approach to determine the stellar surface brightness. We derived the correction of dust absorption using the F547M and F814W WFPC2 images, following the steps listed in Cappellari et al. (2002). The process consists of construction of a colour excess map  $E(V-I)$ , from a calibrated V-I colour image. The colour excess map is used to correct the pixels above a given  $E(V-I)$  threshold using the standard Galactic extinction curve. We assumed that the dust is a screen in front of the galaxy and that dust-affected pixels have the same intrinsic colour as the surrounding unaffected pixels. Figure 2 shows the calibrated V-I colour of pixels in the inner part of the PC images. The best fit to the colours was obtained by minimising the absolute deviation of the pixel values. This fit, represented by a line in Fig. 2, was used to calculate the colour excess by subtracting the measured colour from the fit. The resulting  $E(V-I)$  image is shown in the second panel of Fig. 3. The other panels on the same figure present the inner parts of the F814W PC image before and after the correction of dust absorption. The colour excess image highlights the dust structure visible also on Fig. 3 of EGF03 and suggests a non-uniform distribution of dust in the central region of NGC 2974.

### 3 Quantitative analysis of velocity maps

Two-dimensional kinematic maps offer a large amount of information and are often superior to a few long-slit velocity profiles. The two-dimensional nature of these data motivates us to quantify the topology and structure of these kinematic maps, just as is

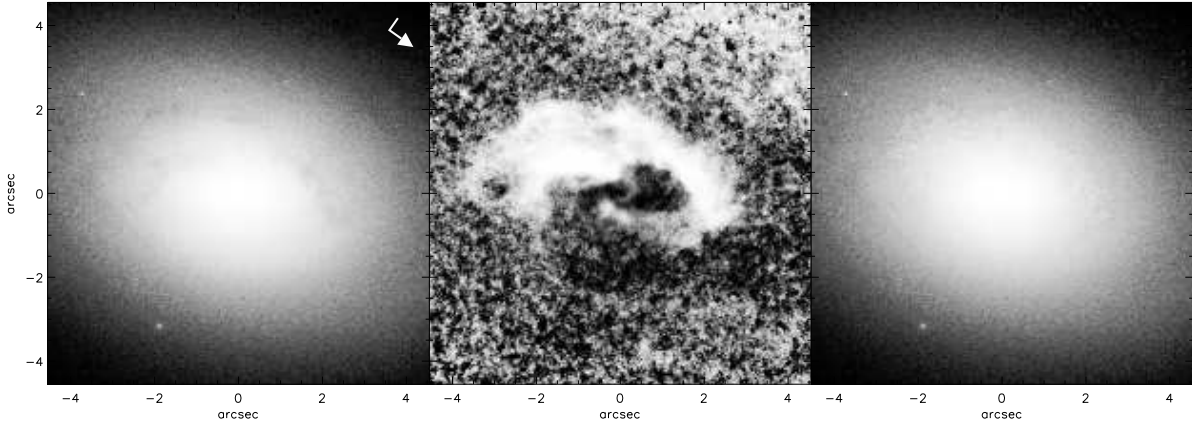


**Figure 3** — Dust correction on the F814W WFPC2 image of NGC 2974. From left to right: observed F814W image; colour excess  $E(V-I)$  obtained as described in the text; dust corrected F814W image. The arrow points to the north and associated dash to the east. All images were constructed using histogram equalisation. Lighter shades represent brighter regions. The  $E(V-I)$  map is stretched between -0.1 (dark) and 0.2 (bright) magnitudes.

commonly done for simple imaging. We have developed a new technique to deal with kinematic maps based on the Fourier expansion, and, due to its similarity to the photometry, we named it kinemetry (Copin et al. 2001). This method is a generalisation of the approach developed for two-dimensional radio data (Franx et al. 1994; Schoenmakers et al. 1997; Wong et al. 2004). The aim of the method is to extract general properties from the kinematic maps of spheroidal systems (early-type galaxies) without assuming a specific intrinsic geometry (e.g. thin disc) for the distribution of stars. This changes the interpretation and the approach to the terms of the harmonic expansion from the case of cold neutral hydrogen or CO discussed in the above mentioned papers. In this section we briefly present the method and apply it to the stellar and gaseous velocity maps. The detailed treatment of kinemetry with examples and tests is presented in Chapter 4 of this thesis.

### 3.1 Harmonic Expansion

The kinemetry method consists of the straightforward Fourier expansion of the line-of-sight kinematic property  $K(r, \theta)$  in polar coordinates:

$$K(r, \theta) = a_0(r) + \sum_{n=1}^N c_n(r) \cos[n(\theta - \phi_n(r))]. \quad (1)$$

The expansion is done on a set of concentric circular rings (although other choices are possible), and its main advantage is linearity at constant  $r$ . The expansion is possible for all moments of the LOSVD, but in this paper we restrict ourselves to the mean velocity maps.

The kinematic moments (moments of LOSVD) of triaxial galaxies in a stationary configuration have different parity, e.g., mean velocity is odd, while the second moment  $\langle v^2 \rangle$ , is even. The parity of a moment generates certain symmetries of the kinematics maps. More generally, the maps of odd moments are *point – anti – symmetric*,

or:

$$V(r, \theta + \pi) = -V(r, \theta). \quad (2)$$

If axisymmetry is assumed, in addition to the previous relation, maps are *mirror – anti – symmetric*, or:

$$V(r, \pi - \theta) = -V(r, \theta). \quad (3)$$

These symmetry conditions translate into the requirement on the harmonic expansion (eq. 1) that for point-anti-symmetric maps the even coefficients in the expansion are equal to zero, while in the case of mirror-anti-symmetry, additionally, the odd phase angles have a constant value, equal to the photometric position angle (PA) of the galaxy in the case of a true axisymmetric galaxy. This means that to reconstruct the mean velocity map of a stationary triaxial galaxy, it is sufficient to use only odd terms in the expansion.

These properties of the velocity maps enable certain natural filtering (point-(anti)-symmetric - eq. (2), and mirror-(anti)-symmetric - eq. (3)) using the harmonic expansion with coefficients set to zero or phase angles fixed at certain values. For (visual) comparisons of the data with the results of axisymmetric modelling it is useful to apply the axisymmetric filtering to the data, as we will see below (Section 6).

### 3.2 Kinematic analysis of velocity maps

We wish to know the intrinsic shape of NGC 2974 and, in particular, whether it is consistent with axisymmetry, which would permit the construction of three-integral axisymmetric dynamical models of the galaxy. In order to obtain the necessary information we applied the kinematic expansion to the observed stellar velocity map. If NGC 2974 is an axisymmetric galaxy, the kinematic terms should have odd parity (even terms should be zero) and the kinematic position angle should be constant and equal to the PA.

The amplitude and phases of the first five terms in the expansion are presented in Fig. 4. The first panel presents the dominant term in the expansion,  $c_1$ , which gives the general shape and amplitude of the stellar velocity map. The correction to this term is given by the next significant term,  $c_3$ , which is already much smaller than  $c_1$  and is presented in the second panel as a fraction of  $c_1$ . Even terms in the expansion,  $c_2$  and  $c_4$ , are also plotted on the same panel, and are much smaller ( $\sim 1\%$  of  $c_1$ )<sup>1</sup>. For comparison, the fifth term in the expansion,  $c_5$ , is also plotted and is larger than both  $c_2$  and  $c_4$ . The SAURON pixel size is  $\sim 1''$  and measurement of higher-order terms at radii smaller than  $2''$  cannot be trusted. Clearly, the velocity map in NGC 2974 can be represented by the first two odd terms in the expansion. Neglecting all higher terms results at most in a few percent error.

The lower two panels in Fig. 4 present the phases of the dominant terms. The  $\phi_1$  phase is defined as the kinematic angle of the velocity map, here measured east of north. This angle is compared with measurements of two important angles: (i) the PA measured on the WFPC2/PC F814W dust-corrected image using the IRAF ellipse fitting task `ellipse` and (ii) the PA measured on the reconstructed SAURON flux image

<sup>1</sup>The zeroth term,  $a_0$ , gives the systemic velocity of the galaxy and is not important for this analysis.

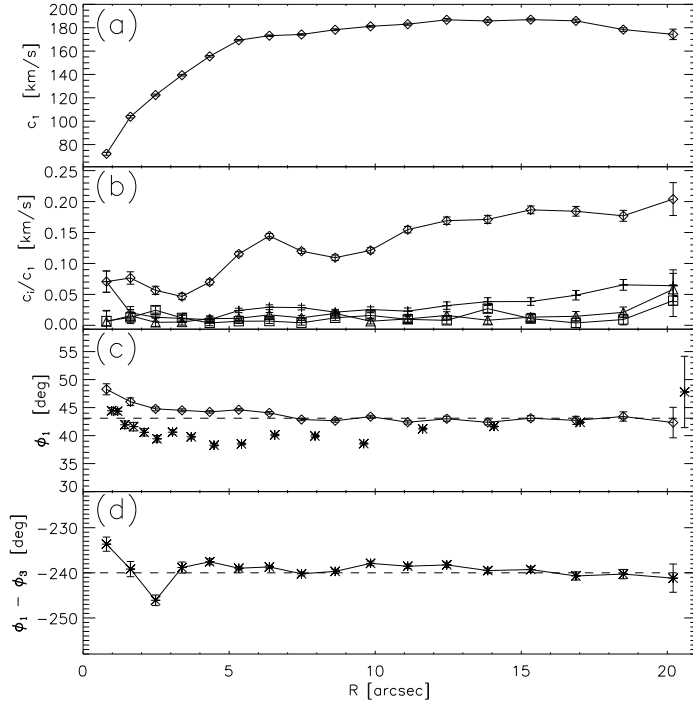


**Figure 4** — Kinematic expansion of the stellar velocity field as a function of radius. From top to bottom: (a) first amplitude coefficient in the harmonic expansion  $c_1$ ; (b) ratios of amplitude coefficients presented by: triangles  $c_2/c_1$ , diamonds  $c_3/c_1$ , squares  $c_4/c_1$  and pluses  $c_5/c_1$ ; (c) important position angles: phase angle  $\phi_1$  representing the kinematic position angle (diamonds), photometric position angle as measured on WFPC2/PC1 F814W image (asterisks) and adapted value for photometric position angle measured from the integrated SAURON flux image (dashed straight line); (d) difference between the first and third phase from the kinematic expansion.

obtained by integrating the spectra in each bin. The agreement between the different angles measured on the SAURON observations is excellent, with slight departures in the inner  $3''$ . The PA measured on the high resolution WFPC2 image suggests a small photometric twist in the inner  $10''$  of  $\approx 3^\circ$ , which can be also seen in Fig. 9.

The phase angle  $\phi_3$  is the phase of the third term in the kinematic extraction. It is easy to show, if the galaxy is axisymmetric (requiring in eq. 1,  $K(r, \theta) = 0$  for  $\theta = \phi_1 + \pi/2$ ), and the higher terms can be neglected, that the phases  $\phi_1$  and  $\phi_3$  satisfy the relation:

$$\phi_1 - \phi_3 = \frac{n\pi}{3} \quad (4)$$

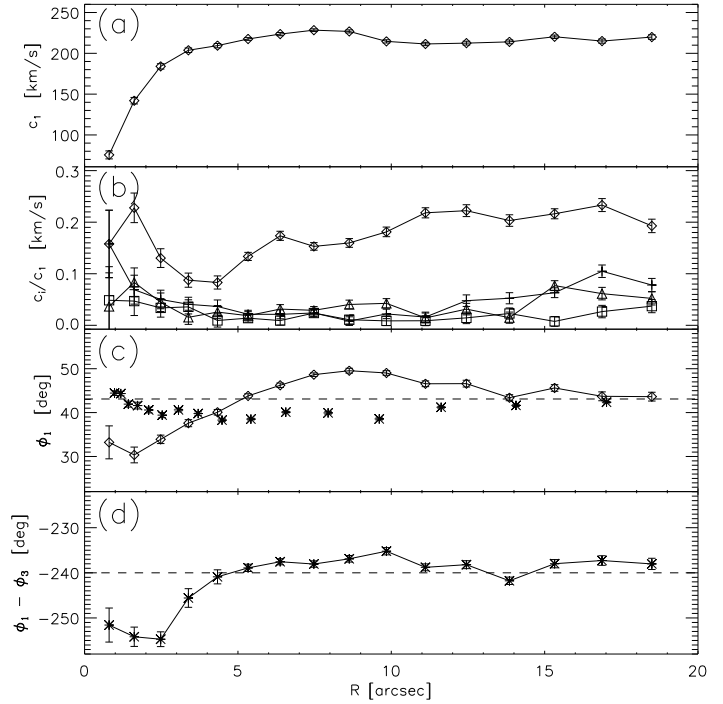
where  $n \in \mathbb{Z}$ . The last panel in Fig. 4 shows this phase difference. The condition given by eq.( 4) is satisfied along the entire investigated range with a small deviation in the inner  $3''$ . Summarising all the above evidence, we conclude that the observed stellar kinematics in NGC 2974 is consistent with axisymmetry.

We repeated the kinematic analysis<sup>2</sup> on the emission-line gas velocity maps and present the results in Fig. 5. While the amplitude coefficients,  $c_i$ , are similar to the stellar coefficients (small values of all terms higher than  $c_3$ ), the behaviour of the phase angles is quite different.

The last panel of Fig. 5 is perhaps the best diagnostic tool. The dashed line presents the required value for the difference between the phase angles,  $\phi_1 - \phi_3$ , assuming axisymmetry. Deviations are present in the inner  $4''$  and, although much smaller, between  $9''$  and  $11''$ . These deviations indicate departures from axisymmetry, which are

<sup>2</sup>A similar analysis approach for a gas disc would be using the Schoenmakers et al. (1997) harmonic analysis on a tilted-ring model of the gas disc, interpreting the results within epicycle theory (see also Wong et al. 2004).

**Figure 5** — Same as Fig 4, but for the gas velocity map.



strongest in the central few arcsecs.

### 3.3 Signature of bars in NGC 2974

In previous section, we quantified the signatures of non-axisymmetry on the gas velocity maps, especially strong in the inner 4". Inside this radius, EGF03 discovered a two-armed spiral and explained it by a weak bar with the corotation resonance (CR) at 4".9 and outer-Lindblad resonance (OLR) at 8".5. These scales are consistent with the observed departures from axisymmetry in our SAURON maps. Assuming that the emission-line velocity field is generated by gas in a disc, the change in the phase difference and the crossing of the "axisymmetric" value can be interpreted as evidence of the influence of the bar-potential, where the streaming of the gas changes direction as one crosses the corotation radius.

As mentioned above, the distribution of the [OIII] emission-line intensity (Fig. 1) exhibits an elongated structure in the central 5". Similarly, around 8" – 10" [OIII] is also elongated, but this time approximately perpendicular to the first elongated structure. Following this, the [OIII] map has a plateau between 12" and 15". The end of the plateau is followed by a dip in the [OIII] distribution with a possible turn up at radii larger than 20".

Although the central structure and kinematics of the [OIII] distribution are influenced by the inner bar, the large-scale structure (beyond  $\approx 10''$ ) is not likely to be influenced by this weak inner bar. On a more speculative basis, we can infer the existence of a large-scale bar. The primary (large-scale) bar should be 5 to 10 times bigger than the secondary (inner) bar (Erwin & Sparke 2002, 2003), therefore, between  $\approx 12''.5$  and 25".

A more precise, although still approximate, estimate of the properties of the pri-

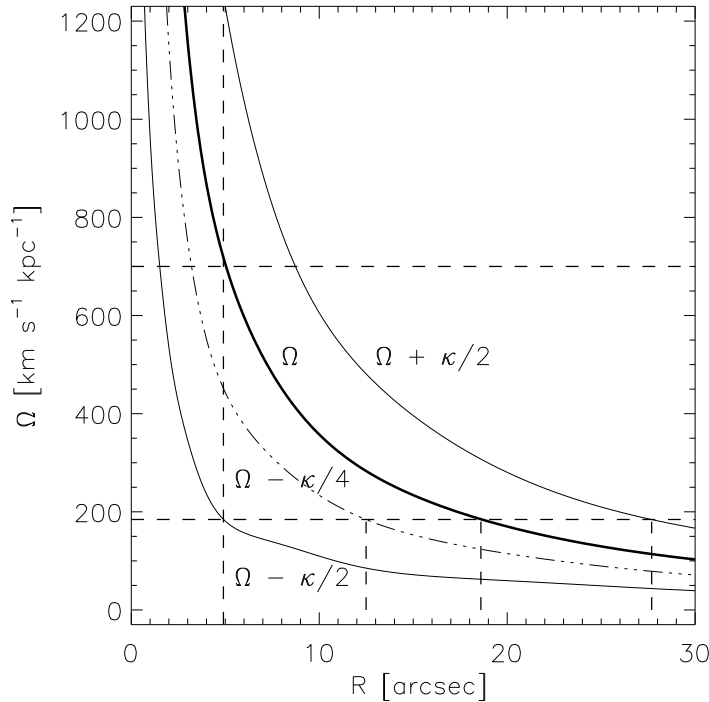


**Figure 6** — Diagram of resonances in NGC 2974, derived from the potential of the best-fitting stellar dynamical model. The upper horizontal line is the pattern speed of the nuclear (secondary) bar from EGF03 study ( $\Omega_p^s = 700 \text{ km s}^{-1} \text{ kpc}^{-1}$ ). The lower horizontal line shows the position of the inferred pattern speed of the large-scale primary bar ( $\Omega_p^p = 700 \text{ km s}^{-1} \text{ kpc}^{-1}$ ). The vertical lines show the assumed radial positions of important resonances of the primary bar. From left to right: ILR (CR of the secondary bar), UHR, CR and OLR.

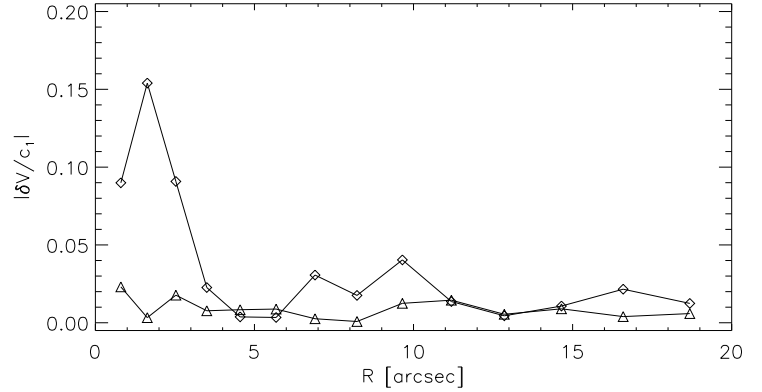
primary bar can be obtained from the resonance curves of NGC 2974. Using the potential of the best-fitting stellar dynamical model (see Section 4) we constructed the resonance diagram presented in Fig. 6. We calculated profiles of  $\Omega$ ,  $\Omega - \kappa/2$ ,  $\Omega + \kappa/2$  and  $\Omega - \kappa/4$ , where  $\Omega$  is the angular velocity,  $V/r$ , and  $\kappa$  is epicyclic frequency, defined as  $\kappa^2 = r \frac{d\Omega^2}{dr} + 4\Omega^2$ . Assuming that the resonances of the primary and the secondary bar are coupled to minimise the chaos produced around the resonances (Friedli & Martinet 1993; Pfenniger & Norman 1990), where the inner Lindblad resonance (ILR) of the primary bar is the CR of the secondary bar, we can estimate the main resonances of the primary bar (indicated by the vertical lines on Fig. 6). The pattern speed of the primary component is then  $\approx 185 \text{ km s}^{-1} \text{ kpc}^{-1}$ , ILR is at  $4''.9$ , ultra harmonic resonance (UHR) at  $\approx 12''.5$ , CR at  $\approx 18''.6$  and OLR at  $\approx 27''.7$ . The size of the primary bar can be taken to be 80% of its CR, so about  $13''$  to  $14''$ .

These size estimates are only approximate, but indicative, since the presented analysis is strictly valid only for an axisymmetric potential with an infinitesimal bar perturbation. We see several features in the [OIII] distribution and velocity maps that support the assumption of a large-scale primary bar: the dip in the gas velocity map around  $12''$ , the plateau between  $12''$  and  $15''$  in [OIII] distribution as well as the dip in the [OIII] distribution around  $18''$ . The last one corresponds to the position of the CR, which is a chaotic region devoid of gas, consistent with the observed lower flux in that region.

### 3.4 Case for axisymmetry in NGC 2974

The alignment of the gaseous and stellar component, previously detected and also confirmed in this study, suggests that NGC 2974 is an axisymmetric galaxy. However, the gaseous component shows signatures of non-axisymmetric perturbations. The contri-

**Figure 7** — Contribution of the non-axisymmetric motion to the stellar and gaseous velocity fields, as a fraction of the dominant term in the kinematic expansion,  $c_1$ . Diamonds present the emission-line gas velocity contribution, while triangles present the stellar velocity contribution.



bution of the non-axisymmetric motion,  $\Delta V/c_1$  (see Chapter 4 for details), to the total velocity field can be quantified from the phase difference  $\phi_3 - \phi_1$ . If the condition in eq. (4) is not satisfied then:

$$\frac{\Delta V}{c_1} = \frac{c_3}{c_1} \sin 3(\phi_1 - \phi_3), \quad (5)$$

which is presented in Fig. 7 for both stellar and gaseous velocity maps. At  $\sim 3''$ ,  $\Delta V/c_1$  for the emission-line gas is  $\approx 0.1$  and at  $\sim 10''$  it is  $\approx 0.04$ , confirming that the non-axisymmetric contribution is significant in the centre of the emission-line velocity map. Its influence on the stellar velocity is not significant over the SAURON field. Emission-line gas is a more responsive medium and unlike the stars, due to the viscosity of the gas particles, shows evidence of weak non-axisymmetric perturbations. It is possible that other early-type galaxies with disc-like components harbour such weak and hidden bar systems.

Summarising, the stellar velocity map is mirror-anti-symmetric, supporting an axisymmetric shape for NGC 2974. On the other hand, the gaseous velocity map shows strong deviations from mirror-anti-symmetry in the centre and the distribution of [OIII] emission lines supports the weak inner bar found by EGF03 and suggests the existence of a weak large-scale bar. However, since the bar perturbations on the axisymmetric potential are weak and do not influence the stellar kinematics, we ignore them in the remainder of the paper, and describe NGC 2974 with an axisymmetric potential.

## 4 Stellar Dynamical Modelling

In order to investigate the orbital structure of NGC 2974 we construct fully general axisymmetric models of the galaxy's stellar component. The three-integral models presented here are based on Schwarzschild's orbit superposition method (Schwarzschild 1979, 1982), further developed by Rix et al. (1997), van der Marel et al. (1998) and Cretton et al. (1999), and adapted for more general surface-brightness distributions by Cappellari et al. (2002, hereafter C02) and Verolme et al. (2002, hereafter V02), similarly as in Cretton & van den Bosch (1999). The three-integral modelling technique is widely used for constructing dynamical models of axisymmetric galaxies, and has been thoroughly described in the literature by the aforementioned authors as well as by other groups (e.g. Gebhardt et al. 2003; Valluri et al. 2004). It is most commonly used to determine the masses of the central black holes in nearby galaxies and investigate the

j	$G_j$	$\sigma_k$ (arcsec)
1	0.352	0.024
2	0.531	0.072
3	0.082	0.365
4	0.035	0.908

**Table 4** — The MGE parameters of the circular PSF of HST/WFPC2/F814W filter.

j	$I_j (L_\odot pc^{-2})$	$\sigma_j$ (arcsec)	$q_j$	$L_j (\times 10^9 L_\odot)$
1	190297.	0.0378596	0.580000	0.0108
2	44170.6	0.0945030	0.800000	0.0215
3	24330.8	0.185143	0.800000	0.0455
4	27496.3	0.340087	0.583279	0.1264
5	23040.6	0.591227	0.720063	0.3952
6	10299.6	1.15500	0.777448	0.7279
7	5116.29	3.41758	0.658664	2.6820
8	1902.25	8.67562	0.597636	5.8305
9	388.278	17.5245	0.677645	5.5060
10	139.447	43.9864	0.580000	10.663
11	16.9405	82.9488	0.800000	6.3538

**Table 5** — The parameters of the MGE model of the deconvolved I-band WFPC2 surface brightness of NGC 2974. Columns present (from left to right): number of the two-dimensional Gaussian, central intensity of the Gaussian, width (sigma) of the Gaussian, axial ratio of the Gaussian, total intensity contained in the Gaussian.

internal orbital structure of the galaxies. The SAURON observations of NGC 2974 do not have the necessary resolution to probe the sphere of influence of the central black hole and we therefore restrict ourselves to the determination of the mass-to-light ratio  $\Upsilon$  and the inclination  $i$  of the galaxy, as well as the internal orbital structure.

#### 4.1 The Multi-Gaussian Expansion mass model

The starting point of the stellar dynamical modelling is the determination of the gravitational potential of the galaxy. The potential can be obtained by solving the Poisson equation for a given density distribution which can be derived by deprojecting the observations of the 2D stellar surface density. In this work we used the multi-Gaussian expansion (MGE) method (Emsellem et al. 1994), following the approach of C02 and V02.

In order to get the MGE model, we simultaneously fitted the ground-based I-band image and the dust-corrected PC part of the WFPC2/F814W image using the method and software developed by Cappellari (2002). The dust correction (Section 2.4) successfully removed the dust contamination from the high-resolution image of the nucleus, but the large-scale image was badly polluted by several stars, with a particularly bright one almost on the galaxy's major axis. We masked all stars inside the model area to exclude them from the fit. The ground-based image, used to constrain the fit outside  $25''$ , was scaled to the WFPC2/PC1 image. We computed the PSF of the F814W PC1 image at the position of the nucleus of NGC 2974, using TinyTim software (Krist & Hook 2001), and parametrised it by fitting a circular MGE model with constant position angle as in C02. Table 4 presents the relative weights  $G_j$  (normalised such that

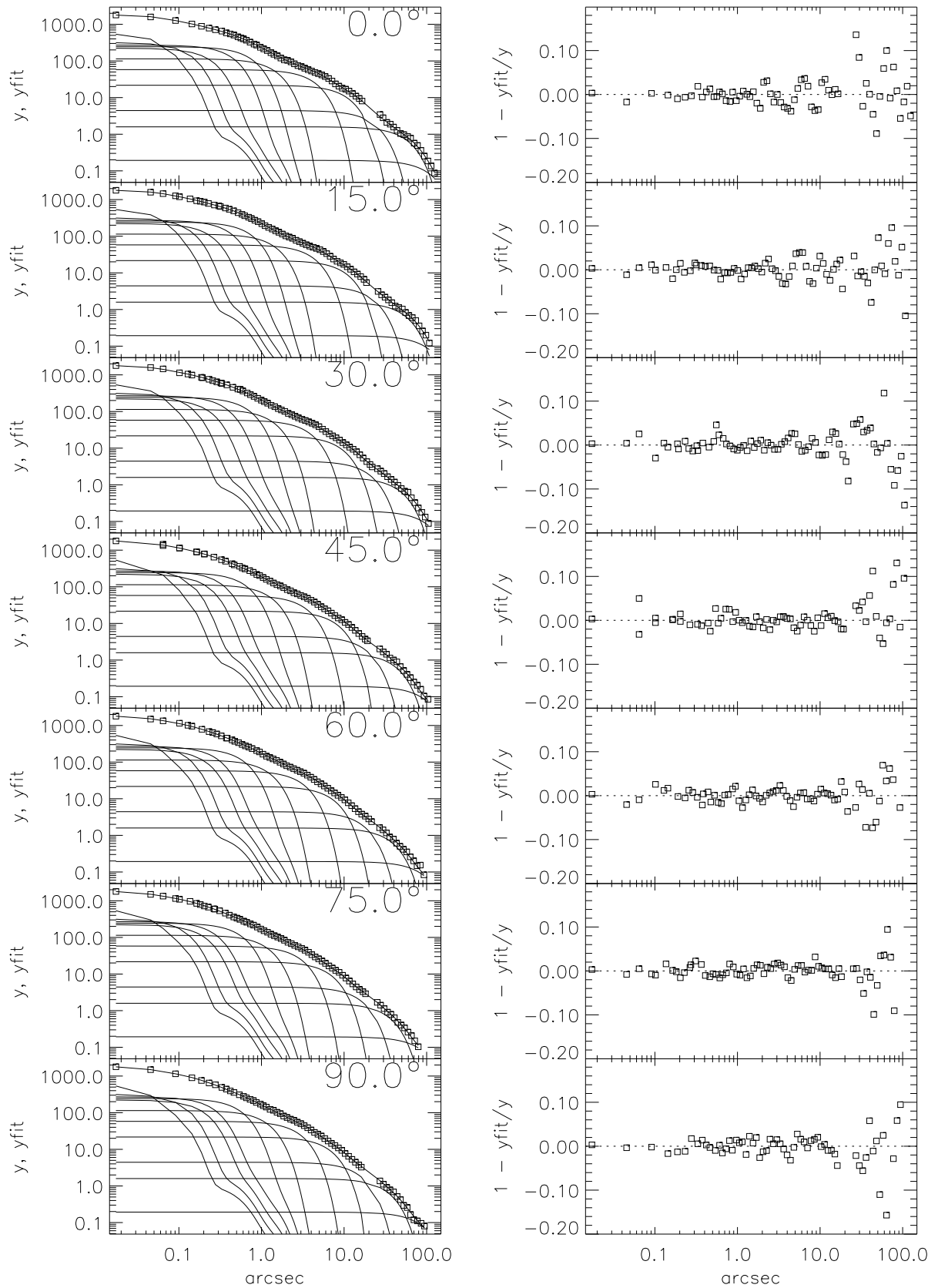


**Figure 8** — *Left Panels:* Comparison between the combined WFC2/F814W and ground-based photometry of NGC 2974 (open squares) and the MGE model (solid line) in seven angular sectors as function of radius. The individual convolved Gaussian are also shown. *Right panels:* radial variation of the relative error along the profiles.

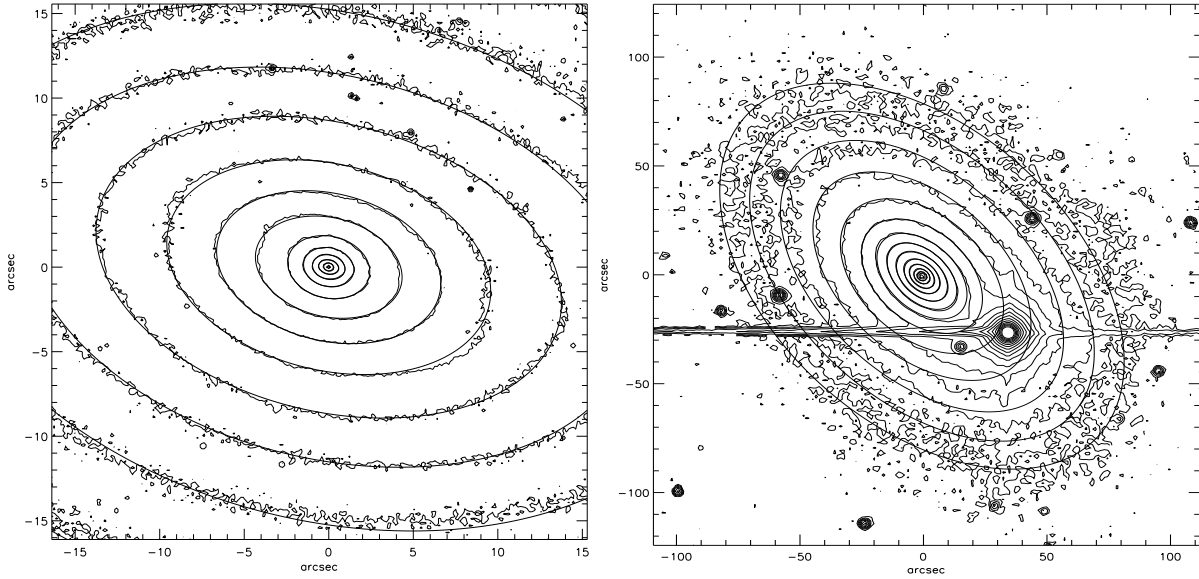
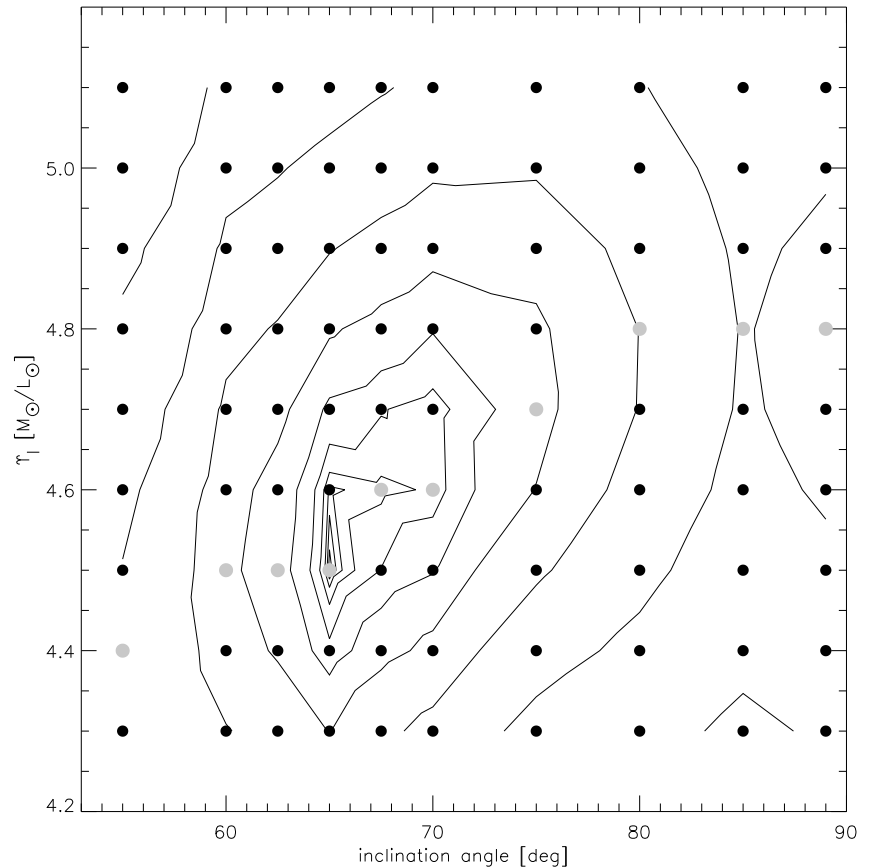


**Figure 9** — Contour maps of the ground-based I-band and dust corrected WFC2/F814W images. The brightest star on the ground-based image as well as four additional stars covered by the model were masked out and excluded from the fit. Superposed on the two plots are the contours of the MGE surface brightness model, convolved with the WFC2 PSF.

their sum is equal to unity) and the corresponding dispersions  $\sigma$  of the four Gaussians. Table 5 gives the parameters of the MGE model analytically deconvolved from the PSF. Following the prescription of Cappellari (2002), we increased the minimum axial ratio of the Gaussians,  $q_j$ , until the  $\chi^2$  significantly changed, in order to make as large as possible the range of allowed inclinations by the MGE model. The upper limit to the  $q_j$  was also constrained such that the MGE model is as close as possible to a density stratified on similar ellipsoids. Although the deprojection of an axisymmetric density distribution is non-unique (Rybicki 1987), our ‘regularisation’ on the MGE model produce realistic intrinsic densities, while preventing sharp variations, unless they are required to fit the surface brightness. We verified that the MGE model used in this study is consistent with the MGE model presented in EGF03.

The comparison between the MGE model and the photometry along different angular sectors is shown in Fig. 8. The profiles are reproduced to within 3%, and the RMS error is about 2%. The fluctuation of the relative error (right-hand panel in Fig. 8) at larger radii is caused by the light pollution of the bright star on the major axis of the galaxy and can be better understood by looking at the comparison of the convolved model and the actual observation. Fig. 9 presents both ground- and space-based images and the MGE model. On the WFC2/PC image there is a slight deviation from the model (of constant PA) about  $10''$  from the nucleus. The deviating structure is point-symmetric and reminiscent of a spiral perturbation, as suggested by other studies (Bregman et al. 1992; Buson et al. 1993; EGF03). Except for this slight departure from the model the galaxy surface brightness is well represented by the MGE model and we use it to calculate the representative gravitational potential.

**Figure 10** — A grid of inclination angle versus  $M/L$  ratio. Contours present constant  $\Delta\chi^2$ , measuring the goodness of fit of the dynamical models. Every symbol corresponds to a three-integral axisymmetric model with given inclination angle,  $i$ , and  $\Upsilon$  ratio. The best-fitting model for each inclinations are presented with grey symbols. The first three contours show the formal 68.3%, 95.4% and 99.73% (thick contour) confidence regions for two degrees of freedom. The best-fitting model on the grid is constructed for inclination of  $65^\circ$  and  $\Upsilon = 4.5 M_\odot/L_\odot$ .



## 4.2 Construction of three-integral models

Briefly, Schwarzschild's method can be divided in four steps. In the first step, one derives the stellar potential assuming the shape of the potential (axisymmetry) and stellar mass-to-light ratio,  $\Upsilon$  (free parameter), through deprojection of a parametrisation of the surface density (in this case MGE parametrisation which can be deprojected analytically). The second step involves the construction of a representative orbit library by integrating the orbits in the derived potential. Each orbit is specified by three integrals of motion  $(E, L_z, I_3)$ , where  $E$  is the energy,  $L_z$  the component of the angular momentum along the  $z$  symmetry axis, and  $I_3$  is a non-classical integral, which is not known analytically. The integral space is constructed on a grid that includes  $>99\%$  of the total luminous mass of the galaxy. The next step consists of projecting the orbits onto the space of observables  $(x', y', v_{los})$ , where  $(x', y')$  are in the plane of the sky and  $v_{los}$  is the line-of-sight velocity given by the observations. In our implementation, this is done taking into account the PSF convolution and aperture binning. The final step of the method is to determine the set of weights for each orbit that, when added together, best corresponds to the observed kinematics in the given spatial bin as well as reproducing the stellar density. In our implementation of the method, this best-fitting set is found by solving a nonnegative least-squares (NNLS) problem using the routine written by Lawson & Hanson (1974).

The software implementation used here is similar to that used in the V02 and C02 studies, but it has evolved substantially since. The improvements are described in

detail in Cappellari et al. (in prep.). We verified that the results from the new code are the same as from the old one if identical settings are adopted. An application to the elliptical galaxy NGC 4473 was presented in Cappellari et al. (2004). Here we give a quick overview of the changes with respect to the description in C02:

1. The method requires that the orbits sample a three-dimensional space of integrals of motion, the energy  $E$ ,  $L_z$  and  $I_3$ . In the new scheme (see Cretton et al. 1999 for details of the previous approach), at each  $E$ , we construct a polar grid of initial starting positions on the meridional plane (linear in angle and in radius), going from  $R = z = 0$  to the curve defined by the thin tube orbits (to avoid duplication) which is well approximated by the equation  $R^2 + z^2 = R_c^2(E)$ , where  $R_c(E)$  is the radius of the circular orbit at energy  $E$ . The orbits are released with  $v_R = v_z = 0$  and  $L_z \neq 0$ . In this way we sample the observable space by uniformly distributing the position of the orbital cusps (see Cappellari et al. 2004) on the sky plane.
2. Improved treatment of seeing effects and instrumental point spread function (PSF) by a Monte Carlo method. The PSF can be considered as the probability that an observed photon arriving at a detector will be displaced from its original position by a given amount (specified by the PSF characteristics). The projected orbital points (results of the orbit integration and projection onto the sky-plane) are stored in the apertures in which they landed after applying a random displacement taken from the Gaussian probability distribution defined by the PSF.
3. Generalisation of the projection of the orbits into the space of the observables. The bins of the optimal Voronoi binning of the two-dimensional integral-field data have non-rectangular shapes. The orbital observables now can be stored on apertures of any shape that can be represented by polygons.

### 4.3 Stellar dynamics - modelling results and discussion

Our stellar kinematic maps of NGC 2974 consist of 708 Voronoi bins. Each bin contributes with 6 kinematic observables to which we also add the intrinsic and projected mass density observables, resulting in a grand total of 5664 observables. The largest orbit library that was computationally possible for the given number of observables, consists of  $2 \times 41 \times 10 \times 10 = 8200$  orbits (for each of the 41 different  $E$  we construct a polar grid of starting points sampling 10 angles and 10 radii). With this choice of orbit library, the number of observables is smaller than the number of orbits, and the NNLS fit will not have a formally unique solution. Moreover the recovery of the orbital weights for the orbits from the observations is an inverse problem, and as such is intrinsically ill-conditioned. For these reasons a direct solution of the problem generally consists exclusively of sharp isolated peaks. It is unlikely for the DF of real galaxies to be very jagged, since (violent) relaxation processes tend to smooth the DF. Moreover observational constraints on the smoothness of the DF, at least for the bulk of the stars in a galaxy, come from the smoothness of the observed surface brightness, down to the smallest spatial scales sampled by HST.

A standard mathematical approach to solve inverse problems is by regularising (e.g. Press et al. 1992, Chapter 18). This has been generally applied by all groups involved in this modelling approach (e.g. Rix et al. 1997; Gebhardt et al. 2003; Valluri et al. 2004; Cretton & Emsellem 2004). Regularisation inevitably biases the solution, by forc-

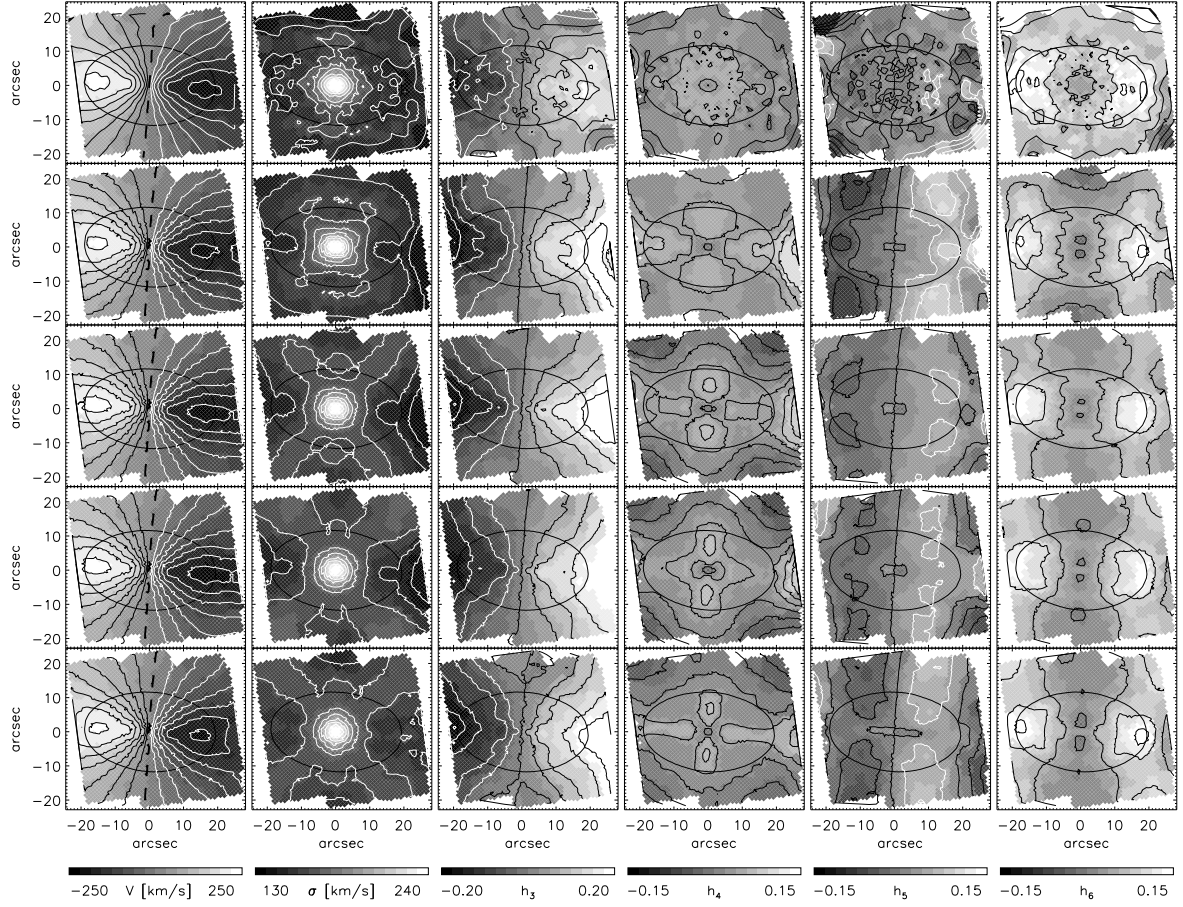


**Figure 11** — Comparison of the symmetrised observation of NGC 2974 (first row) and four orbital superposition models with best mass-to-light ratio  $Y$ , for a given inclination  $i$ . From second row to bottom:  $(i, Y) = (55, 4.4)$ ,  $(65, 4.5)$ ,  $(75, 4.7)$ ,  $(89, 4.8)$ . From left to right each panel presents: mean velocity  $V$ , velocity dispersion  $\sigma$ , and Gauss-Hermite moments:  $h_3, h_4, h_5$  and  $h_6$ . Isophotal contours of total light are shown with elliptical solid lines. The overplotted kinematic contours were obtained by interpolation between the bin generators and extrapolation to the edge of the maps.

ing most orbits to have a non-zero weight. The key here is to apply the right amount of regularisation. Previous tests with the Schwarzschild code suggested a value of the regularisation parameter  $\Delta = 4$  (see Cretton et al. 1999; V02). After initial testing we also adopted this value. For more details on regularisation, see McDermid et al. (in prep.).

The models are axisymmetric by construction. In order to avoid possible systematic effects we additionally symmetrise the stellar kinematics as usually done in other studies. The symmetrisation uses the mirror-(anti)-symmetry of the kinematic fields, such that kinematic values from four symmetric positions  $((x, y), (x, -y), (-x, y), (-x, -y))$  were averaged. However, the Voronoi bins have irregular shapes and they are not equally distributed with respect to the symmetry axes of the galaxy (minor and major axes). In practice, we average the four symmetric points, and, if for a given bin there are no bins on the symmetric positions, we interpolate the values on those positions

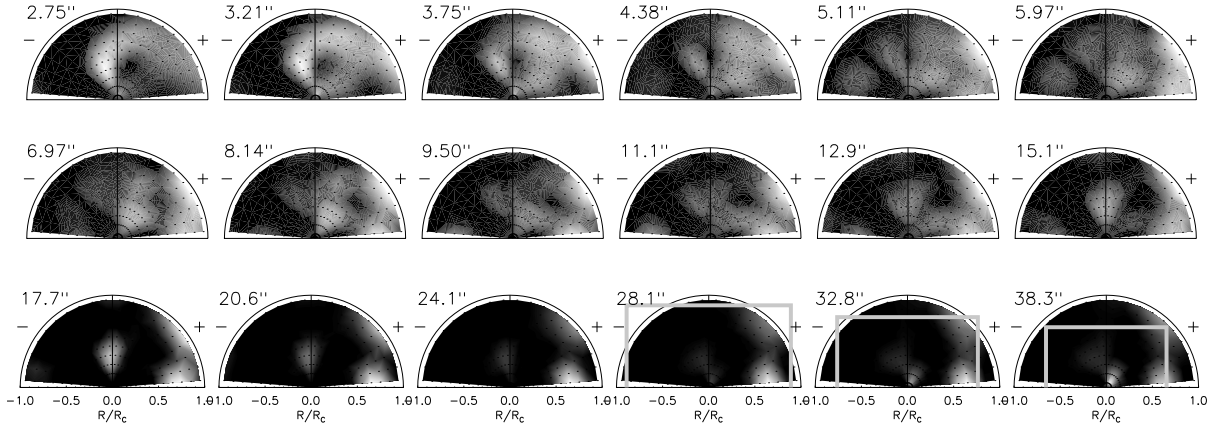


**Figure 12** — Integral space of the best fitting orbit superposition model for NGC 2974. Each panel plots the meridional plane ( $R, z$ ) with the starting positions of orbits (dots) for the given energy. Orbital starting positions correspond to the position of cusps ( $v_R = v_z = 0$ ). Overplotted is the fraction of mass assigned to orbits at constant energy, labelled by the radius of the circular orbit in arcseconds (printed at the upper left corner of each panel). The radius of the circular orbit is the size of the horizontal axis (measured from the centre). Negative values are obtained by sign reversal, since orbits can be prograde and retrograde. Orbits with high angular momentum are found in the right and left corner respectively on the plots. We show only the radii constrained by the data. The last three panels have the size of the SAURON field overplotted for comparison (grey rectangle). The area inside the rectangle is constrained by the kinematic data. Brighter colour correspond to higher mass weights.

and then average them.

Finally, we fitted axisymmetric dynamical models to symmetrised observations of velocity, velocity dispersion and Gauss-Hermite moments ( $h_3 - h_6$ ) while varying the mass-to-light ratio  $\Upsilon$  and the inclination  $i$ . Figure 10 shows a grid of our models with overplotted  $\Delta\chi^2$  contours. The best-fit parameters are  $\Upsilon = 4.5 \pm 0.1$  (in the  $I$  band) and  $i = 65^\circ \pm 2.5^\circ$ . The data – model comparison for these values is given in Fig. 11 (symmetrised data are shown in the first row and the best-fitting model in the third row). In the same figure we present the best-fitting models for the given inclinations. The formal statistical analysis firmly rules out (with  $3\sigma$  confidence) all inclinations outside  $i = 65^\circ \pm 2.5^\circ$ . The differences between the models are only marginally visible on Fig. 11. However, comparing the models with the top row of symmetrised data, it is noticeable that the velocity dispersion is less well fitted with increasing inclination. On the other hand, the fit to  $h_3$  improves with higher inclinations. Higher-order moments change similarly and the final  $\chi^2$  is the result of this combined effect. Surprisingly, the difference between the best-fit model and the data are bigger than the difference between the other models and the best-fit model, provoking a question whether the determination of the inclination is robust.

Recently, EGF03 used two-integral  $f(E, L_z)$  dynamical models and found a best fit for an inclination  $60^\circ$  but also stated that models with  $58^\circ \leq i \leq 65^\circ$  fit equally well. Our three-integral models have a larger freedom in fitting the observations and it is unknown whether these models can uniquely constrain the inclination. Our obtained inclination is close to the previous measurements in the literature (references in Sections 1 and 2), and also to the inclination measured from gas and dust. NGC 2974 is

perhaps a special case (in terms of its intrinsic structure and geometry) for which three-integral models are able to give a stronger constraint on the inclination. We return to this issue in Section 5.2.

The integral space of the best-fitting model, (i.e. the space defined by the isolating integrals of motion  $(E, L_z, I_3)$  that define the orbits and the DF  $f = f(E, L_z, I_3)$ ), is shown in Fig. 12. Each panel presents mass assigned to orbits of constant energy, parameterised by the radius of the circular orbit. This orbit also has the maximum angular momentum and circular orbits of negative and positive angular momentum are in the bottom left and right corner of each plot, while the low angular momentum orbits are close to the symmetry ( $y$ ) axis. An interesting feature appears on the panels for radii between  $5''.97$  and  $17''.7$ . A high fraction of mass is assigned to orbits with high angular momentum. This indicates that the bulk of the stars rotate with high angular momentum. A possible physical interpretation is that a large fraction of the stars orbit in a disc. Cinzano & van der Marel (1994) argued that NGC 2974 has an embedded stellar disc and in their two-integral Jeans models they were not able to fit the stellar kinematics without introducing a disc with  $\approx 7\%$  of the total galaxy light. On the other hand, the two-integral models of EGF03 did not need to invoke a stellar disc component to fit data consisting of their TIGER data and the three long slits of Cinzano & van der Marel (1994). The integral space presented here suggests that the three-integral models need orbits with high angular momentum, but the selected orbits also have different values of  $I_3$ , and therefore do not represent a very thin stellar disc as assumed by Cinzano & van der Marel (1994), but a somewhat flattened distribution of stars like in a normal S0. The relative light contribution of the high-angular momentum orbits is  $\approx 10\%$ , which corresponds to a total stellar mass of  $1.5 \times 10^{10} M_\odot$  assuming the best-fit model inclination and  $Y$ .

## 5 Tests of Schwarzschild's orbit-superposition models

In the previous section we used three-integral models to recover the inclination, mass-to-light ratio and the internal structure of NGC 2974. Surprisingly, we find that the inclination is tightly constrained by  $\chi^2$  contours (Fig. 10), although the difference between the models (Fig. 11) are smaller than the difference between formally the best-fitting model and the data. In this section, we wish to test the robustness of those results as well as the general ability of the three-integral models to recover the given parameters. For this purpose we constructed an axisymmetric model mimicking NGC 2974 using two integrals of motion: the energy  $E$ , and the  $z$ -component of the angular momentum,  $L_z$ . This two-integral galaxy model has the advantage of a known DF,  $f = f(E, L_z)$ , everywhere, which we want to compare with the results of the three-integral modelling. There are three issues we wish to test:

1. Recovery of the input parameters of the two-integral model galaxy. This is a general test to show whether the three-integral method can recover the parameters used in construction of a test model. We wish to be consistent with the observations and consider only the recovery of the input mass-to-light ratio and inclination, especially in light of the results from the Section 4.
2. Influence of the spatial coverage. The SAURON kinematic observations of NGC

	2I model (1)	Full field (2)	SAURON field (3)
$\Upsilon$	4.6	$4.6 \pm 0.1$	$4.4 \pm 0.1$
$i$	$60^\circ$	$60^\circ \pm 5^\circ$	$65^\circ \pm 5^\circ$

**Table 6** — The properties of two-integral models and comparison to three-integral best-fit results. Col.(1): parameters of the two-integral model of NGC 2974; Col.(2): recovered parameters using the *Full field* spatial coverage ( $100'' \times 100''$  effectively) of kinematic constraints; Col.(3): recovered parameters using the *SAURON field* spatial coverage ( $40'' \times 40''$  effectively) of kinematic constraints.

2974 roughly cover one effective radius. This is also the typical size of most kinematic observations of other early-type galaxies from the SAURON sample. Here we want to test the influence of the limited extent of the kinematic coverage on the recovery of the orbital distribution. We do this by comparing the difference between models using a *limited* and a *full* spatial kinematic information provided by the two-integral galaxy model.

3. The recovery of the input DF. We wish to test the ability of our three-integral models to correctly recover the true input (two-integral) DF. Similar tests were also presented by Thomas et al. (2004) for their implementation of Schwarzschild's method. Cretton et al. (1999), Verolme & de Zeeuw (2002) and Cretton & Emsellem (2004) described similar tests using two-integral Schwarzschild models.

### 5.1 The input two-integral test model

An  $f(E, L_z)$  model of NGC 2974 was constructed using the Hunter & Qian (1993) contour integration method (hereafter HQ, see also Qian et al. 1995). We used the mass model from Section 4.1 parameterised by MGE. This approach follows in detail Emsellem et al. (1999), and, due to the properties of Gaussian functions, simplifies the numerical calculations significantly. Given the density of the system, the HQ method gives the unique even part of the DF,  $f_e = \frac{1}{2}[f(E, L_z) + f(E, -L_z)]$  (even in  $L_z$ ). The odd part can be calculated as a product of the even  $f_e$  and a prescribed function  $h = h(L/L_z)$ . The magnitude of the function  $h$  is chosen to be smaller than unity, which ensures that the final DF,  $f = f_e + f_o$ , is physical (i.e. non-negative, provided that  $f_e \gg 0$  everywhere). In practice, the odd part is chosen to fit the observed kinematics (mean streaming) by flipping the direction of orbits with respect to the symmetry axis (photometric minor axis).

The two-integral model of NGC 2974 was computed using  $i = 60^\circ$  and  $\Upsilon = 4.6$ . In order to construct a realistic DF we also included a black hole with mass  $M_{BH} = 2.5 \times 10^8 M_\odot$ , from the  $M_{BH} - \sigma$  relation. The MGE model, constructed from a finite spatial resolution HST WFPC2 image, has by construction an unrealistic flat asymptotic density profile well inside the central observed pixel ( $r \lesssim 0''.02$ ) and therefore we assumed a cusp with a power-law slope of 1.5 ( $\rho = r^{-1.5}$ ) inside that radius, following the prescription of Emsellem et al. (1999). The final two-integral DF was computed on a fine adaptive grid (i.e. more points in the region of strongly-changing DF with  $E/E_{max} < 2$ , where  $E_{max}$  is the value of the central potential of the model excluding the black hole) of  $140 \times 79$  points in  $(E, L_z)$ . A fine grid of LOSVDs was computed from this DF. These LOSVDs were used to compute the observable LOSVDs on 3721 posi-

tions, two-dimensionally covering one quadrant of the sky plane ( $50'' \times 50''$ ), accounting for the instrumental set up (size of SAURON pixels) and atmospheric seeing (which matched the observations of NGC 2974 and was used for the three-integral models in Section 4.2). The parameters of the two-integral model of NGC 2974 are listed in the first column of Table 6.

In order to mimic the real observations (as well as to reduce the number of observables in the fit) we adaptively binned the spatial apertures using the Voronoi tessellation method of Cappellari & Copin (2003) as it was done for the observations, assuming Poissonian noise. The final LOSVDs were used to calculate the kinematic moments ( $V$ ,  $\sigma$ ,  $h_3$  to  $h_6$ ) by fitting a Gauss-Hermite series (first row on Fig. 14). These values were adopted as kinematic observables for the three-integral models. From these data we selected two sets of kinematic observables:

- The first set consisted of all 513 spatial bins provided by the two-integral model. In terms of radial coverage this *Full field* set extended somewhat beyond two effective radii for NGC 2974.
- The second set had a limited spatial coverage. It was limited by the extent of the SAURON observations of NGC 2974, approximately covering one effective radius. We call this observational set of 313 bins the *SAURON field*.

## 5.2 Recovery of input parameters

Our two-integral models are axisymmetric by construction and all necessary information is given in one quadrant bounded by the symmetry axes (major and minor photometric axes). Hence, the inputs to the three-integral code covered only one quadrant of the galaxy. Although only one quadrant was used for the calculations we show all maps unfolded for presentation purposes.

The three-integral models were constructed in the same way as described in Section 4.2. For both (*Full field* and *SAURON field*) sets of kinematic data we created orbit libraries of  $2 \times 41 \times 10 \times 10$  orbits and constructed models on grids of  $(Y, i)$ . As for the real data, we used a regularisation parameter  $\Delta = 4$ . The resulting grids are presented in Fig. 13, and the best-fitting models are listed in the Table 6. The three-integral models were able to recover the true input parameters within the estimated errors, although the *SAURON field* models were less accurate.

The kinematic observables computed from the two-integral models are noiseless, without errors nor intrinsic scatter typical of real measurements. For each kinematic observable we assigned a constant error, but representative to the SAURON observations of NGC 2974:  $1\sigma$  errors for  $V$ ,  $\sigma$ ,  $h_3$ , and  $h_4 \dots h_6$  were  $4 \text{ km s}^{-1}$ ,  $7 \text{ km s}^{-1}$ ,  $0.03$  and  $0.04$  respectively.

As we wanted to test an ideal situation we computed the kinematic observables from the two-integral model without adding noise (intrinsic scatter) typical for real measurements. However, given the fact that the input model is noiseless, the  $\chi^2$  levels computed from the fit to the kinematics are meaningless. In order to have an estimate of the uncertainties in the recovery of the parameters we computed half a dozen Monte Carlo realisations of the kinematic data, introducing the intrinsic scatter to the noiseless data. For each Monte Carlo data sets we constructed a three-integral model grid like

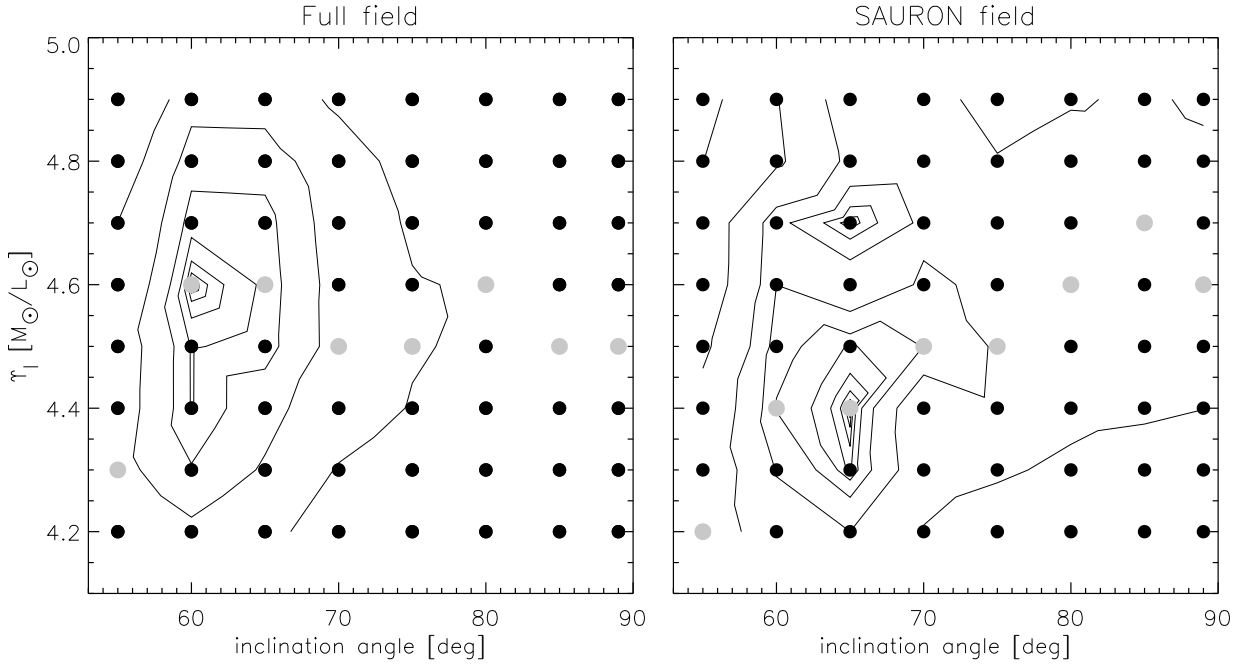


**Figure 13** — Three-integral model grids of inclination angle versus  $M/L$  ratio,  $Y$ . Contours present constant  $\Delta\chi^2$ , measuring the goodness of fit of the models. Every symbol corresponds to a three-integral axisymmetric model with given inclination angle and  $Y$ . The red symbols indicate the best fitting models at a given inclination. The top grid presents models using the *Full field* set of kinematic constraints. The global minimum is for the model with  $i = 60^\circ$  and  $Y = 4.6$ . The bottom panel presents models using the *SAURON field* set of kinematic constraints. The global minimum here is for the model with  $i = 65^\circ$  and  $Y = 4.4$ .

in Fig. 13. Due to time limitations we calculated parameter grids ( $Y, i$ ) of models with smaller orbit libraries ( $2 \times 21 \times 7 \times 7$  orbits) of both *Full field* and *SAURON field* data sets. In this case we also applied regularisation  $\Delta = 4$ . Approximate  $3\sigma$  confidence levels assigned to the best-fitting parameters are listed in Table 6. Setting the regularisation to zero, we observed similar trends.

The numbers in Table 6 suggest that the inclination is formally recovered by three-integral models, as seen in the case of the observation (Section 4.3). We repeat the exercises of plotting a sequence of models with different inclinations (using the *Full field* kinematics). They are presented in Fig. 15 and we can see a very similar trend as in Fig. 11: there appears to be little difference between the models, although by scrutinising the details, it is possible to choose the best model by eye.

The smoothness of the data of the two-integral test model helps in recognising the best-fit model. The models with lower inclination (towards face-on) are generally smoother than the higher inclination (towards edge-on) models, which systematically show radial structures. These “rays” visible on Fig. 15 are artifacts of the discreteness of our orbit library. The starting points of the orbits correspond to the positions of orbital cusps, which carry the biggest contribution to the observables. The total number of cusps is determined by the number of orbits, and the finiteness of the orbit library is reflected in the discrete contributions of the cusps to the reconstructed observables (see Fig. 1.2 of Cappellari et al. 2004). The projection effects, however, increase the smooth-

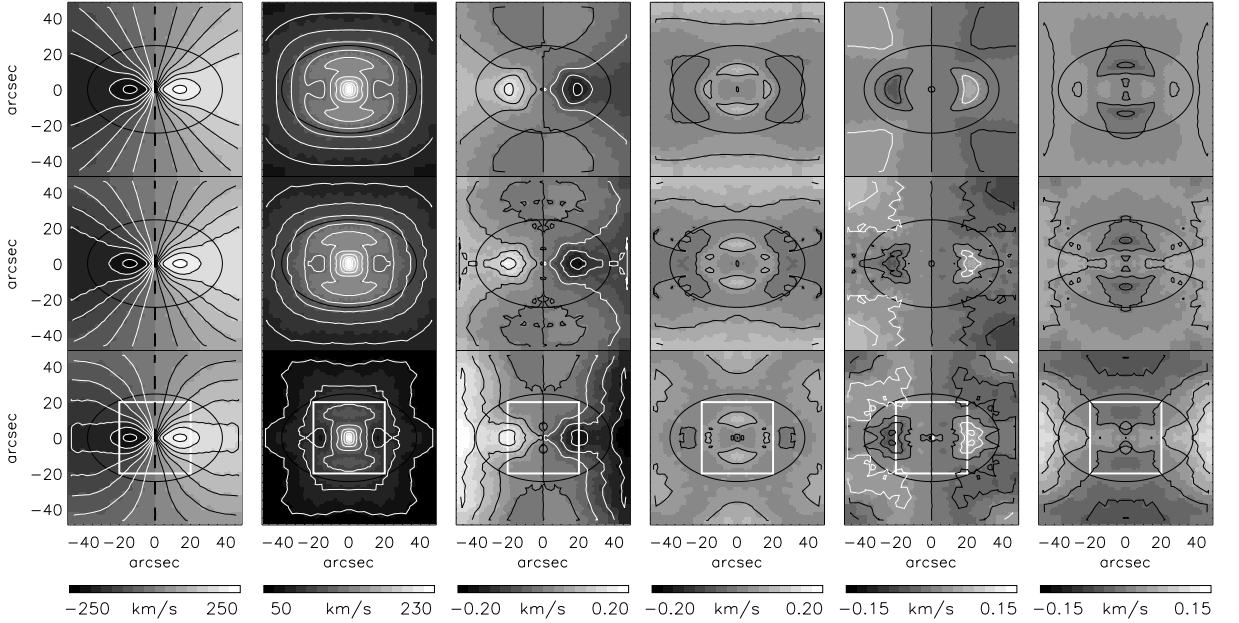


**Figure 14** — Comparison between two-integral analytical model kinematics and three-integral models. First row: two-integral model used as input to the three-integral code. Second row: best fitting three-integral model ( $i = 60^\circ, Y = 4.6$ ) using the *Full field* set of kinematic constraints. Third row: best-fitting three-integral model ( $i = 65^\circ, Y = 4.4$ ) using the *SAURON field* set of kinematics. The spatial extent of this set is marked by white squares on the maps. From left to right each panel presents: mean velocity  $V$ , velocity dispersion  $\sigma$ , and Gauss-Hermite moments:  $h_3, h_4, h_5$  and  $h_6$ . Isophotal contours of total light are shown with the elliptical solid lines.

ness by spatially overlapping different cusps; hence, models projected at e.g.  $i = 60^\circ$  will be smoother than models viewed edge on. We believe this effect could influence the  $\chi^2$ , favouring the lower inclination models.

Although present, this effect does not provide the only constraint on the inclination. When examined more closely, models with low inclination do reproduce better certain features. For example: the shape and amplitude of the velocity dispersion in the central  $20''$ ,  $h_3$  and  $h_4$  at the larger radii (towards the edge of the field), the central  $10''$  of  $h_5$  and  $h_6$ . In all cases the model with  $i = 60^\circ$  reproduces these features better than other models. Comparing the models, the most significant contribution to the  $\chi^2$  comes from the velocity dispersion, but generally, individual observables have slightly different  $\chi^2$  values, which increase with the inclination moving away from  $60^\circ$  and is visible only as a cumulative effect. This explains the similarities of the different models to the eye, although they are formally significantly different.

The difference in the model observables (which include moments up to  $h_6$ ) are below the level of the systematics in the data (e.g. template mismatch), or in the models (e.g. regularisation or variations in the sampling of observables with orbits). In the case of NGC 2974, using high signal-to-noise two-dimensional data, the difference between the models themselves are smaller than between the best-fitting model and the data, implying that the inclination is only weakly constrained. This result suggests a fundamental degeneracy for the determination of inclination with three-integral models, which is contrary to indications from previous work by Verolme et al. (2002). Theoret-

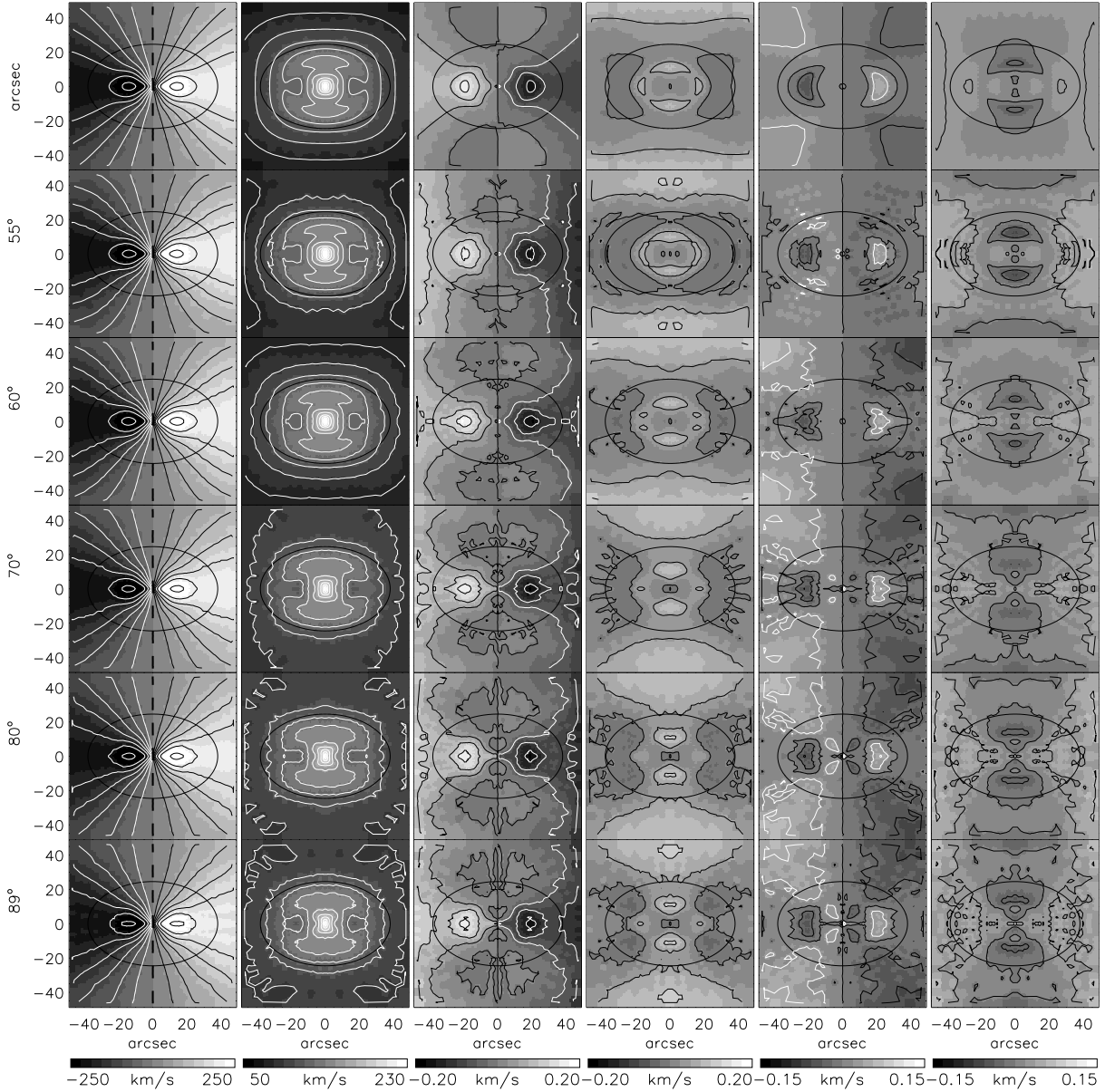


**Figure 15** — Sequence of three-integral models for different inclinations fitting the (*Full field* of kinematic observables. First row: two-integral test model. Subsequent rows: three-integral models for  $i = (55^\circ, 60^\circ, 70^\circ, 80^\circ, 89^\circ)$ . Columns from left to right present moments of the LOSVD:  $v$ ,  $\sigma$ , and from  $h_3$  to  $h_6$ . Isothermal contours of total light are shown with elliptical solid lines.

ical work and more general tests on other galaxies are needed for a better understanding of this issue.

### 5.3 Effect of the field coverage on orbital distribution

The next step is to compare in more detail the three-integral models using the two different kinematic data sets. The kinematic structures of the best-fitting models are presented in Fig. 14. In the region constrained by the kinematic data both models reproduce equally well the input kinematics. As expected the regions outside the SAURON

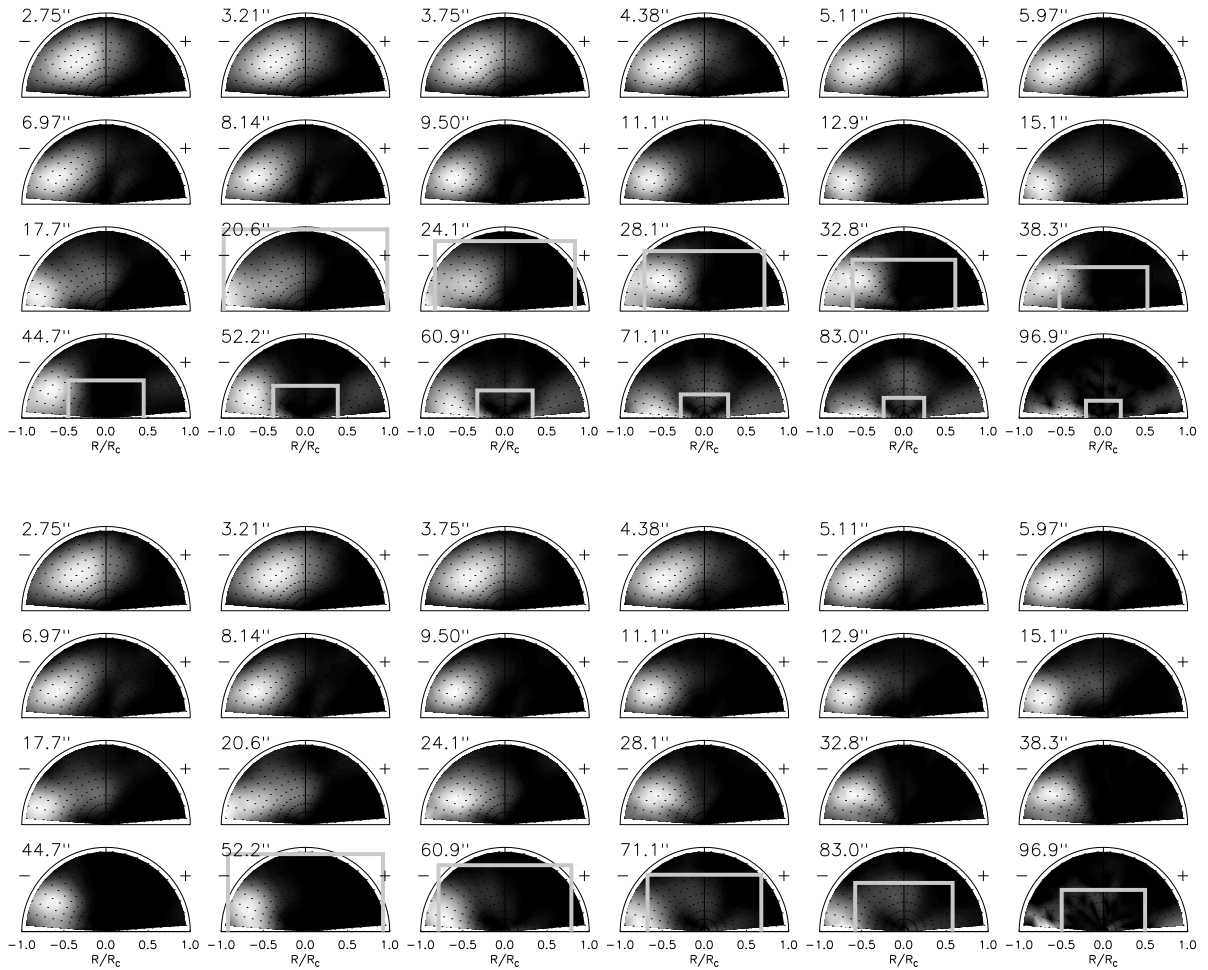


**Figure 16** — Comparison of the integral spaces of the  $f(E, L_z)$  test models. Upper five rows belong to the model constrained by the SAURON *field* kinematics and the lower five rows to the model constrained by the *Full field* kinematics. The meaning of each panel is the same as in Fig. 12. In the region constrained by the both kinematic sets the two integral spaces are indistinguishable.

*field* are not reproduced well. It is more interesting to compare the phase spaces of the models. In particular, we wish to see whether the mass weights assigned to the orbits (represented by the integrals of motion) are the same for the two models.

The corresponding integral-spaces are shown in Fig. 18. Red rectangular boxes represent the extent of the kinematics used to constrain the models. In the regions constrained by both kinematic sets, the two integral spaces are identical: both models recover the same orbital mass weights. The differences appear at larger radii (beyond  $20''$ ), outside the area constrained by the SAURON *field* kinematic set. Putting this result in the perspective of observations, the resulting phase space (in the region constrained by the observations) does not depend on the extent of the radial coverage used to constrain the model. This result strengthens the case of the NGC 2974 modelling results, where we have integral-field observations reaching  $\approx 1 r_e$ . The recovered integral space and its features would not change if we had a spatially larger observational field.

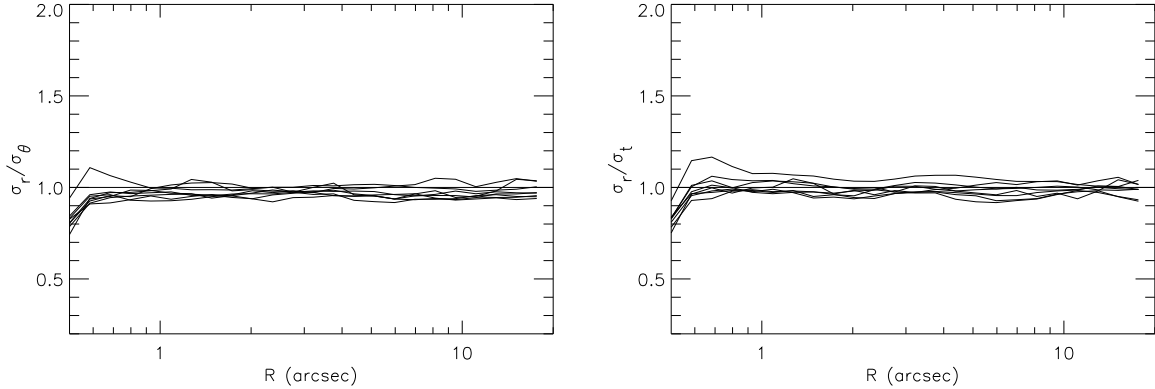


**Figure 17** — Moments of the velocity ellipsoid for the two-integral test galaxy recovered by the three-integral model (constrained by the *Full field* kinematic set). The left panel presents the ratio of the radial and longitudinal moments. The right panel shows the ratio of the radial and tangential moment as defined in the text. Different lines show the ratio of the moments in the meridional plane at different position angles, starting from the major-axis to the minor axis. In a true two-integral galaxy, all three moments of the velocity ellipsoid have to be equal. Note that the deviation inside  $1''$  are expected since the data do not constrain the model in that region.

#### 5.4 Recovery of the internal moments

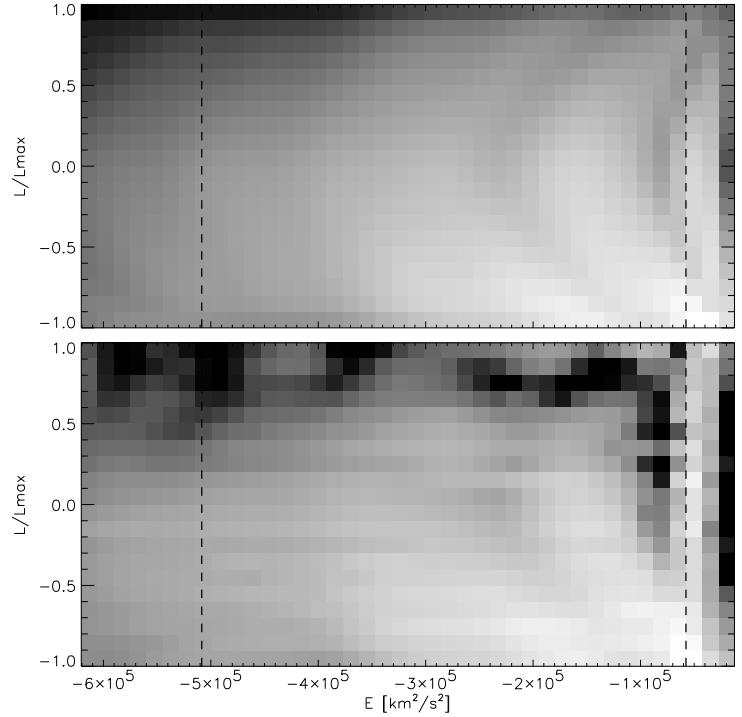
We wish to see if the best-fitting three-integral model to the  $f(E, L_z)$  test galaxy model is consistent with the input, i.e., whether three-integral models will recognise the true structure of the test galaxy. A first estimate can be achieved by investigating the internal structure of the resulting model galaxy, specifically the shape of the velocity ellipsoid. We define the tangential dispersion as  $\sigma_t = [\frac{1}{2}(\sigma_\theta^2 + \sigma_\phi^2)]^{1/2}$ . Note that  $\sigma_\phi$  includes only random motion so that for an isotropic distribution, under the given definition, the radial ( $\sigma_r$ ) and tangential dispersion are equal. Since two-integral models are isotropic in the meridional plane per definition, we expect to recover that  $\sigma_r$  is equal to  $\sigma_\theta$  and the cross-term  $\sigma_{R\theta}$  is equal to zero. In Fig. 17 we show the ratios of the moments of the velocity ellipsoids at different positions in the meridional plane and at different radii from the model constrained by the *Full field* kinematics. One can see that  $\sigma_r = \sigma_\theta$  within  $\approx 5\%$ , confirming that our three-integral model recovers the true internal moments. Also, computing the cross-terms  $\sigma_{R\theta}$ , we verified that it is negligible everywhere. Similar results are also recovered from the SAURON *field* model: in the constrained region the ratio of  $\sigma_r$  and  $\sigma_\theta$  moments are consistent with unity.

#### 5.5 Recovery of the distribution function

The previous result shows that the constructed three-integral model is a consistent representation of the input  $f(E, L_z)$  model. A more conclusive test, however, is to compare the distribution functions.

The results of the three-integral Schwarzschild method are orbital mass weights,  $\gamma'_{31}(E, L_z, I_3)$ , for each set of integrals of motion  $(E, L_z, I_3)$ , which define an orbit. The DF is related to the mass weights via the phase-space volume (for a detailed treatment

**Figure 18** — Comparison of the mass weights from the two-integral model (upper panel) and the results of the three-integral modelling (lower panel) using the two-integral model as input. The galaxy centre is on the left side. The first bin containing the contribution of the black hole was not plotted, since the resolution of the models do not allow for its recovery. The two vertical lines enclose the region constrained by the kinematic data.



see Vandervoort 1984):

$$\gamma(E, L_z, I_3) dEdL_z dI_3 = f(E, L_z, I_3) \Delta V(E, L_z, I_3) dEdL_z dI_3, \quad (6)$$

where

$$\Delta V(E, L_z, I_3) = \int_{\Omega} \mathcal{J}(\vec{x}, E, L_z, I_3) d^3x, \quad (7)$$

and  $\mathcal{J}(\vec{x}, E, L_z, I_3)$  is the Jacobian of the coordinate transformation from  $(\vec{x}, \vec{v})$  to  $(\vec{x}, E, L_z, I_3)$ , and  $\Omega$  is the configuration space accessible to an orbit defined by the integrals  $(E, L_z, I_3)$ . Unfortunately,  $I_3$  is not known analytically, so the above relation can not be explicitly evaluated, except for separable models. For this reason we limit ourselves to test the *consistency* of our three-integral mass weights with the input two-integral DF. This is possible, since if the recovered three-integral DF is equal to the input DF, then the mass  $\gamma_{2I}(E, L_z)$  assigned to the stars in a given range of  $(E, L_z)$  by the three-integral model has to be equal to the mass in the same range of the input model.

There exists a precise relation between the input two-integral DF,  $f = f(E, L_z)$ , and the corresponding orbital mass weights,  $\gamma_{2I}(E, L_z)$ . The total mass of the system is the integral of the DF over the phase-space. Using this, Cretton et al. (1999) derived the expression for the mass weights in Appendix B of their paper (eq. B4):

$$\gamma_{2I}(E, L_z) = \int_{\Omega} \frac{dM}{dEdL_z} dEdL_z \quad (8)$$

with

$$\frac{dM}{dEdL_z} = f(E, L_z) \times \oint_{ZVC(E, L_z)} (Rdz - zdR) \quad (9)$$

where the contour integral yields the area of the zero velocity curve (ZVC). Before applying eqs. (8) and (9) on the two-integral DF we rebinned it to the same grid of  $\Delta E$  and  $\Delta L_z$  as the three-integral mass weights. Finally, we approximate the integral (8) by multiplying the mass fraction in each grid cell by  $\Delta E \Delta L_z$ .

For our comparison we defined as the energy intervals the set of energies used in the construction of the three-integral models (total of 41). The interval in angular momentum was defined as a step of 0.1 of  $L_z/L_z^{max}$  from  $-1$  to  $+1$  (total of 20) for a given energy. The resulting grid of orbital weights is relatively coarse, but is representative of the model. The agreement between the two sets of mass weights is shown in Fig. 18. The main features of the given two-integral test model are reproduced quite accurately by the three-integral model. Again, the mass weights should be compared in the region constrained by the data (between the vertical lines in the figure). The mass weights of the three-integral model are relatively noisy which is mostly the consequence of imposed discreteness as well as the numerical nature of the method.

We conclude that the Schwarzschild method provides accurate dynamical models for galaxies when constrained by two-dimensional kinematics out to an effective radius.

## 6 Modelling of emission-line gas

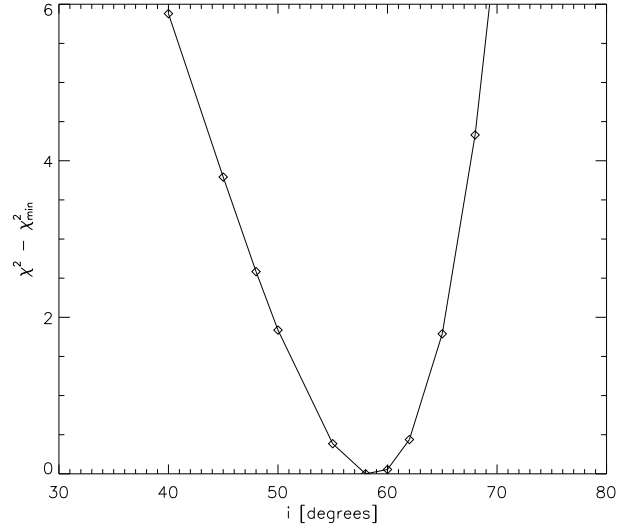
Clearly, with its prominent gas component, NGC 2974 is an unusual elliptical galaxy. The observations indicate the morphological similarity between the small (HII) and large scale (HI) gas discs. Also, long-slit measurements of stellar and gas motions detect similarities between the stellar and gas kinematics (Kim 1989; Cinzano & van der Marel 1994). In this section we investigate the inclination of the gaseous component as well as construct dynamical Jeans model of the gas disc similar to one used by Cinzano & van der Marel (1994), in order to compare them to the results of the stellar dynamical modelling.

### 6.1 Inclination of the gas disc

The existence of the emission-line gas disc in NGC 2974 can be used to infer the inclination of the galaxy assuming an equilibrium dynamical configuration. This has been attempted before and in all studies the inclination of the gas disc was consistent with  $55^\circ - 60^\circ$  (Amico et al. 1993  $55^\circ$ ; Buson et al. 1993  $59^\circ$ ; CvdM94  $57.5^\circ$ ; Plana et al. 1998  $60^\circ$ ). The high quality of the two-dimensional SAURON kinematics allows us to estimate the inclination of the emission-line gas disc more accurately.

We assume the motion of the emission-line gas is confined to a thin axisymmetric disc. We neglect the deviations from axisymmetry discussed in section 3. Using the kinematic expansion, we symmetrised the observed velocity field applying mirror-(anti)-symmetric filtering (using the first six terms) on the coefficients of the expansion (eq. 3), interpolating onto a regular grid. We set all phase coefficients to the mean kinematic angle,  $\phi_1$ , of the emission-line gas velocity field. This velocity field is an axisymmetric representation of the observed field, which can be compared to an axisymmetric model of the disc velocity field. Constructing the full two-dimensional velocity field requires only the kinematic major axis velocity profile  $v_{mj}$ . The entire field is then given

**Figure 19** —  $\Delta\chi^2$  as a function of inclination obtained by comparing the symmetrised data for NGC 2974 and the model gas disc velocity map described in 6.1.



by the standard projection formula:

$$v_{\text{LOS}}(x', y') = v_{\phi} \left( \frac{x' \sin i}{r} \right) = v'_{mj} \left( \frac{x'}{r} \right), \quad (10)$$

where  $r^2 = x'^2 + (y'/\cos i)^2$  and  $i$  is the inclination of the disc. It is clear from this formula that for a given observed major-axis velocity, the velocity field is just a function of inclination. From the first three odd coefficients ( $c_1$ ,  $c_3$  and  $c_5$ ) of the kinematic expansion we construct the velocity profile  $v'_{mj}$  along the major axis ( $\theta = \phi_1$ ). Using the major axis velocity profile, we created a set of disc velocity fields inclined at different values of  $i$ , and compared them with the symmetrised velocity field. We did not correct for the influence of the PSF as this effect is small and is confined to the central few arcseconds, which we excluded from the comparison. We also compared the models with the non-symmetrised velocity map and the results were in very good agreement, but with a slightly larger uncertainty range.

Figure 19 presents the  $\Delta\chi^2$  obtained by subtracting the disc model velocity field from the symmetrised measurements. The best-fitting inclination is  $i = 58^\circ \pm 5^\circ$  (at one  $\sigma$  level). Fig. 20 shows a comparison between the symmetrised and model velocity fields for a few representative inclinations. The differences between the model fields are mostly in the opening angle of the iso-velocity contours, which change with the inclination of the field. The model for  $i = 58^\circ$  has this angle the most similar to the observed velocity field and this significantly lowers the  $\chi^2$  of the fit.

The best-fit inclination of  $58^\circ$  for the emission-line gas is in excellent agreement with literature values determined from the various gas components. This suggests the gas is in the principal plane of the galaxy. Our best-fitting three-integral stellar dynamical model was obtained for an inclination of  $65^\circ$  with  $3\sigma$  uncertainty of  $2.5^\circ$ . This inclination is close to the inclination of  $58^\circ$  presented in this section, suggesting a good agreement between the stellar and gaseous models. There is, however, the concern that the agreement may not be as significant as it seems in light of the tests and results from Section 5.2.

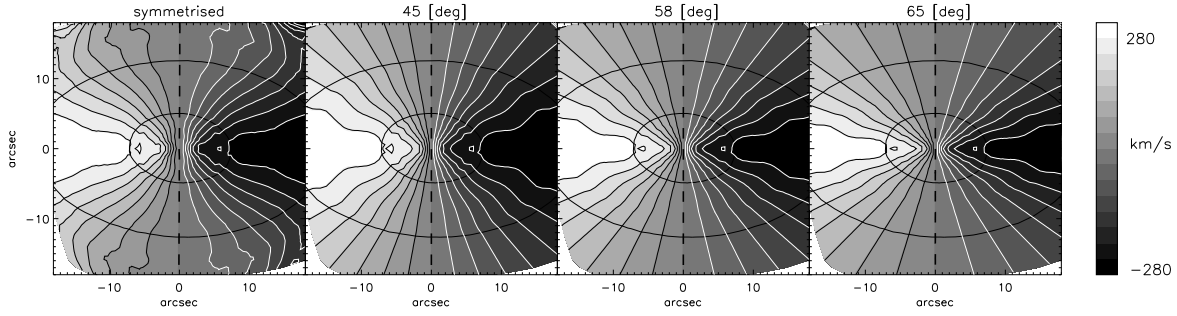


**Figure 20** — Comparisons between observed and model gas disc velocity fields. From left to right: observations (symmetrised), model fields for inclination of  $45^\circ$ ,  $55^\circ$  (best-fitting),  $65^\circ$ . Isophotal contours of total light are shown with elliptical solid lines.

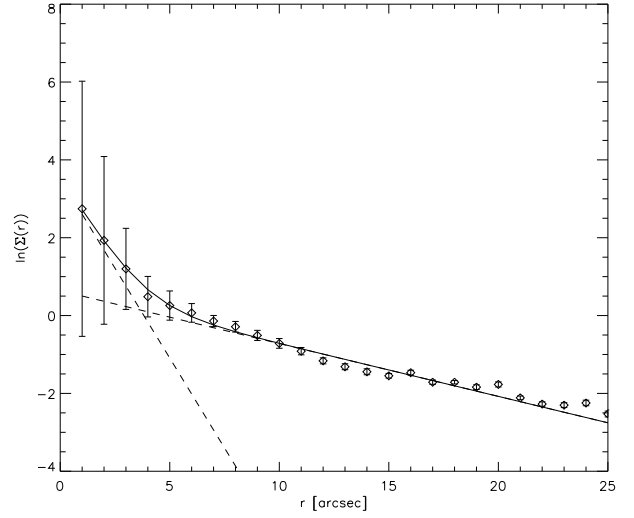
## 6.2 A simple dynamical model for the disc

At large scale, the gas kinematic maps are consistent with the assumption that the emission-line gas is moving in a thin disc. This assumption clearly breaks down in the inner few arcseconds, but at this point we neglect this effect. The observed gas velocity dispersion is high everywhere in the disc and is much larger than the thermal velocity dispersion which should be  $\sigma_{thermal} \sim 10 \text{ km s}^{-1}$  only (Osterbrock 1989). Clearly, in addition to the thermal dispersion, the gas has another source of motion, which is not presently understood, but is seen in many galaxies (Bertola et al. 1995). Several studies (e.g. van der Marel & van den Bosch 1998; Verdoes Kleijn et al. 2000) assumed that the non-thermal gas velocity dispersion is the result of ‘local turbulence’, without describing the details of the underlying physical processes. In this assumption, the gas still rotates at the circular velocity and the invoked turbulence does not disturb the bulk flow of the gas on circular orbits. The alternative to this assumption is that the non-thermal velocity dispersion component comes from collisionless gravitational motion of the gas, where the gas acts like stars: clumps of gas move on self-intersecting orbits. This is, perhaps, not very physical for gas in general, but it can be applied to estimate the difference between the circular and streaming velocity (and including the projection effect on the observed velocity) of the gas. Several studies used this approach successfully (e.g. Cinzano & van der Marel 1994; Cretton et al. 2000; Barth et al. 2001; Aguerri et al. 2003; Debattista & Williams 2004). Presently, the role and importance of the asymmetric drift remains an unresolved issue.

In constructing our simple disc model we assumed that the emission-line gas is moving in individual clumps that interact only collisionlessly. The clumps move along ballistic trajectories in a thin disc, under the influence of the galaxy potential given by the stellar distribution (Section 4). The gas kinematics are determined by solving the Jeans equations for radial hydrostatic equilibrium. Following Binney & Tremaine (1987, eq. 4-33), the streaming velocity of gas can be written in cylindrical coordinates as:

$$\bar{v}_\phi^2 = V_c^2 - \sigma_R^2 \left[ -R \frac{d \ln \rho}{dR} - R \frac{d \ln \sigma_R^2}{dR} - \left( 1 - \frac{\sigma_R^2}{\sigma_\phi^2} \right) \right], \quad (11)$$

**Figure 21** — Fit to the surface density profile of the [OIII] emission lines. Dashed lines present individual exponentials given by eq.(12).



where we have assumed the distribution function depends on the two classical integrals of motion,  $f = f(E, L_z)$ , which implies  $\sigma_R = \sigma_z$  and  $\overline{v_R v_z} = 0$ . In eq. (11),  $V_c$  is the circular velocity ( $\sqrt{R(d\Phi/dR)}$ ),  $\Phi$  is the total potential of the galaxy obtained from the MGE fit assuming inclination  $i$ ,  $\sigma_R$  and  $\sigma_\phi$  are the radial and azimuthal velocity dispersions, and  $\rho(R)$  is the spatial number density of gas clouds in the disc. Lacking any alternative, we use the surface brightness of the gas to estimate  $\rho(R)$ . Instead of using the actual measured values of the [OIII] and H $\beta$  flux, we parametrise the emission-line surface brightness with a double exponential law,

$$\rho = \rho_0 e^{-\frac{R}{R_0}} + \rho_1 e^{-\frac{R}{R_1}}, \quad (12)$$

in order to decrease the noise. The parameters are obtained from the fit to the [OIII] data shown in (Fig. 21), where the two-dimensional surface brightness was collapsed to a profile by averaging along ellipses of constant ellipticity (ellipticity of the galaxy) and position angle (PA of the galaxy). The errors are standard deviations of the measurements along each ellipse.

The relation between radial and azimuthal velocity dispersions can be obtained using the epicyclic approximation. This gives (following eq. 4-52 in Binney & Tremaine 1987):

$$\frac{\sigma_\phi^2}{\sigma_R^2} = \frac{1}{2} \left( 1 + \frac{d \ln V_c}{d \ln R} \right), \quad (13)$$

This approximation is valid for small values of the asymmetric drift  $v_\phi - V_c$ , or, in other words, in the limit of a cold disc with small velocity dispersion,  $\sigma \ll V_c$ . This is marginally the case in NGC 2974, clearly violated in the central  $< 5''$ , but it is acceptable in most of the observed regions (Fig. 22).

The observed quantities can be obtained from the calculated intrinsic properties projecting at an inclination angle  $i$ . The projected two-dimensional line-of-sight (LOS) velocity field is given by eq. (10). Within these assumptions of the disc model, the projected LOS velocity dispersion is:

$$\sigma_{LOS}^2 = (\sigma_\phi^2 - \sigma_R^2) \left( \frac{x' \sin i}{r} \right)^2 + \sigma_R^2. \quad (14)$$

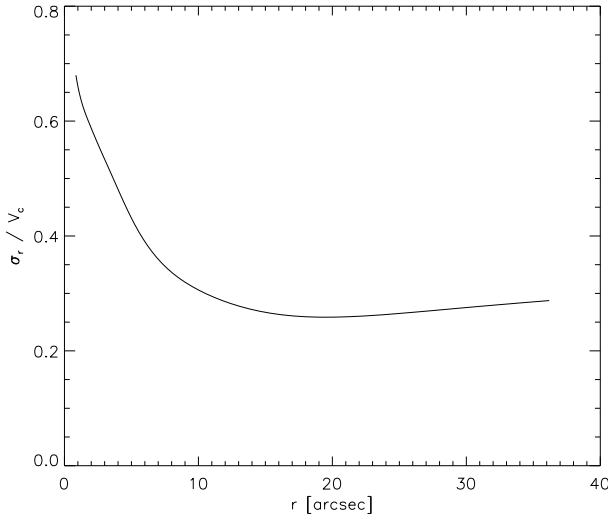


**Figure 22** — Ratio  $\sigma_R/V_C$  for the best-fitting model to the emission-line gas data.

We constructed the asymmetric drift models of the emission-line gas in NGC 2974 using the MGE parametrisation of the potential,  $Y=4.5$ , inclination  $i = 58^\circ$ , and simultaneously accounting for the atmospheric seeing and pixel size of the SAURON observations (see Qian et al. 1995 for details). In the process we assumed an exponential law for the radial velocity dispersion:

$$\sigma_R = \sigma_0 + \sigma_1 e^{-\frac{R}{R_\sigma}}, \quad (15)$$

and varying  $\sigma_0$ ,  $\sigma_1$ , and  $R_\sigma$  we constructed gaseous disc models of NGC 2974. The best-fitting model was obtained for  $\sigma_0 = 90 \pm 5 \text{ km s}^{-1}$ ,  $\sigma_1 = 190 \pm 10 \text{ km s}^{-1}$ , and  $R_\sigma = 5 \pm 1''$ . Comparison of this model with the symmetrised observations is presented in Fig. 23.

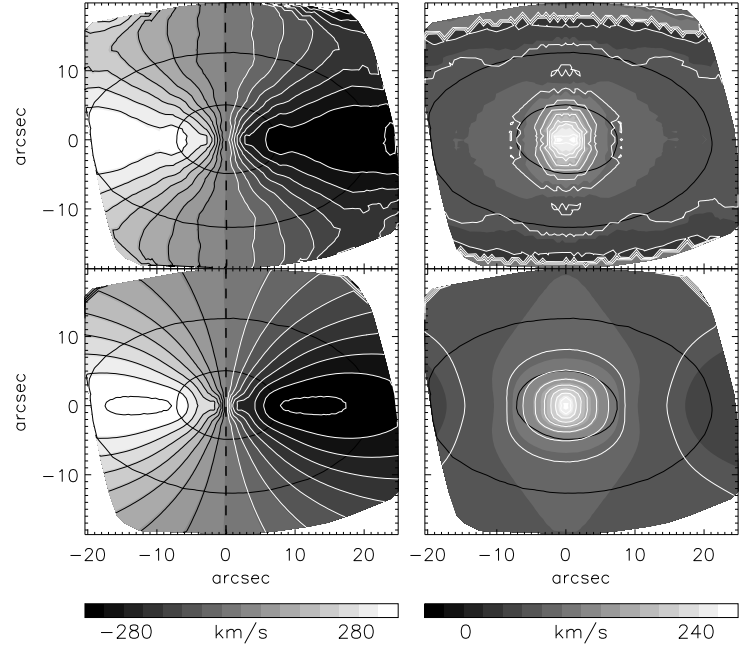
Summarising, the asymmetric drift model can reproduce the general properties of the emission-line gas disc. Using the circular velocity obtained from the stellar potential, the model is able to reproduce the bulk of the streaming velocity as well as the significant non-zero velocity dispersion of the emission-line gas. A similar finding was reported by Cinzano & van der Marel (1994). The simple asymmetric drift model, however, is not able to reproduce several details: the velocity field in the centre, the decrease of velocity at  $\sim 10''$ , and the minor axis elongation of the velocity dispersion. This is not surprising since those features are signatures of non-axisymmetry in NGC 2974 and cannot be represented by simple axisymmetric models.

## 7 Concluding remarks

This paper presents a case study of the early-type galaxy NGC 2974, which was observed in the course of the SAURON survey of nearby E/S0 galaxies.

Kinematic position angles of the stellar and gaseous kinematics of this galaxy are on average well aligned. The stellar kinematic maps exhibit mirror-(anti)-symmetry, with the kinematic angle equal to the photometric PA, and are consistent with an axisymmetric intrinsic shape. The gaseous velocity map is more complicated, with clear departures from axisymmetry in the centre of the galaxy ( $< 4''$ ). At larger radii, the gas kinematic angle is not constant, although is largely consistent with the photomet-

**Figure 23** — *Bottom Panels:* Asymmetric drift model for the best fitting parameters compared to *Top Panels:* the symmetrised (mirror-(anti)-symmetric filtering with 6 terms) mean velocity (first column) and velocity dispersion (second column). Overplotted elliptical solid lines represent typical total intensity isophotes.



ric PA, showing deviations of a few degrees. The SAURON observations of NGC 2974 confirm the existence of non-axisymmetric perturbations consistent with a nuclear bar (EGF03) as well as a possible large-scale bar. The departures from axisymmetry are not visible in the stellar kinematic maps and therefore are likely to be weak. This allows us to construct axisymmetric models of NGC 2974.

We constructed self-consistent three-integral axisymmetric models based on the Schwarzschild's orbit superposition method, varying mass-to-light ratio and inclination. The observed surface brightness was parameterised by multi-Gaussian expansion model on both ground- and space-based imaging. The models were compared with the SAURON kinematic maps of the first six moments of the LOSVD ( $v$ ,  $\sigma$ ,  $h_3 - h_6$ ). The best-fitting model has  $\Upsilon = 4.5 \pm 0.1$  and  $i = 65^\circ \pm 2.5^\circ$ . The inclination is formally well constrained, but there are several indications that the recovery of the inclination is uncertain: (i) differences between the models are on the level of systematics in the data (e.g. template mismatch); (ii) difference between the best-fit model and the data are bigger than differences between other models and the best-fit model; (iii) limitations of the models (discreteness of the cusps) may artificially constrain the inclination.

The internal structure of NGC 2974 (assuming axisymmetry) reveals the existence of a rapidly rotating component contributing with about 10% of the total light. This component is composed of orbits allowing the third integral and does not represent a cold stellar disc, although suggests a flattened structure similar to an S0 galaxy.

The results of the stellar dynamical models were compared with the results of modelling the gas component. The inclination of the gas disc, calculated from the emission-line velocity map is  $i = 58^\circ \pm 5^\circ$ , in agreement with the formally constrained stellar inclination. A simple model of the gas disc in the same potential used for the stellar modelling ( $\Upsilon = 4.5$ , but  $i = 58^\circ$ ) was able to reproduce the characteristics of the gas kinematics ( $v$  and  $\sigma$ ) on the large scale, but failed in the centre, as expected.

We performed a set of tests of our implementation of the Schwarzschild's orbit

superposition method. For this purpose we constructed a general two-integral model of NGC 2974, and used the reconstructed kinematics as inputs to the Schwarzschild's method. We tested (i) the influence of the radial coverage of the kinematic data on the internal structure, (ii) the recovery of the test model parameters ( $Y, i$ ), and (iii) the recovery of the test model DF. The tests show that:

1. Increasing the radial coverage of the kinematic data from  $1r_e$  to  $2r_e$  does not change the internal structure within  $1r_e$ . The results of the dynamical models of the SAURON observations of NGC 2974 would not change if the radial coverage would be increased by a factor of 2.
2. We find that three-integral models can accurately recover the mass-to-light ratio. Although the models are also able to constrain the inclination of the test model formally, the apparent differences between the models are small (as in the case of the real observations). Under careful examination, it is possible to choose the best model by eye, but the decisive kinematic features are below (or at the level) of the systematics in the data (e.g. template mismatch) and might be influenced by the uncertainties in the models (e.g. regularisation or variations in the sampling of observables with orbits). This suggests a degeneracy of models with respect to the recovery of inclination. More general tests on other galaxies and theoretical work is needed for a better understanding of this issue.
3. Three-integral models constrained by integral-field kinematics out to an effective radius are able to recover the true input DF, to the level of the discreteness effects in the models.

## Acknowledgments

We thank Glenn van de Ven for fruitful discussions about the recovery of the DF. DK was supported by NOVA, the Netherlands Research school for Astronomy. MC acknowledges support from a VENI grant award by the Netherlands Organization of Scientific Research (NWO).

## References

- Aguerri J. A. L., Debattista V. P., Corsini E. M., 2003, MNRAS, 338, 465  
 Amico P., Bertin G., Bertola F., Buson L. M., Danziger I. J., Dejonghe H., Pizzella A., Sadler E. M., et al., 1993, in Structure, Dynamics and Chemical Evolution of Elliptical Galaxies, p225, ed I. John Danziger, W. W. Zeilinger, and Kurt Kjaerp  
 Bacon R., Copin Y., Monnet G., Miller B. W., Allington-Smith J. R., Bureau M., Carollo C.M., Davies R. L., et al., 2001, MNRAS, 326, 23  
 Barth A. J., Sarzi M., Rix H., Ho L. C., Filippenko A. V., Sargent W. L. W., 2001, ApJ, 555, 685  
 Bender R., 1988, A&A, 193, L7  
 Bertola F., Cinzano P., Corsini E. M., Rix H., Zeilinger W. W., 1995, ApJ, 448, L13  
 Binney J., Tremaine S., 1987, Galactic dynamics. Princeton, NJ, Princeton University Press, 1987  
 Bregman J. N., Hogg D. E., Roberts M. S., 1992, ApJ, 387, 484  
 Buson L. M., Sadler E. M., Zeilinger W. W., Bertin G., Bertola F., Danziger J., Dejonghe H., Saglia R. P., de Zeeuw P. T., 1993, A&A, 280, 409  
 Cappellari M., 2002, MNRAS, 333, 400  
 Cappellari M., Copin Y., 2003, MNRAS, 342, 345  
 Cappellari M., Emsellem E., 2004, PASP, 116, 138

- Cappellari M., Verolme E. K., van der Marel R. P., Verdoes Kleijn G. A., Illingworth G. D., Franx M., Carollo C. M., de Zeeuw P. T., 2002, *ApJ*, 578, 787
- Cappellari M., et al., 2004, in *Carnegie Observatories Astrophysics Series, Vol. 1: Coevolution of Black Holes and Galaxies*, ed. L. C. Ho (Pasadena: Carnegie Observatories; <http://www.ociw.edu/ociw/symposia/series/symposium1/proceedings.html>)
- Cinzano P., van der Marel R. P., 1994, *MNRAS*, 270, 325
- Copin Y., Bacon R., Bureau M., Davies R. L., Emsellem E., Kuntschner H., Miller B., Peletier R., et al., 2001, in *SF2A-2001: Semaine de l'Astrophysique Francaise*, p 289, eds., F. Combes, D. Barret, F. Thvenin, EdP-Sciences, Conference Series
- Copin Y., Cretton N., Emsellem E., 2004, *A&A*, 415, 889
- Cretton N., de Zeeuw P. T., van der Marel R. P., Rix H., 1999, *ApJS*, 124, 383
- Cretton N., Emsellem E., 2004, *MNRAS*, 347, L31
- Cretton N., Rix H., de Zeeuw P. T., 2000, *ApJ*, 536, 319
- Cretton N., van den Bosch F. C., 1999, *ApJ*, 514, 704
- de Zeeuw P. T., Bureau M., Emsellem E., Bacon R., Carollo C.M., Copin Y., Davies R. L., Kuntschner H., et al., 2002, *MNRAS*, 329, 513
- Debattista V. P., Williams T. B., 2004, *ApJ*, 605, 714
- Emsellem E., Cappellari M., Peletier R. F., McDermaid R. M., Geacon R., Bureau M., Copin Y., Davies R. L., Krajnović D., Kuntschner H., Miller B. W., de Zeeuw P. T., 2004, *MNRAS*, 352, 721
- Emsellem E., Dejonghe H., Bacon R., 1999, *MNRAS*, 303, 495
- Emsellem E., Goudfrooij P., Ferruit P., 2003, *MNRAS*, 345, 1297
- Emsellem E., Monnet G., Bacon R., 1994, *A&A*, 285, 723
- Erwin P., Sparke L. S., 2002, *AJ*, 124, 65
- Erwin P., Sparke L. S., 2003, *ApJS*, 146, 299
- Franx M., van Gorkom J. H., de Zeeuw T., 1994, *ApJ*, 436, 642
- Friedli D., Martinet L., 1993, *A&A*, 277, 27
- Gebhardt K., Richstone D., Tremaine S., Lauer T. R., Bender R., Bower G., Dressler A., Faber S. M., Filippenko A. V., Green R., Grillmair C., Ho L. C., Kormendy J., Magorrian J., Pinkney J., 2003, *ApJ*, 583, 92
- Gerhard O. E., 1993, *MNRAS*, 265, 213
- Goudfrooij P., Hansen L., Jorgensen H. E., Norgaard-Nielsen H. U., de Jong T., van den Hoek L. B., 1994, *A&AS*, 104, 179
- Hunter C., Qian E., 1993, *MNRAS*, 262, 401
- Kim D., 1989, *ApJ*, 346, 653
- Kim D.-W., Jura M., Guhathakurta P., Knapp G. R., van Gorkom J. H., 1988, *ApJ*, 330, 684
- Lawson C. L., Hanson R. J., 1974, *Solving least squares problems*. Prentice-Hall Series in Automatic Computation, Englewood Cliffs: Prentice-Hall, 1974
- Osterbrock D. E., 1989, *Astrophysics of gaseous nebulae and active galactic nuclei*, University Science Books, 1989, 422 p.
- Pfenniger D., Norman C., 1990, *ApJ*, 363, 391
- Plana H., Boulesteix J., Amram P., Carignan C., Mendes de Oliveira C., 1998, *A&AS*, 128, 75
- Press W. H., Teukolsky S. A., Vetterling W. T., & Flannery B. P., 1992, *Numerical Recipes in FORTRAN 77* (2d ed; Cambridge: Cambridge Univ. Press)
- Qian E. E., de Zeeuw P. T., van der Marel R. P., Hunter C., 1995, *MNRAS*, 274, 602
- Rix H., de Zeeuw P. T., Cretton N., van der Marel R. P., Carollo C. M., 1997, *ApJ*, 488, 702
- Rix H., White S. D. M., 1992, *MNRAS*, 254, 389
- Rybicki G. B., 1987, in *IAU Symp. 127: Structure and Dynamics of Elliptical Galaxies*, p 397, ed. P. T. de Zeeuw (Reidel, Dordrecht)
- Schoenmakers R. H. M., Franx M., de Zeeuw P. T., 1997, *MNRAS*, 292, 349
- Schwarzschild M., 1979, *ApJ*, 232, 236
- Schwarzschild M., 1982, *ApJ*, 263, 599
- Tonry J. L., Dressler A., Blakeslee J. P., Ajhar E. A., Fletcher A. B., Luppino G. A., Metzger M. R., Moore C. B., 2001, *ApJ*, 546, 681
- Tremaine S., Gebhardt K., Bender R., Bower G., Dressler A., Faber S. M., Filippenko A. V., Green R.,

- Grillmair C., Ho L. C., Kormendy J., Lauer T. R., Magorrian J., Pinkney J., Richstone D., 2002, *ApJ*, 574, 740
- Valluri M., Merritt D., Emsellem E., 2004, *ApJ*, 602, 66
- van der Marel R. P., Cretton N., de Zeeuw P. T., Rix H., 1998, *ApJ*, 493, 613
- van der Marel R. P., Franx M., 1993, *ApJ*, 407, 525
- van der Marel R. P., van den Bosch F. C., 1998, *AJ*, 116, 2220
- Vandervoort P. O., 1984, *ApJ*, 287, 475
- Verdoes Kleijn G. A., van der Marel R. P., Carollo C. M., de Zeeuw P. T., 2000, *AJ*, 120, 1221
- Verolme E. K., de Zeeuw P. T., 2002, *MNRAS*, 331, 959
- Verolme E. K., Cappellari M., Copin Y., van der Marel R. P., Bacon R., Bureau M., Davies R. L., Miller B. M., de Zeeuw P. T., 2002, *MNRAS*, 335, 517
- Wong T., Blitz L., Bosma A., 2004, *ApJ*, 605, 183

# Nederlandse samenvatting

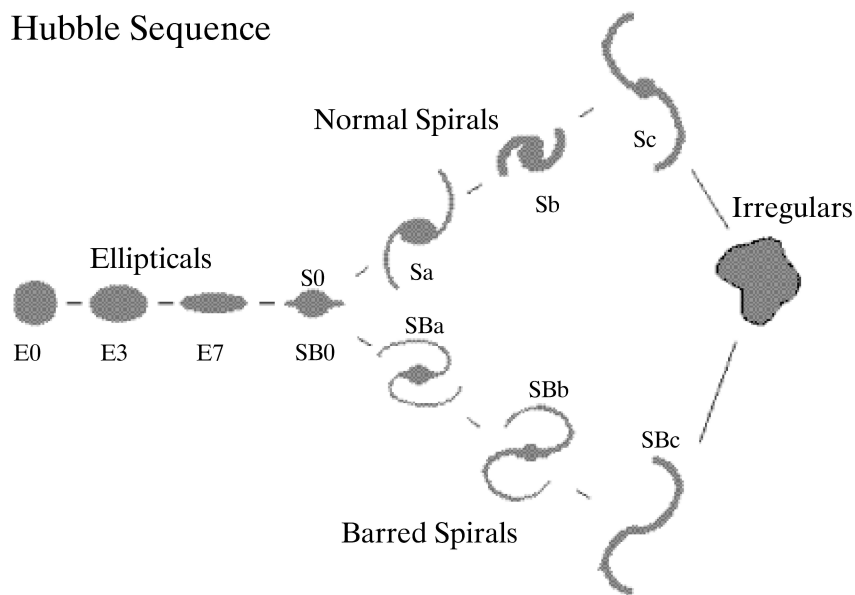
## Het begrijpen van de wereld

**D**E drang om de wereld te begrijpen en te beschrijven is karakteristiek voor mensen. Een gedenkwaardig voorbeeld van deze drang is op de omslag van dit proefschrift te zien. Dit keramisch vat, met een geordende volgorde van verschillende symbolen, is ongeveer 4500 jaar oud. Het is door een handwerksman van de *Vučedol* cultuur gemaakt en is opgegraven in 1978 in de stad Vinkovci in Oost-Kroatië. De klassieke *Vučedol* cultuur is in de tijd van het Europese Neolithicum ontwikkeld door het nieuw opkomende Indo-Europese volk. Deze wijd verspreide cultuur is genoemd naar zijn archeologisch centrale lokatie gelegen aan de rivier de Donau. De betekenis van de symbolen op het vat was tot voor kort een mysterie, totdat de archeoloog Aleksander Durman een verband ontdekte. De symbolen vertonen de dominerende sterrenbeelden aan de Europese hemel van vijfduizend jaar geleden. Dit halfgebroken vat is waarschijnlijk de oudste Europese kalender, gebruikt door de mensen van *Vučedol* voor de organisatie van hun alledaagse leven.

Vijfduizend jaar geleden keken veeboeren van de Panonische vlakte naar de nachtelijke hemel. Ze ontdekten regelmatigheden en ontwikkelden een ingewikkeld systeem voor het meten van tijd. Op deze manier konden ze een belangrijk aspect van de wereld beschrijven, met het gebruik van primitieve maar directe sterrenkundige waarnemingen. Vandaag is de sterrenkunde een wetenschap, die de weg heeft afgelegd van het *voorspellen van de toekomst* door de eerste astrologen tot het *verklaren van de feiten* door astronomen, geholpen door het waarnemen met moderne telescopen en instrumenten en het gebruik van natuurkundige wetten. In het hart van de sterrenkunde als wetenschap ligt dezelfde wens die de *Vučedol* mensen leidde: beschrijven, begrijpen en temmen van de wereld rondom ons.

Onze methoden zijn verder ontwikkeld, maar ook de astronomische thema's zijn veranderd. De sterrenkunde had een kenmerkende invloed op de mensen van de *Vučedol* cultuur, en schonk hen de kalender. Het was een bron van belangrijke informatie voor het leven. In tegenstelling tot sommige andere wetenschappen heeft de sterrenkunde tegenwoordig geen directe invloed op ons alledaagse leven meer. Het moderne sterrenkundig onderzoek is gericht op de processen die het Heelal vorm geven: van de Zon, haar burens, de Melkweg en andere sterrenstelsels, tot de verre quasars en de overblijfselen van de Oerknal. In bredere zin is de sterrenkunde vandaag een geïdealiseerde zoektocht naar de kennis van het Heelal. In aanvulling hierop legt de sterrenkunde de menselijke perceptie van de wereld vast. De vooruitgang in de sterrenkunde reflecteert zich in de veranderingen in de filosofie en cultuur.

In de jaren zestig van de vorige eeuw veranderde de grootte van het Heelal bijna ieder dag met de ontdekkingen van verre quasars. Het is nu alleen nog een kwestie van



**Figuur 1** — Het Hubble diagram. Het diagram is een classificatie van sterrenstelsels op basis van hun vorm. Aan de linker kant liggen de elliptische stelsels, die verschillende afplattingen (ellipsvormen) hebben: van de ronde E0 tot de platste E7. Daarna volgen lensvormige stelsels, die de overgang naar schijfvormige sterrenstelsels kenmerken. Schijfvormige stelsels hebben indrukwekkende spiraalarmen (rechtsboven), maar er zijn ook schijven met een balk tussen de spiralen (linksonder). Aan het einde van het diagram ligt een groep van alle andere sterrenstelsels, zonder een bepaalde vorm.

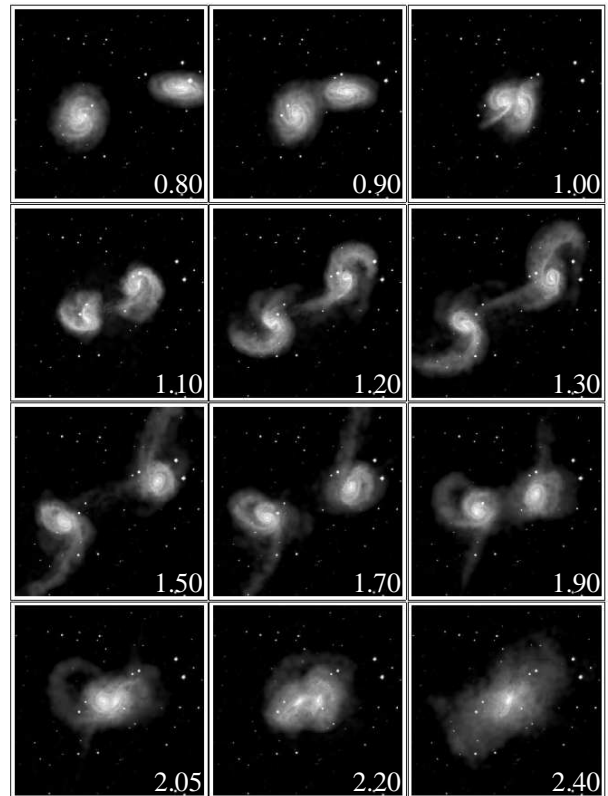
tijd tot de eerste planeet vergelijkbaar met de Aarde ontdekt zal worden<sup>1</sup>. De volgende stap is de zoektocht naar leven op zo'n planeet. De sterrenkunde is ons venster naar de complexiteit van het Heelal. Dit proefschrift richt zich op een speciaal thema binnen de sterrenkunde: de vorming en evolutie van sterrenstelsels.

## De “vroeg-type” sterrenstelsels

Sterrenstelsels zijn het elegantste beschreven door Immanuel Kant in de 18de eeuw als “eilanden universa”. Noch hij noch iemand anders wist destijds wat deze “eilanden universa” waren: ze lijken op nevels aan de hemel, maar waarvan ze gemaakt zijn en hoe ver ze van de Aarde af staan was onbekend totdat de sterrenkundigen van de 20ste eeuw nieuwe ontdekkingen deden. De waarnemingen met de 100 inch telescoop op Mount Wilson toonden aan wat de nevels werkelijk waren. Ze zijn opgebouwd uit sterren en bevinden zich op grote afstand van ons eigen “eiland universum”, de Melkweg. Er zijn veel verschillende soorten sterrenstelsels en ze worden meestal geclassificeerd in vier groepen op basis van hun schijnbare vorm (Figuur 1). De classificatie werd geïntroduceerd door Edwin Hubble in het jaar 1936 en is vandaag bekend als het Hubble diagram (Hubble reeks of Hubble's stamvorkdiagram zijn ook vaak gebruikte uitdrukkingen). Het diagram begint met *elliptische* sterrenstelsels, die er eenvoudig uit zien. Aan de andere kant liggen de schijfvormige sterrenstelsels, met hun indrukwekkende spiraalstructuren. Ze worden daarom vaak spiraalstelsels

<sup>1</sup>Meer dan honderd planeten vergelijkbaar met Jupiter zijn al gevonden rond andere sterren.

**Figuur 2** — Een tijdserie van de simulatie van een botsing van twee gelijke schijfstelsels. De tijd (in miljarden jaren) is rechtsonder van de beelden geprint. Toen de stelsels voor de eerste keer dicht bij elkaar kwamen, zorgde de zwaartekracht voor de opvallend open spiralen. Na de ontmoeting zijn de sterren en het gas van de schijven uitgeworpen in de vorm van getijdestaarten. Aan het einde van de botsing zijn de schijven vernietigd en het stelsel vormt een bolvormige verdeling van gas en sterren die er bijna als een elliptisch sterrenstelsel uitziet. Met dank aan V. Springel, MPA.



genoemd. De *lensvormige* stelsels (aangeduid met S0) liggen tussen de elliptische en spiraalstelsels in. Ze hebben een prominente schijf, zonder de kenmerkende spiraalstructuur, verzonken in een bolvormige verdeling van sterren. De vierde groep van sterrenstelsels bestaat uit de stelsels zonder bepaalde vorm: de *onregelmatige* stelsels. Hubble interpreteerde het diagram in termen van evolutie: de spiraalstelsels, met hun gecompliceerde en duidelijk zichtbare structuur, waren de logische kandidaten voor ingewikkelde en ontwikkelde systemen, terwijl de elliptische stelsels voorbeelden waren van eenvoudige systemen. De lensvormige stelsels waren een tussenvorm van deze twee soorten sterrenstelsels. Alhoewel deze verklaring niet meer aannemelijk is en de evolutie van sterrenstelsels waarschijnlijk in de andere richting van het Hubble diagram “verloopt”, worden de elliptische en lensvormige stelsels nog steeds “vroeg-type” stelsels genoemd en zijn de spiraalstelsels bekend als “laat-type” stelsels.

Sterrenstelsels zijn niet alleen uit sterren opgebouwd. Ze bevatten ook gas en stof in verschillende hoeveelheden, afhankelijk van het Hubble type: de vroeg-type stelsels hebben minder gas en stof dan de laat-type stelsels. In de zeventiger jaren van de twintigste eeuw werd een nieuw bestanddeel van spiraalstelsels ontdekt: deze sterrenstelsels zijn omringd door donkere materie. Men neemt aan dat alle sterrenstelsels omgeven zijn door halo’s van donkere materie, maar de waarnemingen voor het bewijs van donkere materie rondom elliptische stelsels geven nog geen uitsluitsel. De samenstelling van donkere materie is nog steeds niet bekend, maar de waarnemingen wijzen erop dat het de dominante vorm van materie in het Heelal is. Een theorie van de vorming en evolutie van sterrenstelsels moet alle waargenomen feiten kunnen verklaren.

Helaas is de leeftijd van een sterrenkundige veel korter dan de evolutietijd van sterrenstelsels. De sterrenkundigen werken dus als detectieven op zoek naar aanwijzingen van de processen die een rol spelen in de vorming en evolutie van sterrenstelsels. De vroeg-type stelsels zijn belangrijk, want ze bevatten maar kleine hoeveelheden van gas en stof en vormen geen nieuwe sterren: ze hebben de blauwdrukken van hun vorming bewaard.

## Een korte gids over de vorming en evolutie van sterrenstelsels

Sterrenstelsels zijn ontstaan uit schommelingen in de dichtheid van de donkere materie in het vroege Heelal. Gebieden met een grotere dichtheid verzamelen door hun zwaartekracht stof en vormen kleine objecten. Door botsingen van de kleine objecten vormen zich grotere structuren. De donkere materie domineert deze systemen, die vaak schijven van gas in hun middelpunt hebben. Onder bepaalde voorwaarden vormt het gas sterren, die het Heelal verlichten en de nieuwe sterrenstelsels zichtbaar maken.

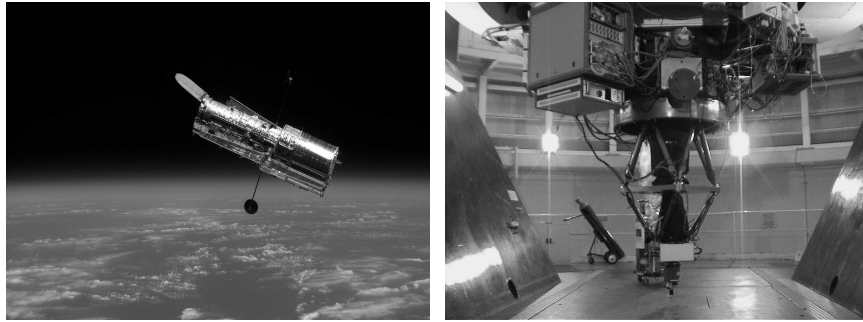
Het botsen van de kleine sterrenstelsels gaat door en als twee schijfstelsels dicht genoeg bij elkaar komen, kunnen ze versmelten en een elliptisch stelsel vormen. Figuur 2 toont een simulatie van een botsing van twee schijfstelsels. Het eindresultaat, na 2.5 miljard jaar, is een elliptische verdeling van gas en sterren. De elliptische stelsels zijn niet het eind van de evolutie. Een elliptisch stelsel kan weer een schijfstelsel worden als zij genoeg intergalactisch gas invangt, dat opnieuw een schijf van sterren kan maken. Dit spel tussen botsing en invangen wisselt vaak, maar dat zijn niet alle mogelijke processen die de evolutie van sterrenstelsels beïnvloeden. In sterrenstelsels vinden ook langzamere processen plaats ("secular processes"). Deze processen zijn het resultaat van een specifieke toestand in de sterrenstelsels, zoals hun vorm, vorm van hun zwaartekracht potentiaal (de vorm van de donkere materie halo), de hoeveelheid gas en de wisselwerking met aangrenzende (en kleinere) stelsels. De vorming van spiraalstructuren, balken, ringen van gas en jonge sterren zijn typische gevolgen van deze langzame evolutie.

## Het waarnemen van vroeg-type sterrenstelsels

Sterrenkunde is een observationele wetenschap die verschilt van andere wetenschappen, omdat de astronomische objecten niet aangepast kunnen worden voor experimenten en het niet mogelijk is ze van alle kanten te bekijken.

Gelukkig zijn er ontelbaar veel sterrenstelsels in het Heelal en met waarnemingen van ver weg gelegen stelsels kijken we naar het verleden, naar een jonger Heelal. Dit betekent dat met onderzoek van een groter aantal sterrenstelsels het mogelijk is om hun vorming en evolutie te verklaren. Om dat te doen is het belangrijk veel gegevens te verzamelen van verschillende bronnen. Voor een onderzoek naar de structuur en dynamica van elliptische sterrenstelsels bijvoorbeeld, zijn gegevens over de verdeling, kinematica en soorten van sterren nodig, evenals de verdeling van gas en stof. Daarom is dit proefschrift gebaseerd op veel verschillende waarnemingen, vanaf de grond en vanuit de ruimte, van radio tot optische golflengten.

De verdeling van sterren kan bepaald worden door het afbeelden van sterrenstelsels. Eind 19de eeuw veroorzaakte het foto toestel een revolutie binnen de sterrenkunde.



**Figuur 3** — Links: Hubble Space Telescope (HST) in zijn baan. De instrumenten van HST werden in dit proefschrift gebruikt (hoofdstuken 2 en 3). Rechts: SAURON, de twee-dimensionale spektrograaf, gemonteerd onder het focus van de 4.2m William Herschel Telescope op La Palma. De waarnemingen met SAURON werden in hoofdstuk 4 en 5 van dit proefschrift gebruikt. Met dank aan NASA en het SAURON team.

Ook de verschijning van digitale detectors, zoals CCD's in de jaren zeventig van de 20ste eeuw, heeft een enorme vooruitgang van onderzoek naar de objecten in het Heelal mogelijk gemaakt. Maar de grootste stap in het onderzoek naar sterrenstelsels was de lancering van de Hubble Space Telescope (HST) in een baan rondom de Aarde. Figuur 3 toont de HST in de ruimte. Het licht dat is verzameld met de spiegel van de HST gaat niet door de atmosfeer, die de baan van het licht verstoort en de informatie van de hemellichamen filtreert.

Waarnemingen met de HST hebben ons beeld van de “eenvoudige” elliptische stelsels drastisch veranderd: ze hebben gecompliceerde structuren met ontkoppelde kernen en schijfjes van stof en sterren in hun centra.

De bewegingen en soorten sterren in een sterrenstelsel worden onderzocht met waarnemingen van hun spectra. De sterren produceren het licht van een sterrenstelsel. Maar alleen in de dichtstbijzijnde (op minder dan 3 miljoen lichtjaar<sup>2</sup>) sterrenstelsels is het mogelijk waarnemingen aan individuele sterren te doen. Dat betekent dat het licht van sterrenstelsels het gezamenlijke licht van alle sterren langs de gezichtlijn is. We kunnen daarom alleen de gemiddelde eigenschappen van grote aantallen sterren meten. Het is ook nodig om te weten waar in een stelsel het waargenomen spectrum vandaan komt. De moderne technologie heeft het fabriceren van speciale twee-dimensionale spectrografen mogelijk gemaakt. Deze spectrografen nemen de spectra waar en registreren ook de plaats aan de hemel waar het licht vandaan komt. Het eind resultaat is een drie-dimensionale dataset met informatie over de ruimtelijke positie en de golflengte ( $x, y, \lambda$ ). SAURON (Figuur 3) is zo'n spectrograaf. Hij bevindt zich aan de William Herschel Telescoop op het Canarische eiland La Palma en wordt gebruikt voor onderzoek naar de structuur en kinematica van vroeg-type sterrenstelsels en de soorten van sterren waaruit ze bestaan.

<sup>2</sup>Een lichtjaar is de afstand die het licht in een jaar aflegt, en komt overeen met tienduizend miljard km. Sterrenkundigen gebruiken vaak de eenheid parsec:  $1\text{pc} \sim 3.3$  lichtjaar.

## Gids door dit proefschrift

De theorie van de vorming en evolutie van sterrenstelsels is ingewikkeld en bestaat uit veel stukken die begrepen moeten worden en in een samenhangend geheel moeten worden gegoten. Ieder hoofdstuk van dit proefschrift legt zich toe op een onderdeel van de theorie van de vorming en evolutie van sterrenstelsels. Het onderzoek beschreven in dit proefschrift concentreert zich op de activiteit, structuur, kinematica en dynamica van nabije<sup>3</sup> vroeg-type sterrenstelsels.

### Actieve sterrenstelsels

De kernen van veel vroeg-type sterrenstelsels zenden straling uit die niet van sterren afkomstig is. Deze kernen worden *actieve kernen* genoemd. De theorie van de activiteit in deze kernen is op het *zwarte gaten* paradigma gebaseerd. Volgens dit paradigma bevindt zich in de kernen van (bijna) alle sterrenstelsels een massief object: een zwart gat, met zo veel massa dat niets, zelfs niet het licht, kan ontsnappen aan de invloed van zijn zwaartekracht. In het verre Heelal liggen krachtige actieve kernen: quasars en radio sterrenstelsels zijn voorbeelden hiervan. Daarentegen vertonen de kernen van nabije sterrenstelsels geen, of in ieder geval niet veel, activiteit. Als we bedenken dat de nabije “slapende” kernen nakomelingen zijn van “wakkere” verre sterrenstelsels, dan moeten nabije sterrenstelsels ook in hun kernen zwarte gaten herbergen<sup>4</sup>. Eén van de mogelijke redenen van het ontbreken van activiteit in de nabije sterrenstelsels is dat er geen materiaal (brandstof) is, die in de zwarte gaten (machine) valt en de activiteit op gang brengt.

Activiteit in nabije sterrenstelsels wordt onderzocht in **hoofdstuk twee** van dit proefschrift. Een groep sterrenstelsels met en zonder stof is waargenomen met de Very Large Array radio interferometer en met de HST. Het resultaat van de waarnemingen is dat, hoewel de sterrenstelsels met stof vaker actief zijn, de sterrenstelsels zonder stof ook actieve kernen hebben. Dat betekent dat de aanwezigheid van stof, dat waarneembaar is met de HST, niet nodig is voor het bestaan van actieve kernen in nabije sterrenstelsels.

### Nucleaire stellaire schijfjes

De waarnemingen met de HST tonen het bestaan van stellaire schijfjes in de centrale delen van nabije vroeg-type sterrenstelsels aan. Deze schijfjes zijn extra dun (30 pc vergeleken met de 300 pc van de dunne schijf in onze eigen Melkweg) en soms op

<sup>3</sup>Nabij is een heel relatieve term in de sterrenkunde. De Andromedanevel, een sterrenstelsel lijkend op onze Melkweg, ligt op een afstand van circa 3 miljoen lichtjaar. De sterrenstelsels in dit proefschrift, die “nabij” worden genoemd, bevinden zich op een afstand van 20 tot 100 miljoen lichtjaar. De sterrenkundigen gebruiken deze term ook voor objecten die zich 10 keer verder weg bevinden. Hierachter begint het verre Heelal.

<sup>4</sup>Zwarte gaten zijn indirect ontdekt in zo’n 30 nabije sterrenstelsels op basis van hun invloed op de beweging van het gas en de sterren in hun nabijheid. De massa van het zwarte gat blijkt gerelateerd aan de grootte van het sterrenstelsel, en tot nu ontdekte massa’s zijn tussen de miljoen en een paar miljard zonsmassa’s. Er bestaan ook stellaire zwarte gaten van slechts enkele zonsmassa’s, die uit exploderende sterren zijn ontstaan. Het is niet bekend hoe de zwaarste zwarte gaten in de kernen van sterrenstelsels ontstonden.

een bepaalde manier verbonden met grotere schijven die ook kunnen voorkomen. Nucleaire sterschijfjes zijn heel interessante structuren, die ons informatie over centrale dichtheden, mogelijke zwarte gaten en over de evolutie van sterrenstelsels kunnen opleveren.

Er zijn twee mogelijke scenario's die beschrijven hoe de stersschijfjes ontstaan zijn. Eén is verbonden met de botsing van twee sterrenstelsels, waarvan één veel groter is dan de andere. Dan valt het gas van het kleine stelsel in de put van de zwaartekracht potentiaal, dus tot in de kern van het grotere stelsel, en onder gunstige condities wordt een schijf gevormd. In de wisselwerking met het centrale zwarte gat stabiliseert het schijfje zich en vormt het sterren. In het tweede scenario kunnen stersschijfjes het resultaat zijn van één van de langzame processen, bijvoorbeeld als gevolg van een instabiliteit van de veel grotere schijf, waar gas uit de buitendelen van het sterrenstelsel naar binnen wordt getransporteerd. Het is ook mogelijk dat een combinatie van de processen de nucleaire stellaire schijfjes vormt. In ieder geval, als de evolutie van de schijfjes anders is dan in de rest van het sterrenstelsel, kunnen we verwachten dat er verschillen zijn in de chemisch structuur en leeftijd van de sterren.

Het **derde hoofdstuk** beschrijft waarnemingen van vier nabije sterrenstelsels met bekende nucleaire stellaire schijfjes (NGC 4128, NGC 4570, NGC 4621 en NGC 5308). De sterrenstelsels werden met twee instrumenten op de HST waargenomen. Het resultaat zijn spectra en afbeeldingen met de grootste resolutie tot nu toe ( $0''.05$  en  $0''.0455^5$  respectievelijk). De waarnemingen hebben verschillende en enigszins onverwachte structuren in de kernen ontdekt, die niet noodzakelijk met de schijfjes zijn verbonden. De sterren in de onderzochte sterrenstelsels zijn oud, maar met een verschillende chemische samenstelling. Het is waarschijnlijk dat stersschijfjes zich vormen als een combinatie van zowel snelle als langzame processen. In beelden van sterrenstelsel NGC 4128 is een tijdelijk verschijnsel ontdekt. Dit is misschien de eerste supernova beschreven voor NGC 4128, maar de werkelijke oorsprong blijft onbekend.

### **Twee-dimensionele kinematische kaarten**

Als er zich geen objecten voor en achter het waargenomen sterrenstelsel bevinden, is het mogelijk met spectroscopische waarnemingen de kinematische eigenschappen vast te stellen. De snelheid van een ster is met spectraalanalyse vast te stellen, maar de gemeten spectra van sterrenstelsels bestaan uit spectra van vele sterren langs de gezichtslijn. Deze sterren hebben verschillende snelheden en het gevolg is dat de spectraallijnen veel breder zijn dan die van een enkele ster. Dat betekent dat het gezamenlijke spectrum van de sterren langs de gezichtslijn de informatie over de verdeling van snelheden bevat.

Twee-dimensionele kinematische kaarten zijn de resultaten van waarnemingen met twee-dimensionale spectrografen. Deze kaarten laten zien hoe een kinematische parameter, zoals snelheid, verandert met de positie in het sterrenstelsel geprojecteerd aan de hemel. De kaarten zijn indrukwekkend, maar het is ook nodig ze goed te analyseren. In het **vierde hoofdstuk** van dit proefschrift wordt een methode voor

---

<sup>5</sup>Een handbal balancerend op de torenspits van de kathedraal van Zagreb, gezien vanaf een terrasje in Leiden, heeft een afmeting van ongeveer  $0''.04$ .

de analyse van twee-dimensionele kinematische kaarten beschreven. De methode is gebaseerd op de harmonische analyse van de kaarten langs concentrische ringen en lijkt op de methoden van oppervlakte helderheid fotometrie en op de analyse van de snelheidskaarten van radio waarnemingen. Op grond hiervan is het *kinemetry* genoemd. De methode is voor modellen en echt gemeten kinematische kaarten (van SAURON waarnemingen) beschreven, getest en gebruikt. Het verrassende eerste resultaat is dat de twee-dimensionale snelheidskaarten van elliptische sterrenstelsels heel veel lijken op de snelheidskaarten van sterren die zich in schijven bewegen, hoewel de sterren in elliptische sterrenstelsels zich niet in schijven bevinden.

### Dynamische modellen

Het compleet begrijpen van de intrinsieke vormen en structuren van sterrenstelsels is alleen mogelijk door gedetailleerd dynamisch modelleren. Het maken van dergelijke modellen is een theoretische onderneming, die op natuurkundige wetten is gebaseerd en ideeën en veronderstellingen omvat over de te onderzoeken objecten (of processen). Alle modellen die waarnemingen reproduceren kunnen beschouwd worden als fysisch. De theoretische samenstellingen worden alleen begrensd door de menselijke fantasie, maar de wereld rondom ons is uniek. Om die te verklaren, moet de theorie kloppen met de waarnemingen.

Het **vijfde hoofdstuk** van dit proefschrift presenteert de gedetailleerde dynamische studie van sterren en gas in elliptische sterrenstelsel NGC 2974. De waarnemingen bestaan uit metingen met grond- en ruimtetelescopen en met de SAURON spectrograaf. Ze worden gebruikt voor het bouwen en het controleren van de theoretische modellen. NGC 2974 is een ongewoon elliptisch sterrenstelsel, omdat ze grote hoeveelheden gas bevat, dat geïoniseerd is door de straling van de sterren. De dynamische modellen van het gasbestanddeel zijn gebaseerd op de veronderstelling dat het gas zich in een dunne schijf bevindt, die onder een bepaalde hoek wordt waargenomen. Het gas beweegt in hetzelfde zwaartekrachtsveld als de sterren en het resultaat kan vergeleken worden met de resultaten van de modellen van de sterbewegingen.

De waargenomen verdeling van sterren in het sterrenstelsel NGC 2974 is consistent met een drie-dimensionale structuur met axiale symmetrie. De modellen van het sterrenstelsel moeten dan ook axisymmetrisch zijn. Een elegante methode voor het bouwen van sterrenstelsels is de Schwarzschild methode van superpositie van sterbanen. In deze methode worden de sterrenstelsels opgebouwd als een verzameling van sterbanen, die zich onafhankelijk gedragen, en niet als een verzameling van sterren die bewegen door onderlinge zwaartkrachtsinvloeden. De banen beschrijven dan de beweging van verzamelingen van sterren en in plaats van  $10^{11}$  sterren is een sterrenstelsel opgebouwd uit  $10^4$  sterbanen. Gebruik makend van kinematische waarnemingen van NGC 2974 worden Schwarzschild modellen voor de bewegingen van sterren gebouwd. De resultaten van deze dynamische modellen kloppen met de resultaten van de gasmodellen, maar er is ontdekt dat de modellen niet precies de inclinatie van het sterrenstelsel kunnen vaststellen.

Deze studie wordt ook voor het gedetailleerd testen van de Schwarzschild methode gebruikt. De tests worden aan een theoretisch sterrenstelselmodel gedaan waarvan alle eigenschappen bekend zijn. De methode is succesvol, omdat het mogelijk is alle

---

parameters van het model te reproduceren, ook de interne structuur en de verdeling van de sterbanen. Maar de testen hebben laten zien dat de inclinatie van sterrenstelsels met de huidige waarnemingen niet met zekerheid kan worden vastgesteld.

### **Blik naar de toekomst**

De fundamentele concepten van de vorming en evolutie van sterrenstelsels, alsook hun kosmologische achtergrond, kunnen we als bekend beschouwen. Ze zijn in een nieuw paradigma van de moderne sterrenkunde vastgelegd. Maar er zijn nog veel onopgeloste raadsels, die ons uitdagen en op ons antwoord wachten.

Het onderzoek beschreven in dit proefschrift heeft een basis gelegd voor het toekomstige werk aan twee-dimensionale kinematische kaarten. De volgende stap is het toepassen van kinometrie en dynamische modellen op een grotere verzameling van sterrenstelsels om hun structuur en eigenschappen, die het gevolg zijn van evolutie processen, te analyseren.

In het algemeen is vooruitgang mogelijk in zowel de waarnemingen als in het bouwen van theoretische modellen. De modellen van sterrenstelsels gebruiken nu de informatie van de positie en kinematica, maar niet van de soort van sterren. De sterrenstelsels zijn verzamelingen van sterren met verschillende leeftijden en chemische samenstellingen. Deze informatie moet ook in de modellen gebruikt worden om precies de evolutie van de sterrenstelsels te bevatten. Aan de andere kant zullen de modellen ook sterrenstelsels met triaxiale symmetrie gaan beschrijven. De leden van het SAURON team zijn al begonnen aan deze ideeën te werken.

Gezien vanuit de observationele kant openen de opkomst van 8 - 10m telescopen met technologie van adaptieve optiek, die de invloed van de atmosfeer corrigeert, en ook een breed gebruik van twee-dimensionale spektrografen nieuwe waarneem mogelijkheden. Deze gaan nieuw licht werpen op de structuur, kinematica en de soorten van sterren in nabije sterrenstelsels, en ook inzicht in de eigenschappen van verre kosmologisch objecten waaruit sterrenstelsels zijn ontstaan.



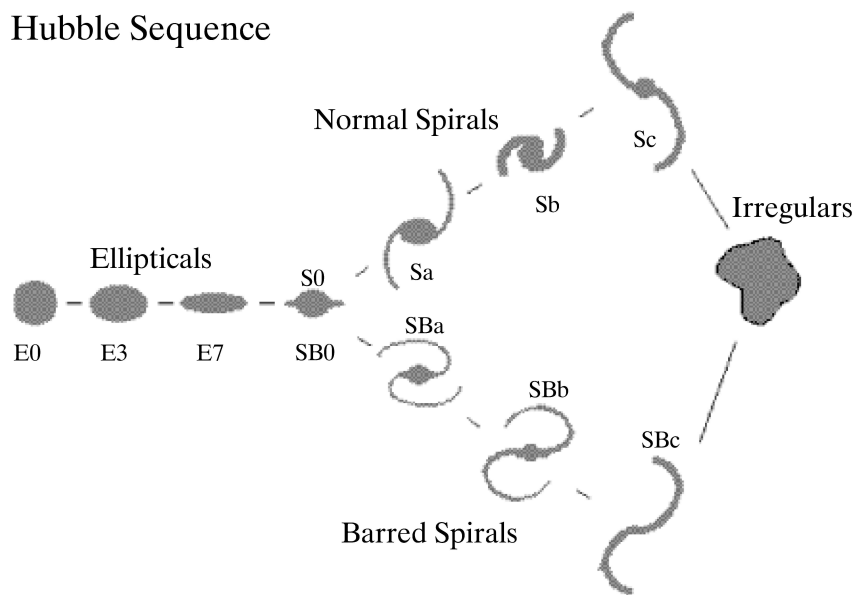
# Hrvatski sažetak

## Razumijevanje svijeta

**P**ORIV za spoznajom i opisom svijeta osnovna je karakteristika čovjeka. Znamenit primjer tog poriva nalazi se na naslovnici ove disertacije. Keramički lonac, ukrašen usklađenim nizom znakova, star je otprilike 4500 godina. Izradio ga je zanatlija Vučedolske kulture, a iskopan je 1978. godine u Vinkovcima. Klasičnu Vučedolsku kulturu razvili su tokom europskog neolitika novodošli Indo-europljani. Ova raširena kultura nazvana je po svom središnjem lokalitetu na rijeci Dunav u istočnoj Hrvatskoj. Značenje znakova na loncu bilo je do nedavno nepoznato kada je arheolog Aleksandar Durman predložio da oni predstavljaju sazviježđa koja su dominirala europskim nebom prije pet tisućljeća. Polurazbijeni lonac iz Vučedola je vrlo vjerojatno najstariji Europski kalendar, kojeg su ljudi iz Vučedola koristili za organizaciju svakodnevnog života.

Prije pet tisuća godina, stočari Panonske nizine gledali su u noćno nebo. Primijetili su pravilnosti i stvorili složen sustav mjerenja vremena. Na taj način mogli su opisati bitnu značajku svijeta koristeći primitivna, ali direktna astronomska opažanja. Danas je astronomija znanost, koja je prošla put od *proricanja budućnosti* prvih astrologa do *objašnjavanja činjenica* suveremenih astronoma, opažanih modernim teleskopima i instrumentima koristeći zakone fizike. Ipak, u središtu astronomije kao znanosti čući ista želja koja je vodila ljude iz Vučedola: razumijeti, opisati i ukrotiti svijet oko nas.

Naše metode su puno složenije, no i astronomske teme su se promijenile. Astronomija je imala značajan utjecaj na ljude Vučedolske kulture podarivši im kalendar. On je bio izvor informacija važnih za život. Za razliku od nekih drugih znanosti u sadašnje vrijeme, astronomija ne utječe izravno na naš svakodnevni život. Moderna astronomska istraživanja su usmjerena na procese koji oblikuju Svemir, počevši od Sunca, njegovih susjeda, Mliječne staze, i drugih galaksija, do udaljenih kvazara i ostataka Velikog Praska. U širem smislu, astronomija danas je idealizirana potraga za spoznajom Svemira. Sukadno s tim, astronomija bilježi ljudsko poimanje svijeta. Napretci u astronomiji se odražuju u promjenama u filozofiji i kulturi. U 1960tima veličina Svemira se mijenjala gotovao svakog dana otkrićima sve udaljenijih kvazara. Sada se čini samo pitanje vremena kada će prva planeta nalik Zemlji biti otkrivena van Sunčevog sustava<sup>1</sup>. Slijedeći korak biti će potraga za životom na takvoj planeti. Astronomija ne mijenja izravno naše živote, ali ima dugotrajan utjecaj na ljudsko društvo. Astronomija je naš prozor u složenost Svemira. Ova disertacija usredotočena je na posebnu temu astronomije: nastanak i evoluciju galaksija.



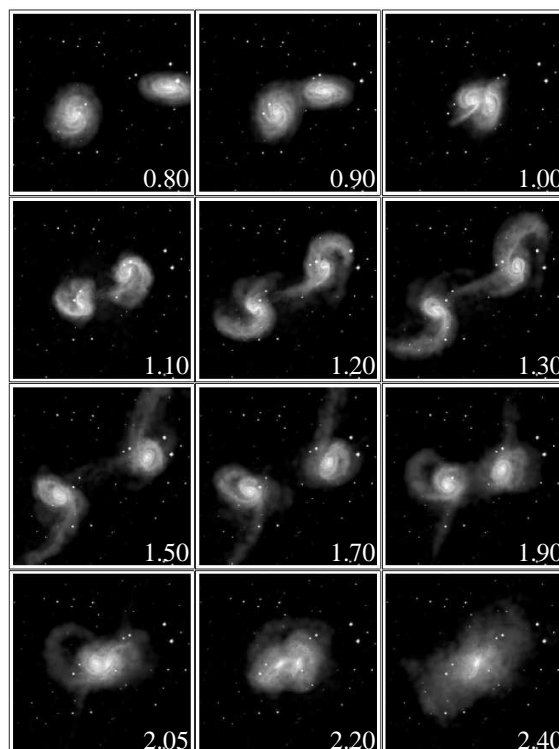
**Slika 1** — Hubblov niz galaksija. Hubblov niz je osnova klasifikacije galaksija. Galaksije su klasificirane prema svom obliku. Na lijevoj strani nalaze se eliptične galaksije koje se međusobno razlikuju prema svojoj prividnoj spljoštenosti (eliptičnosti). Gotovo okrugle galaksije su nazvane E0, a najspljoštenije su E7. Nakon njih slijede lentikularne galaksije koje označavaju prijelaz od eliptičnih do disk galaksija. Disk galaksije imaju znamenite spiralne krakove (gore), ali postoje i spiralne galaksije s tzv. prečkama koje prolaze centrom i povezuju krakove spirala (dolje). Na samom kraju nalaze se nepravilne galaksije. U tu skupinu spadaju sve galaksije bez određenog oblika.

## Galaksije ranog-tipa

Galaksije je vjerojatno najelegantnije opisao Immanuel Kant u 18. stoljeću kao "svemirske otoke". Ni on niti itko drugi nije znao što su ustvari ti "svemirski otoci". Izgledaju poput maglica na nebu, ali od čega su izgrađeni i koliko su udaljeni od Zemlje bilo je nepoznato do početka 20. stoljeća. Opažanja s 100 inčnim teleskopom na Mount Wilsonu pružila su prve naznake prave prirode galaksija. One su sastavljene od zvijezda i nalaze se daleko od našeg "svemirskog otoka", Mliječne staze. Mnogo je različitih vrsta galaksija i obično su klasificirane prema svom prividnom obliku u četiri istaknute skupine (Slika 1). Razredovanje galaksija uveo je Edwin Hubble 1936. godine, a danas je poznato kao Hubblov niz galaksija (Hubblov dijagram ili Hubblova tonska vilica su također često upotrebljavani izrazi). Niz započinje sa *eliptičnim* galaksijama koje se čine vrlo jednolike i jednostavne. Na drugom kraju su disk galaksije, sa svojim vrlo upadljivim spiralnim kracima. One se obično nazivalju *spiralnim* galaksijama, da se naglasi njihova uočljiva struktura. *Lentikularne* galaksije (često kratko zvane S0), koje nalikuju lećama, izgledaju kao prijelazni objekti između eliptičnih i spiralnih galaksija. One imaju istaknuti disk, bez značajne spiralne strukture, uronjen u skoro potpuno sferičnu raspodjelu zvijezda. U četvrtu skupinu galaksija pripadaju sve ostale galaksije bez pravilnog oblika, koje su prikladno nazvane *nepravilne* galaksije. Izrađujući niz Hubble je razmišljao o evoluciji galaksija. Spiralne galaksije, sa svojom zamršenom i lako uočljivom strukturom, bile su prirodni kandidati za složene i razvi-

<sup>1</sup>Poznato je više od stotinu planeta sličnih Jupiteru u orbitama oko drugih zvijezda.

**Slika 2** — Vremenski niz simulacije sudara dviju jednakih disk galaksija. Vrijeme (u milijardama godina) je označeno u donjem desnom kutu svake slike. Kada se galaksije približe po prvi put gravitacijske sile stvaraju izražene otvorene spirale. Nakon susreta, zvijezde i plin iz galaksija su izbačeni u obliku plimnih repova. Na kraju sudara diskovi su uništeni i pretvoreni u sferičnu nakupinu zvijezda i plina, pomalo nalik na eliptičnu galaksiju. S dopuštanjem V. Springela, MPA.



jene sustave, dok su eliptične galaksije bile primjer jednostavnih sustava. Lentikularne galaksije su pak bile stepenica između tih dviju vrsta galaksija. Iako ovo objašnjenje nije više prihvatljivo i evolucija galaksija ustvari “ide” u suprotnom smjeru na Hubblovom dijagramu, eliptične i lentikularne galaksije se još uvijek zovu galaksije ranog-tipa, a spiralne su galaksije sukladno poznate kao galaksije starog-tipa.

Galaksije se ne sastoje samo od zvijezda. One također sadrže plin i prašinu u različitim količinama, ovisno o Hubblovim tipu: galaksije ranog-tipa sadrže manje količine u odnosu na galaksije starog-tipa. U 1970tima otkrivena je nova sastavna komponenta spiralnih galaksija: ove galaksije su okružene tamnom materijom. Vjeruje se da su sve galaksije uronjene u haloe tamne tvari, ali opažački dokazi za tamnu tvar oko eliptičnih galaksija nisu potpuni. Neovisno o tome, priroda tamne tvari još uvijek nije poznata, iako opažnja jasno upućuju da je većina materije u Svemiru upravo ta tamna tvar. Teorija nastanka i evolucije galaksija mora moći objasniti sve ove opažalačke činjenice. Nažalost, životni vijek astronoma je puno kraći od vremena potrebnog za evoluciju galaksija. Astronomi stoga djeluju poput detektiva tražeći dokaze procesa koji su sudjelovali u nastajanju i daljnjem razvoju galaksija. Galaksije ranog-tipa posebno su tome pogodne jer sadrže male količine plina i prašine i, ne stvarajući nove zvijezde, sačuvali su nacрте svog nastanka.

## Kratki vodič kroz nastanak i evoluciju galaksija

Galaksije potječu od fluktuacija u gustoći tamne tvari u ranom Svemiru. Područja veće gustoće, gravitacijski djelujući na okolinu, sakupljaju materiju starajući tako malene kozmičke objekte. Manji objekti se međusobno sudaraju i spajaju stvarajući sve veće

objekte. Oni su definirani gravitacijskim utjecajem tamne tvari, a u središtu se često nalazi plin u obliku diska. Pod određenim uvjetima, iz plina nastaju zvijezde koje obasjavaju prostor i otkrivaju novo nastale disk galaksije.

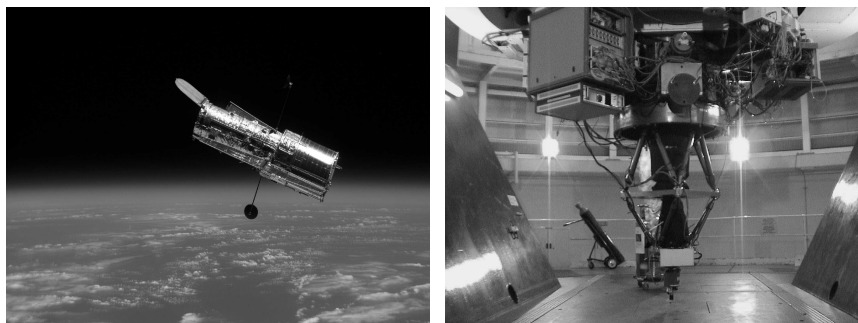
Sudaranje galaksija se i dalje odvija i ukoliko se dvije disk galaksije dovoljno približe spojiti će se, a kao produkt nastat će eliptična galaksija. Slika 2 prikazuje simulaciju sudara dvije disk galaksije. Konačni rezultat, nakon nekoliko milijardi godina, je sferična raspodjela zvijezda. Međtim, eliptične galaksije nisu kraj evolucijskog puta galaksija. Eliptična galaksija može ponovo postati disk galaksija ukoliko uhvati plin iz međugalaktičkog prostora, koji će iznova stvoriti disk zvijezda. Ova igra sudara i hvatanja dešava se naizmjenice, ali ne opisuje sve procese koji utječu na evoluciju galaksija. Uz gore navedene brze, u galaksijama, djeluju i polaganiji procesi, koje se stoga i naziva sporim procesima. Ti procesi uglavnom su rezultat specifičnosti galaksija u kojem se zbivaju, poput njihovog oblika, oblika gravitacijskog potencijala (odnosno oblika haloa tamne tvari), količine plina ili interakcije sa susjednim manjim galaksijama. Nastanak spiralnih struktura, zvijezdanih prečki, prestenovala plina i mladih zvijezda tipične su posljedice spore unutarnje evolucije galaksija. Slika 1 Uvoda u ovu disertaciju shematski prikazuju osnovne procese koji djeluju u galaksijama.

## Opazanje galaksija ranog-tipa

Astronomija je opažalačka znanost koja se od ostalih znanosti razlikuje po tome što ne možemo proizvoljno prilagođavati galaksije (ili ostale objekte) našim eksperimentima, kao niti promijeniti naš položaj u odnosu na njih. Na sreću, galaksija u Svemiru ima gotovo neizmjereno mnogo, a i opažanjem udaljenih objekata, promatra se u prošlost, u mlađi Svemir, tako da je proučavanjem većeg broja galaksija moguće dokučiti njihov nastanak i evolucijski razvoj. Ipak, da bi dobili što potpuniji uvid u trodimenzionalnu strukturu i dinamiku galaksija, nužno je sakupiti podatke iz što raznovrsnijeg i većeg broja izvora. Za proučavanje strukture i dinamike eliptičnih galaksija, na primjer, potrebni su podaci o raspodjeli, kinematici i vrsti zvijezda, te o količini i raspodjeli plina i prašine. U ovoj je disertaciji, iz tog razloga, predstavljen širok opseg opažanja: s površine Zemlje i iz Svemira, od radio do optičkih valnih duljina.

Raspodjela zvijezda utvrđuje se slikanjem galaksija. Krajem 19. stoljeća fotografski aparat je revolucionirao astronomiju, a pojava digitalnih detektora, tzv. CCDa, sedamdesetih godina dvadesetog stoljeća, omogućila je gotovo neslućeni napredak u proučavanju detalja svemirskih objekata. Ipak, pravi korak naprijed u istraživanju detalja galaksija bilo je lansiranje Hubbleovog svemirskog teleskopa (HST) u orbitu 1990. godine. Slika 3 prikazuje HST u orbiti. Svjetlost koju sakuplja zrcalo na HSTu ne prolazi kroz atmosferu, koja djeluje poput filtera odstranjajući i zaglađujući informacije koje donose fotoni iz udaljenih svemirskih objekata. Zaista, opažanja HSTom promijenila su naše poimanje "jednostavnih" eliptičnih galaksija, koje su pokazale komplicirane strukture odvojenih komponenti i malenih diskova prašine i zvijezda u svojim središtima.

Kinematiku i vrstu zvijezda u galaksiji moguće je istraživati snimanjem njihovih spektara. Svjetlost galaksije, koju teleskopi skupljaju i koja, prolazeći kroz prizmu, biva razložena po valnim duljinama, stvaraju zvijezde. Međutim, osim u najbližim



**Slika 3** — Lijeva slika - Hubblov svemirski teleskop (HST) u orbiti. Instrumenti s HSTa korišteni su u studijama predstavljenim u drugom i trećem poglavlju. Desna slika - SAURON, dvodimenzionalni spektrograf, namješten na fokus 4.2m William Herschel teleskopa na La Palmi. Opažanja SAURONom korištena su u četvrtom i petom poglavlju ove disertacije. Otisnuto sa dopuštenjem NASAe i SAURON tima.

galaksijama (udaljenih do otprilike 3 milijuna svjetlosnih godina<sup>2</sup>), nije moguće opažati spektre pojedinih zvijezda, već snimljeni spektri nose integriranu informaciju o mnoštvu zvijezda koje se nalaze na našoj liniji gledanja. Tako proučavajući spektre galaksija mi ustvari istražujemo prosječne karakteristike mnoštva zvijezda. Ipak, potrebno je znati i od kuda iz galaksije, koja se vidi kao dvodimenzionalna projekcija na nebu, dolazi snimljeni spektar. Suvremena je tehnologija omogućila izradu posebnih *dvodimenzionalnih spektrografa*, koji dijele svjetlost po valnim duljinama, istovremeno bilježeći informaciju odakle je svjetlost došla s neba. Na taj način, krajnji rezultat je trodimenzionalni skup podataka s informacijom o položaju na nebu i valnoj duljini ( $x, y, \lambda$ ). SAURON, prikazan desno na Slici 3, je upravo takav instrument. Nalazi se na William Herschel teleskopu na kanarskom otoku La Palmi i izgrađen je za proučavanje strukture i kinematike galaksija ranog tipa, kao i vrsta zvijezda koje se nalaze u njima.

## Vodič kroz disertaciju

Teorija nastanka i evolucije galaksija je složena i sastoji se od mnogo dijelova koje treba dobro razumijeti i uklopiti u sukladnu sliku. Svako poglavlje ove disertacije posvećeno je jednoj strani teorije o nastanku i evoluciji galaksija. Istraživanja predstavljena u disertaciji usredotočena su na aktivnost, strukturu, kinematiku i dinamiku bliskih<sup>3</sup> galaksija ranog-tipa.

### Aktivne galaksije

Središnji dijelovi mnogih galaksija ranog-tipa odašilju zračenje koje nije zvjezdanog porijekla. Takva središta galaksija se nazivaju *aktivnim galaktičnim jezgrama* - AGJ. Trenutno shvaćanje aktivnosti u jezgrama galaksija se bazira na paradigmi da se u središtu

<sup>2</sup>Jedna svjetlosna godina je udaljenost koju svjetlost prođe u godinu dana i iznosi otprilike deset tisuća milijardi kilometara. Astronomi često koriste i jedinicu parsek, gdje je  $1\text{pc} \sim 3.3$  svjetlosne godine.

<sup>3</sup>Blisko je vrlo relativan termin u astronomiji. Andromeda, galaksija slična našoj, nalazi se na otprilike 3 milijuna svjetlosnih godina. Galaksije u ovoj disertaciji, koje se smatra *blikim*, nalaze se na udaljenostima od oko 20 do 100 milijuna svjetlosnih godina, a astronomi će koristiti ovaj termin i na objekte koji su do 10 puta udaljeniji. Nakon toga počinje udaljeni Svemir.

svake aktivne galaksije nalazi masivni objekt, nazvan *crna rupa*, koji ima toliku masu da ništa, čak ni svjetlost, ne može uteći njegovom gravitacijskom djelovanju. Materija privučena gravitacijom crne rupe, pada na nju i tokom tog procesa snažno zrači u okolni prostor. U dalekom Svemiru postoje snažni AGJ-ovi; kvazari i radio galaksije su dva primjera. Međutim, jezgre bliskih galaksija, iako pokazuju određenu aktivnost, puno su slabije. Uoliko se uzme u obzir da su "tihe" bliske galaksije svojevrsni potomci "bučnih" dalekih galaksija, sve one moraju imati crne rupe u svojim jezgrama<sup>4</sup>. Jedan od mogućih razloga neaktivnosti u bliskim galaksijama je nepostojanje materijala (goriva), koji pada na crne rupe (strojeve) i prouzrokuje aktivnost u jezgrama.

Aktivnost u bliskim galaksijama je proučavana u **drugom poglavlju** disertacije. Skup galaksija, opažan s Very Large Array radio interferometrom i sa HSTom, je bio podijeljen na dva dijela: galaksije sa i bez prašine. Opažanja su pokazala da iako galaksije s prašinom češće pokazuju aktivnost u svojim jezgrama, galaksije bez prašine isto posjeduju aktivne jezgre. To znači da postojanje prašine vidljive sa HSTom nije nužan uvjet za postojanje AGJ u bliskim galaksijama.

### Nuklearni zvjezdani diskovi

Opažanja Hubblovim svemirskim teleskopom otkrila su postojanje malenih ( $< 1''$ ) zvjezdanih diskova u jezgrama bliskih galaksija ranog tipa. Ovi diskovi su vrlo tanki (30 pc u usporedbi s 300 pc tankog diska u našoj galaksiji), i često na neki način povezani s velikim diskovima koji postoje u nekim galaksijama. Zvjezdani diskovi su vrlo zanimljive strukture, koje se mogu iskoristiti za proučavanje centralnog gravitacijskog potencijala galaksija (npr. mjerenje centralnih gustoća i masa crnih rupa), ali i za istraživanje evolucije galaksija.

Dva su vjerojatna scenarija nastajanja nuklearnih zvjezdanih diskova. Jedan je vezan uz scenarijo interakcije galaksija, kada se veća galaksija spaja s manjom. Tada uhvaćeni plin tone do dna gravitacionog potencijala, do jezgre galaksije, i pri povoljnim uvjetima stvara disk. U interakciji sa crnom rupom u središtu, disk se dinamički stabilizira i stvara zvijezde. Po drugom scenariju, mali zvjezdani disk može nastati i pod utjecajem nekog od sporih procesa, na primjer, kao posljedica transporta materijala iz vanjskog dijela galaksije prema centru uzrokovanog nestabilnošću velikog galaktičkog diska. Moguće je da i kombinacije procesa djeluju u nastajanju nuklearnih zvjezdanih diskova. U svakom slučaju, ukoliko su diskovi imali drugačiji evolucijski put od ostatka galaksije, za očekivati je da će se to odraziti na razlikama u kemijskoj strukturi i starosti zvijezda.

U **trećem poglavlju** disertacije prikazana su opažanja četiri bliske galaksije s poznatim nuklearnim diskovima (NGC 4128, NGC 4570, NGC 4621 i NGC 5308). Galaksije su opažane s dva instrumenta na HSTu, rezultirajući sa spektrima i slikama trenutno

---

<sup>4</sup>Crne rupe su indirektno otkrivene u središtu 30tak bliskih galaksija na osnovu njihovog gravitacijskog utjecaja na kretanje plina i zvijezda u neposrednoj blizini. Njihove mase su, izgleda, povezane sa veličinom galaksije u kojoj se nalaze, a dosada otkrivene se kreću u rasponu od milijun do nekoliko milijardi sunčevih masa. U Svemiru postoje i manje, zvjezdane, crne rupe sa masom nekoliko puta većom od mase Sunca, za koje se vjeruje da nastaju u eksplozijama zvijezda. Porijeklo velikih crnih rupa u središtima galaksija nije poznato.

najviše moguće razolucije ( $0''.05$ , odnosno  $0''.0455$ )<sup>5</sup>. Opažanja su otkrila raznovrsne i pomalo neočekivane strukture u jezgrama, ne nužno povezane sa zvjezdanim diskovima. Zvijezde u proučavanim galaksijama su uglavnom stare, ali imaju različit kemijski sastav. Vjerojatno je da zvjezdani diskovi nastaju kombinacijom različitih brzih i sporih procesa. Na slikama galaksije NGC 4128 otkriven je i tranzijent, koji bi mogao biti prva zabilježena supernova u NGC 4128 galaksiji, ali čije stvarno porijeklo ostaje nepoznanica.

### Dvodimenzionalne kinematičke mape

Ukoliko nema svemirskih objekata ispred i iza opažane galaksije, spektroskopskim opažanjima moguće je odrediti njezina kinematička svojstva. Brzinu gibanja jedne zvijezde moguće je odrediti analizom njezinog spektra, ali opažani spektri galaksije se sastoje od spektara mnogih zvijezda koje se nalaze na liniji gledanja. Te zvijezde imaju različite brzine, i posljedica toga je da su spektralne linije puno šire nego u spektru jedne zvijezde. Iz tog razloga, zajednički spektar donosi informaciju o raspodjeli brzina zvijezda u galaksiji duž linije gledanja.

Dvodimenzionalne kinematičke mape produkti su opažanja sa dvodimenzionalnim spektrografima. One prikazuju kako se kinematički parametar, poput brzine, mijenja ovisno o položaju u galaksiji projiciranoj na nebo. Mape su vizualno vrlo zahvalne, međutim potrebno ih je i pažljivo proučiti. U **četvrtom poglavlju** ove disertacije opisana je metoda kojom se mape mogu opisati i u detalje proučavati. Metoda se bazira na harmoničkoj analizi mapa, i slična je metodama korištenim u istraživanju površinskog sjaja galaksija (fotometrija) i analizi mapa brzina od radio opažanja. Iz tog razlog nazvana je *kinometrija*. Metoda je prezentirana, testirana i upotrebljena na modelima kinematičkih mapa, kao i mapama opažanja sa SAURONom. Iznenadujući preliminarni rezultat je da su dvodimenzionalne mape brzina opažanih eliptičnih galaksija vrlo slične mapama brzina zvijezda koje se gibaju po kružnim putanjama u diskovima, iako se zvijezde u eliptičnim galaksijama uglavnom ne nalaze u diskovima.

### Dinamički modeli

Potpuno razumijevanje intrinzičnih oblika i struktura galaksija moguće je samo detaljnim dinamičkim modeliranjem. Stvaranje takvih modela je teoretski pothvat koje se osniva na zakonima fizike, a uključuje ideje i pretpostavke o istraživanim objektima (ili procesima). Ipak, samo modeli koji mogu reproducirati opažanja se smatraju fizikalnim. Teoretske konstrukcije su ograničene tek maštom ljudi, ali svijet oko nas je jedinstven. Da bi ga objasnila, teorija se mora slagati s opažanjima.

**Peto poglavlje** ove disertacije sadrži detaljnu dinamičku studiju zvjezdane i plinovite komponente eliptične galaksije NGC 2974. Opažanja se sastoje od opažanja sa zemaljskim i svemirskim teleskopima i dvodimenzionalnim spektrografom SAURONom, te su korištena u konstrukciji i provjeri teoretskih modela. NGC 2974 je neobična eliptična galaksija jer sadrži veliku količinu plina, koji je ioniziran zračenjem zvijezda. Dinamički modeli plinovite komponente galaksije su bazirani na pretpostavci da se

<sup>5</sup>Rukometna lopta na vrhu zagrebačke katedrale, gledana iz barke u Leidenu, bila bi velika otprilike  $0''.04$  (lučne sekunde).

plin giba u tankom disku koji je nagnut pod određenim kutem prema našem pravcu gledanja. S obzirom da se plin giba u istom gravitacijskom polju kao i zvijezde, rezultati se mogu usporediti s rezultatima modeliranja zvijezdane komponente.

Opažanja zvijezda u galaksiji NGC 2974 upućuju da njihova raspodjela čini trodimenzionalnu strukturu sa osnom simetrijom. Prema tome potrebno je napraviti modele galaksije koji imaju istu simetriju. Elegantna metoda konstrukcije galaksija je Schwarzschildova metoda superpozicije zvjezdanih orbita. Metoda se bazira na ideji da su galaksije dinamički objekti koji se bolje mogu opisati kao nakupine neovisnih orbita nego kao nakupine zvijezda koje međudjeluju svojom gravitacijom. Pojedine orbite tada ne predstavljaju zvijezde, već skupine zvijezda i umjesto  $10^{11}$  neovisnih zvijezda moguće je konstruirati galaksiju sa  $10^4$  neovisnih orbita. Koristeći kinematička opažanja galaksije NGC 2974 napravljeni su Schwarzschildovi modeli njezine zvjezdane komponente. Rezultati zvjezdanih modela se slažu sa rezultatima modela plina, iako je otkriveno da korišteni modeli ne mogu precizno odrediti nagib galaksije.

Ova studija je iskorištena i za detaljno testiranje Schwarzschildove metode konstrukcije osno simetričnih galaksija. Testovi su obavljani na teoretskoj galaksiji, dakle, modelu kojem se znaju sve osobine. Metoda se pokazala uspješnom, jer je odredila sve parametre korištenog modela galaksije, kao i njezinu unutarnju strukturu i raspodjelu zvjezdanih orbita. Ipak, testovi su potvrdili da se nagib galaksije, koristeći raspoloživa opažanja, ne može odrediti sa sigurnošću.

## Pogled u budućnost

Osnovni koncepti nastanka i evolucije galaksija, kao i kozmološka pozadina procesa koji djeluju, se smatraju poznatim i oblikovani su u paradigmatu moderne astronomije. Mnogo je, ipak, neriješenih pitanja koja nas izazivaju i očekuju naš odgovor.

Istraživanja predstavljena u ovoj disertaciji postavila su temelje budućem radu sa dvodimenzionalnim kinematičkim mapama galaksija ranog-tipa. Sljedeći korak je primijeniti kinometriju i dinamičke modele na većem broju galaksija te analizirati njihovu strukturu, kao i simetrije i svojstva koja se odražavaju na opažanim mapama i posljedica su procesa koji su oblikovali galaksije. Također, opažanja nuklearnih zvjezdanih diskova iskoristiti će se za mjerenje masa crnih rupa u tim galaksijama.

Općenito, napretci su mogući u opažanjima, ali i u konstrukciji teoretskih modela. Modeli galaksija za sada uzimaju u obzir poziciju i kinematiku, ali ne i vrste zvijezda. Galaksije su sastavljene od zvijezda različite starosti i kemijskog sastava, i ta se informacija također treba uvrstiti u modele da bi oni mogli u potpunosti opisati galaksiju, kao i njezinu prošlost. S druge strane modele treba generalizirati tako da mogu opisivati i galaksije koje imaju triakslalnu simetriju. Članovi SAURON tima započeli su već rad na ovim idejama.

S opažalačke strane, pojava teleskopa s 8 - 10 metarskim zrcalima opremljenim tehnologijom adaptivne optike, koja ispravlja utjecaj atmosfere, te široka upotreba dvodimenzionalnih spektrografa otvaraju nove opažalačke mogućnosti. One će otvoriti novi prozor u strukturu, kinematiku i vrste zvijezda bliskih galaksija, kao i uvid u svojstva udaljenih kozmoloških objekata od kojih galaksije nastaju.

# Curriculum vitae

I saw the first light on June 10, 1975 in Zagreb, Croatia, where I also spent the next twenty five years. My parents encouraged me in all my interests, and astronomy did not play a major role in my adolescent years. In the winter of 1996, I was fortunate enough to have the opportunity to go on a working visit to Višnjan Observatory. The vastness of the night sky that my eyes then saw, enticed me to investigate the processes that turn the darkness into light. On November 12, 1999 I graduated from the Faculty of Mathematics and Natural Sciences of the University of Zagreb, with a study of “Ultra-high energy cosmic rays and Greisen-Zatsepin-Kuzmin cutoff”, under the supervision of Dr. Mladen Martinis.

After a period of work at the Institute Ruđer Bošković, in the group of Dr. Martinis, I moved to Leiden to work on a PhD project “Nuclei of nearby early-type galaxies” under supervision of Dr. Walter Jaffe and Prof. Tim de Zeeuw. The goal of this project was to study in detail the structure, kinematics and dynamics of nearby galaxies using observations from the Hubble Space Telescope and by the new integral-field spectrograph, SAURON, at the William Herschel Telescope. During this project, I joined numerous observing runs at the William Herschel Telescope on La Palma, the Canada-France-Hawaii Telescope on Mauna Kea, and the MDM telescope on Kitt Peak. I participated in a NOVA fall school in Dwingeloo (2000), in conferences on La Palma (2001) and in Ringberg (2002), in the IAU Symposium in Sydney (2003) and the Lorentz Center meeting with the Nukers (2004). During the last four years I have taken part in all meetings of the SAURON team, of which I become a full member in 2003. I enjoyed organising the seasons of the observatory football team, as well as helping and participating in Science and Open day activities. I learned a great deal by assisting in the course of Active Galactic Nuclei given by Prof. Tim de Zeeuw.

My investigations of light in the Universe will continue at Oxford University where I will join the group of Prof. Roger Davies.

## Nawoord / Acknowledgments

FOUR years ago I started on a journey, with two suitcases and a back-pack. How lonely I felt on that September day! The journey is about to come to its end, and I feel everything but alone. During the last four years I carried old friendships along, but I also met so many interesting people on the way. The last four years were not only spent on the work presented in this thesis, and you all made them pass too quickly.

I am greatly indebted to Michele Cappellari, who was always available and had ready advice that helped in the making of this thesis. I am also grateful to Richard, Glenn, Ellen and Jesus for numerous discussions and patiently letting me use their computers. My sincere thanks go to the members of the SAURON team, who offered so much inspiration necessary for finishing this thesis. I am proud to be a member of this team. I am very grateful to Anne-Marie Weijmans for correcting and adding many a beauty mark to "my Dutch" in the Nederlandse samenvatting. I am greatly indebted to the secretarial support of Marja Zaal, Kirsten Groen and Jeanne Drost. The members of the Leiden computer group deserve all the praise, for readily answering all my questions and often working after-hours to make the system reliable. I am also grateful to Prof. Pavlovski for telling me The Netherlands is the place to be, and to Dr. Martinis for encouraging and helping me to go. I have enjoyed the hospitality of the Johns Hopkins University in Baltimore, where a part of this thesis research was conducted. I thank het Leids Kerkhoven Bosscha Fonds for financial support. I would also like to thank M.E.J. van den Bos - van Sambeek and the workers at IPA/ECM for helping an "allochtoon" to feel at home.

Dragi moji roditelji, bez vaše dobrote, podrške i pouzdanja u mene, a ponajviše bez vas samih, sigurno ne bih pisao ove redove i zato ovu knjigu posvećujem vama. Brate moj, ti i tvoja obitelj ste bili uvijek spremni pomoći i razveseliti me. MariaRosa, you melted most of the stress and helped along the way so much!

There are many people at the Sterrewacht that made the past four years unforgettable. The friendship with Wouter and Kirsten started over combined cooking and Dutch lessons, and it went on to many relaxing activities, trips and outings. Gijs, thanks for the hint to put a lot of onion on a herring. Garrelt, I enjoyed our cycling trips. Kirsten and Richard, I will never forget all the tasty meals you cooked for me, as well as your support, friendship, books and, of course, the name of the best whiskey ever. Pedro and Ivo, our outings, movies and Friday evening discussions kept me sane in the last year. Mariska, Erik-Jan, Kristen, Nadine, spelers van de Forza voetbal team, Zan, Ammerentie, Carlo, Jaap, Robb en de andere schermers van de LUSV, hartelijk bedankt voor alles. Joško, Bojan, Robi, Fanči, Hrčo, Ico, Božo, Šime, Hrvoje i Tomo - naši razgovori, susreti, bordanja, ronjenja, morski i zagrebački provodi, nezaboravni su trenutci koji su smanjivali udaljenost od domovine.

At the end I would like to thank all the good people of Leiden, who made my stay so enjoyable and made me feel at home here. The hardest part of the PhD project comes now: to leave you all.